DYNAMIC ANALYSIS AND CONTROL OF LIGHTWEIGHT MANIPULATORS WITH FLEXIBLE PARALLEL LINK MECHANISMS

By

Jeh Won Lee

DOCTOR OF PHILOSOPHY DISSERTATION

The George W. Woodruff School of Mechanical Engineering

GEORGIA INSTITUTE OF TECHNOLOGY
ATLANTA, GA 30332

DYNAMIC ANALYSIS AND CONTROL OF LIGHTWEIGHT MANIPULATORS WITH FLEXIBLE PARALLEL LINK MECHANISMS

A DISSERTATION

Presented to

The Faculty of the Division of Graduate Studies

By

Jeh Won Lee

In Partial Fullfillment

of the Requirement for the Degree

Doctor of Philosophy

in the School of Mechanical Engineering

Georgia Institute of Technology

June 1990

DYNAMIC ANALYSIS AND CONTROL
OF LIGHTWEIGHT MANIPULATORS
WITH FLEXIBLE PARALLEL LINK MECHANISMS

Approved: Date Approved by Chairman: _____

_____ _____

Wayne J. Book, Chairman Anthony J. Calise, A.E.

_____ _____

Stephen L. Dickerson, M.E. James I. Craig, A.E.

_____

Aldo A. Ferri, M.E.

Dedicated to

my Parents,

Kyung Hee, and Yoo Jin

ACKNOWLEDGMENTS

Many people helped me to complete this work. First of all, I wish to express my appreciation to my advisor, Professor Wayne J. Book for suggesting the subject of the thesis, for his invaluable support and guidance over the course of this research.

I would also like to thank Professors Stephen L. Dickerson, Anthony J. Calise, James I. Craig, and Aldo A. Ferri for their review and comments.

Special thanks are given to James D. Huggins for his help in the controller implementation and the hardware building which made the experiment possible, for his tremendous effort in reading my dissertation, for his devotional help whenever needed. It was my best luck to have an opportunity to work with him.

I wish to thank three staff members of Marshall Space Flight Center, John Rakoczy, John Sharkey, and Dr. Waites, for their help of implementing and running TREETOPS.

My appreciation is extended to members of the Flexible Automation Laboratory, in particular to my Korean fellows, Dong-Soo Kwon, Soo- Han Lee, Jae-Young Lew, Eun-Ho Lee for their beneficial discussion and help.

I wish to express my gratitude to my parents for their devotional love and continued encouragement and support to a higher education. To Kyung Hee and Yoo Jin, my beloved wife and daughter, I express my appreciation for her love and patience during my hard times.

This work was supported by the NASA Grant NAG 1 - 623.

TABLE OF CONTENTS

LIST OF TABLES

LIST OF FIGURES

SUMMARY

The flexible parallel link mechanism is designed for increased rigidity to sustain the buckling when it carries a heavy payload. Compared to a one link flexible manipulator, a two link flexible manipulator, especially the flexible parallel mechanism, has more complicated characteristics in dynamics and control. The objective of this research is the theoretical analysis and the experimental verification of dynamics and control of a two link flexible manipulator with a flexible parallel link mechanism.

Nonlinear equations of motion of the lightweight manipulator are derived by the Lagrangian method in symbolic form to better understand the structure of the dynamic model. The resulting equations of motion have a structure which is useful to reduce the number of terms calculated, to check correctness, or to extend the model to higher order. A manipulator with a flexible parallel link mechanism is a constrained dynamic system whose equations are sensitive to numerical integration error. This constrained system is solved using singular value decomposition of the constraint Jacobian matrix. Singular value decomposition is a stable algorithm for the dynamic analysis of a constrained system. Elastic motion is expressed by the assumed mode method. Mode shape functions of each link are chosen using the load interfaced component mode synthesis. The discrepancies between the analytical model and the experiment are explained using a simplified and a detailed finite element model. The step response of the analytical model and the TREETOPS model match each other well. The nonlinear dynamics is studied using a sinusoidal excitation. The nonlinear dynamics due to the flexibility is significant. However, the nonlinearity of RALF (Robotic Arm, Large and Flexible) is not fully studied experimentally due to the speed limitation of the hydraulic cylinder. The actuator

dynamic effect on a flexible robot was investigated. The effects are explained by the root loci and the Bode plot theoretically and experimentally. For the base performance for the advanced control scheme, a simple decoupled feedback scheme is applied.

CHAPTER I

Introduction

1.1 Motivation

A large two degree of freedom flexible manipulator designated RALF (Robotic Arm, Large and Flexible) as shown Fig. 1.1 has been constructed in the Flexible Automation Laboratory at Georgia Tech. The structure consists of two ten foot long links made of aluminum tubing actuated by hydraulic cylinders. The upper link is driven by a parallel link mechanism. This large manipulator can reach farther than a traditional robot. Such a configuration would be useful for material handling, for welding, or for ultrasonic inspection of a large structure such as an airframe . Using a lightweight material, it is possible to construct a large manipulator with low power consumption and high speed operation. However, the control law must take into account the reduction of the structural vibrations due to the distributed flexibilities of links.

In a conventional serial link mechanism, the upper link is driven by a motor attached at the tip of the lower link. The weight of the second motor must be carried by the first motor which increases the torque and power the first motor must provide. Especially in lightweight arms, the weight and reaction torque of the second motor increases the structural vibration of the lower link. The structural vibration makes the lower link fatigue more quickly. To reduce these effects, the rigidity of the lower link should be increased. One possible remedy is to include

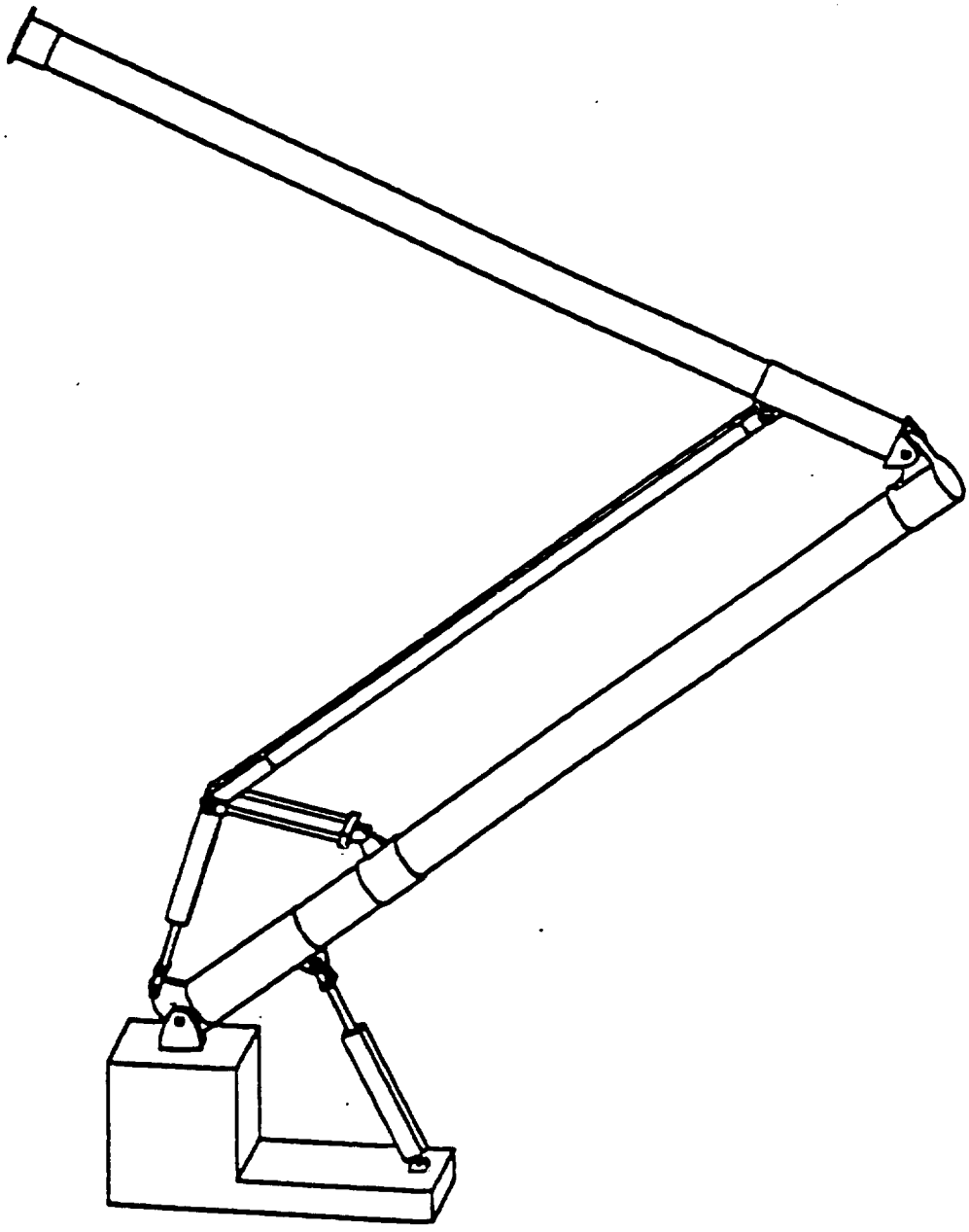

Figure 1.1: RALF (Robotic Arm, Large and Flexible)

a parallel drive mechanism. The advantages of parallel drive mechanisms are high rigidity, high loading capacities, and lower interaction between joints.

Although a variety of research on serial link mechanisms can be found in the robotics literature, the studies of closed-loop chains such as the parallel mechanism are rare and mostly concerned with rigid manipulators. In a parallel mechanism with rigid links, there is a simple relationship between generalized coordinates. However, in a parallel mechanism with flexible links, this relationship is expressed in the form of a complicated nonlinear algebraic constraint equation. To solve the dynamics of a flexible parallel link mechanism, a mixed set of differential equations of motion and nonlinear algebraic equations must be solved simultaneously. Because the numerical integration of these equations is sensitive to numerical error, a stable integration algorithm is required.

One link flexible manipulators have been studied in both theoretical and experimental aspects recently. However, a different approach is needed in dynamic analysis and control of two link flexible manipulators.

First, two link flexible manipulators have highly nonlinear interaction terms between links. Furthermore, dynamic equations of motion of flexible manipulators are more complicated than those of rigid manipulators. The number of equations of motion increases as the number of modes to be included increases. It is difficult to understand the effect of flexible motion on rigid motion via recursive forms of the equations of motion for a multi-link arm even if it were efficient to derive a inverse dynamics. On the other hand, a closed form of the equations of motion is useful in understanding the characteristics of model parameters. However, the equations resulting from existing closed forms are too complex to serve this purpose. Therefore, a method which is structurally well organized and computationally efficient must be developed.

Secondly, mode shape functions of each link are not simple to derive due to coupling between links. The common approach to determine modes has been the finite element method. Even though the finite element method is a systematic modeling technique for complex mechanisms, computational efficiency is lost due to the fact that a large number of elements are needed to obtain appropriate and accurate results. Because of its use in control design, the resulting model should be simple enough to render the analysis at hand tractable while retaining the significant features of the original structure. For simple structural shapes, a continuous system approach using assumed modes seems to be an easier way. Using appropriate modes, a lower order model can be obtained.

Third, the control of a flexible manipulator has different characteristics compared to the control of a rigid manipulator. Even though control inputs are applied only at the joint, rigid body motion and elastic body motion have to be controlled simultaneously. The control law constructed on the basis of a reduced order model must have robustness for truncation error and for uncertainty of its parameters. The control bandwidth with joint feedback alone is below the lowest vibration frequency. Low control bandwidth means a long settling time and poor disturbance rejection to external forces. Increased control bandwidth can be obtained by feedback of additional states such as strain and tip position which provide information on the elastic motion of the manipulator. The approximate mode shapes are necessary to get these additional states. Whereas the one link arm is essentially linear, the two link arm is strongly nonlinear and its dynamics change according to its configuration.

1.2 Review of Previous Work

This review consists of several topics which are mentioned in the previous section on motivation.

1.2.1 Derivation of Equations of Motion

One of the primary concerns in manipulator dynamics is computational efficiency. For the efficient form of the manipulator dynamic equations, various recursive formulations for rigid manipulators using Lagrangian [26], Newton - Euler [42], or Kane's method [34], have been proposed. For flexible manipulators, Book used the method of homogeneous transformation matrices. He first considered small linear motions of a massless elastic chain [7] and later considered distributed mass and elasticity [10]. When the recursive formulation is used, the structure of the dynamic model which is quite useful in providing insight for designing the controller is destroyed. To overcome this problem, several programs for rigid manipulators have been developed to derive the equations of motion in symbolic form [13,52]. Symbolic formulation has the advantage of allowing the identification of the distinct components of the model. For flexible manipulators, Maizza-Neto [45] derived symbolically the equations of motion of a two link flexible manipulator by hand. A systematic method to symbolically derive the nonlinear dynamic equations of multi-link flexible manipulators was presented by Cetinkunt [14]. However, he did not explore the structure of the terms in the flexible manipulator model. The conceptual framework leads to guidelines for simplifying robot dynamics. The physical interpretations and structural characteristics of the Lagrangian dynamic model for rigid robots were derived by Tourassis and Neuman [71,72]. The inertia matrix is induced by the masses and center of mass of links. In turn, the centrifugal and Cori-

olis coefficients are derived from an inertia matrix through the Christoffel symbol. But, the method of deriving mass matrices is not efficient for a flexible manipulator. Asada [2] presented a method which uses the Jacobian matrix to derive the mass and gravity matrices. His method is found in this thesis to be very efficient in modelling a flexible manipulator. Low [41] used the Jacobian matrix in deriving the equations of motion of a flexible manipulator. However, the structure of centrifugal and Coriolis force is still complicated and hard to understand.

1.2.2 Mode Shape Function

A flexible manipulator that undergoes large rigid body rotation can be modelled in terms of either an *unconstrained* modes method where the entire body vibrates, or a *constrained* modes method where the joint is held motionless. The unconstrained modes approach is more rigorous. However, the calculation of the natural frequencies and the mode shapes is relatively complicated and it is difficult to extend this approach to multi-link arms. On the other hand, the constrained modes method is an approximate solution of the unconstrained modes method when the beam to hub inertia is small enough. Because with the constrained modes method it is simple to derive the natural frequencies and the mode shapes, it can be applied to multi-link arms. The unconstrained modes and constrained modes methods were compared by Barbieri [3]. Hughes [29] and Hablani [23] compared the accuracy of these two methods by modal identities and completeness indexes respectively. Schmitz [62] and Hastings [25] experimentally verified their model with unconstrained modes method and constrained modes method respectively. In the case of multi-link arms, the boundary conditions at the joint are not clear because there is coupling between links. In most studies of multi-link flexible arms, the boundary conditions of each link are assumed to be clamped -free. The accuracy of this assumption has not been

yet experimentally confirmed.

The reduced order model for design of controllers can be obtained by truncating the modes with frequencies higher than the actuator bandwidth. This is reasonable because high frequency modes generally have small amplitudes and can be regarded as disturbances. Furthermore, actuators which are not excited by the high frequency modes act as lowpass filters . Hughes [30] and Skelton [68] investigated the criteria of model order reduction. Hastings [25] and Schmitz [62] got good experimental results using only two or three modes. Tsujisawa [74] derived a reduced order model for RALF by the modal cost analysis method. He suggested that using the first two modes of each link is optimal from the control point of view.

The elastic deformation of links can be expressed by a set of admissible functions. The selection of admissible function sets is not unique. The finite element method (FEM) uses simple admissible functions. FEM can easily deal with complicated structures with complex boundary conditions. However, a large number of elements are required to obtain accurate modes and frequencies. To reduce the dimension of the model, a component mode synthesis (or substructure modal synthesis) has been developed. A complete structure can be regarded as an assembly of substructures. The lower frequencies and corresponding mode shape functions of the complete structure can be obtained by synthesizing a truncated set of modal properties of the substructure. Three basic methods have been developed depending on whether its interface is held fixed [19], free [27], or loaded [6]. Sunada [70] and Shabana [66] obtained a nonlinear finite element model of a flexible structure for a large rigid body motion by using the component mode synthesis. However, these programs still execute too slow for a real time control.

1.2.3 Constrained Dynamic System Analysis

The dynamics of robot manipulators containing general closed chains in their structures has been studied very little. The parallelogram, a special case of the closed chain, has been well studied by Asada [1]. Chung [18] derived the equations of motion of RALF, but he assumed that the actuating link and the lower link had the same mode shapes so that the constraints did not need to be considered. Megahed [48] and Luh [43] derived the equations of motion of rigid robots with closed chains by Lagrangian and Newton-Euler methods respectively. However, a computationally stable algorithm is required because the model is sensitive to numerical error.

There are two conceptual approaches to solve the constrained equations of motion. One approach solves the equations of motion simultaneously with the constraint equations. The other approach uses a reduction method that eliminates the constraint forces explicitly from the equations of motion. It is difficult to solve a mixed set of differential equations of motion (dimension n) and nonlinear algebraic equations of kinematic constraint (dimension m). For this purpose, Nikravesh [54] reviewed three integration algorithms. These are the direct integration method, the constraint violation stabilization method and the generalized coordinate partitioning method. The direct integration method [48,43] converts the algebraic equations to second order differential equations, then solves these equations with equations of motion. This method results in constraint violations because, as time progress, the integration numerical error accumulates. The constraint violation stabilization method [4] introduces constraint violations as a feedback term to correct the violations in the next integration step. One difficulty of this method is the selection of proper feedback gains. These two methods are sensitive to initial conditions on

the system. In the third method [76], the generalized coordinates are partitioned into independent (dimension n - m) and dependent (dimension m) sets. Numerical integration is solves for the independent generalized coordinates. The choice of the correct initial condition is not critical and the dimension of the equations of motion is minimum. When generalized coordinates are partitioned, an important consideration is the choice of independent generalized coordinates. An arbitrary selection of independent generalized coordinates often results in ill - conditioned matrices. Wehage [76] identified independent generalized coordinates by using LU partitioning of the constraint Jacobian matrix. Mani [46] and Singh [67] used singular value decomposition, and Kim [37] used QR decomposition. A unique and accurate independent set of generalized coordinates can be obtained from the last two methods. Singular value decomposition is a more robust algorithm than the QR method and has a variety of applications in linear control systems.

1.2.4 Motion Control of a Flexible Robot

A colocated control scheme, in which sensors are colocated with actuators, has been used for most flexible manipulator control. With a PD control for each joint (Independent Joint Control), Book [7] showed that the maximum closed loop bandwidth of rigid body motion is a half of the system first natural frequency. If interjoint feedback terms are included between actuators (Generalized Rigid Control), the closed loop bandwidth can be increased up to the system first natural frequency. Golla et al. [21] showed that IJC also provided control as good as GRC.

A noncolocated control, where the tip position was measured by an optical sensor, was implemented by Schmitz [62]. Because tip position feedback alone creates a nonminimum phase system, the achievable gain is limited. However, improved response, two times faster than the first natural cantilever frequency, was obtained by

the combined feedback of tip position, link strain, and hub rate. Better disturbance rejection to end position external forces than with joint feedback alone was also obtained . However, the response time is limited by the inherent wave propagation delay for the beam. A precise dynamic model and a sophisticated control law are required for satisfactory response.

Control of flexible robots is characterized by control concepts similar to those being used in the control of rigid body robots. Four major methods have been developed: linear feedback control, computed torque control, adaptive control, singular perturbation control.

For a one link flexible manipulator, Hastings [25] implemented a Linear Quadratic Regulator with full state feedback. The time varying modal amplitudes were reconstructed from strain measurements. A reduced order observer was utilized to obtain estimates of the modal velocities from the reconstructed modal amplitudes. Sakawa [61] also used LQR. Schmitz [62] used a Linear Quadratic Gaussian regulator and its reduced order compensator. These compensators were experimentally verified regarding robustness and disturbance rejection. Krishnan and Vidyasagar [40] experimentally showed that the performance obtained using the bounded input H_2 optimal controller was better than that obtained using a discrete time LQG controller. For a two link flexible manipulator, Maizza-Neto [45] discussed the use of a pole placement algorithm to obtain full state feedback gains. Full state feedback showed high sensitivities to parameter perturbations and higher torque requirements. Ower and Van De Vegte [56] applied a classical design technique using Bode plots to a transfer function model of a two link flexible manipulator. The last two methods were not experimentally verified.

Unlike one link flexible manipulators, the two link flexible manipulator is strongly nonlinear due to interactions between links. Bayo [5] used a computed torque

method for trajectory control. The torque at each joint can be found in the frequency domain by means of an iteration procedure. However, the iteration aspect prevents this method from being used in real time. Pfeiffer et al. [58] developed a multistage control scheme. First, the rigid body motion is controlled by a conventional computed torque method. Second, the elastic deviations from the reference path are quasi-statically corrected by modifying the reference path. Third, the remaining elastic vibrations are actively damped by strain feedback for each link. Schutter et al. [63] presented a nonlinear feedback which linearized the rigid body dynamics, followed by linear feedback of the full state. The last two methods, like other computed torque methods, lead to a computationally intensive controller, sensitive to model parameters.

Various adaptive concepts are categorized into two types; MRAC(Model Reference Adaptive Control) and self-tuning control. Siciliano, Yuan and Book [65] proposed a full state type MRAC for one link flexible arm. Meldrum and Balas [47] used direct adaptive type MRAC, in which the controller parameters are adjusted with only the plant output and input signals. Yuh [83] and Yang and Gibson [80] presented an indirect adaptive control approach based on an identified linear prediction model of the plant. Rovner [60] developed an adaptive algorithm based on the self- tuning regulator concept for the noncolocated control case and experimentally proved its performance. Nelson and Mitra [53] and Yurkovich and Pacheco [84] presented load estimation and load adaptive control. Most researches and experiments of adaptive control are performed for one link flexible arms because an assumption that during the adaptation process the elements of the linearized system remains constant is well satisfied for one link flexible arms. However, in multi-link flexible arms, the controller has to be applicable to rapidly time varying nonlinear couplings. Cetinkunt [15] applied Adaptive Model Following Control (AMFC) based

on the generalized inertia matrix for a two link flexible robot. This controller relaxes some of the restrictive assumptions made by previous AMFC design procedures so that the use of the AMFC techniques in high speed manipulators becomes possible. Yuan [82] applied a robust controller based on MRAC for RALF.

Under the assumption that only small elastic deviation from rigid body motion occurs, the decoupled control of rigid and elastic coordinates can be considered. Such a concept leads to a two stage control scheme, a slow control for the rigid body motion and a fast control for the elastic motion. Siciliano and Book [64] applied a singular perturbation method to a one link flexible arm.

1.3 Thesis Outline

In chapter 2, nonlinear equations of motion of RALF are derived by the Lagrangian method in symbolic form. The derivation procedures for the equations of motion are described in detail.

In chapter 3, the nonlinear algebraic constraint equations of RALF are derived. A mixed set of differential equations and algebraic equations are solved using singular value decomposition. The main concept of this method is explained using a simple example.

In chapter 4, the method for determining mode shape functions of each link is described. The loaded interface component mode synthesis is used to find the proper mode shape functions. The discrepancies between the predicted frequencies and the measured frequencies are explained by the finite element models.

In chapter 5, first, the time response of the analytical model is compared to that of the TREETOPS model for the model verification. Secondly, the nonlinear dynamics of RALF are studied by sinusoidal excitation. Third, the effect of hydraulic

actuator dynamics on flexible arm dynamics is discussed.

In chapter 6, a decentralized control scheme using cylinder position and strain of each link is applied to check the characteristics of the control of a two link flexible robot.

1.4 Contributions

The major contribution of this thesis is the theoretical analysis and the experimental verification of dynamics and control of two link flexible robots with flexible parallel link mechanisms.

Detailed descriptions of contributions are as follows:

First, nonlinear equations of motion of RALF are derived in symbolic form systematically and efficiently. The resulting equations of motion have a structure which is useful to reduce the number of terms calculated, to check correctness, or to extend the model to higher order.

Secondly, the dynamics of a closed kinematic chain system with a flexible parallel link mechanism is solved without any significant constraint violation.

Third, the proper mode shape functions of each link of RALF are determined using component mode synthesis. It is verified that component mode synthesis provides rigorous boundary conditions for modal data of components.

Fouth, nonlinear dynamics of RALF is verified using a sinusoidal excitation. The degree of nonlinearity of RALF is observed from the power spectra of the tip acceleration.

Fifth, the effect of actuator dynamics on the flexible robot dynamics is studied. The hydraulic actuator dynamics is modeled and compared with the dynamics of the electric D.C. motor. The difference in velocity feedback for the two actuators

is shown to result in significantly different joint behavior for a flexible structure.

Sixth, a decentralized control algorithm using cylinder position and beam strain has been demonstrated for the control of RALF. It is shown through experiments that position feedback through a lag compensator and strain feedback through an nonminimum allpass filter yield a good trajectory following and beam vibration suppression respectively.

CHAPTER II

Derivation of Equations of Motion

2.1 Introduction

In this chapter, a Lagrangian method is used to derive the equations of motion for a flexible manipulator with parallel link mechanisms. Because flexible manipulator dynamics is more complicated than rigid manipulator dynamics, the amount of computation increases and there is a possibility of ending up with incorrect equations. Therefore, an efficient and systematic derivation method is required to reduce these problems. Furthermore, it is desirable to simplify elements of the mass matrices and the centrifugal and Coriolis forces for a real time control.

2.2 Description of Structure

The structure as shown in Fig. 2.1 consists of lower, upper, connecting, and actuating links. Each link is connected to another by a pin. The upper link is driven by a parallel link mechanism. Motion is restricted to the vertical plane. The joint parts of the lower and the upper link are stiffened by increasing the cross sectional area. Detailed structural data are given in Wilson [79]. In deriving equations of motion using the Lagrangian method, the coordinates involved in a closed kinematic chain are not independent. In the flexible parallel link mechanism, the relationship among coordinates are described by nonlinear algebraic equations. Therefore, a

constraint dynamic analysis is required to solve nonlinear algebraic equations and differential equations of motion simultaneously. To derive the equations of motion of this closed kinematic chain system, one joint of the parallel link mechanism is virtually cut to form an open tree structure as shown in Fig 2.2. The unknown constraint force is applied at the virtually cut joint.

2.3 Equations of Motion

The open tree structure is regarded as an assembly of two serial link manipulators - the lower and upper link part plus the connecting and actuating link part. The equations of motion of each part can be written symbolically.

$$\sum_{j=1}^{n} M_{ij}\ddot{q}_j + \sum_{j=1}^{n} K_{ij}q_j + \sum_{j=1}^{n}\sum_{k=1}^{n} C_{jk}(i)\dot{q}_j\dot{q}_k + G_i g = \tau_i \tag{2.1}$$

where q_j is an element of the generalized coordinate vector, M_{ij} is an element of the generalized mass matrix, K_{ij} is an element of the elastic stiffness matrix, $C_{jk}(i)$ is an element of the velocity coupling matrix which is the coefficient matrix of Coriolis and centrifugal force, G_i is an element of the gravity force matrix, g is the gravitational acceleration vector, τ_i is an element of the generalized force vector.

The mass matrix and the gravity force matrix can be derived using the Jacobian matrix as shown in Appendix A.

$$M_{ij} = \sum_{p=1}^{b} \int_0^{l_p} J_p^T J_p \rho_p A_p dx_p \tag{2.2}$$

where b is the number of links. J_p, ρ_p, A_p, and l_p are the Jacobian matrix, the density, the area, and the length of link p respectively.

$$G_i = \sum_{p=1}^{b} \int_0^{l_p} J_p^{(i)} \rho_p A_p dx_p \tag{2.3}$$

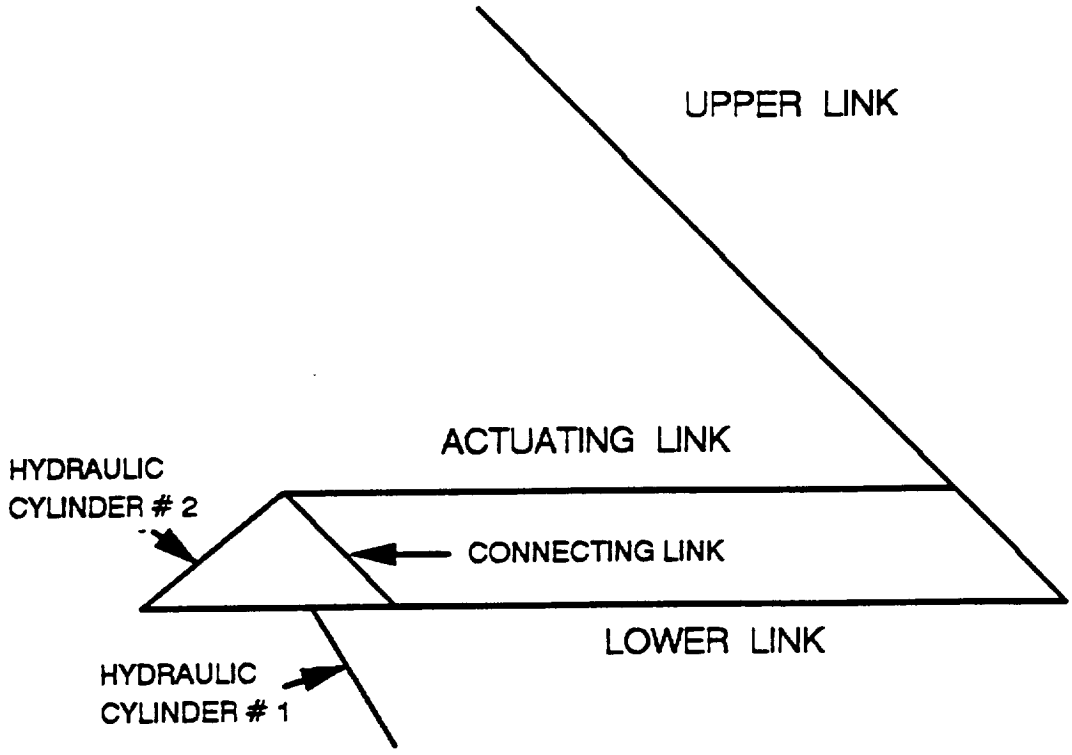

Figure 2.1: Structural data of RALF

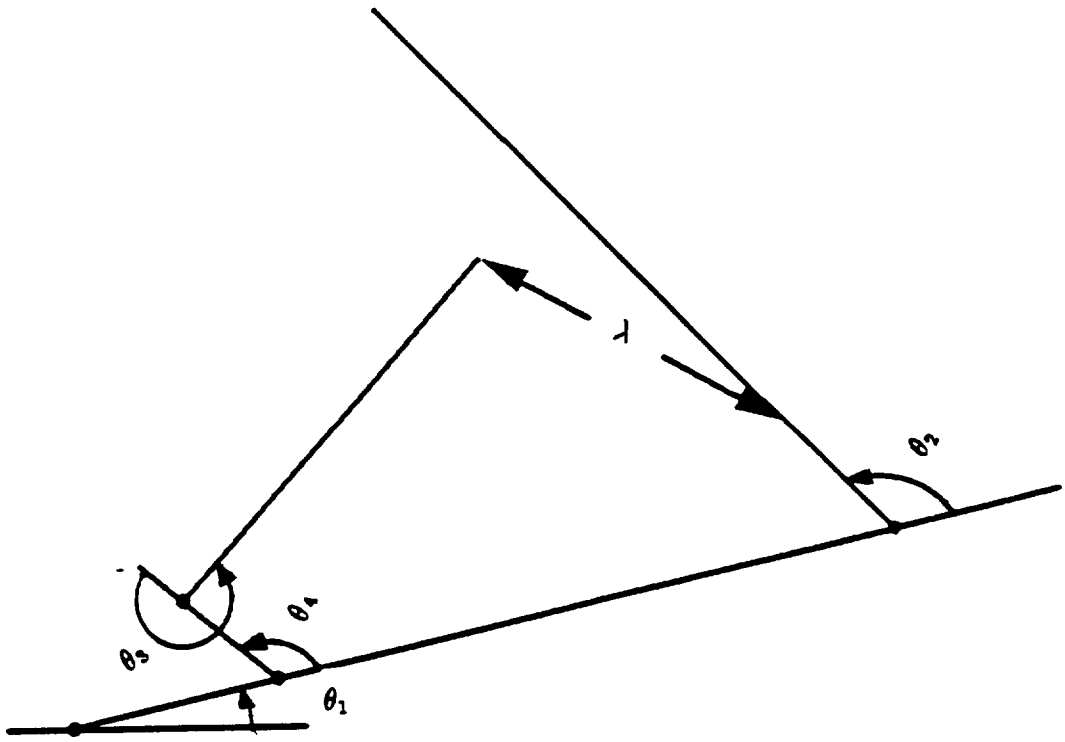

Figure 2.2: Open tree structure of RALF

where $J_p^{(i)}$ is the i th column of Jacobian matrix J_p. The velocity coupling matrix can be derived from the mass matrix.

$$C_{jk}(i) = \frac{1}{2}\left(\frac{\partial M_{ij}}{\partial q_k} + \frac{\partial M_{ik}}{\partial q_j} - \frac{\partial M_{jk}}{\partial q_i}\right) \tag{2.4}$$

The stiffness matrix is related to the mode shape function φ_{ij}.

$$K_{ij} = \int_0^{l_i} E_i I_i \left(\frac{\partial^2 \varphi_{ij}}{\partial q_j^2}\right)^2 dx_i \tag{2.5}$$

Next, equations of motion of two parts are combined using unknown constraint force for the complete equations of motion. Equations of motion of the closed kinematic chain system can be written symbolically as follows.

$$\sum_{j=1}^{n} M_{ij}\ddot{q}_j + \sum_{j=1}^{n} K_{ij} q_j + \sum_{j=1}^{n}\sum_{k=1}^{n} C_{jk}(i)\dot{q}_j \dot{q}_k + G_i g + \sum_{k=1}^{m} (\Phi_q)_{ki}^T \lambda_k = \tau_i \tag{2.6}$$

where m is the number of the constraint equations, λ_k is element of the unknown constraint force vector, $(\Phi_q)_{ki}$ is element of the constraint Jacobian matrix which is derived by differentiating the constraint equations (2.7) with respect to time.

$$\Phi(q) = 0 \tag{2.7}$$

$$\frac{\partial \Phi(q)}{\partial t} = \frac{\partial \Phi(q)}{\partial q}\frac{\partial q}{\partial t} = \Phi_q(q)\dot{q} = 0 \tag{2.8}$$

In the following sections 2.4 and 2.5, the derivation procedure of the equations of motion of each part is described in detail. The constrained dynamic analysis will be described in Chapter III.

2.4 Lower and Upper Link

2.4.1 Mass Matrices and Gravity Force Vectors

Deformed position vectors of each link in Fig. 2.3a and 2.3b are described as follows:

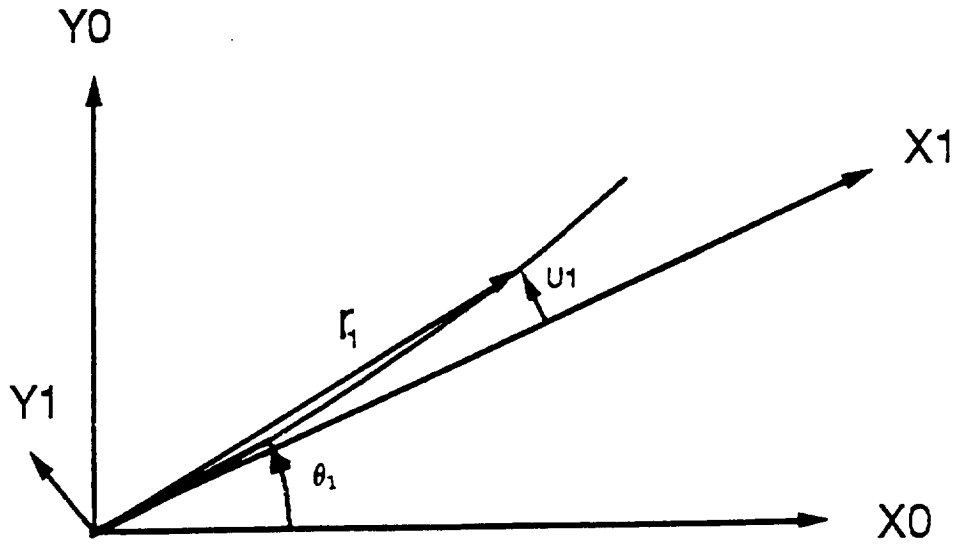

Figure 2.3.a: Position vector of the lower link

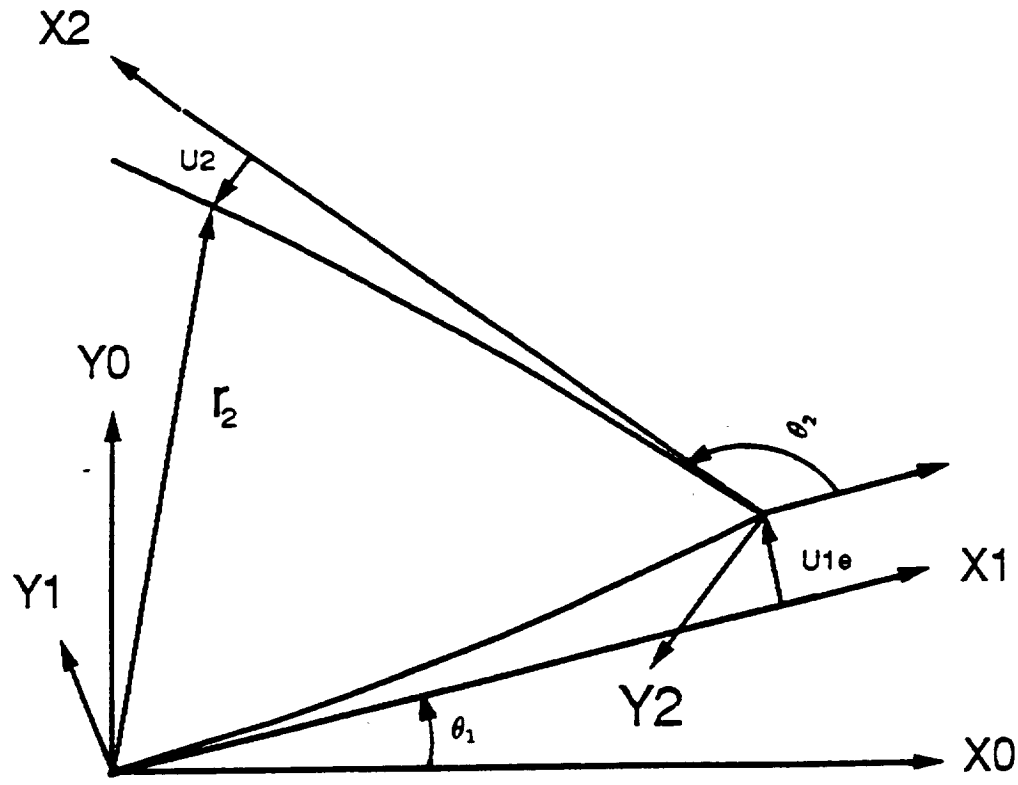

Figure 2.3.b: Position vector of the upper link

$$\vec{r}_1 = (x_1 cos\theta_1 - u_1 sin\theta_1)i + (x_1 sin\theta_1 + u_1 cos\theta_1)j \tag{2.9}$$

$$\vec{r}_2 = [l_1 cos\theta_1 - u_{1e} sin\theta_1 + x_2 cos(\theta_1 + \theta_2) - u_2 sin(\theta_1 + \theta_2)]i$$

$$+ [l_1 sin\theta_1 + u_{1e} cos\theta_1 + x_2 sin(\theta_1 + \theta_2) + u_2 cos(\theta_1 + \theta_2)]j \tag{2.10}$$

where i and j are unit vectors along the inertial frame, X_0 and Y_0. The elastic deformation, u_i, can be expressed by finite series of mode shape functions which satisfy assumed boundary conditions multiplied by time dependent modal coordinates. Suppose that the amplitude of the higher modes is relatively small compared with the first mode, two modes per link are considered in this model.

$$u_1(x_1, t) = \psi_{11}(x_1)\xi_{11}(t) + \psi_{12}(x_1)\xi_{12}(t) \tag{2.11}$$

$$u_2(x_2, t) = \psi_{21}(x_2)\xi_{21}(t) + \psi_{22}(x_2)\xi_{22}(t) \tag{2.12}$$

The elastic displacement of the end point is

$$u_{1e} = u_1(l_1, t) \tag{2.13}$$

Velocity vectors are related to generalized coordinates by the Jacobian matrices [2]:

$$\dot{\vec{r}}_1 = J_1 \dot{q}_{12} \tag{2.14}$$

$$\dot{\vec{r}}_2 = J_2 \dot{q}_{12} \tag{2.15}$$

where the generalized coordinates are

$$q_{12} = \{\theta_1, \theta_2, \xi_{11}, \xi_{12}, \xi_{21}, \xi_{22}\}^T \tag{2.16}$$

and the Jacobian matrices are

$$J_1 = \begin{bmatrix} -u_1 C_1 - x_1 S_1 & 0 & -\psi_{11} S_1 & -\psi_{12} C_1 & 0 & 0 \\ -u_1 S_1 + x_1 C_1 & 0 & \psi_{11} C_1 & \psi_{12} C_1 & 0 & 0 \end{bmatrix} \tag{2.17}$$

$$J_2 = \begin{bmatrix} -l_1 S_1 - u_{1e} C_1 - u_2 C_{12} - x_2 S_{12} & -u_2 C_{12} - x_2 S_{12} \\ +l_1 C_1 - u_{1e} S_1 - u_2 S_{12} + x_2 C_{12} & -u_2 S_{12} + x_2 C_{12} \\ -\psi_{11e} S_1 & -\psi_{12e} S_1 & -\psi_{21} S_{12} & -\psi_{22} S_{12} \\ \psi_{11e} C_1 & \psi_{12e} C_1 & \psi_{21} C_{12} & \psi_{22} C_{12} \end{bmatrix} \tag{2.18}$$

where $cos(\theta_i + \theta_j)$ and $sin(\theta_i + \theta_j)$ are expressed as C_{ij} and S_{ij} for convenience. The Jacobian matrices, J_1 and J_2, can be easily derived from the position vector using the MJac function of SMP (Symbolic Manipulation Program) [69]. Using these Jacobian matrices, mass matrices and gravity force matrices are calculated by the following equations:

$$M_{ij} = \int_0^{l_1} J_1^T J_1 \rho_1 A_1 dx_1 + \int_0^{l_2} J_2^T J_2 \rho_2 A_2 dx_2 \tag{2.19}$$

$$G_1 = \int_0^{l_1} J_1[2,1] \rho_1 A_1 dx_1 + \int_0^{l_2} J_2[2,1] \rho_2 A_2 dx_2$$

$$G_2 = \int_0^{l_2} J_2[2,2] \rho_2 A_2 dx_2 \tag{2.20}$$

$J_p[2,i]$ is the second row and the ith column of J_p selected since the gravity is acting in the negative direction of Y_0. The gravitational potential energy change due to the link deformation is assumed to be negligible.

Elements of mass matrices and gravity forces are:

$$\begin{aligned} M_{11} &= \int_0^{l_1} (x_1^2 + u_1^2) \rho_1 A_1 dx_1 \\ &+ \int_0^{l_2} (l_1^2 + u_{1e}^2 + u_2^2 + x_2^2 \\ &+ 2(l_1 x_2 C_2 - l_1 u_2 S_2 + u_{1e} u_2 C_2 + u_{1e} x_2 S_2)) \rho_2 A_2 dx_2 \end{aligned}$$

$$M_{12} = \int_0^{l_2} (x_2^2 + u_2^2 + l_1 x_2 C_2 - l_1 u_2 S_2 + u_{1e} u_2 C_2 + u_{1e} x_2 S_2) \rho_2 A_2 dx_2$$

$$M_{13} = \int_0^{l_1} x_1 \psi_{11} \rho_1 A_1 dx_1 + \psi_{11e} \int_0^{l_2} (l_1 + x_2 C_2 - u_2 S_2) \rho_2 A_2 dx_2$$

$$M_{14} = \int_0^{l_1} x_1 \psi_{12} \rho_1 A_1 dx_1 + \psi_{12e} \int_0^{l_2} (l_1 + x_2 C_2 - u_2 S_2) \rho_2 A_2 dx_2$$

$$M_{15} = \int_0^{l_2} \psi_{21} (x_2 + l_1 C_2 + u_{1e} S_2) \rho_2 A_2 dx_2$$

$$M_{16} = \int_0^{l_2} \psi_{22} (x_2 + l_1 C_2 + u_{1e} S_2) \rho_2 A_2 dx_2$$

$$M_{22} = \int_0^{l_2} (x_2^2 + u_2^2) \rho_2 A_2 dx_2$$

$$M_{23} = \psi_{11e} \int_0^{l_2} (x_2 C_2 - u_2 S_2) \rho_2 A_2 dx_2$$

$$M_{24} = \psi_{12e} \int_0^{l_2} (x_2 C_2 - u_2 S_2) \rho_2 A_2 dx_2$$

$$M_{25} = \int_0^{l_2} x_2 \psi_{21} \rho_2 A_2 dx_2$$

$$M_{26} = \int_0^{l_2} x_2 \psi_{22} \rho_2 A_2 dx_2 \qquad (2.21)$$

$$M_{33} = \int_0^{l_1} \psi_{11}^2 \rho_1 A_1 dx_1 + \psi_{11e}^2 \int_0^{l_2} \rho_2 A_2 dx_2$$

$$M_{34} = \int_0^{l_1} \psi_{11} \psi_{12} \rho_1 A_1 dx_1 + \psi_{11e} \psi_{12e} \int_0^{l_2} \rho_2 A_2 dx_2$$

$$M_{35} = \psi_{11e} C_2 \int_0^{l_2} \psi_{21} \rho_2 A_2 dx_2$$

$$M_{36} = \psi_{11e} C_2 \int_0^{l_2} \psi_{22} \rho_2 A_2 dx_2$$

$$M_{44} = \int_0^{l_1} \psi_{12}^2 \rho_1 A_1 dx_1 + \psi_{12e}^2 \int_0^{l_2} \rho_2 A_2 dx_2$$

$$M_{45} = \psi_{12e} C_2 \int_0^{l_2} \psi_{21} \rho_2 A_2 dx_2$$

$$M_{46} = \psi_{12e} C_2 \int_0^{l_2} \psi_{22} \rho_2 A_2 dx_2$$

$$M_{55} = \int_0^{l_2} \psi_{21}^2 \rho_2 A_2 dx_2$$

$$M_{56} = \int_0^{l_2} \psi_{21}\psi_{22}\rho_2 A_2 dx_2$$

$$M_{66} = \int_0^{l_2} \psi_{22}^2\rho_2 A_2 dx_2$$

$$G_1 = \int_0^{l_1} (x_1 C_1 - u_1 S_1)\rho_1 A_1 dx_1 + \int_0^{l_2} (l_1 C_1 - u_1 S_1 + x_2 C_{12} - u_2 S_{12})\rho_2 A_2 dx_2$$

$$G_2 = \int_0^{l_2} (x_2 C_{12} - u_2 S_{12})\rho_2 A_2 dx_2 \tag{2.22}$$

where

$$\psi_{ije} = \psi_{ij}(l_i)$$

SMP files of equations (2.9 - 2.22) are included in Appendix D.

The integral in the above elements are defined as follows.

$$m_i = \int_0^{l_i} \rho_i A_i dx_i \tag{2.23}$$

$$m_i l_{ic} = \int_0^{l_i} x_i \rho_i A_i dx_i \tag{2.24}$$

$$D_i = \int_0^{l_i} x_i^2 \rho_i A_i dx_i \tag{2.25}$$

$$LM_{ij} = \int_0^{l_i} \psi_{ij}(x_i)\rho_i A_i dx_i \tag{2.26}$$

$$AM_{ij} = \int_0^{l_i} x_i \psi_{ij}(x_i)\rho_i A_i dx_i \tag{2.27}$$

$$NM_{ij} = \int_0^{l_i} \psi_{ij}^2(x_i)\rho_i A_i dx_i \tag{2.28}$$

where l_{ic} is center of mass of link i. The first three terms are parameters which are related to a rigid motion. These are called zeroth, first, and second moments of inertia respectively. On the other hand, the last three terms are parameters which are related to a flexible motion. LM_{ij} and AM_{ij} are called the modal momentum coefficients and the modal angular momentum coefficients respectively [29,30]. The

physical meaning of these terms is not easy to explain. However, these have the following properties [29.30].

$$\sum_{j=1}^{\infty} LM_{ij}^2 = m_i \tag{2.29}$$

$$\sum_{j=1}^{\infty} LM_{ij} AM_{ij} = m_i l_{ic} \tag{2.30}$$

$$\sum_{j=1}^{\infty} AM_{ij}^2 = D_i \tag{2.31}$$

NM_{ij} is used for the normalization of mode shape functions.

Using these six inertia parameters and the orthogonality of modes and linearizing about zero deflection, the linearized mass matrices and gravity vectors are rewritten as follows:

$$M_{11} = D_1 + D_2 + m_2 l_1 (l_1 + 2 l_{2c} C_2)$$

$$M_{12} = D_2 + m_2 l_1 l_{2c} C_2$$

$$M_{13} = AM_{11} + \psi_{11e} m_2 (l_1 + l_{2c} C_2)$$

$$M_{14} = AM_{12} + \psi_{12e} m_2 (l_1 + l_{2c} C_2)$$

$$M_{15} = AM_{21} + LM_{21}\, l_1 C_2$$

$$M_{16} = AM_{22} + LM_{22}\, l_1 C_2$$

$$M_{22} = D_2$$

$$M_{23} = \psi_{11e} m_2 l_{2c} C_2$$

$$M_{24} = \psi_{12e} m_2 l_{2c} C_2$$

$$M_{25} = AM_{21}$$

$$M_{26} = AM_{22} \tag{2.32}$$

$$M_{33} = NM_{11} + m_2\psi_{11e}^2$$

$$M_{34} = 0$$

$$M_{35} = \psi_{11e}LM_{21}C_2$$

$$M_{36} = \psi_{11e}LM_{22}C_2$$

$$M_{44} = NM_{12} + m_2\psi_{12e}^2$$

$$M_{45} = \psi_{12e}LM_{21}C_2$$

$$M_{46} = \psi_{12e}LM_{22}C_2$$

$$M_{55} = NM_{21}$$

$$M_{56} = 0$$

$$M_{66} = NM_{22}$$

$$G_1 = m_1 l_{1c}C_1 + m_2(l_1C_1 + l_{2c}C_{12})$$

$$G_2 = m_2 l_{2c}C_{12} \tag{2.33}$$

Finally, the elastic stiffness matrix,K_{ij}, can be derived by the partial differentiation of the elastic potential energy, V :

$$V = \frac{1}{2}\int_0^{l_1} EI_1[\frac{\partial^2 u_1}{\partial x_1^2}]^2 dx_1 + \frac{1}{2}\int_0^{l_2} EI_2[\frac{\partial^2 u_2}{\partial x_2^2}]^2 dx_2 \tag{2.34}$$

$$K_{ij} = \int_0^{l_1} EI_i[\frac{\partial^2 \psi_{ij}}{\partial {x_i}^2}]^2 dx_i \quad (i,j = 1,2) \tag{2.35}$$

where E is Young's modulus of elasticity, and I_i is the area moment of inertia of link i.

2.4.2 Payload

When masses are loaded at the end of the lower link and the upper link, position vectors of the payload are derived from (2.9) and (2.10) by substituting x_i into l_i and u_i into u_{ie}.

$$\vec{r}_{1e} = (l_1 cos\theta_1 - u_{1e} sin\theta_1)i + (l_1 sin\theta_1 + u_{1e} cos\theta_1)j \tag{2.36}$$

$$\vec{r}_{2e} = [l_1 cos\theta_1 - u_{1e} sin\theta_1 + l_2 cos(\theta_1 + \theta_2) - u_{2e} sin(\theta_1 + \theta_2)]i$$
$$+ [l_1 sin\theta_1 + u_{1e} cos\theta_1 + l_2 sin(\theta_1 + \theta_2) + u_{2e} cos(\theta_1 + \theta_2)]j \tag{2.37}$$

where

$$u_{1e} = u_1(l_1, t) \tag{2.38}$$

$$u_{2e} = u_2(l_2, t) \tag{2.39}$$

Velocity vectors are expressed by Jacobian matrices:

$$\dot{\vec{r}}_{1e} = J_{1e}\dot{q}_{12} \tag{2.40}$$

$$\dot{\vec{r}}_{2e} = J_{2e}\dot{q}_{12} \tag{2.41}$$

where

$$J_{1e} = \begin{bmatrix} -u_{1e}C_1 - l_1S_1 & 0 & -\psi_{11e}S_1 & -\psi_{12e}C_1 & 0 & 0 \\ -u_{1e}S_1 + l_1C_1 & 0 & \psi_{11e}C_1 & \psi_{12e}C_1 & 0 & 0 \end{bmatrix} \tag{2.42}$$

$$J_{2e} = \begin{bmatrix} -l_1S_1 - u_{1e}C_1 - u_{2e}C_{12} - l_2S_{12} & -u_{2e}C_{12} - l_2S_{12} \\ +l_1C_1 - u_{1e}S_1 - u_{2e}S_{12} + l_2C_{12} & -u_{2e}S_{12} + l_2C_{12} \\ -\psi_{11e}S_1 & -\psi_{12e}S_1 & -\psi_{21e}S_{12} & -\psi_{22e}S_{12} \\ \psi_{11e}C_1 & \psi_{12e}C_1 & \psi_{21e}C_{12} & \psi_{22e}C_{12} \end{bmatrix} \tag{2.43}$$

Mass matrices and gravity force vectors due to the payload, m_{1p} and m_{2p}, are expressed by Jacobian matrices.

$$M_{ij}^p = m_{1p}J_{1e}^T J_{1e} + m_{2p}J_{2e}^T J_{2e} \tag{2.44}$$

$$G_1^p = m_{1p}J_{1e}[2,1] + m_{2p}J_{2e}[2,1] \tag{2.45}$$

$$G_2^p = m_{2p}J_{2e}[2,2]$$

Following the procedure of the previous section, the linearized mass matrices and gravity force vectors are written as follows:

$$M_{11}^p = m_{1p}l_1^2 + m_{2p}l_2^2 + m_{2p}l_1(l_1 + 2l_2C_2)$$

$$M_{12}^p = m_{2p}l_2^2 + m_{2p}l_1l_2C_2$$

$$M_{13}^p = m_{1p}l_1\psi_{11e} + m_{2p}(l_1 + l_2C_2)\psi_{11e}$$

$$M_{14}^p = m_{1p}l_1\psi_{12e} + m_{2p}(l_1 + l_2C_2)\psi_{12e}$$

$$M_{15}^p = m_{2p}(l_2 + l_1C_2)\psi_{21e}$$

$$M_{16}^p = m_{2p}(l_2 + l_1C_2)\psi_{22e}$$

$$M_{22}^p = m_{2p}l_2^2$$

$$M_{23}^p = m_{2p}l_2\psi_{11e}C_2$$

$$M_{24}^p = m_{2p}l_2\psi_{12e}C_2$$

$$M_{25}^p = m_{2p}l_2\psi_{21e}$$

$$M_{26}^p = m_{2p}l_2\psi_{22e} \tag{2.46}$$

$$M_{33}^p = (m_{1p} + m_{2p})\psi_{11e}^2$$

$$M_{34}^p = (m_{1p} + m_{2p})\psi_{11e}\psi_{12e}$$

$$M_{35}^p = m_{2p}\psi_{11e}\psi_{21e}C_2$$

$$M_{36}^p = m_{2p}\psi_{11e}\psi_{22e}C_2$$

$$M_{44}^p = (m_{1p} + m_{2p})\psi_{12e}^2$$

$$M_{45}^p = m_{2p}\psi_{12e}\psi_{21e}C_2$$

$$M_{46}^p = m_{2p}\psi_{12e}\psi_{22e}C_2$$

$$M_{55}^p = m_{2p}\psi_{21e}^2$$

$$M_{56}^p = m_{2p}\psi_{21e}\psi_{22e}$$

$$M_{66}^p = m_{2p}\psi_{22e}^2$$

$$G_1^p = m_{1p}l_1C_1 + m_{2p}(l_1C_1 + l_2C_{12})$$

$$G_2^p = m_{2p}l_2C_{12} \tag{2.47}$$

Comparing (2.46 - 47) with (2.32 - 33), six inertia parameters of mass matrices and gravity vectors have an analogy as shown in Table 2.1.

Therefore, when payloads are added, six inertia parameters are changed as follows:

$$m_i \rightarrow m_i + m_{ip} \tag{2.48}$$

$$m_i l_{ic} \rightarrow m_i l_{ic} + m_{ip} l_i \tag{2.49}$$

$$D_i \rightarrow D_i + m_{ip} l_i^2 \tag{2.50}$$

$$LM_{ij} \rightarrow LM_{ij} + m_{ip}\psi_{ije} \tag{2.51}$$

$$AM_{ij} \rightarrow AM_{ij} + m_{ip} l_i \psi_{ije} \tag{2.52}$$

$$NM_{ij} \rightarrow NM_{ij} + m_{ip}\psi_{ije}^2 \tag{2.53}$$

Table 2.1: Analogy of six inertia parameters

without payload	with payload
m_i	m_{ip}
$m_i l_{ic}$	$m_{ip} l_i$
D_i	$m_{ip} l_i^2$
LM_{ij}	$m_{ip} \psi_{ije}$
AM_{ij}	$m_{ip} l_i \psi_{ije}$
NM_{ij}	$m_{ip} \psi_{ije}^2$

2.4.3 Centrifugal and Coriolis Force

The velocity coupling matrix can be derived from the mass matrix using the Christoffel symbol (2.4).

$$C_{jk}(i) = \frac{1}{2}\{\frac{\partial M_{ij}}{\partial q_k} + \frac{\partial M_{ik}}{\partial q_j} - \frac{\partial M_{jk}}{\partial q_i}\} \tag{2.54}$$

$C_{jk}(i)$ characterizes the effects on link i which are caused by the coupled velocities of link j and k. The diagonal elements for j = k are the coefficients of the centrifugal force. The offdiagonal elements for j $\neq$ k are the coefficients of the Coriolis force. In equation (2.1), the states can be partitioned into the rigid body state θ and the flexible body state ξ.

$$\begin{aligned}
&\sum_{i=1}^{2} A_{ij}\ddot{\theta}_j + \sum_{j=3}^{6} B_{ij}\ddot{\xi}_j + \sum_{j=1}^{2}\sum_{k=1}^{2} P_{jk}(i)\dot{\theta}_j\dot{\theta}_k + \sum_{j=1}^{2}\sum_{k=3}^{6} Q_{jk}(i)\dot{\theta}_j\dot{\xi}_k \\
&\qquad + \sum_{j=3}^{6}\sum_{k=3}^{6} R_{jk}(i)\dot{\xi}_j\dot{\xi}_k + G_i = \tau_i \quad (i = 1,2) \\
&\sum_{i=1}^{2} B_{ji}\ddot{\theta}_j + \sum_{j=3}^{6} D_{ij}\ddot{\xi}_j + \sum_{j=1}^{2}\sum_{k=1}^{2} \hat{P}_{jk}(i)\dot{\theta}_j\dot{\theta}_k + \sum_{j=1}^{2}\sum_{k=3}^{6} \hat{Q}_{jk}(i)\dot{\theta}_j\dot{\xi}_k
\end{aligned} \tag{2.55}$$

$$+\sum_{j=3}^{6}\sum_{k=3}^{6}\hat{R}_{jk}(i)\dot{\xi}_j\dot{\xi}_k+\sum_{j=1}^{2}K_{ij}\xi_j=0 \quad (i=3,6) \tag{2.56}$$

Therefore, the partitioned velocity coupling matrices can be written as follows:

$$P_{jk}(i)=\frac{1}{2}\{\frac{\partial A_{ij}}{\partial q_k}+\frac{\partial A_{ik}}{\partial q_j}-\frac{\partial A_{jk}}{\partial q_i}\} \tag{2.57}$$

$$Q_{jk}(i)=\frac{1}{2}\{\frac{\partial A_{ij}}{\partial q_k}+\frac{\partial B_{ik}}{\partial q_j}-\frac{\partial B_{jk}}{\partial q_i}\} \tag{2.58}$$

$$R_{jk}(i)=\frac{1}{2}\{\frac{\partial B_{ij}}{\partial q_k}+\frac{\partial B_{ik}}{\partial q_j}-\frac{\partial D_{jk}}{\partial q_i}\} \tag{2.59}$$

$$\hat{P}_{jk}(i)=\frac{1}{2}\{\frac{\partial B_{ij}}{\partial q_k}+\frac{\partial B_{ik}}{\partial q_j}-\frac{\partial A_{jk}}{\partial q_i}\} \tag{2.60}$$

$$\hat{Q}_{jk}(i)=\frac{1}{2}\{\frac{\partial B_{ij}}{\partial q_k}+\frac{\partial D_{ik}}{\partial q_j}-\frac{\partial B_{jk}}{\partial q_i}\} \tag{2.61}$$

$$\hat{R}_{jk}(i)=\frac{1}{2}\{\frac{\partial D_{ij}}{\partial q_k}+\frac{\partial D_{ik}}{\partial q_j}-\frac{\partial D_{jk}}{\partial q_i}\} \tag{2.62}$$

Because mass submatrix D_{ij} are not the function of the flexible body state, the terms related to D_{ij} in $\hat{Q}_{jk}(i)$ and $\hat{R}_{jk}(i)$ are eliminated. The number of independent elements of velocity coupling matrices also can be reduced using the symmetry, the non-interacting, and the reflective coupling properties [71,72].

$$C_{jk}(i)=C_{kj}(i) \tag{2.63}$$

$$C_{ji}(i)=0 \quad for \quad j\leq i \tag{2.64}$$

$$C_{jk}(i)=-C_{ji}(k) \quad for \quad j\leq i,k \tag{2.65}$$

However, the reflective coupling property that Tourassis and Neuman find is not always valid in the flexible case. Therefore, even though the symbolic manipulation program can be used as the computational tool, the simplication procedure must be accomplished under the supervision of the analyst. The symbolic programs are described in Appendix D.

Using those properties, the following independent elements of the velocity coupling matrix are derived.

$$d_1 = \int_0^{l_2} \{(u_{1e}C_2 - l_1S_2)x_2 - (u_{1e}S_2 + l_1C_2)u_2\rho_2 A_2 dx_2\}$$

$$d_{21} = \int_0^{l_1} \psi_{11}^2 q_{11}\rho_1 A_1 dx_1 + \psi_{11e}[\int_0^{l_2} (S_2x_2 + C_2u_2 + u_{1e})\rho_2 A_2 dx_2]$$
$$d_{22} = \int_0^{l_1} \psi_{12}^2 q_{12}\rho_1 A_1 dx_1 + \psi_{12e}[(\int_0^{l_2} (S_2x_2 + C_2u_2 + u_{1e})\rho_2 A_2 dx_2]$$

$$d_{31} = \psi_{11e}\int_0^{l_2} (S_2x_2 + C_2u_2)\rho_2 A_2 dx_2$$
$$d_{32} = \psi_{12e}\int_0^{l_2} (S_2x_2 + C_2u_2\rho_2 A_2 dx_2)$$

$$d_{41} = \int_0^{l_2} \psi_{21}(\psi_{21}q_{21} + \psi_{22}q_{22})\rho_2 A_2 dx_2$$
$$d_{42} = \int_0^{l_2} \psi_{22}(\psi_{21}q_{21} + \psi_{22}q_{22})\rho_2 A_2 dx_2 \qquad (2.66)$$

$$d_{51} = \int_0^{l_2} \psi_{21}\{(\psi_{21}q_{21} + \psi_{22}q_{22}) + (u_{1e}C_2 - l_1S_2)\}\rho_2 A_2 dx_2$$
$$d_{52} = \int_0^{l_2} \psi_{22}\{(\psi_{21}q_{21} + \psi_{22}q_{22}) + (u_{1e}C_2 - l_1S_2)\}\rho_2 A_2 dx_2$$

$$d_{61} = \psi_{11e}S_2\int_0^{l_2} \psi_{21}\rho_2 A_2 dx_2$$
$$d_{62} = \psi_{11e}S_2\int_0^{l_2} \psi_{22}\rho_2 A_2 dx_2$$

$$d_{71} = \psi_{12e}S_2\int_0^{l_2} \psi_{21}\rho_2 A_2 dx_2$$
$$d_{72} = \psi_{12e}S_2\int_0^{l_2} \psi_{22}\rho_2 A_2 dx_2$$

After evaluating the integral,

$$d_1 = (u_{1e}C_2 - l_1S_2)m_2l_{2c} - (u_{1e}S_2 + l_1C_2)(LM_{21}\xi_{21} + LM_{22}\xi_{22})$$

$$d_{21} = \psi_{11e}[m_2l_{2c}S_2 + (LM_{21}\xi_{21} + LM_{22}\xi_{22})C_2 + u_{1e}m_2] + NM_{11}\xi_{11}$$

$$d_{22} = \psi_{12e}[m_2l_{2c}S_2 + (LM_{21}\xi_{21} + LM_{22}\xi_{22})C_2 + u_{1e}m_2] + NM_{12}\xi_{12}$$

$$d_{31} = \psi_{11e}[m_2l_{2c}S_2 + (LM_{21}\xi_{21} + LM_{22}\xi_{22})C_2]$$

$$d_{32} = \psi_{12e}[m_2l_{2c}S_2 + (LM_{21}\xi_{21} + LM_{22}\xi_{22})C_2]$$

$$d_{41} = NM_{21}\xi_{21} + (u_{1e}C_2 - l_1S_2)LM_{21}$$

$$d_{42} = NM_{22}\xi_{22} + (u_{1e}C_2 - l_1S_2)LM_{22} \qquad (2.67)$$

$$d_{51} = NM_{21}\xi_{21}$$

$$d_{52} = NM_{22}\xi_{22}$$

$$d_{61} = \psi_{11e}S_2LM_{21}$$

$$d_{62} = \psi_{11e}S_2LM_{22}$$

$$d_{71} = \psi_{12e}S_2LM_{21}$$

$$d_{72} = \psi_{12e}S_2LM_{22}$$

Using these elements, the velocity coupling matrices can be simplified as follows:

$$C(1) = \begin{bmatrix} 0 & d_1 & d_{21} & d_{22} & d_{41} & d_{42} \\ & d_1 & 0 & 0 & d_{41} & d_{42} \\ & & 0 & 0 & 0 & 0 \\ & & & 0 & 0 & 0 \\ & & & & 0 & 0 \\ & & & & & 0 \end{bmatrix} \tag{2.68}$$

$$C(2) = \begin{bmatrix} -d_1 & 0 & d_{31} & d_{32} & d_{51} & d_{52} \\ & 0 & 0 & 0 & d_{51} & d_{52} \\ & & 0 & 0 & -d_{61}/2 & -d_{62}/2 \\ & & & 0 & -d_{71}/2 & -d_{72}/2 \\ & & & & 0 & 0 \\ & & & & & 0 \end{bmatrix} \tag{2.69}$$

$$C(3) = \begin{bmatrix} -d_{21} & -d_{31} & 0 & 0 & -d_{61} & -d_{62} \\ & -d_{31} & 0 & 0 & -d_{61}/2 & -d_{62}/2 \\ & & 0 & 0 & 0 & 0 \\ & & & 0 & 0 & 0 \\ & & & & 0 & 0 \\ & & & & & 0 \end{bmatrix} \tag{2.70}$$

$$C(4) = \begin{bmatrix} -d_{22} & -d_{32} & 0 & 0 & -d_{71} & -d_{72} \\ & -d_{32} & 0 & 0 & -d_{71}/2 & -d_{72}/2 \\ & & 0 & 0 & 0 & 0 \\ & & & 0 & 0 & 0 \\ & & & & 0 & 0 \\ & & & & & 0 \end{bmatrix} \tag{2.71}$$

$$C(5) = \begin{bmatrix} -d_{41} & -d_{51} & d_{61} & d_{71} & 0 & 0 \\ & -d_{51} & d_{61}/2 & d_{71}/2 & 0 & 0 \\ & & 0 & 0 & 0 & 0 \\ & & & 0 & 0 & 0 \\ & & & & 0 & 0 \\ & & & & & 0 \end{bmatrix} \tag{2.72}$$

$$C(6) = \begin{bmatrix} -d_{42} & -d_{52} & d_{62} & d_{72} & 0 & 0 \\ & -d_{52} & d_{62}/2 & d_{72}/2 & 0 & 0 \\ & & 0 & 0 & 0 & 0 \\ & & & 0 & 0 & 0 \\ & & & & 0 & 0 \\ & & & & & 0 \end{bmatrix} \tag{2.73}$$

2.5 Connecting and Actuating Link

2.5.1 Mass Matrices and Gravity Force Vectors

Derivation of equations of motion of the connecting and actuating link is similar to those of the lower and upper link. Position vectors are shown in Fig. 2.4.a and 2.4.b.

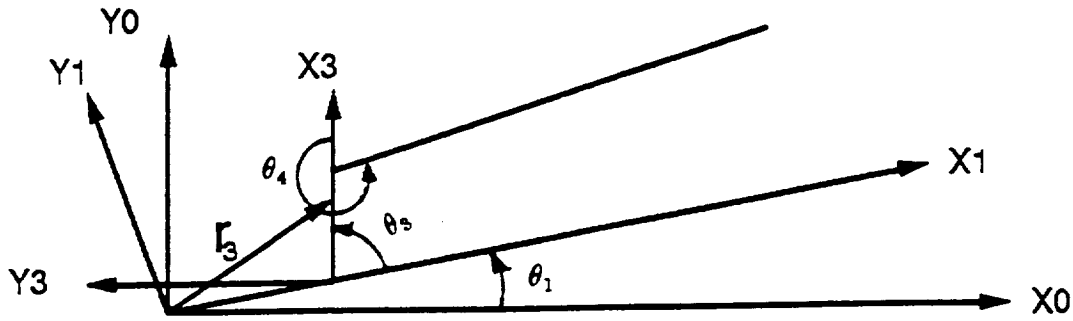

Figure 2.4.a: Position vector of the connecting link

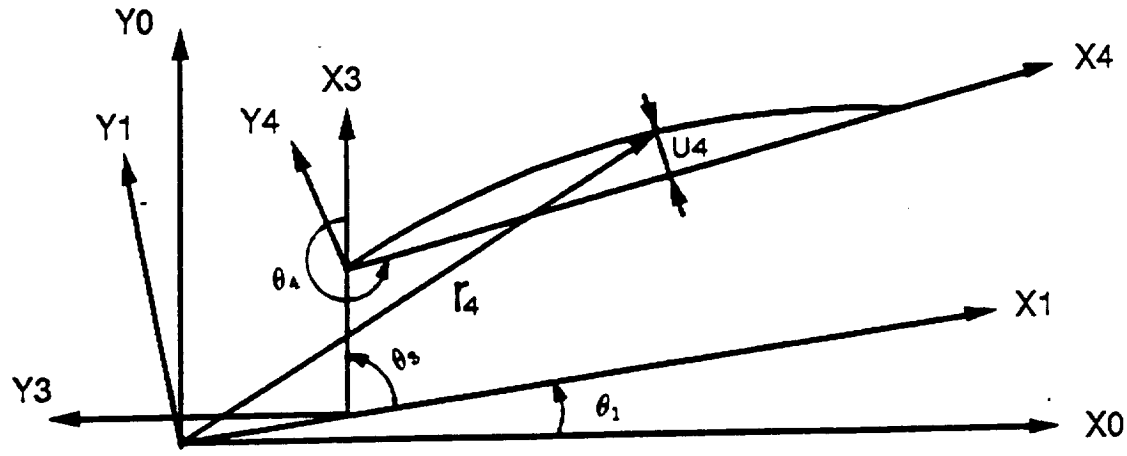

Figure 2.4.b: Position vector of the actuating link

$$\vec{r}_3 = [l_{1r}cos\theta_1 + x_3cos(\theta_1 + \theta_3)]i + [l_{1r}sin\theta_1 + x_3sin(\theta_1 + \theta_3)]j \tag{2.74}$$

$$\vec{r}_4 = [l_{1r}cos\theta_1 + l_{3r}cos(\theta_1 + \theta_3) + x_4cos(\theta_1 + \theta_3 + \theta_4) - u_4sin(\theta_1 + \theta_3 + \theta_4)]i$$

$$+ [l_{1r}sin\theta_1 + l_{3r}sin(\theta_1 + \theta_3) + x_4sin(\theta_1 + \theta_3 + \theta_4) + u_4cos(\theta_1 + \theta_3 + \theta_4)]j \tag{2.75}$$

where

$$u_4(x_4, t) = \psi_{41}(x_4)\xi_{41}(t) + \psi_{42}(x_4)\xi_{42}(t) \tag{2.76}$$

Suppose generalized coordinates are defined as

$$q_{34} = \{\theta_1, \theta_3, \theta_4, \xi_{41}, \xi_{42}\}^T \tag{2.77}$$

Velocity vectors are expressed by the Jacobian matrices:

$$\dot{\vec{r}}_3 = J_3\dot{q}_{34} \tag{2.78}$$

$$\dot{\vec{r}}_4 = J_4\dot{q}_{34} \tag{2.79}$$

where

$$J_3 = \begin{bmatrix} -l_{1r}S_1 - x_3S_{13} & -x_3S_{13} & 0 & 0 & 0 \\ l_{1r}C_1 + x_3C_{13} & x_3C_{13} & 0 & 0 & 0 \end{bmatrix} \tag{2.80}$$

$$J_4 = \begin{bmatrix} -l_{1r}S_1 - l_{3r}S_{13} - u_4C_{134} - x_4S_{134} & -l_{3r}S_{13} - u_4C_{134} - x_4S_{134} \\ l_{1r}C_1 + l_{3r}S_{13} - u_4S_{134} + x_4C_{134} & l_{3r}C_{13} - u_4S_{134} + x_4C_{134} \\ -u_4C_{134} - x_4S_{134} & -\xi_{41}S_{134} & -\xi_{42}S_{134} \\ -u_4S_{134} + x_4C_{134} & \xi_{41}C_{134} & \xi_{42}C_{134} \end{bmatrix} \tag{2.81}$$

Mass matrices and gravity force vectors are derived from the Jacobian matrices.

$$M_{ij}^B = \int_0^{l_3} J_3^T J_3 \rho_3 A_3 dx_3 + \int_0^{l_4} J_4^T J_4 \rho_4 A_4 dx_4 \tag{2.82}$$

$$G_1^B = \int_0^{l_3} J_3[2,1]\rho_3 A_3 dx_3 + \int_0^{l_4} J_4[2,1]\rho_4 A_4 dx_4$$

$$G_3^B = \int_0^{l_3} J_j[2,2]\rho_3 A_3 dx_3 + \int_0^{l_4} J_4[2,2]\rho_4 A_4 dx_4 \tag{2.83}$$

$$G_4^B = \int_0^{l_4} J_4[2,3]\rho_4 A_4 dx_4$$

Elements of mass matrices and gravity force vectors are:

$$\begin{aligned} M_{11}^B &= \int_0^{l_3} (x_3^2 + l_{1r}^2 + 2l_{1r}x_3C_3)\rho_3 A_3 dx_3 \\ &+ \int_0^{l_4} (l_{1r}^2 + l_{3r}^2 + u_4^2 + x_4^2 \\ &+ 2l_{1r}(l_{3r}C_3 + x_4C_{34} - u_4S_{34}) \\ &+ 2l_{3r}(x_4C_4 - u_4S_4))\rho_4 A_4 dx_4 \end{aligned}$$

$$\begin{aligned} M_{12}^B &= \int_0^{l_3} (x_3^2 + l_{1r}x_3C_3)\rho_3 A_3 dx_3 \\ &+ \int_0^{l_4} (l_{3r}^2 + u_4^2 + x_4^2 \\ &+ l_{1r}(l_{3r}C_3 + x_4C_{34} - u_4S_{34}) \\ &+ 2l_{3r}(x_4C_4 - u_4S_4))\rho_4 A_4 dx_4 \end{aligned}$$

$$M_{13}^B = \int_0^{l_4} (x_4^2 + u_4^2 + l_{1r}(x_4C_{34} - u_4S_{34}) + l_{3r}(x_4C_4 - u_4S_4))\rho_4 A_4 dx_4$$

$$M_{14}^B = \int_0^{l_4} \psi_{41}(x_4 + l_{1r}C_{34} + l_{3r}C_4)\rho_4 A_4 dx_4$$

$$M_{15}^B = \int_0^{l_4} \psi_{42}(x_4 + l_{1r}C_{34} + l_{3r}C_4)\rho_4 A_4 dx_4 \qquad (2.84)$$

$$M_{22}^B = \int_0^{l_3} x_3^2\rho_3 A_3 dx_3 + \int_0^{l_4} (l_{3r}^2 + u_4^2 + x_4^2 + 2l_{3r}(x_4C_4 - l_{3r}u_4S_4))\rho_4 A_4 dx_4$$

$$M_{23}^B = \int_0^{l_4} (x_4^2 + +u_4^2 + l_{3r}(x_4C_4 - u_4S_4))\rho_4 A_4 dx_4$$

$$M_{24}^B = \int_0^{l_4} \psi_{41}(x_4 + l_{3r}C_4)\rho_4 A_4 dx_4$$

$$M_{25}^B = \int_0^{l_4} \psi_{42}(x_4 + l_{3r}C_4)\rho_4 A_4 dx_4$$

$$M_{33}^B = \int_0^{l_4} (x_4^2 + u_4^2)\rho_4 A_4 dx_4$$

$$M_{34}^B = \int_0^{l_4} \psi_{41} x_4 \rho_4 A_4 dx_4$$

$$M_{35}^B = \int_0^{l_4} \psi_{42} x_4 \rho_4 A_4 dx_4$$

$$M_{44}^B = \int_0^{l_4} \psi_{41}^2 \rho_4 A_4 dx_4$$

$$M_{45}^B = \int_0^{l_4} \psi_{41}\psi_{42} \rho_4 A_4 dx_4$$

$$M_{55}^B = \int_0^{l_4} \psi_{42}^2 \rho_4 A_4 dx_4$$

$$\begin{aligned} G_1^B &= \int_0^{l_3} (l_{1r}C_1 + x_3 C_{13})\rho_3 A_3 dx_3 \\ &\quad + \int_0^{l_4} (l_{1r}C_1 + l_{3r}C_{13} - u_4 S_{134} + x_4 C_{134})\rho_4 A_4 dx_4 \end{aligned}$$

$$G_2^B = \int_0^{l_3} x_3 C_{13}\rho_3 A_3 dx_3 + \int_0^{l_4} (l_{3r}C_{13} - u_4 S_{134} + x_4 C_{134})\rho_4 A_4 dx_4 \qquad (2.85)$$

$$G_3^B = \int_0^{l_4} (-u_4 S_{134} + x_4 C_{134})\rho_4 A_4 dx_4$$

After the integral are defined using (2.23 - 28), the mass matrices and gravity vectors of linearized equations are :

$$M_{11}^B = m_2 l_{1r}^2 + D_3 + 2m_3 l_{1r} l_{3c} C_3 + D_4 + m_4(l_{1r}^2 + l_{3r}^2)$$

$$+2m_4(l_{1r} l_{3r} C_3 + l_{4c} l_{3r} C_4 + l_{1r} l_{4c} C_{34})$$

$$M_{12}^B = D_3 + m_3 l_{1r} l_{3c} C_3 + m_4 l_{3r}^2 + D_4$$

$$+m_4(l_{1r}l_{3r}C_3 + 2l_{4c}l_{3r}C_4 + l_{4c}l_{1r}C_{34})$$

$$M_{13}^B = D_4 + m_4 l_{4c}(l_{3r}C_4 + l_{1r}C_{34})$$

$$M_{14}^B = AM_{41} + LM_{41}(l_{3r}C_4 + l_{1r}C_{34})$$

$$M_{15}^B = AM_{42} + LM_{42}(l_{3r}C_4 + l_{1r}C_{34}) \tag{2.86}$$

$$M_{22}^B = D_3 + m_4 l_{3r}^2 + D_4 + 2m_4 l_{4c}l_{3r}C_4$$

$$M_{23}^B = D_4 + m_4 l_{4c}l_{3r}C_4$$

$$M_{24}^B = AM_{41} + LM_{41}l_{3r}C_4$$

$$M_{25}^B = AM_{42} + LM_{42}l_{3r}C_4$$

$$M_{33}^B = D_4$$

$$M_{34}^B = AM_{41}$$

$$M_{35}^B = AM_{42}$$

$$M_{44}^B = NM_{41}$$

$$M_{45}^B = \int_0^{l_4} \psi_{41}\psi_{42}\rho_4 A_4 dx_4$$

$$M_{55}^B = NM_{42}$$

$$G_1^B = m_3(l_{1r}C_1 + l_{3c}C_{13}) + m_4(l_{1r}C_1 + l_{3r}C_{13} + l_{4c}C_{134})$$

$$G_3^B = m_3 l_{3c}C_{13} + m_4(l_{3r}C_{13} + l_{4c}C_{134}) \tag{2.87}$$

$$G_4^B = m_4 l_{4c}C_{134}$$

The stiffness matrices are:

$$K_{ij} = \int_0^{l_i} EI_i[\frac{\partial^2 \psi_{ij}}{\partial x_i^{\,2}}]^2 dx_i \quad (i = 4, j = 1, 2) \tag{2.88}$$

2.5.2 Centrifugal and Coriolis force

The velocity coupling terms are obtained from the mass matrix using the Christoffel symbol. These terms are also simplified by several structural properties.

$$e_1 = l_{1r}[\int_0^{l_3} x_3 S_3 \rho_3 A_3 dx_3 + \int_0^{l_4} (l_{3r} S_3 + x_4 S_{34} + u_4 C_{34}) \rho_4 A_4 dx_4]$$

$$e_2 = \int_0^{l_4} \{l_{1r}(x_4 S_{34} + u_4 C_{34}) + l_{3r}(x_4 S_4 + u_4 C_4)\} \rho_4 A_4 dx_4$$

$$e_3 = l_{3r}[\int_0^{l_4} (x_4 S_4 + u_4 C_4) \rho_4 A_4 dx_4]$$

$$\begin{aligned} e_{41} &= \int_0^{l_4} \psi_{41}\{-(\psi_{41}\xi_{41} + \psi_{42}\xi_{42}) + (l_{1r} S_{34} - l_{3r} S_4)\} \rho_4 A_4 dx_4 \\ e_{42} &= \int_0^{l_4} \psi_{42}\{-(\psi_{41}\xi_{41} + \psi_{42}\xi_{42}) + (l_{1r} S_{34} - l_{3r} S_4)\} \rho_4 A_4 dx_4 \end{aligned} \tag{2.89}$$

$$\begin{aligned} e_{51} &= \int_0^{l_4} \psi_{41}\{-(\psi_{41}\xi_{41} + \psi_{42}\xi_{42}) + l_{3r} S_4\} \rho_4 A_4 dx_4 \\ e_{52} &= \int_0^{l_4} \psi_{42}\{-(\psi_{41}\xi_{41} + \psi_{42}\xi_{42}) + l_{3r} S_4\} \rho_4 A_4 dx_4 \end{aligned}$$

$$\begin{aligned} e_{61} &= \int_0^{l_4} \psi_{41}(\psi_{41}\xi_{41} + \psi_{42}\xi_{42}) \rho_4 A_4 dx_4 \\ e_{62} &= \int_0^{l_4} \psi_{42}(\psi_{41}\xi_{41} + \psi_{42}\xi_{42}) \rho_4 A_4 dx_4 \end{aligned}$$

After evaluating the integral,

$$e_1 = l_{1r}[(m_3 l_{3c} + m_4 l_{3r}) S_3 + m_4 l_{4c} S_{34} + (LM_{41}\xi_{41} + LM_{42}\xi_{42}) C_{34}]$$

$$e_2 = l_{1r}[m_4 l_{4c} S_{34} + (LM_{41}\xi_{41} + LM_{42}\xi_{42})C_2]$$

$$+l_{3r}[m_4 l_{4c} S_4 + (LM_{41}\xi_{41} + LM_{42}\xi_{42})C_4]$$

$$e_3 = l_{3r}[m_4 l_{4c} S_4 + (LM_{41}\xi_{41} + LM_{42}\xi_{42})C_4]$$

$$e_{41} = -NM_{41}\xi_{41} + (l_{1r}S_{34} + l_{3r}S_4)LM_{41}m_4 \tag{2.90}$$

$$e_{42} = -NM_{42}\xi_{42} + (l_{1r}S_{34} + l_{3r}S_4)LM_{42}m_4$$

$$e_{51} = -NM_{41}\xi_{41} + l_{3r}S_4 LM_{41}m_4$$

$$e_{52} = -NM_{42}\xi_{42} + l_{3r}S_4 LM_{42}m_4$$

$$e_{61} = -NM_{41}\xi_{41}$$

$$e_{62} = -NM_{42}\xi_{42}$$

Using these coefficients, the velocity coupling matrix can be expressed as follows:

$$C(1)^B = \begin{bmatrix} 0 & -e_1 & -e_2 & -e_{41} & -e_{42} \\ & -e_2 & -e_1 & -e_{41} & -e_{42} \\ & & -e_1 & -e_{41} & -e_{42} \\ & & & 0 & 0 \\ & & & & 0 \end{bmatrix} \tag{2.91}$$

$$C(2)^B = \begin{bmatrix} e_1 & 0 & -e_3 & -e_{51} & -e_{52} \\ & 0 & -e_3 & -e_{51} & -e_{52} \\ & & -e_3 & -e_{51} & -e_{52} \\ & & & 0 & 0 \\ & & & & 0 \end{bmatrix} \tag{2.92}$$

$$C(3)^B = \begin{bmatrix} e_2 & e_3 & 0 & -e_{61} & -e_{62} \\ & e_3 & 0 & -e_{61} & -e_{62} \\ & & 0 & -e_{61} & -e_{62} \\ & & & 0 & 0 \\ & & & & 0 \end{bmatrix} \tag{2.93}$$

$$C(4)^B = \begin{bmatrix} e_{41} & e_{51} & e_{61} & 0 & 0 \\ & e_{51} & e_{61} & 0 & 0 \\ & & e_{61} & 0 & 0 \\ & & & 0 & 0 \\ & & & & 0 \end{bmatrix} \tag{2.94}$$

$$C(5)^B = \begin{bmatrix} e_{42} & e_{52} & e_{62} & 0 & 0 \\ & e_{52} & e_{62} & 0 & 0 \\ & & e_{62} & 0 & 0 \\ & & & 0 & 0 \\ & & & & 0 \end{bmatrix} \tag{2.95}$$

2.6 Conclusion

Mass matrices and gravity vectors are directly derived from the Jacobian matrices which are easily calculated from position vectors by SMP. Because the deriving

procedure is simple, it reduces the possibility of producing incorrect equations. Furthermore, this form can easily be used to expand a series of mode shape functions describing elastic deformation. Six inertia parameters are defined and analogous terms exist for the cases with and without payload. The velocity coupling matrices, which are the coefficients of centrifugal and Coriolis force terms, are derived from the mass matrices using the Christoffel symbol and are simplified using several structural properties. The resulting velocity coupling matrices have a structure which is useful to reduce the number of terms calculated, to check correctness, or to extend the model to higher order.

CHAPTER III

Constrained Dynamic Analysis

3.1 Introduction

In this chapter, a numerical method is presented for dynamic analysis of closed kinematic chain systems such as parallel link mechanisms. Dynamic solution of a closed kinematic chain system requires solution of a mixed set of differential equations of motion and algebraic constraint equations. Singular Value Decomposition (SVD) is used for reducing the equations by eliminating the unknown constraint force. The nonlinear constraint equations of RALF are derived. Natural frequencies and eigenvectors of a closed kinematic chain system are derived and verified by a simple example.

3.2 Singular Value Decomposition

As mentioned in chapter II, the equations of motion of a flexible arm with a parallel link mechanism are expressed by the mixed set of differential equations (2.6) and nonlinear algebraic equations (2.7). The Lagrange multiplier λ is included in differential equations to describe the unknown constraint force by the constraint Jacobian matrix.

$$M\ddot{q} + Kq + F + \Phi_q^T \lambda = Q \tag{3.1}$$

where F is the nonlinear force vector which includes Coriolis and centrifugal forces and the gravity force. Nonlinear algebraic constraint equations describe the relationship among the angles within the closed kinematic chain.

$$\Phi(q) = 0. \tag{3.2}$$

Differentiating the constraint equation (3.2) with respect to time yields the velocity form of constraint equations.

$$\Phi_q \dot{q} = 0 \tag{3.3}$$

For solving this mixed set of differential and algebraic equations, the unknown constraint force vector, λ, has to be eliminated from the differential equations. The constraint Jacobian matrix Φ_q, with rank m, can be decomposed into the following form using Singular Value Decomposition (SVD).

$$\Phi_q = U \Sigma V^T \tag{3.4}$$

With proper partitioning [38], it can be expressed as

$$\Phi_q = [U_1 \; U_2][\Sigma_m \; 0] \begin{bmatrix} V_1^T \\ V_2^T \end{bmatrix} \tag{3.5}$$

where U_i and V_i are orthonormal bases for four fundamental subspaces as shown in Fig 3.1. The columns of U_i are the orthonormal eigenvectors of the matrix $\Phi_q \Phi_q^T$. The columns of V_i are the orthonormal eigenvectors of the matrix $\Phi_q^T \Phi_q$. Σ_m is equal to $\text{diag}(\sigma_1, \sigma_2, ..., \sigma_m)$ ordered $\sigma_1 \geq \sigma_2 \geq ... > 0$. The σ_i are called singular values which are the nonnegative square roots of the corresponding eigenvalues. Notice that V_2 is the null space of Φ_q which satisfies the following relationship.

$$\Phi_q V_2 = 0 \tag{3.6}$$

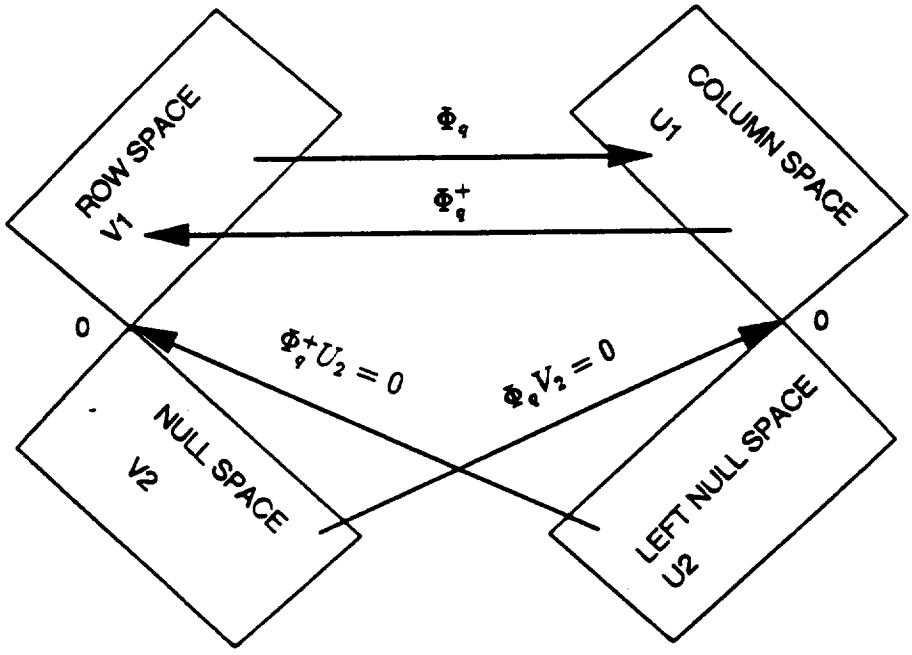

Figure 3.1: Four fundamental subspaces of Φ_q

Also, Φ_q^+, called the pseudo inverse of Φ_q, is defined as follows:

$$\Phi_q^+ = [V_1\ V_2] \begin{bmatrix} \Sigma_m^{-1} \\ 0 \end{bmatrix} \begin{bmatrix} U_1^T \\ U_2^T \end{bmatrix} \tag{3.7}$$

Premultiplying (3.1) by V_2^T and using the orthogonality of (3.6) gives

$$V_2^T M\ddot{q} + V_2^T K q + V_2^T F = V_2^T Q \tag{3.8}$$

The unknown constraint forces are thus eliminated from the equations of motion. However, because $V_2^T M$ is the (n - m) x n rectangular matrix, additional equations are needed to get a solution. Let us define a new variable z which is an independent coordinate with dimension (n - m) x 1. The homogeneous solution to (3.3) is $V_2\dot{z}$.

$$\dot{q} = V_2\dot{z} \tag{3.9}$$

Geometrically, it is the projection of the velocity vector $\dot{q}$ onto the tangent hyperplane of the constraint surface. Moreover, the time derivative of (3.3) gives

$$\begin{aligned} \Phi_q\ddot{q} &= -\dot{\Phi}_q\dot{q} \\ &= -\dot{q}^T(\Phi_q)_q\dot{q} \end{aligned} \tag{3.10}$$

Then, $\ddot{q}$ is represented as

$$\ddot{q} = -\Phi_q^+\dot{q}^T(\Phi_q)_q\dot{q} + V_2\ddot{z} \tag{3.11}$$

The first and second term in the right hand side of (3.11) are the particular solution and the homogeneous solution to equation (3.10) respectively. Physically, they are the normal accelerations and the tangential accelerations of the constraint surface, respectively. Finally, by integrating (3.9), position vectors are expressed as

$$q = V_2 z + C \tag{3.12}$$

where C, a constant, is here chosen to be zero to satisfy initial conditions.

Substituting (3.9),(3.11), and (3.12) into (3.8), the equations of motion become:

$$V_2^T M V_2 \ddot{z} + V_2^T K V_2 z = V_2^T Q + V_2^T \hat{F} \tag{3.13}$$

where

$$\hat{F} = M \Phi_q^+ \dot{q}^T (\Phi_q)_q \dot{q} - F \tag{3.14}$$

Equation (3.13) is a set of n - m equations in terms of the independent generalized coordinate z. As a result, the n equations (3.1) and m constraint equations (3.3) are reduced to n - m equations in (3.13) by the coordinate transformation matrix V_2 [67]. Because the independent generalized coordinate lies on the tangential plane of the constraint surface instantaneously, the changes in generalized coordinates due to the integration of $\dot{z}$ during a small time interval do not result in significant constraint violation [37]. Therefore, the reduced equations of motion (3.13) are free from constraints and stable for numerical integration error.

3.3 Constraint Equations

To apply the SVD method to RALF, the constraint equations must be described first. Suppose the elastic deformation is small compared to the length of the link, the deformed parallel link mechanism is depicted as in Fig 3.3. For the virtually cut joint C', the constraint equations are expressed by two vectors.

$$\vec{AB} + \vec{BB'} + \vec{B'C'} = \vec{AD} + \vec{DC'} \tag{3.15}$$

or

$$\begin{aligned}(l_{1f}C_1 - u_{1e}S_1 + l_{2r}C_{12})i + (l_{1f}S_1 + u_{1e}C_1 + l_{2r}S_{12})j \\ = (l_3 C_{13} + l_4 C_{134})i + (l_3 S_{13} + l_4 S_{134})j\end{aligned} \tag{3.16}$$

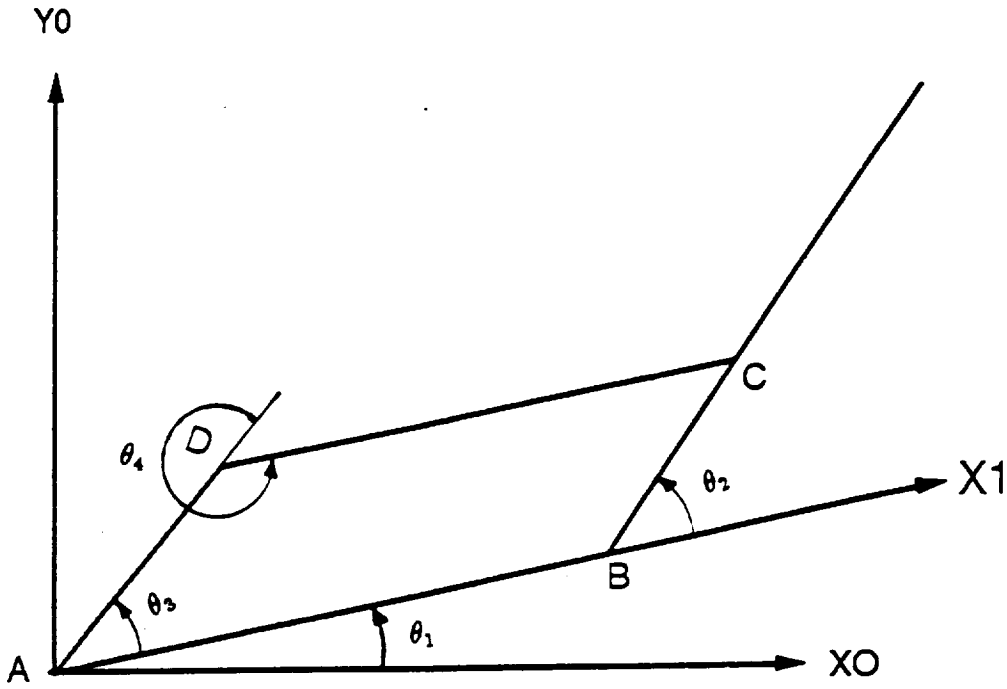

Figure 3.2: Rigid parallel link mechanism

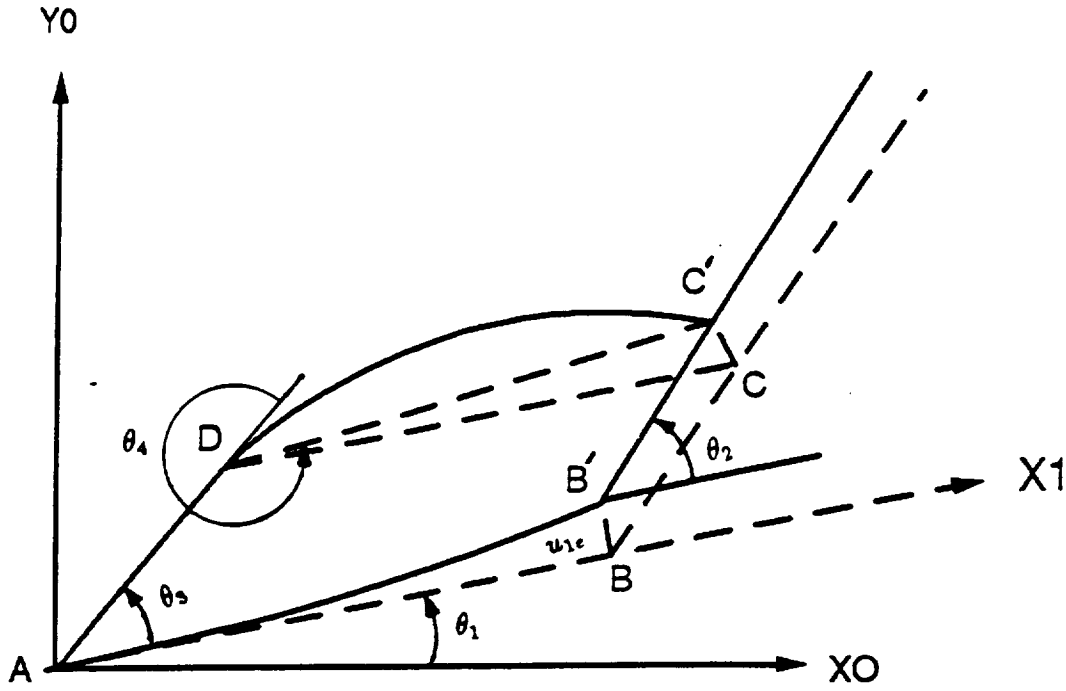

Figure 3.3: Flexible parallel link mechanism

When this equation is expressed in the form of equations (3.2) and (3.3), the position form of constraint equations are

$$\Phi^f = \begin{bmatrix} l_{1f}C_1 - u_{1e}S_1 + l_{2r}C_{12} - l_3C_{13} - l_4C_{134} \\ l_{1f}S_1 + u_{1e}C_1 + l_{2r}S_{12} - l_3S_{13} - l_4S_{134} \end{bmatrix} = 0 \tag{3.17}$$

or, in the velocity form of constraint equations, the elements of the constraint Jacobian matrix are:

$$\Phi_q^f = \begin{bmatrix} l_{1f}S_1 + u_{1e}C_1 + l_{2r}S_{12} - l_3S_{13} - l_4S_{134} \\ l_{1f}C_1 - u_{1e}S_1 + l_{2r}C_{12} - l_3C_{13} - l_4C_{134} \end{bmatrix}$$

$$\begin{matrix} l_{2r}S_{12} & -l_3S_{13} - l_4S_{134} & -l_4S_{134} \\ l_{2r}C_{12} & -l_3C_{13} - l_4C_{134} & -l_4C_{134} \end{matrix}$$

$$\begin{bmatrix} \psi_{11e}S_1 & \psi_{12e}S_1 & 0 & 0 & 0 & 0 \\ \psi_{11e}C_1 & \psi_{12e}C_1 & 0 & 0 & 0 & 0 \end{bmatrix} \tag{3.18}$$

In the rigid parallel link mechanism as shown in Fig 3.2, the elastic deformation is not included in the constraint equations. The coordinates transformation matrix V_2, which is derived from Φ_q^r by SVD, is

$$\Phi_q^r = \begin{bmatrix} l_{1f}S_1 + l_{2r}S_{12} - l_3S_{13} - l_4S_{134} \\ l_{1f}C_1 + l_{2r}C_{12} - l_3C_{13} - l_4C_{134} \end{bmatrix}$$

$$\begin{bmatrix} l_{2r}S_{12} & -l_3S_{13} - l_4S_{134} & -l_4S_{134} \\ l_{2r}C_{12} & -l_3C_{13} - l_4C_{134} & -l_4C_{134} \end{bmatrix} \tag{3.19}$$

$$V_2 = \begin{bmatrix} 1 & 0 \\ 0 & 1/\sqrt{3} \\ 0 & 1/\sqrt{3} \\ 0 & -1/\sqrt{3} \end{bmatrix} = \begin{bmatrix} 1 & 0 \\ 0 & 0.577 \\ 0 & 0.577 \\ 0 & -0.577 \end{bmatrix} \tag{3.20}$$

where

$$q_r = \{\theta_1, \theta_2, \theta_3, \theta_4\}^T \tag{3.21}$$

V_2 is independent of angles and the ratio of the link length. The independent coordinates of the rigid case are θ_1 and $\frac{1}{\sqrt{3}}(\theta_2 + \theta_3 - \theta_4)$ for all configurations. However, if an independent generalized coordinate is selected by Gaussian elimination, it may change frequently [37]. On the other hand, in the flexible parallel link mechanism as shown in Fig 3.3, V_2 depends on the elastic deflection and its configuration, unlike the rigid parallel link mechanism, as shown in equations (3.22 - 3.24).

For $u_{1e}/l_{1f} = 0, \quad \theta_2 = 135\ deg.$

$$V_2 = \begin{bmatrix} -1 & 0 & 0 & 0 & 0 & 0 & 0 & 0 \\ 0 & 0.583 & 0.169 & -0.010 & 0 & 0 & 0 & 0 \\ 0 & 0.583 & 0.169 & -0.010 & 0 & 0 & 0 & 0 \\ 0 & -0.566 & 0.388 & -0.023 & 0 & 0 & 0 & 0 \\ 0 & 0.026 & 0.890 & 0.006 & 0 & 0 & 0 & 0 \\ 0 & 0.002 & 0.006 & 0.999 & 0 & 0 & 0 & 0 \\ 0 & 0 & 0 & 0 & 0 & 0 & 0 & 0 \\ 0 & 0 & 0 & 0 & 0 & 0 & 0 & 0 \\ 0 & 0 & 0 & 0 & 0 & 0 & 0 & 0 \\ 0 & 0 & 0 & 0 & 0 & 0 & 0 & 0 \end{bmatrix} \tag{3.22}$$

For $u_{1e}/l_{1f} = 0.01, \quad \theta_2 = 135\ deg.$

$$V_2 = \begin{bmatrix} -1 & 0 & 0 & 0 & 0 & 0 & 0 & 0 \\ 0 & 0.580 & 0.184 & -0.011 & 0 & 0 & 0 & 0 \\ 0 & 0.580 & 0.173 & -0.011 & 0 & 0 & 0 & 0 \\ 0 & -0.572 & 0.381 & -0.022 & 0 & 0 & 0 & 0 \\ 0 & 0.012 & 0.890 & 0.006 & 0 & 0 & 0 & 0 \\ 0 & 0.001 & 0.006 & 0.999 & 0 & 0 & 0 & 0 \\ 0 & 0 & 0 & 0 & 0 & 0 & 0 & 0 \\ 0 & 0 & 0 & 0 & 0 & 0 & 0 & 0 \\ 0 & 0 & 0 & 0 & 0 & 0 & 0 & 0 \\ 0 & 0 & 0 & 0 & 0 & 0 & 0 & 0 \end{bmatrix} \tag{3.23}$$

For $u_{1e}/l_{1f} = 0.0, \quad \theta_2 = 60\ deg.$

$$V_2 = \begin{bmatrix} -1 & 0 & 0 & 0 & 0 & 0 & 0 & 0 \\ 0 & 0.584 & 0.163 & -0.010 & 0 & 0 & 0 & 0 \\ 0 & 0.584 & 0.163 & -0.010 & 0 & 0 & 0 & 0 \\ 0 & -0.572 & 0.394 & -0.023 & 0 & 0 & 0 & 0 \\ 0 & 0.035 & 0.890 & 0.006 & 0 & 0 & 0 & 0 \\ 0 & 0.002 & 0.006 & 0.999 & 0 & 0 & 0 & 0 \\ 0 & 0 & 0 & 0 & 0 & 0 & 0 & 0 \\ 0 & 0 & 0 & 0 & 0 & 0 & 0 & 0 \\ 0 & 0 & 0 & 0 & 0 & 0 & 0 & 0 \\ 0 & 0 & 0 & 0 & 0 & 0 & 0 & 0 \end{bmatrix} \tag{3.24}$$

where

$$q_f = \{\theta_1, \theta_2, \theta_3, \theta_4, \xi_{11}, \xi_{12}, \xi_{21}, \xi_{22}, \xi_{41}, \xi_{42}\}^T \tag{3.25}$$

The angle θ_4 is mainly changed by the deformation of the lower link. Because the links are vibrating during motion, V_2 is also changing. Therefore, the constraint Jacobian matrix must be decomposed at every step to preserve the direction continuity of the basis of V_2. However, performing SVD at each integration step would result in a tremendous increase in computing time. Furthermore, performing redecomposition and recomputing the initial conditions on z at each time step requires numerical integration algorithms which use information only from the current time step even though this eliminates the need for null space continuity. Therefore, Mani introduced the velocity norm as the criterion for redecomposition [46]. V_2 is held constant until the specified criteria are violated. In order to circumvent the redecomposition, updating algorithm using QR decomposition was developed [37]. For more accurate and stable solution, several algorithms have been developed recently [39,32,57]. But, those methods are not applied in this thesis.

3.4 Computational Algorithm

An algorithm for solving the equation (3.13) is summarized as follows:

1) The constraint Jacobian matrix Φ_q is decomposed by the singular value decomposition subroutine LSVDF of IMSL [33]. Then, the initial condition for independent coordinate z_i at time step i is defined by the following transformation.

$$z_i^0 = V_2^T q_i^0 \tag{3.26}$$

$$\dot{z}_i^0 = V_2^T \dot{q}_i^0 \tag{3.27}$$

Initial conditions for first-order differential equations are

$$Y(t_0) = \begin{bmatrix} q_0 \\ z_0 \\ \dot{z}_0 \end{bmatrix} \tag{3.28}$$

2) Integrate ($\dot{q}_i$, $\dot{z}_i$, $\ddot{z}_i$) of equations (3.9) and (3.13) simultaneously from t_i to t_{i+1} to get (q_{i+1}, z_{i+1}, $\dot{z}_{i+1}$) using the subroutine DGEAR of IMSL which is based on Adams predictor - corrector method.

3) Solve the original velocity vector $\dot{q}_{i+1}$ from $\dot{z}_{i+1}$ using the transformation of equation (3.9).

4) Check the velocity norm. If $\| \dot{z} \|_2$ is less than a predetermined fraction of $\| \dot{q} \|_2$, the constraint Jacobian matrix Φ_q needs to be redecomposed [37,46] and step 1) is repeated. Otherwise, step 2) is executed next.

5)repeat the above steps until the final time is reached.

Application of this algorithm to RALF will be explained in Chapter V.

3.5 Natural Frequencies and Mode Shapes

Natural frequencies and mode shapes can be derived from the linearized equations of motion. Eigenvalues and eigenvectors of the constrained equations can be obtained from the reduced equations (3.13) linearized about zero velocity.

$$V_2^T M V_2 \ddot{z} + V_2^T K V_2 z = 0 \tag{3.29}$$

Eigenvalues of the constrained equations, (3.1) and (3.3), are the same as those of the reduced equations (3.13). Eigenvectors of the constrained equations are derived by transforming those of the reduced equations as follows.

$$q = V_2 \, z \tag{3.30}$$

The validity of the above theory is demonstrated by the following simple example.

Now, the flexible parallel link mechanism is somewhat analogous to two masses connected to one another by springs as shown in Fig 3.4. This system can be fully described by the two coordinates x_1 and x_2. Equations of motion of this system

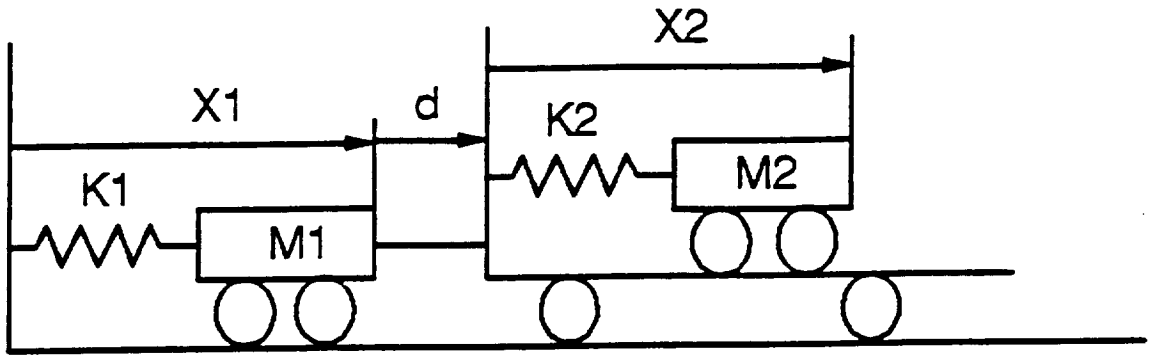

Figure 3.4: Constrained system

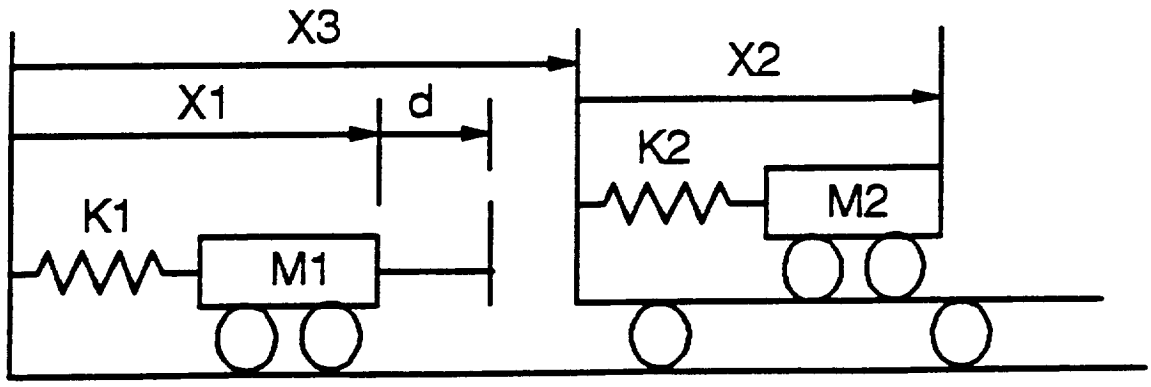

Figure 3.5: Unconstrained system

are:

$$\begin{bmatrix} M_1+M_2 & M_2 \\ M_2 & M_2 \end{bmatrix} \begin{Bmatrix} \ddot{x}_1 \\ \ddot{x}_2 \end{Bmatrix} + \begin{bmatrix} K_1 & 0 \\ 0 & K_2 \end{bmatrix} \begin{Bmatrix} x_1 \\ x_2 \end{Bmatrix} = 0 \tag{3.31}$$

If the values of mass and spring are arbitrarily assumed as

$$M_1 = 1 \qquad K_1 = 1$$

$$M_2 = 2 \qquad K_2 = 2 \quad , \tag{3.32}$$

the equations of motion are

$$\begin{bmatrix} 3 & 2 \\ 2 & 2 \end{bmatrix} \begin{Bmatrix} \ddot{x}_1 \\ \ddot{x}_2 \end{Bmatrix} + \begin{bmatrix} 1 & 0 \\ 0 & 2 \end{bmatrix} \begin{Bmatrix} x_1 \\ x_2 \end{Bmatrix} = 0 \tag{3.33}$$

and

$$M_a^{-1} K_a = \begin{bmatrix} 1 & -2 \\ -1 & 3 \end{bmatrix} \tag{3.34}$$

The characteristic equation is

$$\lambda^2 - 4\lambda + 1 = 0 \tag{3.35}$$

and the natural modes are

$$\Gamma_x = \begin{bmatrix} 1 & -0.7321 \\ 0.3660 & 1 \end{bmatrix} \tag{3.36}$$

The system can be also expressed by three coordinates x_1, x_2, x_3 and a constraint equation as shown in Fig 3.5. The redundant coordinate x_3 describes the relative motion of the two masses. Equations of motion in the new coordinates system, q = $\{x_1, x_2, x_3\}$, are

$$\begin{bmatrix} M_1 & 0 & 0 \\ 0 & M_2 & M_2 \\ 0 & M_2 & M_2 \end{bmatrix} \begin{Bmatrix} \ddot{x}_1 \\ \ddot{x}_2 \\ \ddot{x}_3 \end{Bmatrix} + \begin{bmatrix} K_1 & 0 & 0 \\ 0 & K_2 & 0 \\ 0 & 0 & 0 \end{bmatrix} \begin{Bmatrix} x_1 \\ x_2 \\ x_3 \end{Bmatrix} + \Phi_q^T \lambda = 0 \tag{3.37}$$

and the constraint equation is

$$x_3 = x_1 + d \tag{3.38}$$

The velocity form of constraint equation is

$$\dot{x}_3 = \dot{x}_1 \tag{3.39}$$

and it can be expressed as follows.

$$\Phi_q \dot{q} = \begin{bmatrix} 1 & 0 & -1 \end{bmatrix} \begin{Bmatrix} \dot{x}_1 \\ \dot{x}_2 \\ \dot{x}_3 \end{Bmatrix} = 0 \tag{3.40}$$

The constraint Jacobian matrix, Φ_q, is decomposed by SVD.

$$\Phi_q = 1 \begin{bmatrix} \sqrt{2} & 0 & 0 \\ 0 & 0 & 0 \\ 0 & 0 & 0 \end{bmatrix} \begin{bmatrix} 1/\sqrt{2} & -1/\sqrt{2} & 0 \\ 0 & 0 & 1 \\ -1/\sqrt{2} & -1/\sqrt{2} & 0 \end{bmatrix} \tag{3.41}$$

Here, the null space, V_2, is

$$V_2 = \begin{bmatrix} -1/\sqrt{2} & 0 \\ 0 & 1 \\ -1/\sqrt{2} & 0 \end{bmatrix} \tag{3.42}$$

The orthogonality of Φ_q and V_2 is checked as follows :

$$\Phi_q V_2 = \begin{bmatrix} 1 & 0 & -1 \end{bmatrix} \begin{bmatrix} -1/\sqrt{2} & 0 \\ 0 & 1 \\ -1/\sqrt{2} & 0 \end{bmatrix} = [0 \quad 0] \tag{3.43}$$

Then, the reduced mass and stiffness matrix are used to find the eigenvalues and the eigenvectors.

$$(V_2^T M V_2)^{-1} (V_2^T K V_2) = \begin{bmatrix} 1 & 2\sqrt{2} \\ 1/\sqrt{2} & 3 \end{bmatrix} \tag{3.44}$$

The characteristic equation is

$$\lambda^2 - 4\lambda + 1 = 0 \tag{3.45}$$

and the eigenvectors are

$$\Gamma_z = \begin{bmatrix} 1 & 1.0353 \\ -0.2588 & 1 \end{bmatrix} \tag{3.46}$$

The eigenvectors of the constrained system can be derived using V_2.

$$\Gamma_q = V_2\Gamma_z = \begin{bmatrix} -1/\sqrt{2} & -1/\sqrt{2} \\ -0.2588 & 0.9659 \\ -1/\sqrt{2} & -1/\sqrt{2} \end{bmatrix} = \begin{bmatrix} 1 & -0.7321 \\ 0.3660 & 1 \\ 1 & -0.7321 \end{bmatrix} \tag{3.47}$$

The first and second row are the eigenvector of x_1 and x_2

$$\Gamma_q = \begin{bmatrix} 1 & -0.7321 \\ 0.3660 & 1 \end{bmatrix} \tag{3.48}$$

Therefore, the characteristic equation (3.35) and eigenvectors (3.36) of the second order system are the same as those equations (3.45) and (3.48) of the reduced system respectively.

3.6 Conclusion

Parallel link mechanisms with rigid links have a simple relationship between the angles of the closed kinematic chain. However, the parallel link mechanism with flexible links requires nonlinear constraint equations to describe the relationship between angles because the link deflection gives a perturbation to the relationship. Therefore, a mixed set of differential and algebraic equations must be solved simultaneously. The transformation matrix V_2, which is derived from the constraint

Jacobian matrix by SVD, is used to obtain the reduced set of equations of motion which have no additional constraint equations. The reduced equations have been solved without any significant constraint violation. Therefore, SVD is a stable and efficient numerical method for the closed kinematic chain system. The simple example shows that natural frequencies and eigenvectors of the reduced equations are the same as those of the constrained equations.

CHAPTER IV

Mode Shape Functions of RALF

4.1 Introduction

Mode shape functions are employed to describe the elastic deformation of the flexible manipulator. In the assumed mode method, mode shape functions need only to be admissible functions which satisfy the geometric boundary conditions and form a basis set. However, a large number of modes are required to obtain accurate frequencies. The number of modes to be included can be reduced by choosing appropriate functions which satisfy static equilibrium at the interface between links. These functions can be derived systematically by using the component mode synthesis. Various component mode synthesis approaches have been developed depending on the assumed boundary conditions. Different boundary condition assumptions require different coordinate systems to describe the elastic deformation. Therefore, the method which fits with the current coordinate system is chosen. In order to explain component mode synthesis, an L - shaped beam is analyzed first. Secondly, mode shape functions of RALF are derived. Natural frequencies and mode shape functions of the analytical model of RALF are compared to the results of a finite element method, component mode synthesis and experiment results for validation of the proposed mode shape functions.

4.2 Component Mode Synthesis

A complete structure can be regarded as an assembly of component structures. The dynamic behavior of each component can be represented by a reduced number of component modes. Modes of the complete structure are formed from the component modes by enforcing equilibrium and compatibility along component interfaces. Generally, the constraint modes are introduced to provide shear and moment compatibility when the structure is assembled. Therefore, component mode synthesis is useful for predicting accurately the lower modes and frequencies of a structure using a small number of component modes. Numerous methods for component mode synthesis have been presented. Fixed, free, or loaded boundary conditions are used to determine the component modes. An L - shaped beam as shown in Fig. 4.2.a is used to explain the difference between these methods.

In a fixed interface method [19], modes of each component are expressed by a constraint mode and a normal mode. The constraint mode is defined as a static mode of internal nodes resulting from an imposed unit displacement at the interface node. The normal mode is defined as a dynamic mode of internal nodes when the boundary condition is in effect on the external nodes. In Fig. 4.1.a, link deflections of the lower beam can be expressed by rigid body rotations and clamped - clamped modes. Here the rigid body rotation is the constraint mode and the clamped - clamped modes are the normal modes. The boundary conditions of the lower beam and the upper beam are clamped - clamped and clamped - free, respectively.

In a free interface method [27], modes of each component are expressed by normal modes only. Modes of the upper beam are defined from the mass center. In Fig.4.1.b, the boundary conditions of each beam are clamped - free and free - free.

In a loaded interface method [6], modes of the lower beam are modified by

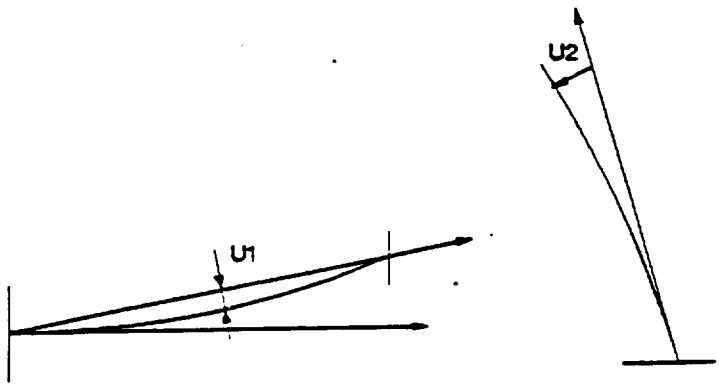

Figure 4.1.a: Coordinate system of a fixed interface method

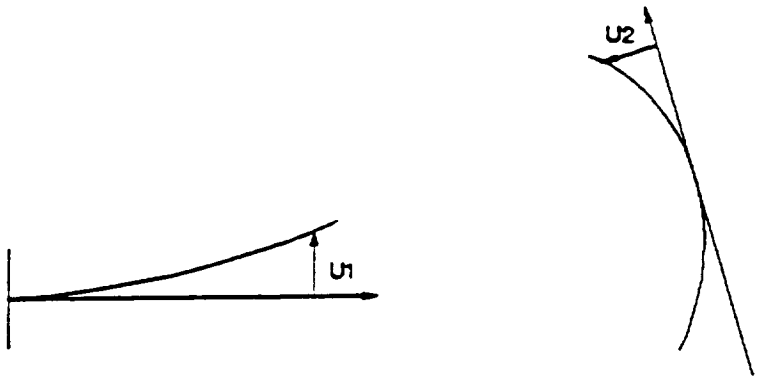

Figure 4.1.b: Coordinate system of a free interface method

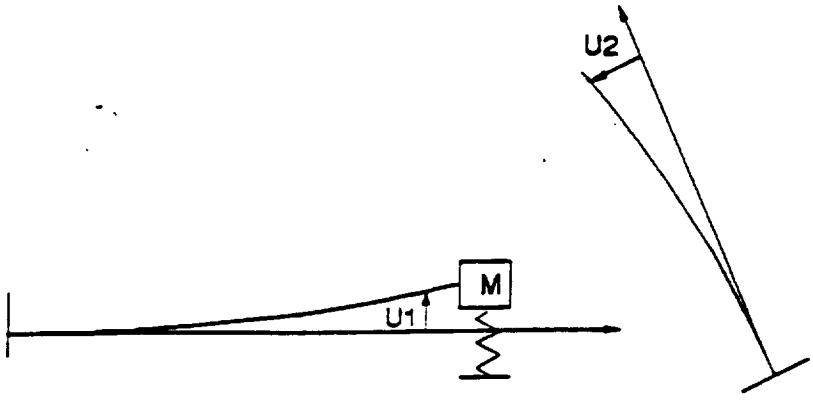

Figure 4.1.c: Coordinate system of a loaded interface method

added inertia and stiffness which are the effects of the upper beam. In Fig. 4.1.c, the boundary conditions of each beam are clamped - mass - spring and clamped - free.

Even though all methods give the same result in the limiting case, the coordinates which are used to describe the elastic deformation are different. Coordinates of the loaded interface method match closely with the coordinate system of RALF as seen in Fig. 2.3. The x_i axis is aligned with the tangent of the respective link at the origin O_i. Therefore, the mode shape functions of each link are derived using the loaded interface method.

4.3 Loaded Interface Method

In this section, a loaded interface method [6] is summarized. An L-shaped beam as shown Fig. 4.2.a is an example configuration of a two serial link manipulator and the typical example of component mode synthesis [31]. In this section, component mode synthesis is explained using the L - shaped beam. In Fig. 4.2.b, the complete structure can be separated into two components - the main component and the branch component. Each component's modes are expressed in terms of internal (i) coordinates and junction (j) coordinates.

A constraint mode is defined by statically imposing a unit displacement at the junction node and zero displacement at the internal node [19].

$$\begin{bmatrix} K_{ii} & K_{ij} \\ K_{ji} & K_{jj} \end{bmatrix} \begin{Bmatrix} \phi_B^{iC} \\ I \end{Bmatrix} = \begin{bmatrix} 0 \\ R \end{bmatrix} \tag{4.1}$$

where R is the reaction at the junction. Thus, the constraint mode is obtained from the top row partition.

$$\phi_B^{iC} = -K_{ii}^{-1} K_{ij} \tag{4.2}$$

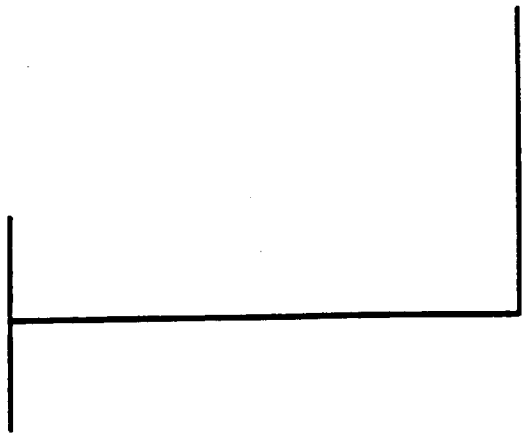

Figure 4.2.a: L - shaped beam

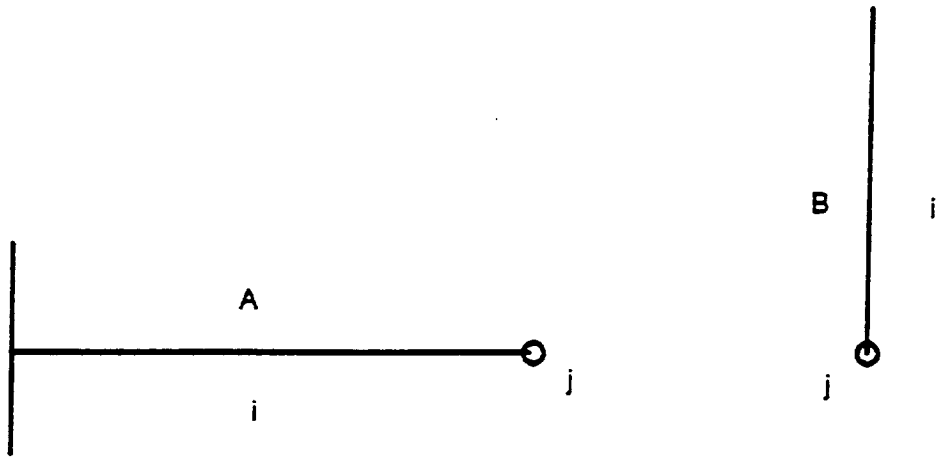

Figure 4.2.b: Components of L - shaped beam

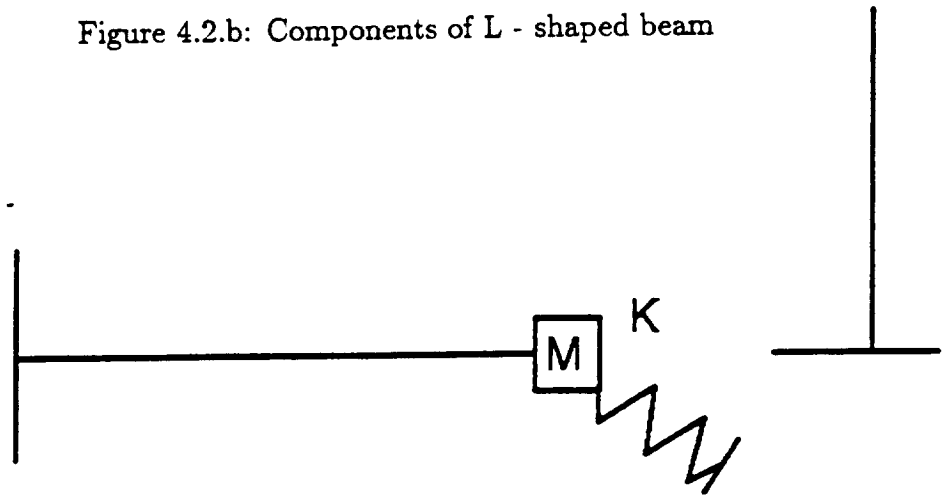

Figure 4.2.c: Boundary conditions of each component of L - shaped beam

A normal mode is obtained from the internal coordinates only.

$$(K_{ii} - \omega^2 M_{ii})\Phi_B^{iN} = 0 \tag{4.3}$$

The normal mode set Φ_B^{iN} is truncated to a set of normal modes ϕ_B^{iN}. Therefore, the internal node displacements of the branch component B can be expressed by superpositions of constraint modes ϕ_B^{iC} and normal modes ϕ_B^{iN}.

$$u_B^i = \phi_B^{iC} u_B^j + \phi_B^{iN} \xi_B \tag{4.4}$$

The total node displacements of branch component B are

$$u_B = \begin{Bmatrix} u_B^j \\ u_B^i \end{Bmatrix} = \begin{bmatrix} I & 0 \\ \phi_B^{iC} & \phi_B^{iN} \end{bmatrix} \begin{Bmatrix} u_B^j \\ \xi_B \end{Bmatrix} \tag{4.5}$$

The total potential energy for uncoupled components A and B can be written as

$$PE = \frac{1}{2} u_A^T K_A u_A + \frac{1}{2} u_B^T K_B u_B \tag{4.6}$$

Components A and B are coupled together by constraining the interface coordinates. This constraint is expressed as

$$u_B^j = u_A^j \tag{4.7}$$

Equation (4.7) assumes that the same reference coordinate system is used for both components. Different coordinate reference systems will require a rotational coordinate transformation using directional cosines. Therefore, the coordinate transformation that couples components A and B together becomes

$$u_B = \begin{Bmatrix} u_B^j \\ u_B^i \end{Bmatrix} = \begin{bmatrix} I \\ \phi_B^{iC} \end{bmatrix} u_B^j$$

$$= \begin{bmatrix} I \\ \phi_B^{iC} \end{bmatrix} u_A^j$$

$$= \begin{bmatrix} I \\ \phi_B^{iC} \end{bmatrix} [\, 0 \; I \,] \begin{Bmatrix} u_A^i \\ u_A^j \end{Bmatrix}$$
$$= T_l \, u_A \tag{4.8}$$

Therefore, equation (4.6) can be rewritten as

$$PE = \frac{1}{2} u_A^T K^A u_A \tag{4.9}$$

where

$$K^A = K_A + T_l^T K_B T_l \tag{4.10}$$

In similar way, the kinetic energy is

$$KE = \frac{1}{2} \dot{u}_A^T M^A \dot{u}_A \tag{4.11}$$

where

$$M^A = M_A + T_l^T M_B T_l \tag{4.12}$$

As shown in Fig. 4.2.c, the mass matrix M_A and the stiffness matrix K_A of component A are modified by the static influence of the branch component B.

Using these modified matrices, equations of motion of main component A are

$$M^A \ddot{u}_A + K^A u_A = 0 \tag{4.13}$$

The eigenvector of (4.13) yields

$$u_A = \Phi_A \xi_A \tag{4.14}$$

Eigenvectors Φ_A are also truncated to a set of normal modes ϕ_A.

$$u_A = \begin{Bmatrix} u_A^i \\ u_A^j \end{Bmatrix} = \begin{bmatrix} \phi_A^i \\ \phi_A^j \end{bmatrix} \xi_A \tag{4.15}$$

Both components are coupled using compatibility of junctions.

$$u_B^j = u_A^j = \phi_A^j \xi_A \tag{4.16}$$

So,

$$\begin{Bmatrix} \xi_A \\ u_B^j \\ \xi_B \end{Bmatrix} = \begin{bmatrix} I & 0 \\ \phi_A^j & 0 \\ 0 & I \end{bmatrix} \begin{Bmatrix} \xi_A \\ \xi_B \end{Bmatrix} \tag{4.17}$$

Therefore, using equations (4.15), (4.5), and (4.17), node displacements of each component can be expressed in terms of reduced order modal coordinates.

$$\begin{aligned} \begin{Bmatrix} u_A^i \\ u_A^j \\ u_B^j \\ u_B^i \end{Bmatrix} &= \begin{bmatrix} \phi_A^i & 0 & 0 \\ \phi_A^j & 0 & 0 \\ 0 & I & 0 \\ 0 & \phi_B^{iC} & \phi_B^{iN} \end{bmatrix} \begin{Bmatrix} \xi_A \\ u_B^j \\ \xi_B \end{Bmatrix} \\ &= \begin{bmatrix} \phi_A^i & 0 \\ \phi_A^j & 0 \\ \phi_A^j & 0 \\ \phi_B^{iC}\phi_A^j & \phi_B^{iN} \end{bmatrix} \begin{Bmatrix} \xi_A \\ \xi_B \end{Bmatrix} \\ &= T_s \begin{Bmatrix} \xi_A \\ \xi_B \end{Bmatrix} \end{aligned} \tag{4.18}$$

The reduced order of the mass and stiffness matrices are derived by the transformation matrix T_s.

$$\left[M \right] = T_s^T \begin{bmatrix} M_A & 0 \\ 0 & M_B \end{bmatrix} T_s \tag{4.19}$$

$$\left[K \right] = T_s^T \begin{bmatrix} K_A & 0 \\ 0 & K_B \end{bmatrix} T_s \tag{4.20}$$

Natural frequencies and modes of the complete system are calculated from eigenvalues and eigenvectors of the following equations.

$$[M]\begin{Bmatrix} \ddot{\xi}_A \\ \ddot{\xi}_B \end{Bmatrix} + [K]\begin{Bmatrix} \xi_A \\ \xi_B \end{Bmatrix} = \{0\} \tag{4.21}$$

The node displacements of each component are derived from eigenvectors of Eq. (4.21) using transformation matrix T_s of Eq. (4.18).

4.4 Component Modes of RALF

For the validity of modes which are derived using component mode synthesis, system natural frequencies of finite element model, component mode synthesis model, and the analytical model are compared.

The finite element model of RALF is modeled as shown in Fig. 4.3.a. Note that for this model the lower link is assumed to be supported where the connecting link attaches. This is a simplification over the physical system. The support sleeves of the lower link and the upper link and the connecting link are assumed as rigid elements by setting Young's modulus of these elements 1000 times bigger than that of the other elements. Because the hydraulic actuators are also assumed rigid, the boundary conditions of node A and C are assumed to be simply supported as well as node O. The finite element model is simulated by MSC/PAL2 program [51].

Component mode synthesis can predict the lower modes and natural frequencies of RALF using a small number of component modes. The derivation procedure is similar to Sec. 4.3. However, a little modification is required because RALF has a parallel link mechanism with components connected by pins.

RALF can be partitioned into three components as shown in Fig. 4.3.b. First, the boundary condition at node D' of the actuator link is assumed as simply sup-

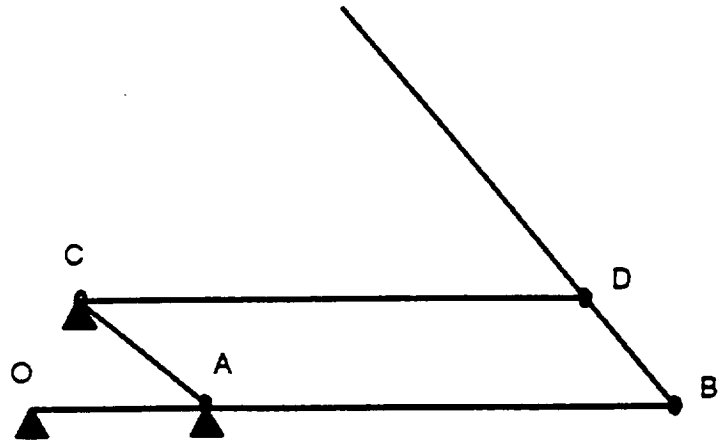

Figure 4.3.a: Schematic diagram of RALF

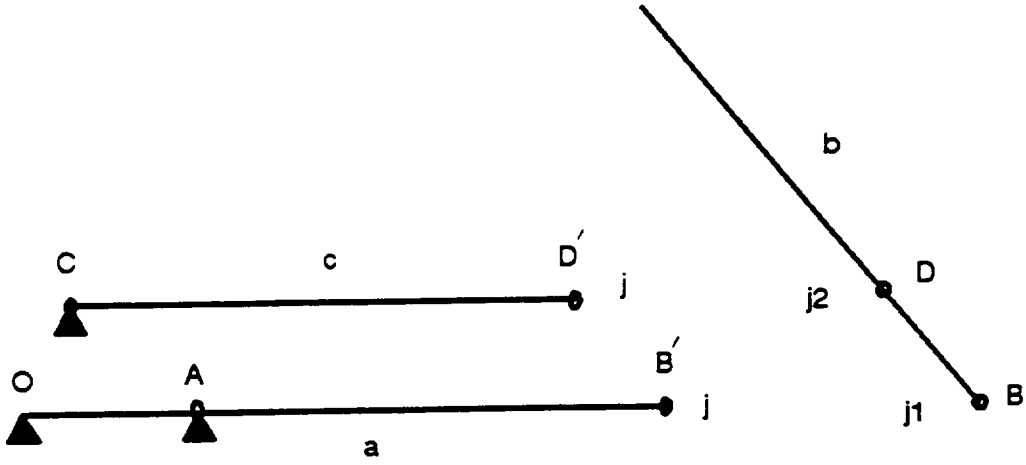

Figure 4.3.b: Components of RALF

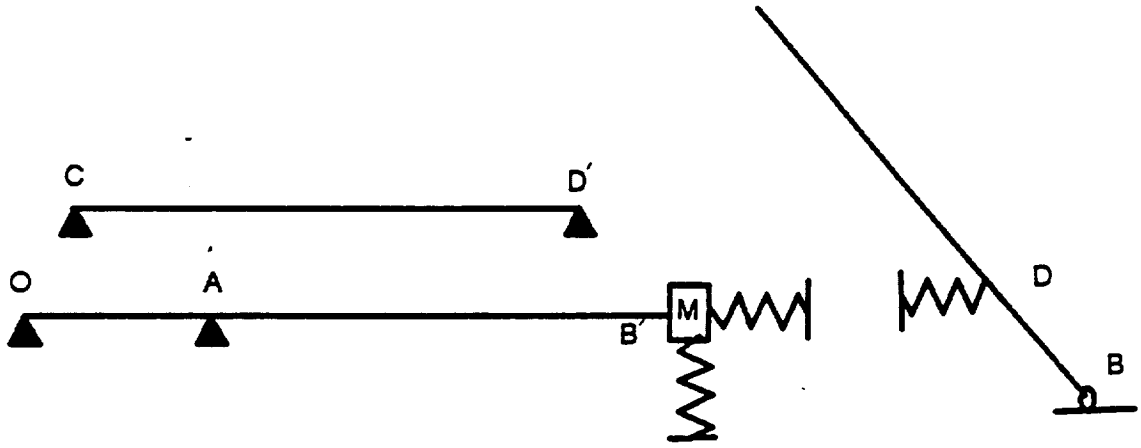

Figure 4.3.c: Boundary conditions of each component of RALF

ported imposing a fixed boundary condition on the pin joint. The reaction force or torque can be expressed by adding the stiffness and the mass at node D' of the upper link using (4.10) and (4.12). Next, the boundary condition at node B of the upper link is also assumed as simply supported. Furthermore, the stiffness and the mass are also added at the node B of the lower link. Using these boundary conditions as shown in Fig. 4.3.c, the node displacements of each link can be obtained by the finite element method. Node displacements of each component of the uncoupled system are expressed as follows.

$$\begin{Bmatrix} u_a^i \\ u_a^j \\ u_b^j \\ u_b^i \\ u_c^j \\ u_c^i \end{Bmatrix} = \begin{bmatrix} \phi_a^i & 0 & 0 & 0 & 0 \\ \phi_a^j & 0 & 0 & 0 & 0 \\ 0 & I & 0 & 0 & 0 \\ 0 & \phi_b^{iC} & \phi_b^{iN} & 0 & 0 \\ 0 & 0 & 0 & I & 0 \\ 0 & 0 & 0 & \phi_c^{iC} & \phi_c^{iN} \end{bmatrix} \begin{Bmatrix} \xi_a \\ u_b^j \\ \xi_b \\ u_c^j \\ \xi_c \end{Bmatrix} = T_1 \begin{Bmatrix} \xi_a \\ u_b^j \\ \xi_b \\ u_c^j \\ \xi_c \end{Bmatrix} \tag{4.22}$$

The upper link has two interface nodes with the actuating link and the lower link.

$$u_b^{j1} = u_a^j = \phi_a^j \xi_a \tag{4.23}$$

$$\begin{aligned} u_c^j = u_b^{j2} &= \phi_b^{j2N} \xi_b + \phi_b^{jC} u_b^{j1} \\ &= \phi_b^{j2N} \xi_b + \phi_b^{jC} \phi_a^j \xi_a \\ &= \psi_b^j \xi_b + \psi_a^j \xi_a \end{aligned} \tag{4.24}$$

Using (4.23) and (4.24), uncoupled generalized coordinates can be described in

terms of generalized modal coordinates.

$$\begin{Bmatrix} \xi_a \\ u_b^j \\ \xi_b \\ u_c^j \\ \xi_c \end{Bmatrix} = \begin{bmatrix} I & 0 & 0 \\ \phi_a^j & 0 & 0 \\ 0 & I & 0 \\ \psi_a^j & \psi_b^j & 0 \\ 0 & 0 & I \end{bmatrix} \begin{Bmatrix} \xi_a \\ \xi_b \\ \xi_c \end{Bmatrix} = T_2 \begin{Bmatrix} \xi_a \\ \xi_b \\ \xi_c \end{Bmatrix} \tag{4.25}$$

Relationships between node displacements and generalized modal coordinates are derived from (4.22) and (4.25).

$$\begin{Bmatrix} u_a^i \\ u_a^j \\ u_b^j \\ u_b^i \\ u_c^j \\ u_c^i \end{Bmatrix} = T_1 T_2 \begin{Bmatrix} \xi_a \\ \xi_b \\ \xi_c \end{Bmatrix} = \begin{bmatrix} \phi_a^i & 0 & 0 \\ \phi_a^j & 0 & 0 \\ \phi_a^j & 0 & 0 \\ \phi_b^{iC}\phi_a^j & \phi_b^{iN} & 0 \\ \psi_a^j & \psi_b^j & 0 \\ \phi_c^{iC}\psi_a^j & \phi_c^{iC}\psi_b^j & \phi_c^{iN} \end{bmatrix} \begin{Bmatrix} \xi_a \\ \xi_b \\ \xi_c \end{Bmatrix} \tag{4.26}$$

In the pin joint connection, equations (4.23) and (4.24) are modified as follows.

$$u_b^{j1} = u_a^j = T_p \phi_a^j \xi_a = \hat{\phi}_a^j \xi_a \tag{4.27}$$

$$\begin{aligned} u_c^j = u_b^{j2} &= T_p(\phi_b^{jN}\xi_b + \phi_b^{jC} T_p u_b^{j1}) \\ &= T_p(\phi_b^{jN}\xi_b + \phi_b^{jc} T_p \phi_a^j \xi_a) \\ &= \hat{\psi}_b^j \xi_b + \hat{\psi}_a^j \xi_a \end{aligned} \tag{4.28}$$

where

$$T_p = \begin{bmatrix} 1 & 0 & 0 \\ 0 & 1 & 0 \\ 0 & 0 & 0 \end{bmatrix} \tag{4.29}$$

because each node is defined in three coordinates - 2 translational and 1 rotational. Therefore, equation (4.26) is also modified as follows.

$$\begin{Bmatrix} u_a^i \\ u_a^j \\ u_b^j \\ u_b^i \\ u_c^j \\ u_c^i \end{Bmatrix} = \begin{bmatrix} \phi_a^i & 0 & 0 \\ \phi_a^j & 0 & 0 \\ \hat{\phi}_a^j & 0 & 0 \\ \phi_b^{iC}\hat{\phi}_a^j & \phi_b^{iN} & 0 \\ \hat{\psi}_a^j & \hat{\psi}_b^j & 0 \\ \phi_c^{iC}\hat{\psi}_a^j & \phi_c^{iC}\hat{\psi}_b^j & \phi_c^{iN} \end{bmatrix} \begin{Bmatrix} \xi_a \\ \xi_b \\ \xi_c \end{Bmatrix} = T_s \begin{Bmatrix} \xi_a \\ \xi_b \\ \xi_c \end{Bmatrix} \tag{4.30}$$

Using this coordinate transformation matrix T_s, the reduced order of mass and stiffness matrices are derived using (4.19) and (4.20). Natural frequencies and the node displacements of RALF can be derived from this reduced order mass matrix and stiffness matrix.

In chapter 2, the following modal data of each component are required for the equations of motion.

$$\begin{aligned} NM &= \int \psi^2 dm \\ KW &= \int (\frac{\partial^2 \psi}{\partial x^2})^2 dx \\ LM &= \int \psi dm \\ AM &= \int x\psi dm \end{aligned} \tag{4.31}$$

where dm is the mass of the small segment. These data can be obtained by several methods.

First, if the values of the interface mass and spring are known, these data can be obtained from the analytical solution. However, it is not easy and it is a time consuming job to get an analytical solution.

In a second method, the mode shape functions can be derived from node displacements of the finite element model using a polynomial. However, this method has

a problem in calculating the stiffness matrix because the second derivative of the estimated polynomial has some difference from the true value. That is, it is not practical to find a polynomial to satisfy the displacement and slope of every node point at the same time.

By the third method used here, modal data can be expressed by summation instead of integration. Therefore, modal data can be obtained from node displacements of lumped mass model of each component.

$$NM = \Psi^T M \Psi$$

$$KW = \Psi^T K \Psi \tag{4.32}$$

$$LM = \sum_{j=1}^{N} m_j \psi_i(x_j)$$

$$AM = \sum_{j=1}^{N} x_j m_j \psi_i(x_j)$$

where

M = unloaded mass matrix

K = stiffness matrix

Ψ = mode shape matrix

m_j = mass of the j^{th} finite element node

$\psi_i(x_j)$ = mode shape of the i^{th} mode at the j^{th} node

x_j = vector locating j^{th} node with respect to the local frame

Mode shape matrices of the lumped mass model are less reliable than those of the consistent mass model. Therefore, it was observed during a simulation that the mass matrix is not positive definite for a model with small number of nodes. However, modal data can be readily and inexpensively computed from the lumped mass model which has a large enough number of nodes.

Table 4.1: Comparison of Natural frequencies

Modes No.	FEM	CMS3	CMS2	AM3	AM2	AM1
1	8.38	8.39	8.43	8.41	8.45	8.46
2	15.49	15.55	15.72	15.61	15.98	16.20
3	30.51	30.52	30.54	30.53	30.54	30.56
4	92.49	94.10	101.81	98.62	106.58	108.61
5	117.60	119.06	123.67	119.88	121.85	122.65
6	120.80	120.84	121.12	120.89	121.22	121.33

The first six natural frequencies of three models - a finite element model, a component mode synthesis model, and an analytical model - are compared as shown in Table 4.1. In this table, component mode sets of the component mode synthesis (CMS) model and the analytical model (AM) are truncated at two mode (CMS2, AM2) and three mode (CMS3, AM3) per link. If three modes are included, all six natural frequencies match each other quite well. On the other hand, if two modes are included, only the first three natural frequencies match each other to within 10 %. However, because we are interested in the lower frequencies, two modes are enough for the reduced order analytical model. Furthermore, AM1 is the model which uses clamped - mass, clamped -free, and pin - pin boundary conditions for the lower, the upper, and the actuator link. This model is more different from the FE model than AM2. Therefore, component mode synthesis is the systematic method which can derive proper mode shape function.

4.5 Discussion of Experiment

In fact, there are discrepancies between the analytical model and the real system because the real system has a complex structure which is difficult to analyze by the

Table 4.2: Comparison of natural frequencies of the modified model

Modes No.	FEM	CMS3	CMS2	AM3	AM2	AM1
1	6.03	6.04	6.08	6.06	6.09	6.11
2	15.24	15.30	15.49	15.37	15.74	15.99
3	30.74	30.74	30.75	30.75	30.76	30.79
4	75.63	77.21	84.91	81.73	89.70	91.73
5	98.25	99.70	101.3	100.5	102.5	103.3
6	120.28	120.32	120.59	120.37	120.70	120.81

analytical method. The sectional areas of beams are not uniform. The links are connected with offset brackets. The connecting joint axis between the hydraulic actuator and the lower link is not colinear with the axis joining the connecting link to the lower link as shown in Fig. C.1 of Appendix C. Therefore, the flexible part of the lower link increases. Table 4.2 shows the natural frequencies of each model of the modified structure. The finite element models are used to explain the discrepancies between the analytical model and the real system. Two types of finite element models are created. One is a simplified model using beam elements with seven different EI (modulus of elasticity times area moment of inertia) values and one lumped mass element at the end of the lower link. The simplified model assumes support sleeves and connecting link as rigid similar to those used in the analytical model. The other finite element model is a detailed model using beam elements in which thirteen different EI values and three kinds of lumped mass elements were used. The detailed model used makes no assumptions about the rigidity of any of the links. In experiments, an electromechanical shaker was attached to the structure at the end point of the lower link (Point B in Fig. 4.3.a). Because turnbuckles were used in place of the hydraulic cylinders, the boundary condition can be assumed

fixed. The detailed procedures of the experiment are described by Huggins [28].

Figure 4.4 shows the mode shapes of RALF and the associated system natural frequencies. The first system mode is dominated by the bending of the lower link. The frequencies of the first mode are nearly equal each other. The second system mode is dominated by the bending of the upper link. However, there is a discrepancy between the frequencies of the second mode of the simplified model and the detailed model. The boundary condition of the upper link is more complicated in the real system. Therefore, a more accurate model is required to predict the true frequency. The third system mode is dominated by the pinned - pinned bending mode of the actuator link. However, there is a discrepancy between the predicted and the measured natural frequencies. A large amount of friction in the pin joint causes the joint to exhibit some characteristics of a clamped end condition. This frequency is measured when the structure was excited by a shaker and the joints are fixed by a turnbuckle with no bearing. However, if the structure is excited by the hydraulic cylinder, the frequency of the actuator link decreases. Therefore, the reason for the frequency difference in the third mode appears to be friction at the joint which is reduced by actuator motion. The higher frequencies and mode shapes have discrepancies between the analytical models and the finite element models because the analytical model included only two modes per link for describing link deflections. The higher modes and frequencies of the experiment also have discrepancies because of their small signal to noise ratio, out of plane motion, and the closeness of the frequencies as shown in Fig. 4.5. Even in the finite element model, the higher modes are sensitive to modeling.

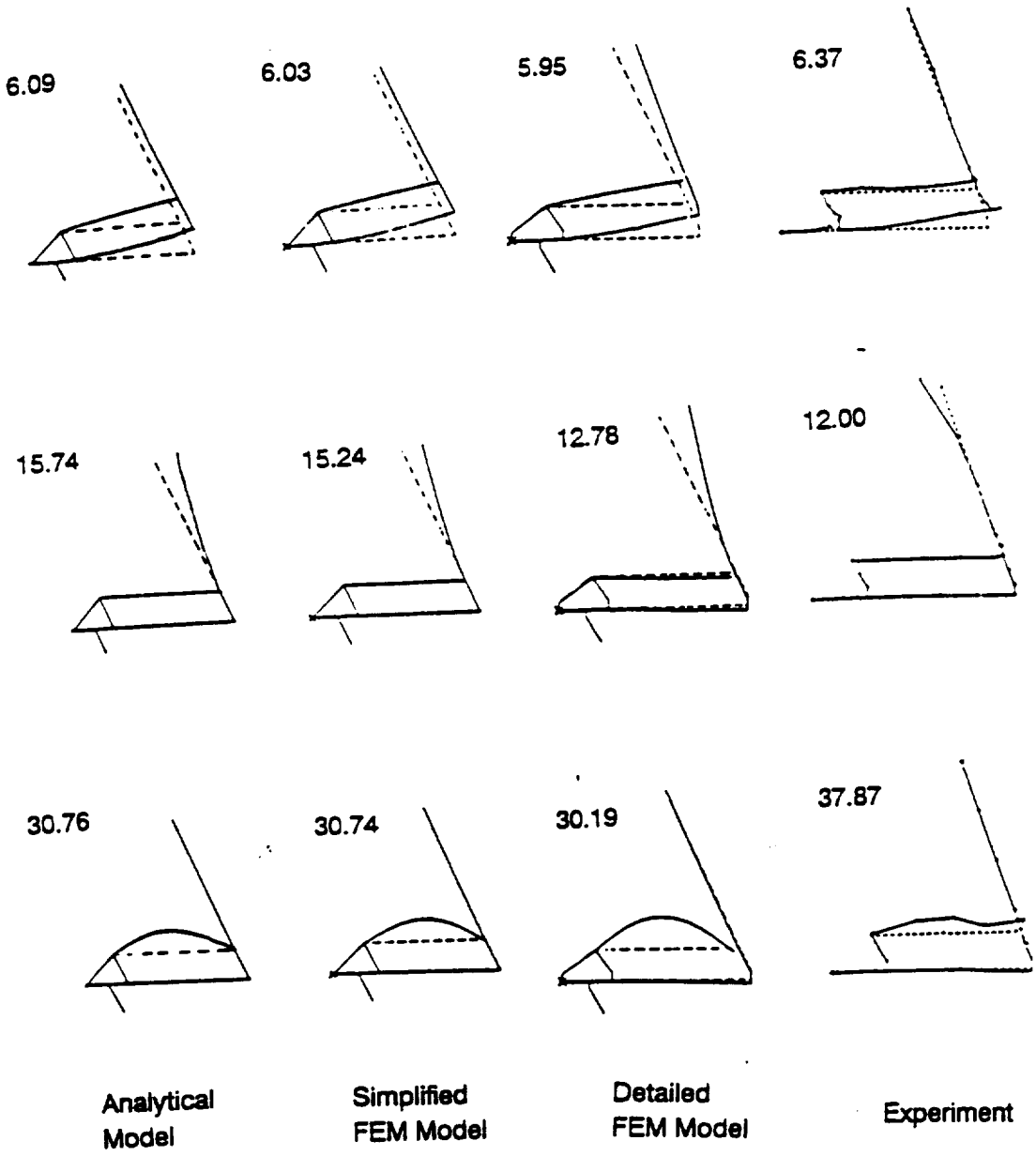

Figure 4.4: Comparison of mode shapes and natural frequencies between analytical model, finite element model and experiment

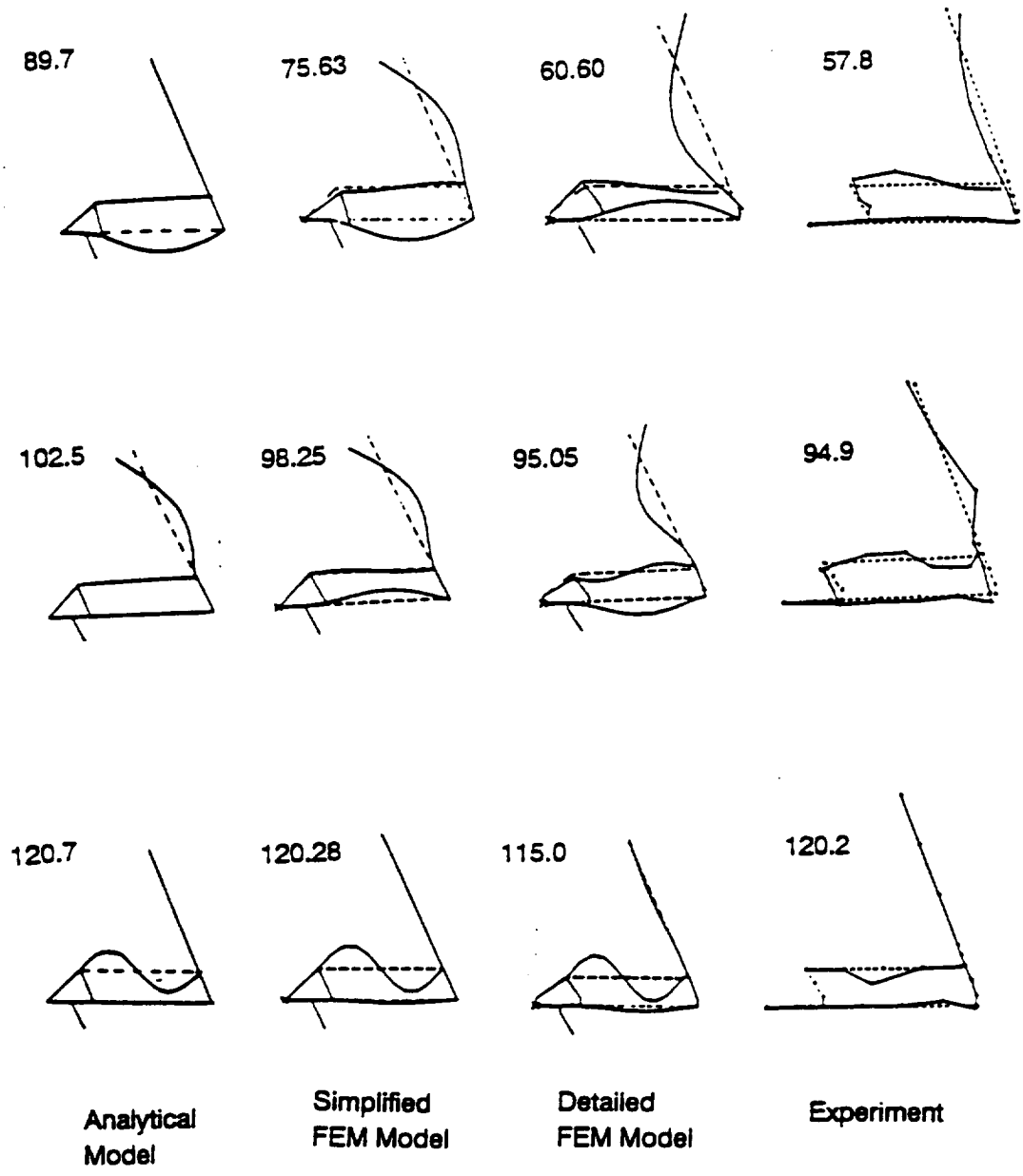

Figure 4.4: (Continued)

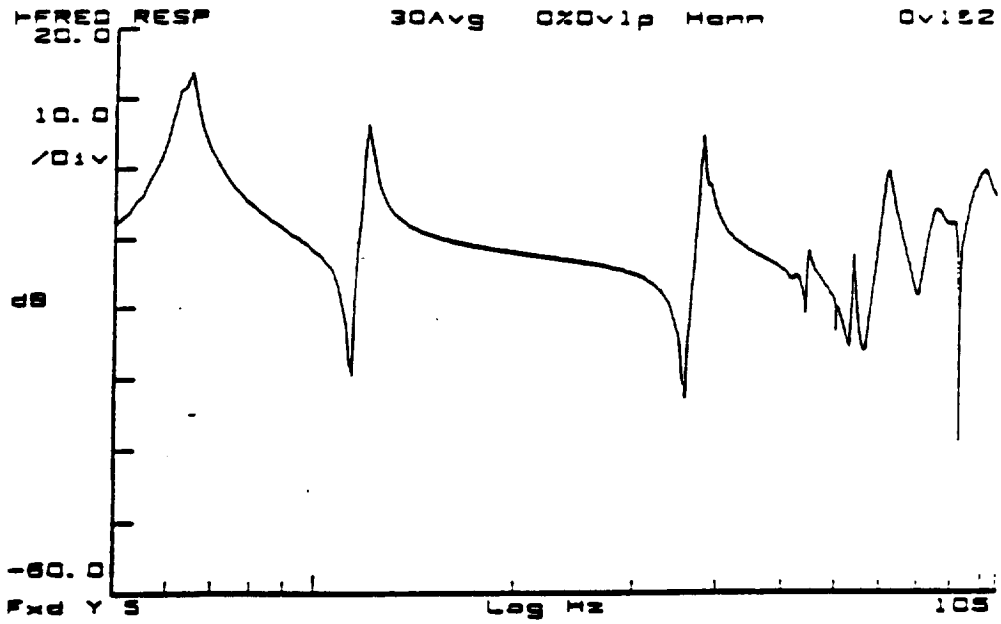

Figure 4.5: Frequency spectrum of RALF

4.6 Conclusion

In the assumed mode method, there are numerous possible choices of admissible functions. However, a large number of modes are required for the completeness of the set of admissible functions. In order to speed up the convergence, mode shape functions which satisfy the static equilibrium are used in component mode synthesis. Among several component mode synthesis approaches, the loaded interface method fits with the current coordinates system. Proper mode shape functions for a reduced order model are obtained using the loaded interface component mode synthesis. Comparison between the finite element model, the component mode synthesis model and the analytical model show that mode shape functions which are determined by component mode synthesis improve the convergence. Because the real system has a complex structure which does not match certain simplification necessary in the analytical model, there are some discrepancies between the analytic model and the experiment. These discrepancies are explained using a simplified and a detailed finite element model.

CHAPTER V

Verification of Analytical Model

5.1 Introduction

The experimental verification of nonlinear dynamics is a difficult job which has not been extensively studied compared to linear dynamics. Possible verification methods include a time domain and a frequency domain methods. However, the time response with nonlinear dynamics depends on initial conditions and input amplitudes. Therefore, an accurate dynamic model is required. As mentioned in the previous chapter, the real system has unmodelled dynamics and parameter uncertainties hard to describe analytically. Hence, direct comparison between the analytical model and the real system was difficult. In this chapter, several techniques are tried to verify the nonlinear dynamics of RALF. First, as an alternative method for a time domain verification, a TREETOPS model is used for the verification of the analytical model. Secondly, as one of the frequency domain methods, the nonlinear dynamics of RALF is studied by a sinusoidal excitation. Finally, actuator dynamics has a significant interaction with flexible body dynamics. The effect of hydraulic cylinder dynamics on flexible body dynamics is discussed.

5.2 Analytical Model Verification using TREETOPS

TREETOPS is a computer simulator of the dynamics of a flexible multibody structure with loop closures. TREETOPS is being developed by DYNACS Inc. under contract to NASA's Marshall Space Flight Center (MSFC). The program was obtained from Dr. Henry B. Waites of MSFC. The name TREETOPS refers to the class of structures which may be simulated by the program, that is those having a tree topology. A tree topology is one in which multiple bodies are connected by rotational and translational joints. TREETOPS can also handle the structure with loop closures by constraining the position or velocity of connecting joints. The primary output of the program is a time history of flexible body motion in response to an active control system consisting of actuators, sensors, and controllers. The equations of motion are derived using Kane's method. The TREETOPS model is described in Appendix E.

The step responses of the analytical model and the TREETOPS model are compared as shown in Fig. 5.1. The time responses of the two models match each other fairly well even though they use different methods for deriving the equations of motion. The constraint error measured at the connection joint is stable as shown in Fig. 5.2. The analytical model used the SVD algorithm to generate the matrix V_2 while TREETOPS model used the QR algorithm. SVD algorithm updates the V_2 matrix based on the given criterion. On the other hand, the QR algorithm updates the V_2 matrix at every time step [37]. Even though the constraint error history using the SVD algorithm is a little different from the constraint error history using the QR algorithm as shown in Fig. 5.2, time responses of other variables are not different as shown in Fig. 5.1 . The constraint error also depends on the integration method. Because the flexible body dynamics produces a stiff system which has

several widely spaced frequencies in one system, Adam's method is used. The Runge-Kutta method allows the constraint error to increase as shown in Fig. 5.3. The simulation time of analytical model is shorter than that of the TREETOPS model. For example, the CPU time of analytical model is about 6 minutes in VAX/750 for 1 second time response and 1 millisecond time step. On the other hand, the CPU time of the TREETOPS model is about 35 minutes. The expected reason for this difference is that TREETOPS is a general program which can handle a 3 dimensional motion of a multi body. Furthermore, the dynamic equations of motion are calculated recursively by matrix manipulation. Whereas, the analytical model is expressed in symbolic form explicitly. In both models, the system frequencies which are related to the upper link are high compared to the experiment results. This difference comes from the actuator dynamics effects on the system dynamics. The hydraulic actuator dynamics will be discussed in the section 5.4.

5.3 Verification of Nonlinear Dynamics

5.3.1 Analysis of Nonlinear Dynamics

In order to verify the nonlinearity, the following questions are expected. *Where does the nonlinearity come from ? Which excitation method is adequate to test the nonlinear dynamics ? Which sensor is adequate to measure the nonlinear effect ?*

First, nonlinear dynamics of a flexible manipulator comes from configuration change, Coriolis and centrifugal force, and the coupling between rigid body motion and flexible body motion as shown in the equations of motion. Secondly, a step time response has been the common method for model verification. However, even though the step input can excite many modes at one time, the time response is susceptible to the unknown dynamics, such as the signal noise and the friction. Furthermore, it

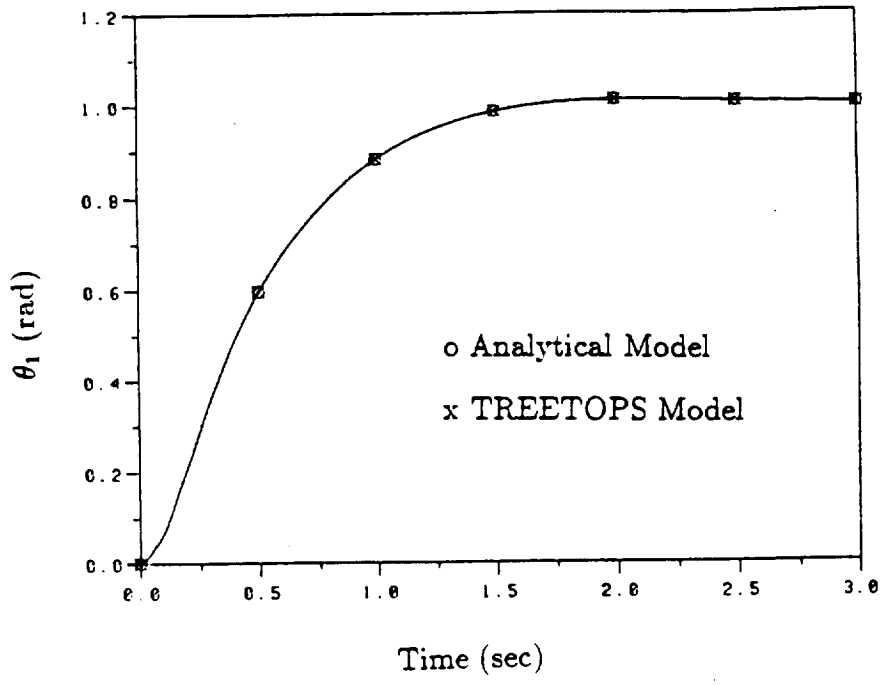

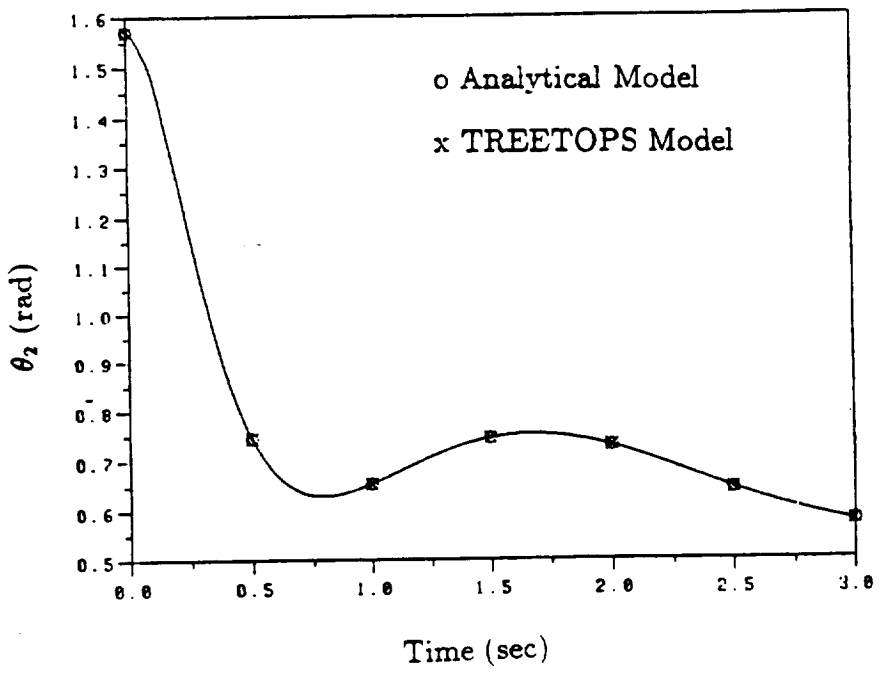

Fig. 5.1: Step response of TREETOPS model and analytical model

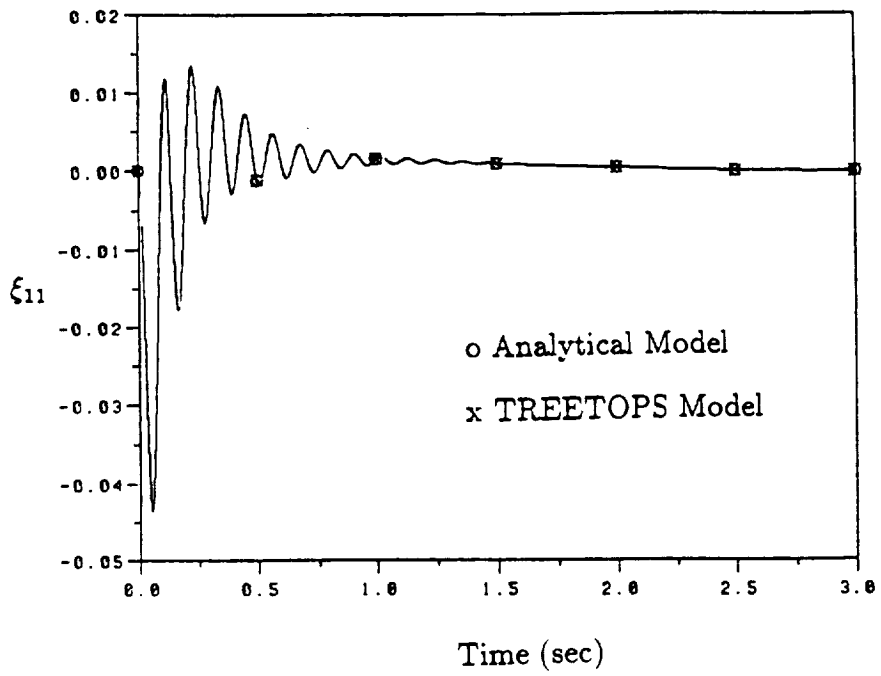

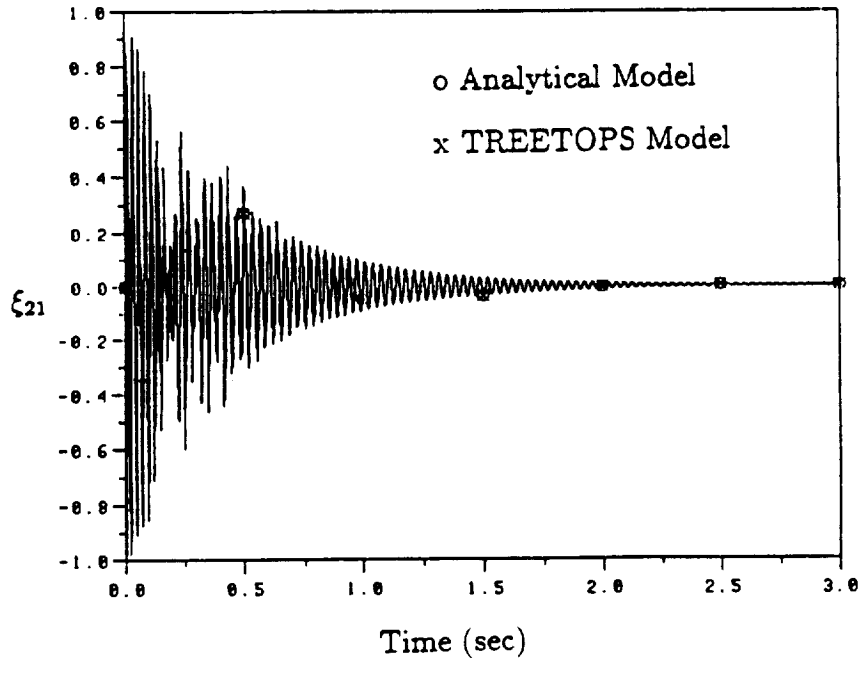

Fig. 5.1: (Continued)

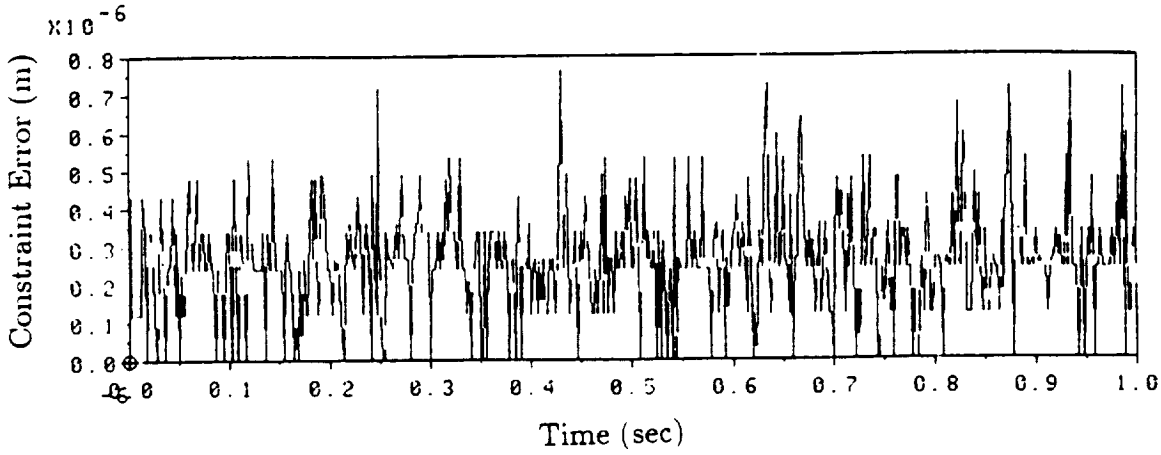

Fig. 5.2.a: Constraint error when SVD algorithm is used

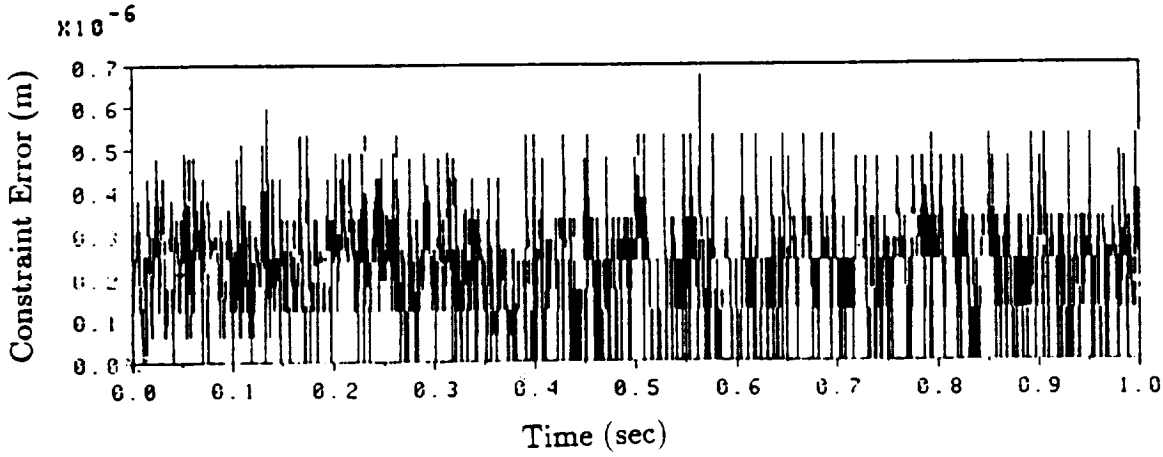

Fig. 5.2.b: Constraint error when QR algorithm is used

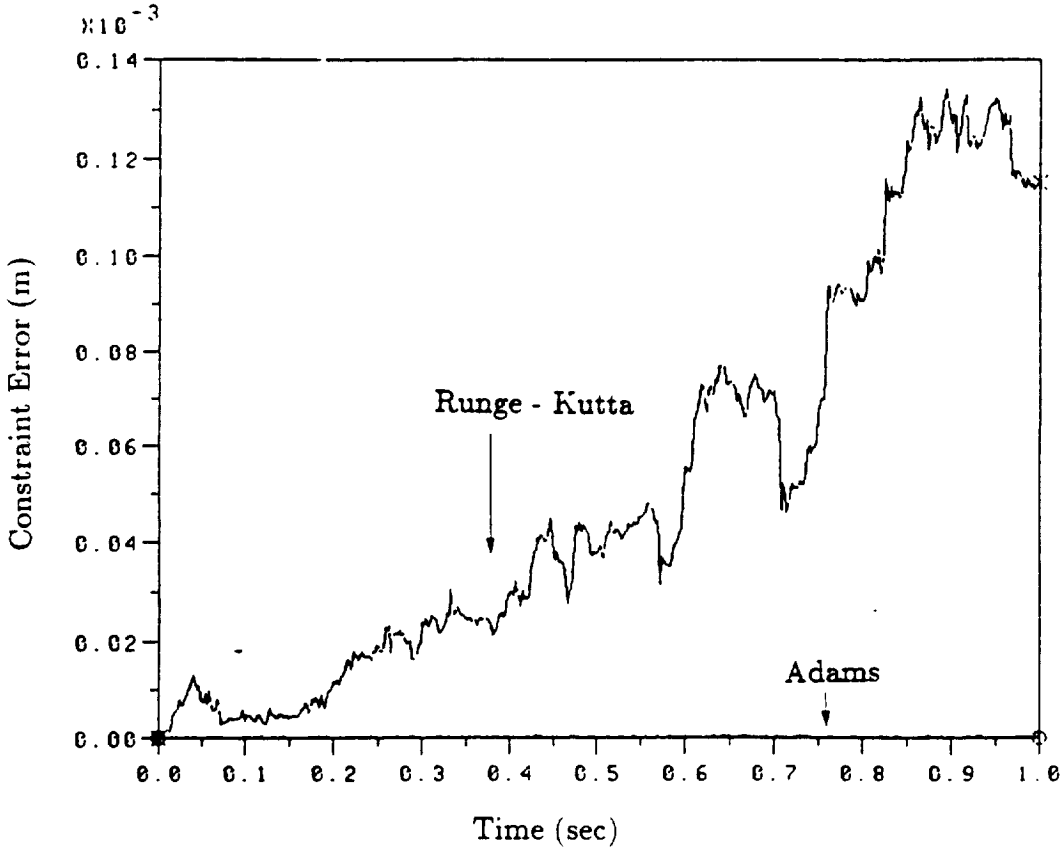

Fig. 5.3: Comparison of constraint error
when the different integration method is used

is difficult to detect the amount of nonlinearity from the step response. On the other hand, the frequency spectrum of the response to a sinusoidal excitation is a method which can detect the nonlinearity. The response of a nonlinear system is dependent on the amplitude of the excitation. One advantage of a sinusoidal excitation is that the input force can be precisely controlled. Furthermore, large amounts of energy can be input to the structure at each particular frequency. Therefore, it results in relatively high signal-to- noise ratios and allows the study of structural nonlinearities at any specific frequency. Third, the time response can be measured by several sensors. The possible sensor types are accelerometer, encoder, tachometer, and strain gauge.

Before the experimental verification, the simulation result can show the general characteristics of the nonlinear dynamics. The flexibility effect can be verified by comparing the rigid body dynamics and the flexible body dynamics. The configuration change effect and Coriolis and centrifugal force effect can be verified by changing the amplitude and the frequency of a sinusoidal excitation. In the simulations, a RALF model is tested with 30 LB payload in order to magnify the effects of the nonlinearity. In Fig. 5.4 and 5.5, several time responses of the rigid RALF model are compared by changing the amplitude (0.05 rad, 0.1 rad, 0.5 rad) with the fixed frequency (1.5 Hz) and the frequency (1.5 Hz, 4 Hz, 7 Hz) with the fixed amplitude (0.05 rad) of a sinusoidal excitation. Time responses are measured by several sensors - encoder, tachometer, and accelerometer. The TREETOPS model is used because the tip acceleration is easily measured using the given sensor option. The differences between each case are not clear in the time response. However, the phase plots in Fig. 5.6, 5.7 and 5.8 are another method to detect the nonlinearity. The ellipse of harmonic excitation is distorted by the nonlinearity as shown in Fig. 5.7 where the sinusoidal responses of different amplitude are drawn in the same

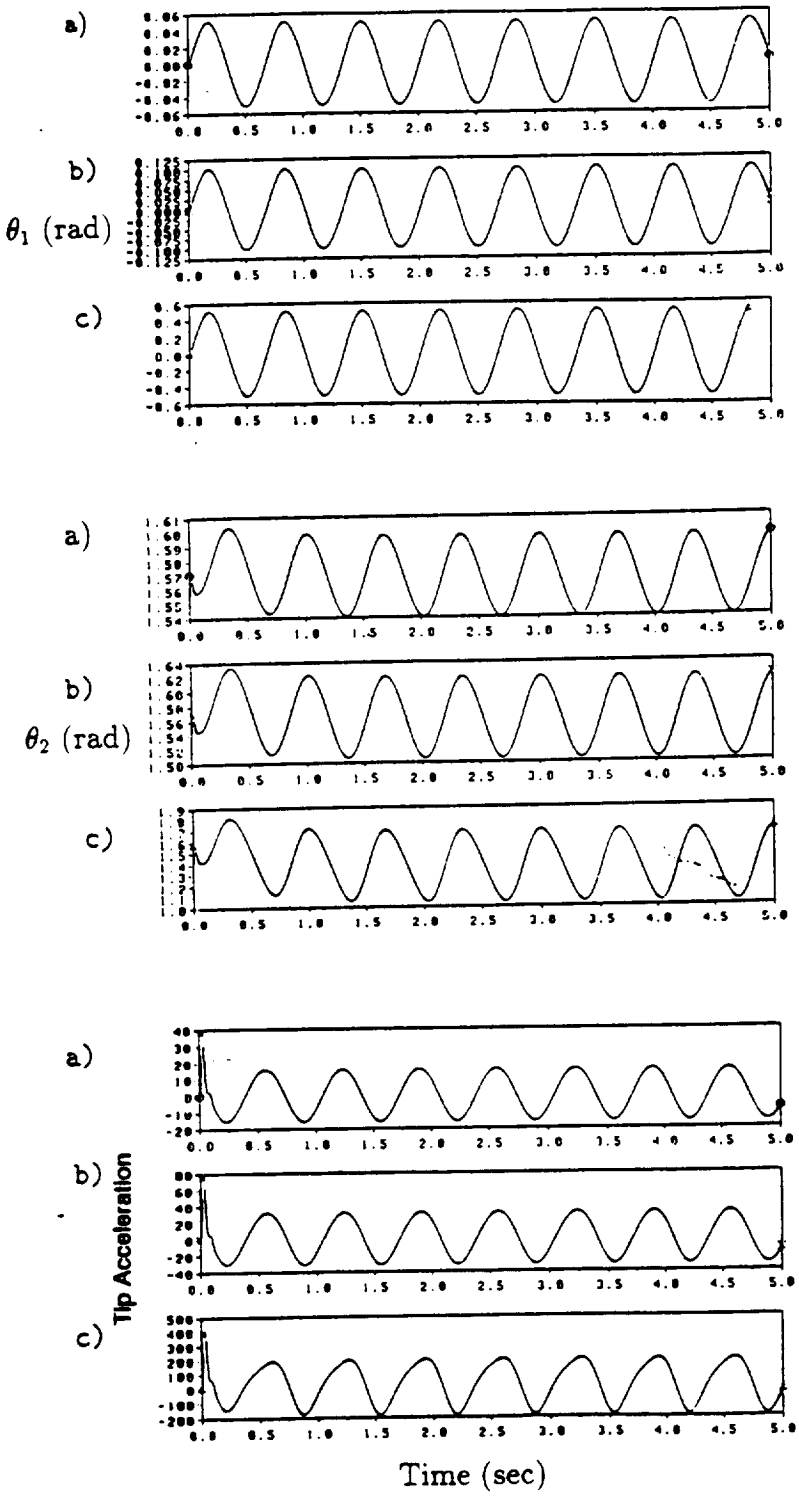

Fig. 5.4: Time response of the rigid RALF model for the different excitation amplitudes (a) 0.05 rad, (b) 0.1 rad, (c) 0.5 rad

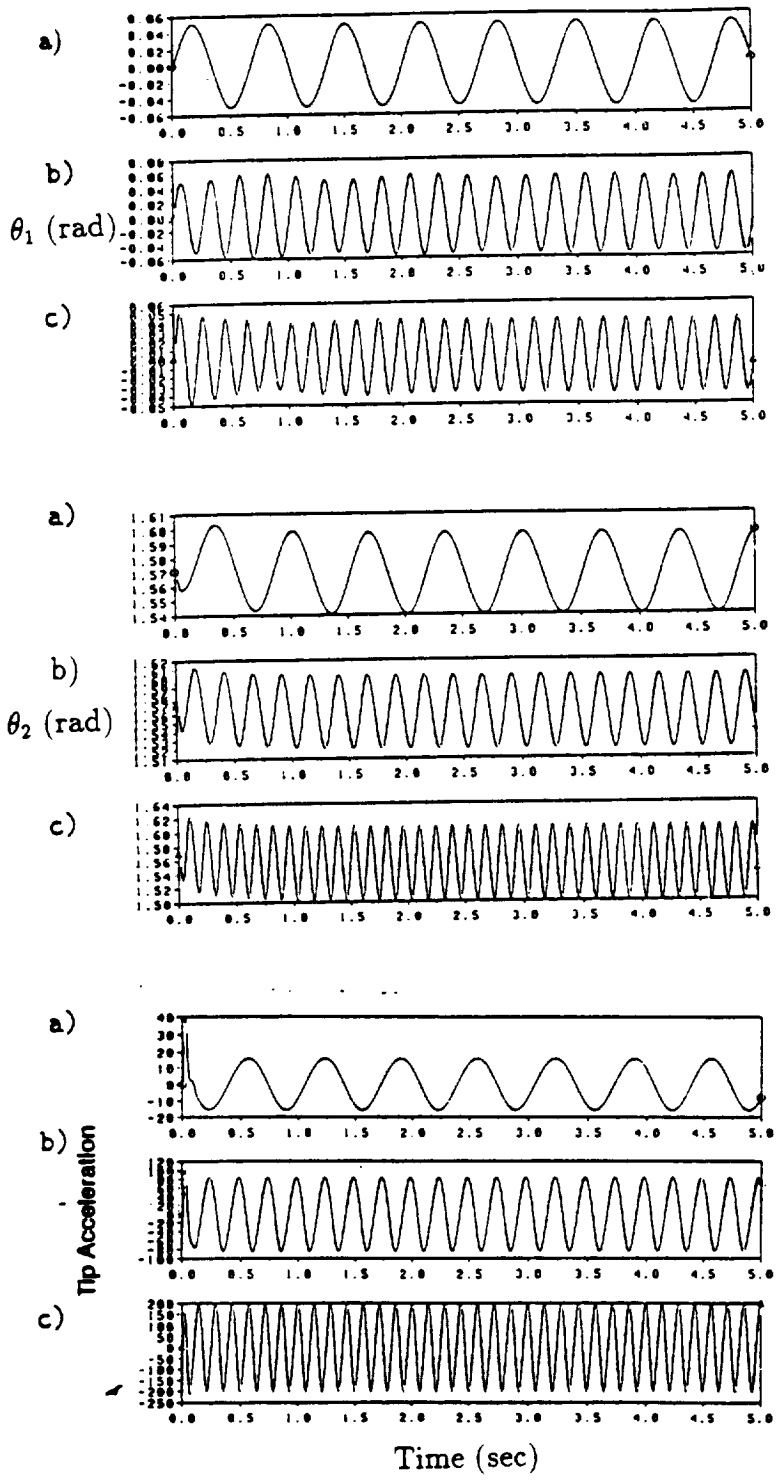

Fig. 5.5: Time response of the rigid RALF model for the different excitation frequencies (a) 1.5 Hz, (b) 4 Hz, (c) 7 Hz

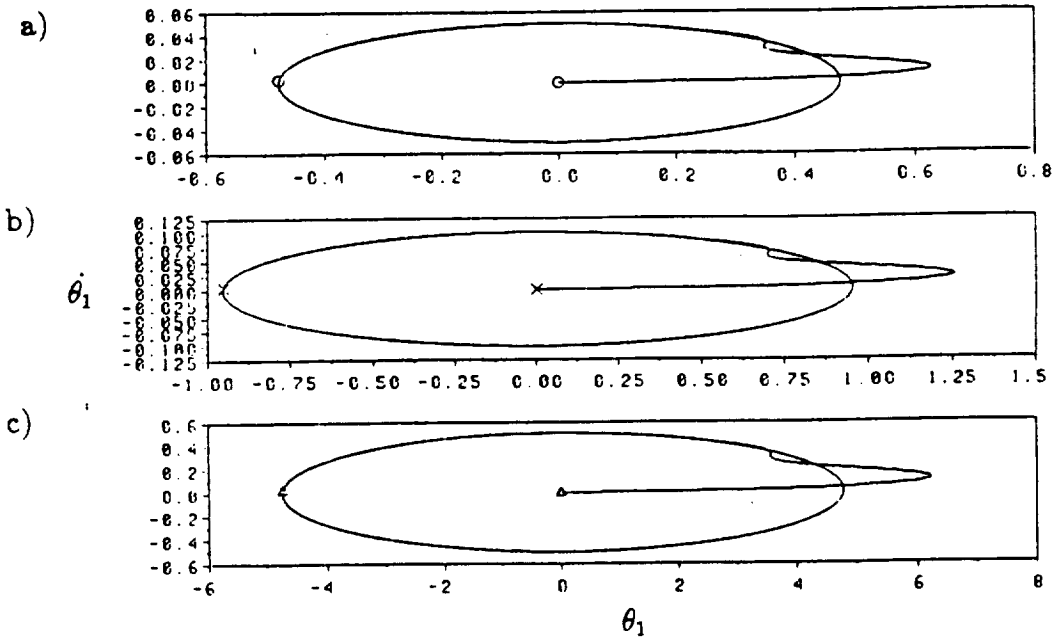

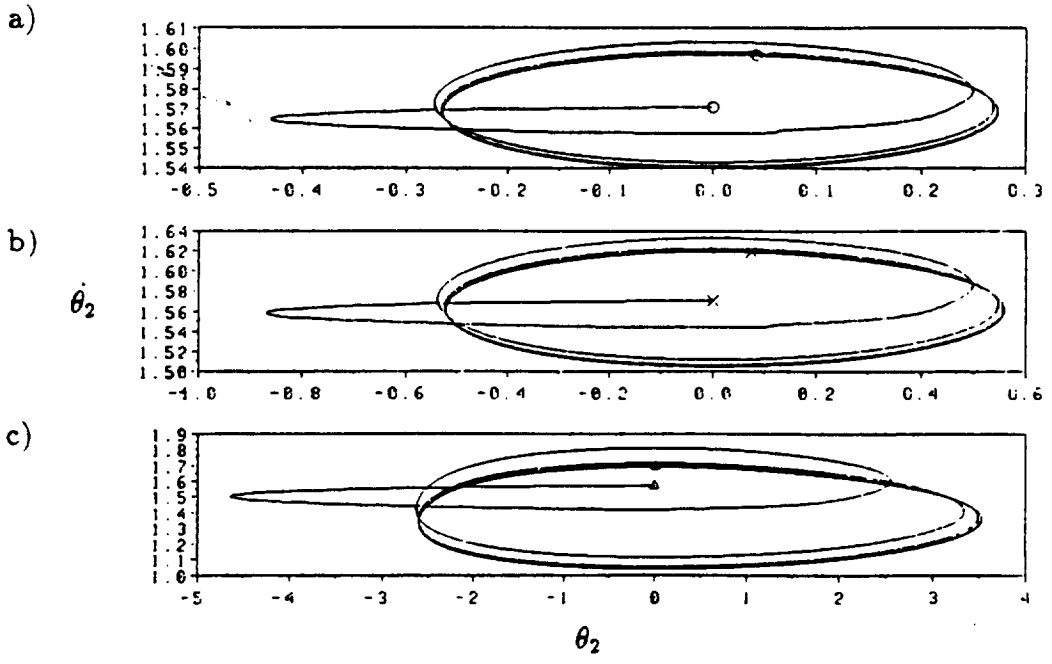

Fig. 5.6: Phase plot of the rigid RALF model for the different excitation amplitudes (a) 0.05 rad, (b) 0.1 rad, (c) 0.5 rad

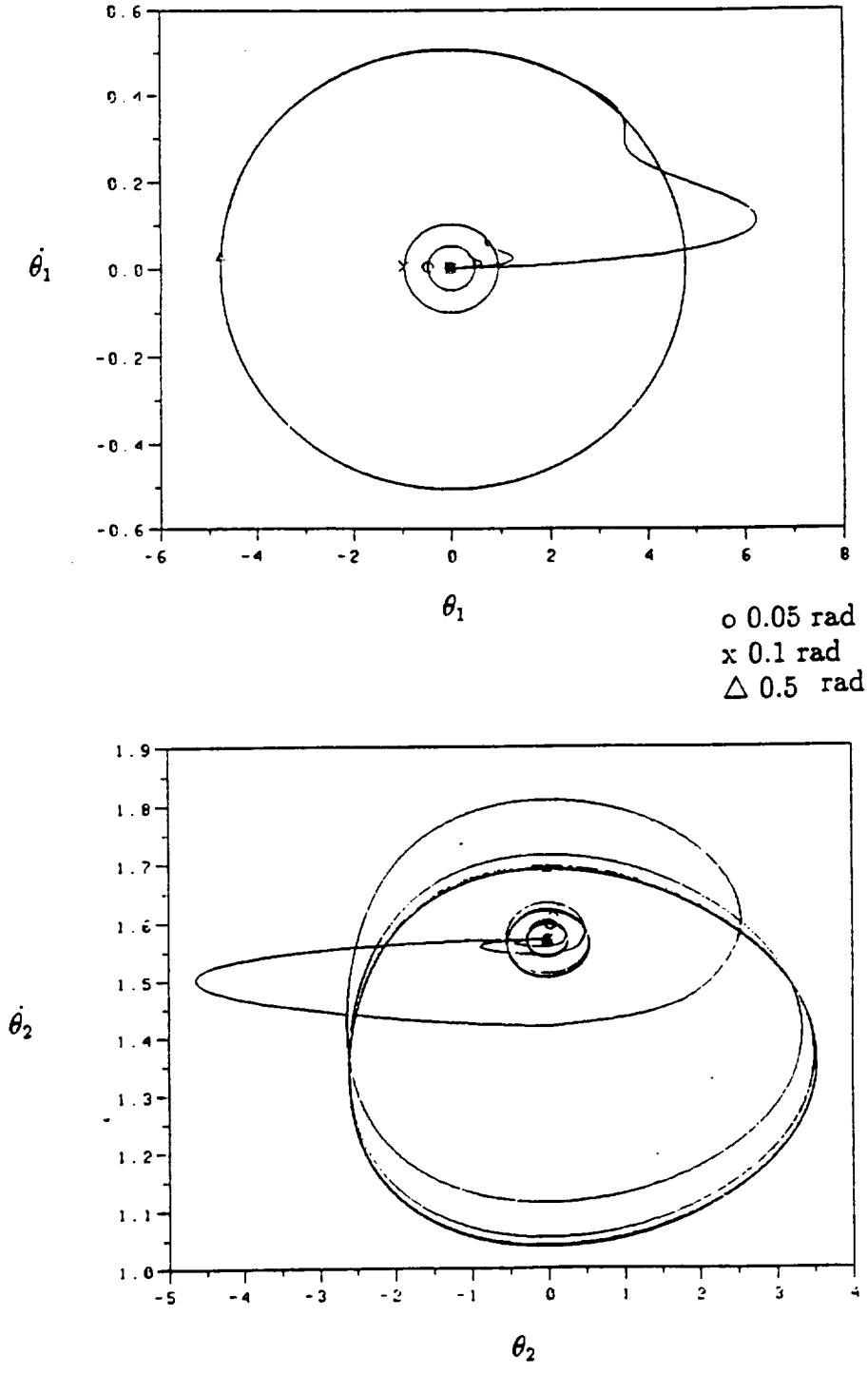

Fig. 5.7: Phase plot of the rigid RALF model in the same scale for the different excitation amplitudes

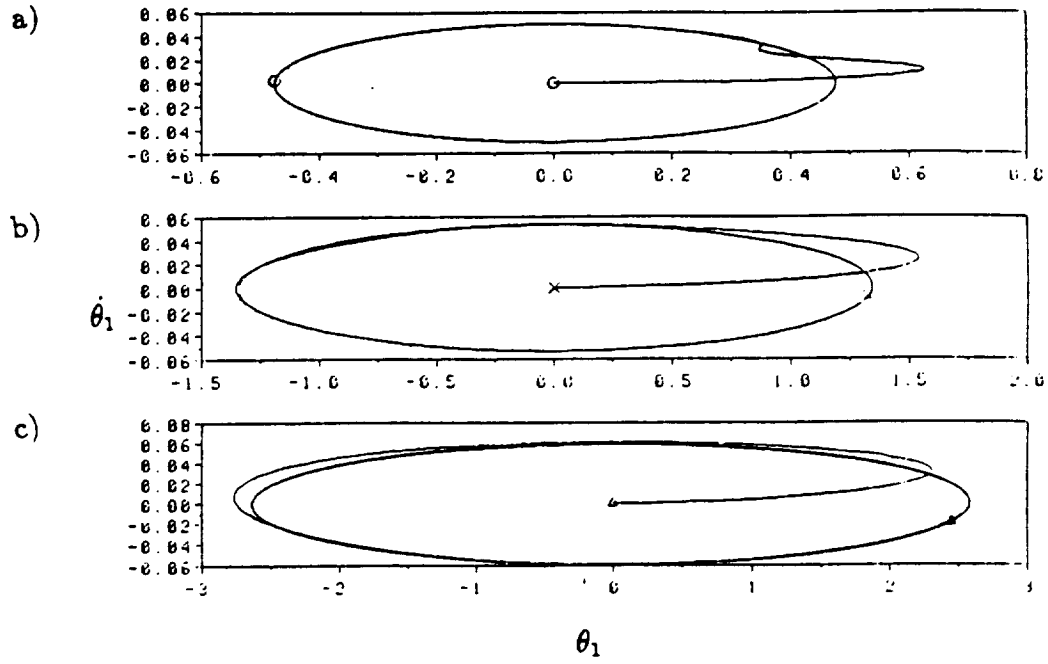

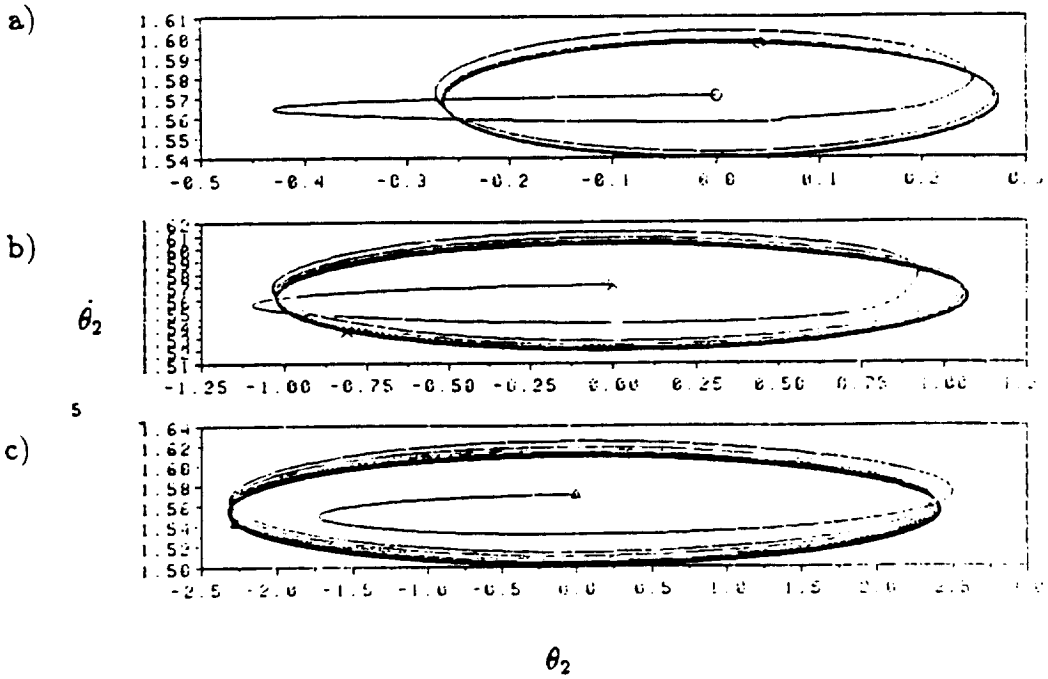

Fig. 5.8: Phase plot of the rigid RALF model for the different excitation frequencies (a) 1.5 Hz, (b) 4 Hz, (c) 7 Hz

plot. The acceleration at the tip shows the difference even in the time response as shown in Fig. 5.4. FFT of the tip acceleration is another method to check the nonlinearity. Fig. 5.9 shows the power spectral density of the tip acceleration in response to the different amplitudes and frequencies of the sinusoidal excitation. To obtain the sharp peak, 4096 data points between 0.9 second and 5.0 second are used. In order to reduce leakage, the Hanning window is used. The relative difference between the first harmonic peak and the second harmonic peak decreases (a factor of more than 80) as the amplitude of sinusoidal excitation increases as shown in Table 5.1.a. However, the relative difference between the first harmonic peak and the second harmonic peak does not change significantly (a factor of less than 3) by changing the frequency of the sinusoidal excitation as shown in Table 5.1.b.

Similar analysis has been done for the flexible body. Fig. 5.10 and Fig. 5.11 show the time responses of θ_1, θ_2, and acceleration at the tip by changing the amplitude and the frequency of the sinusoidal excitation. In these figures, the distortion of the sinusoidal response can be detected even in the time response. Fig. 5.12 and Fig. 5.13 show the phase plot of rotation angles and modal coordinates. Compared to the rigid body case, the effect of nonlinear dynamics is more significant as observed by changing either the amplitude or the frequency of the sinusoidal excitation. For instance, the circle of harmonic excitation with 0.5 rad amplitude and 7 Hz frequency is distorted as shown in Fig. 5.14. Fig. 5.15 shows the power spectral density of the acceleration at the tip. By increasing the amplitude of sinusoidal excitation, the broad range harmonic peaks including system natural frequencies are observable as shown in Fig. 5.15.a. By increasing the frequency of the sinusoidal excitation, the nonharmonic peaks occur between the harmonic peaks as shown in Fig. 5.15.b. Table 5.2.a and 5.2.b shows the first several harmonic peak values and their relative difference for different excitation amplitude and frequency respectively.

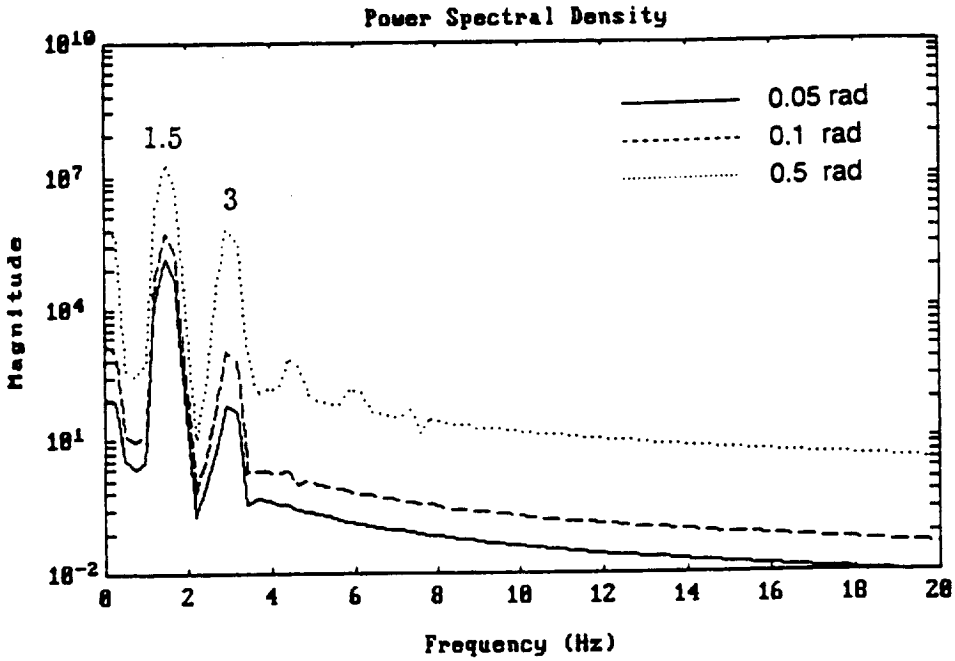

Fig. 5.9.a: The power spectral density of the tip acceleration for the different excitation amplitudes

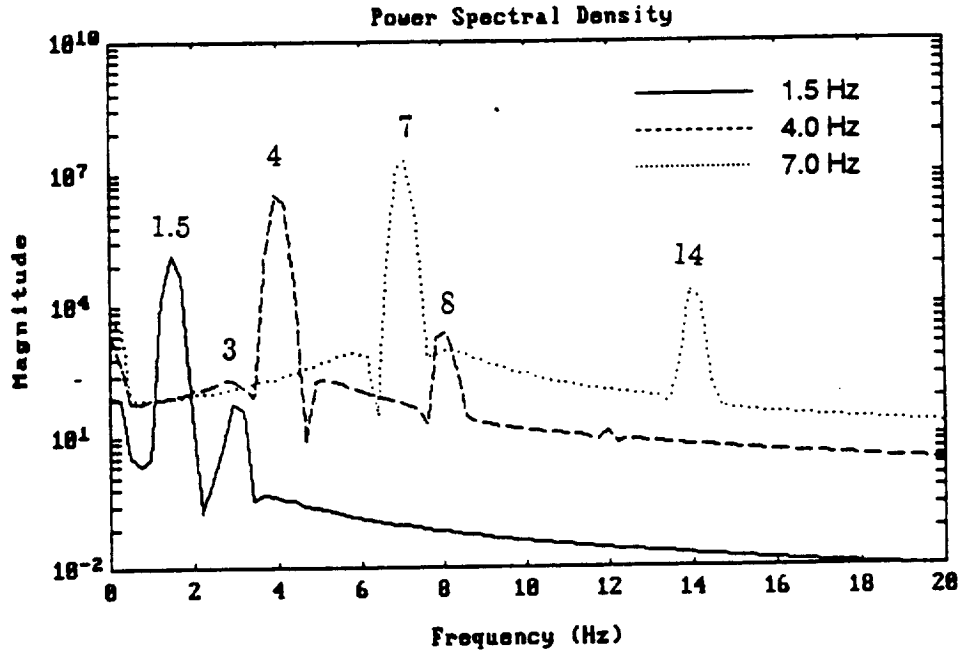

Fig. 5.9.b: The power spectral density of the tip acceleration for the different excitation frequencies

Table 5.1.a: Peaks of power spectrum density of rigid RALF model for different excitation amplitudes

	1st harmonic	2nd harmonic	1st/2nd harmonic
0.05 rad	1.46E5	6.40E1	22.7E2
0.1 rad	5.90E5	1.09E3	5.41E2
0.5 rad	1.99E7	6.97E5	0.28E2

Table 5.1.b: Peaks of power spectrum density of rigid RALF model for different excitation frequencies

	1st harmonic	2nd harmonic	1st/2nd harmonic
1.5 Hz	1.46E5	6.40E1	2.27E3
4.0 Hz	3.40E6	2.70E3	1.26E3
7.0 Hz	2.00E7	6.97E5	0.88E3

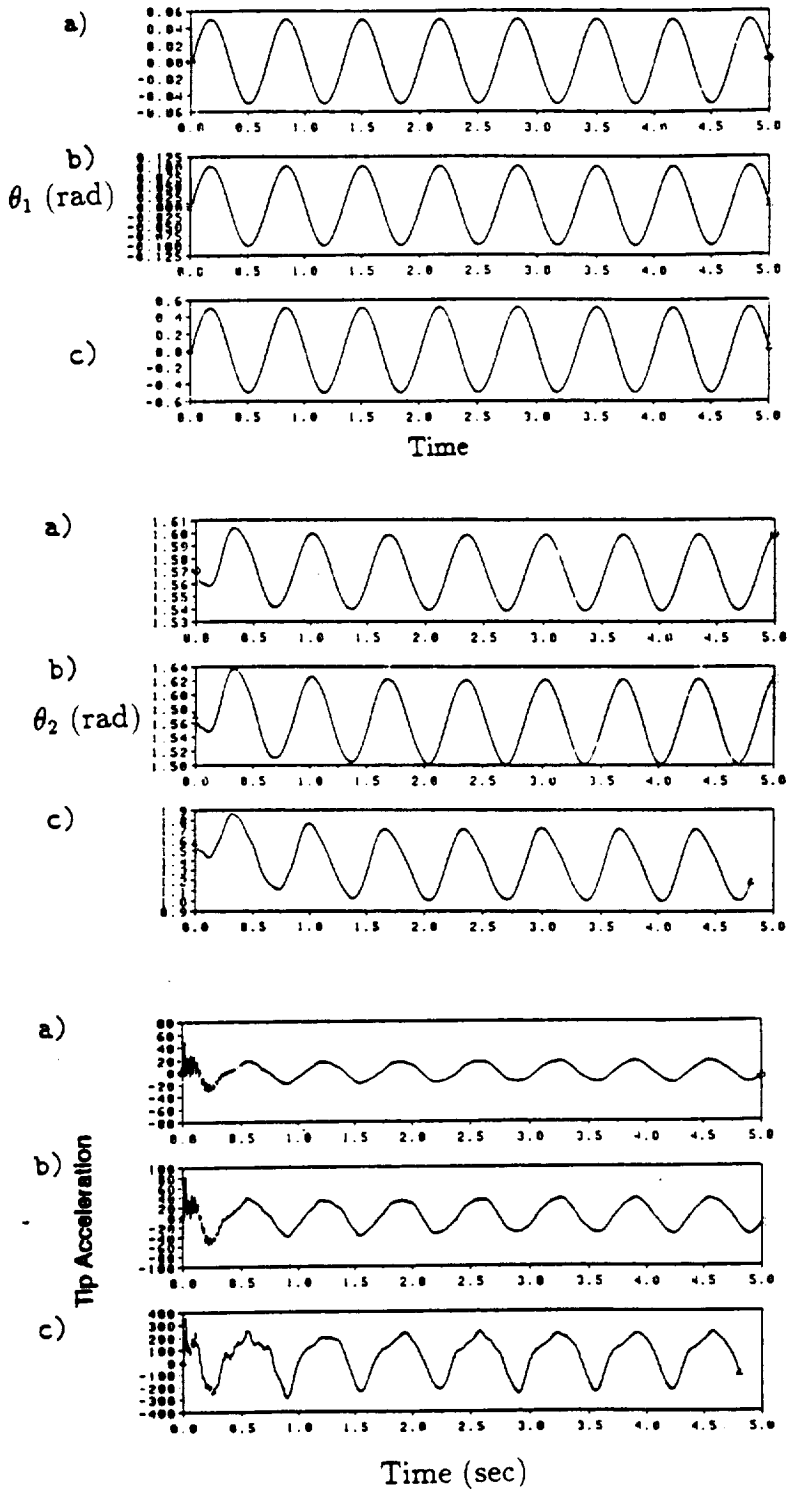

Fig. 5.10: Time response of the flexible RALF model for the different excitation amplitudes (a) 0.05 rad, (b) 0.1 rad, (c) 0.5 rad

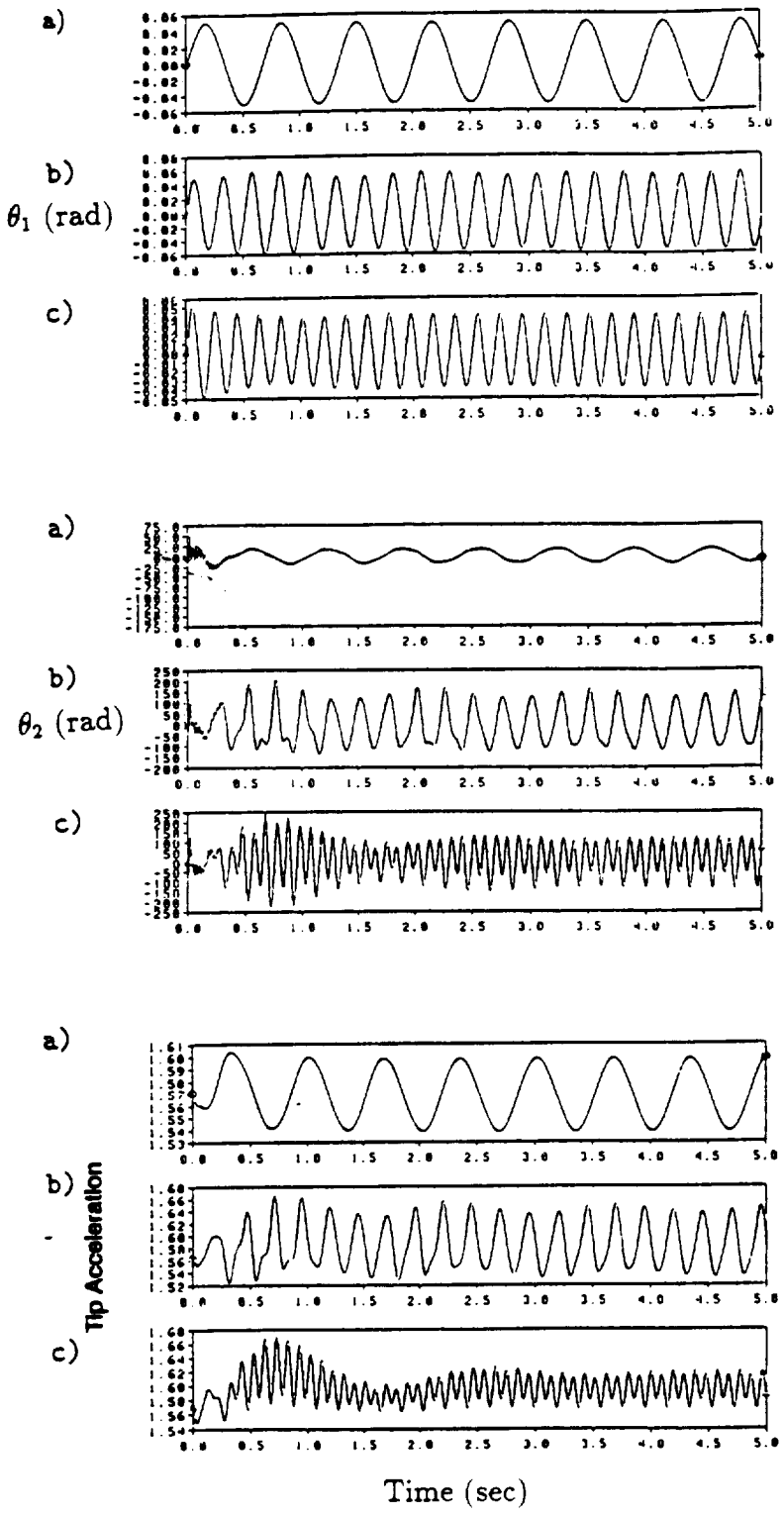

Fig. 5.11: Time response of the flexible RALF model for the different excitation frequencies (a) 1.5 Hz, (b) 4 Hz, (c) 7 Hz

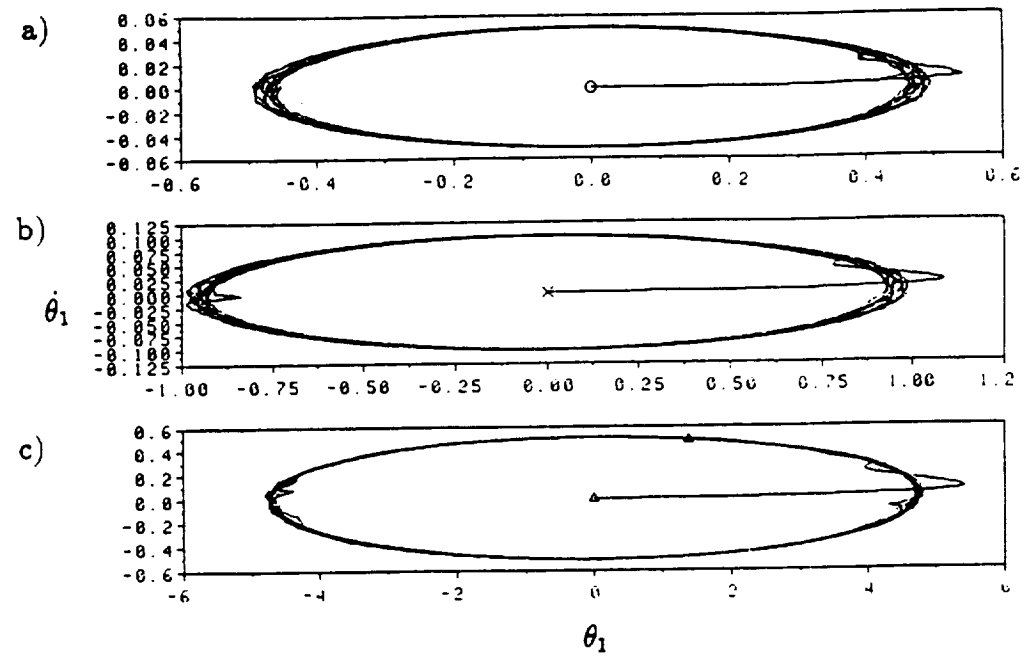

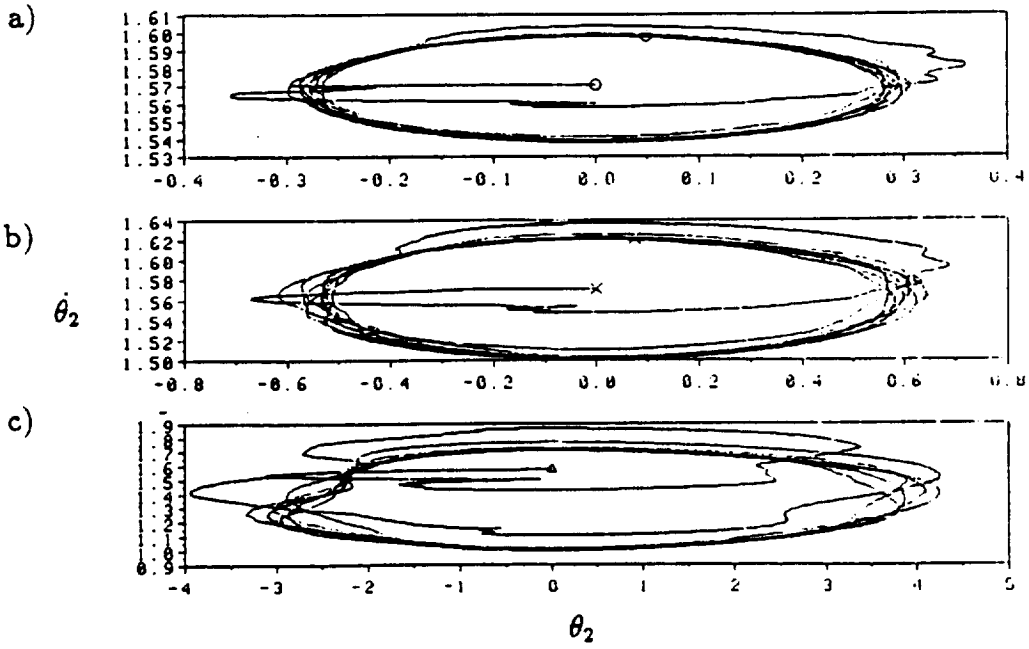

Fig. 5.12: Phase plot of the flexible RALF model for the different excitation amplitudes (a) 0.05 rad, (b) 0.1 rad, (c) 0.5 rad

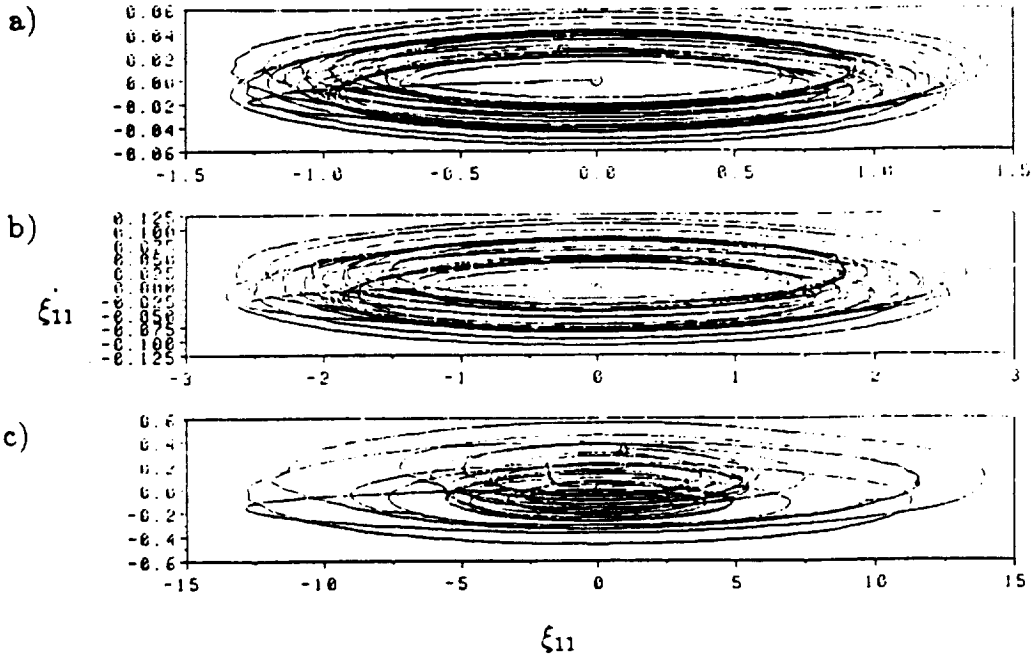

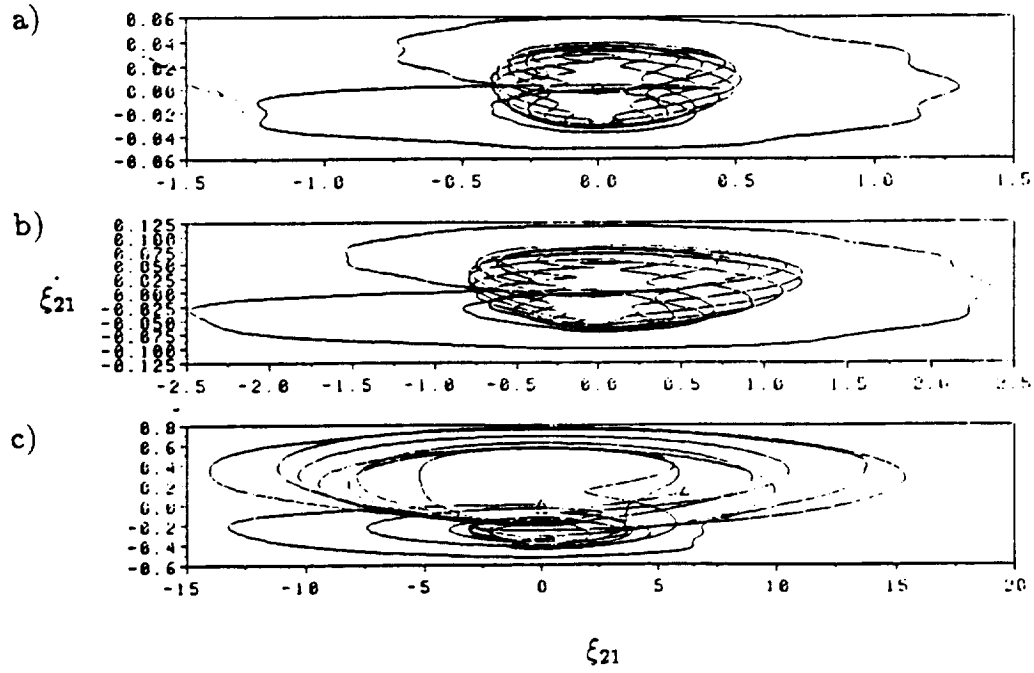

Fig. 5.12: (Continued)

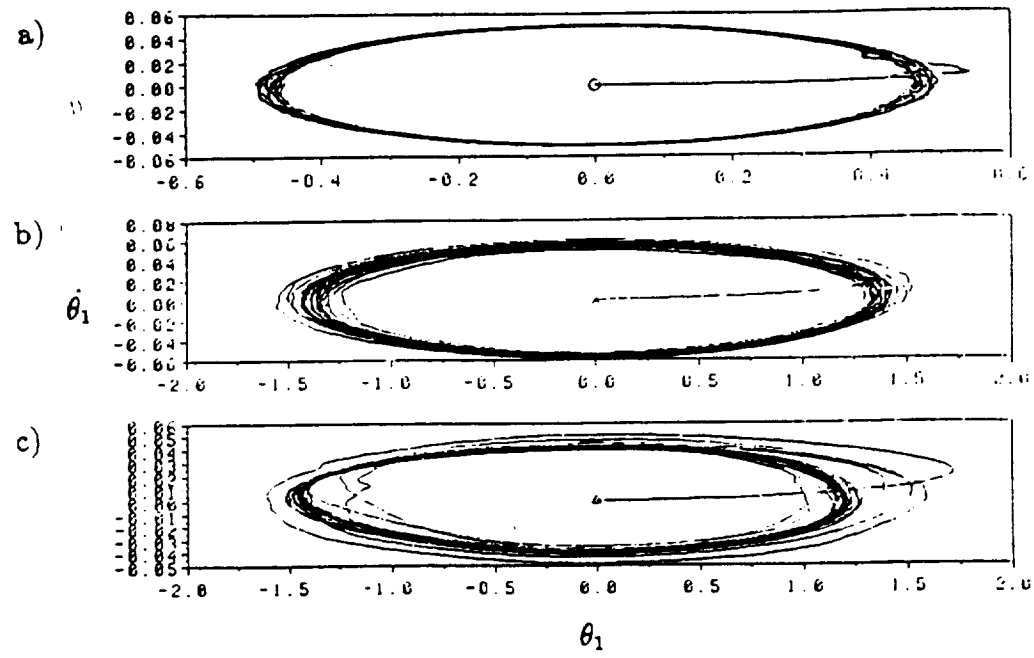

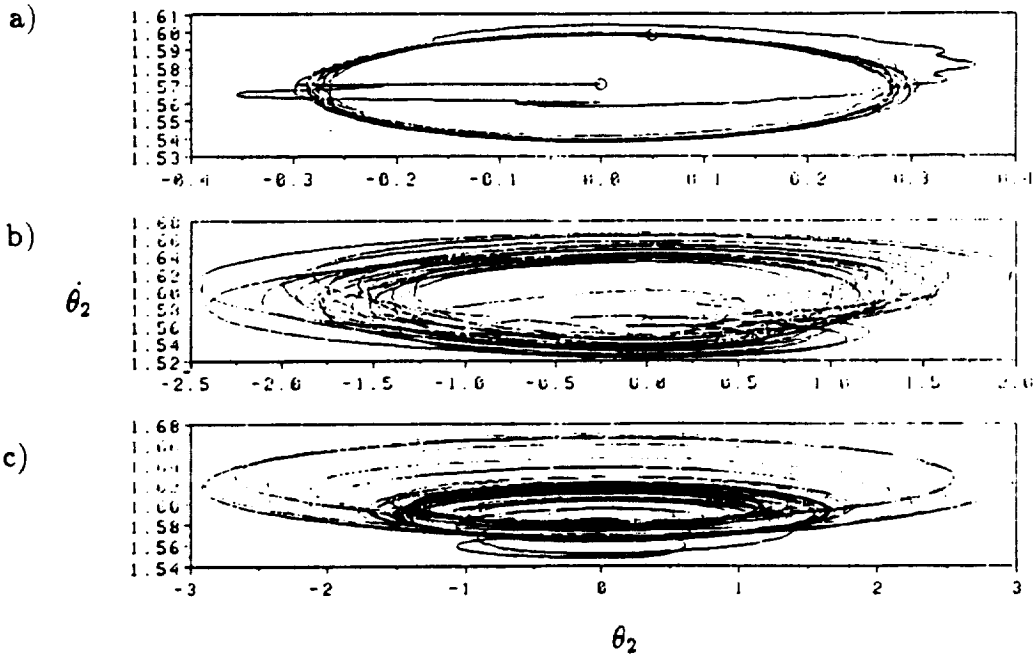

Fig. 5.13: Phase plot of the flexible RALF model for the different excitation frequencies (a) 1.5 Hz, (b) 4 Hz, (c) 7 Hz

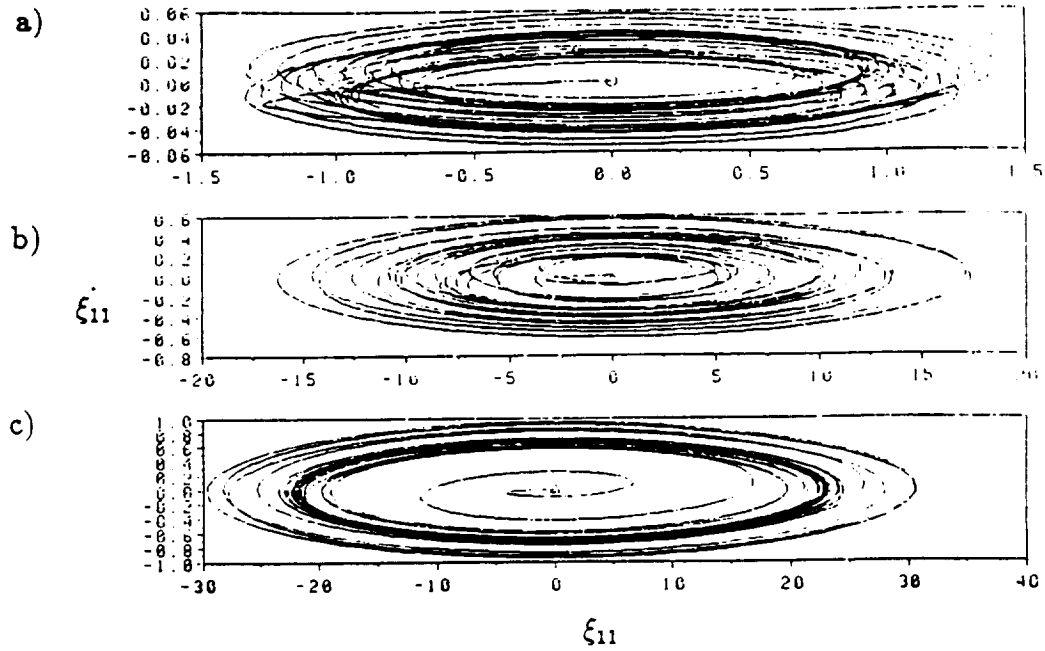

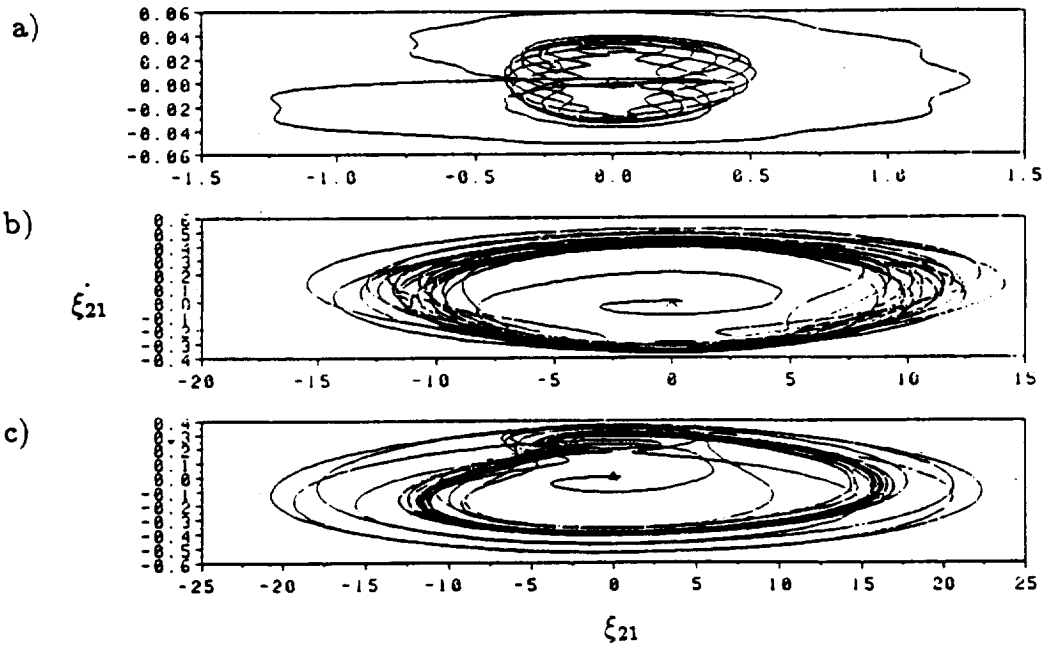

Fig. 5.13: (Continued)

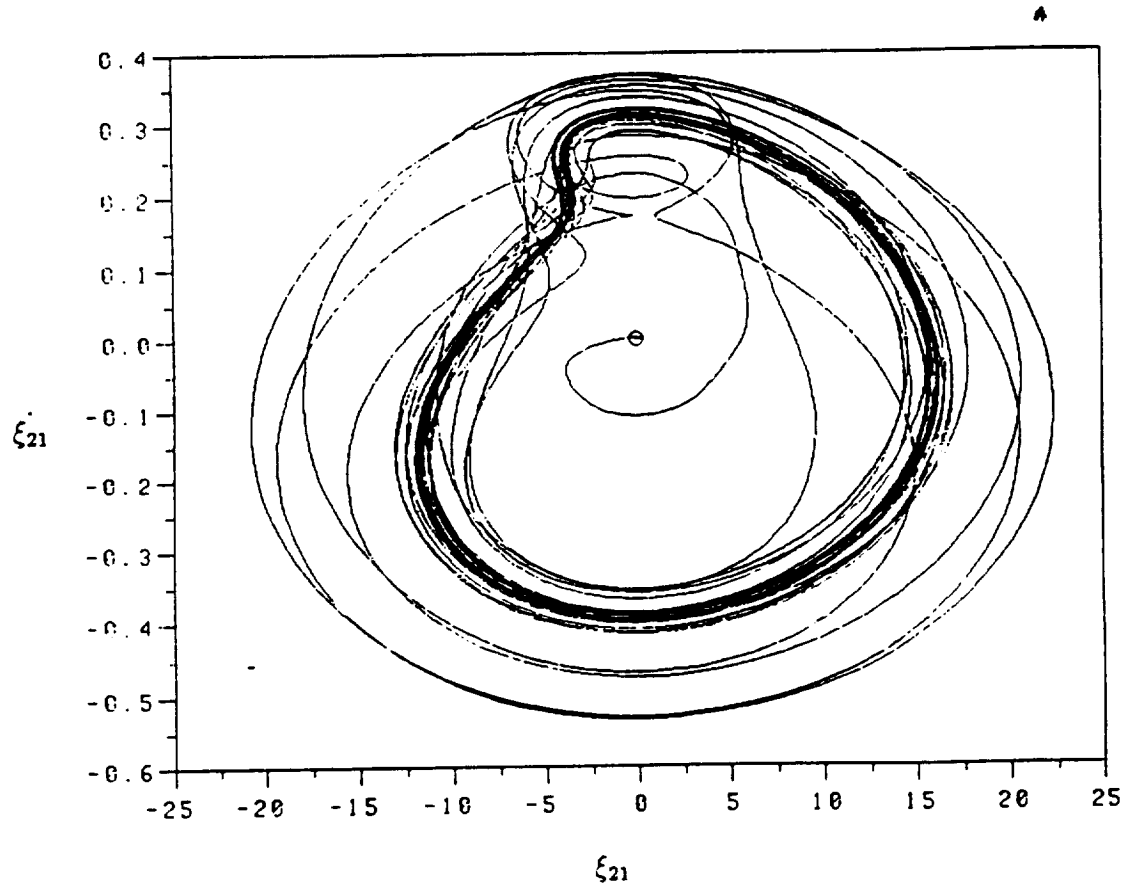

Fig. 5.14: Phase plot of the flexible RALF model for 0.5 rad and 7 Hz sinusoidal excitation

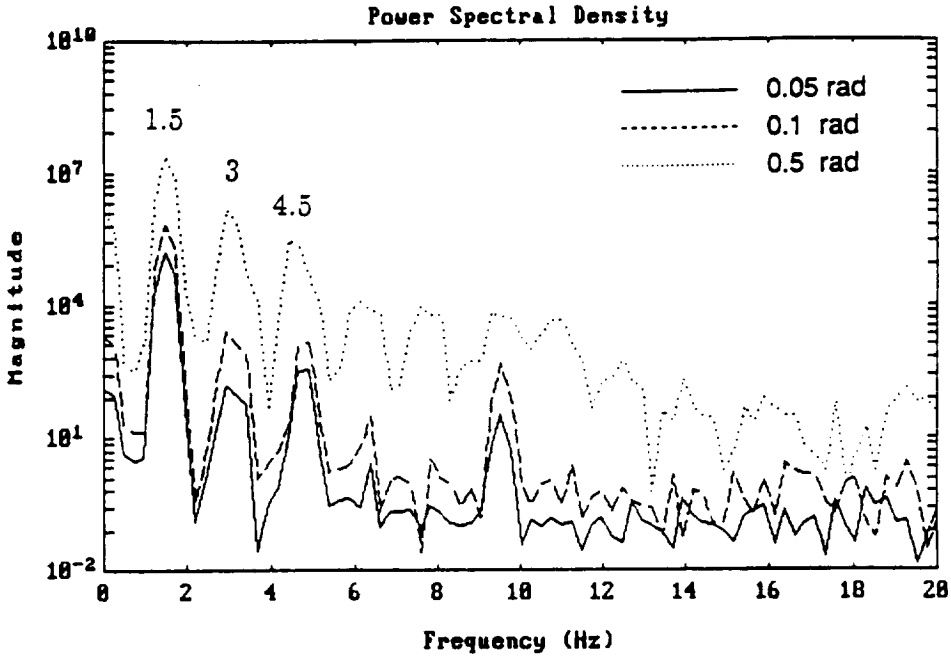

Fig. 5.15.a: The power spectral density of the tip acceleration for the different excitation amplitudes

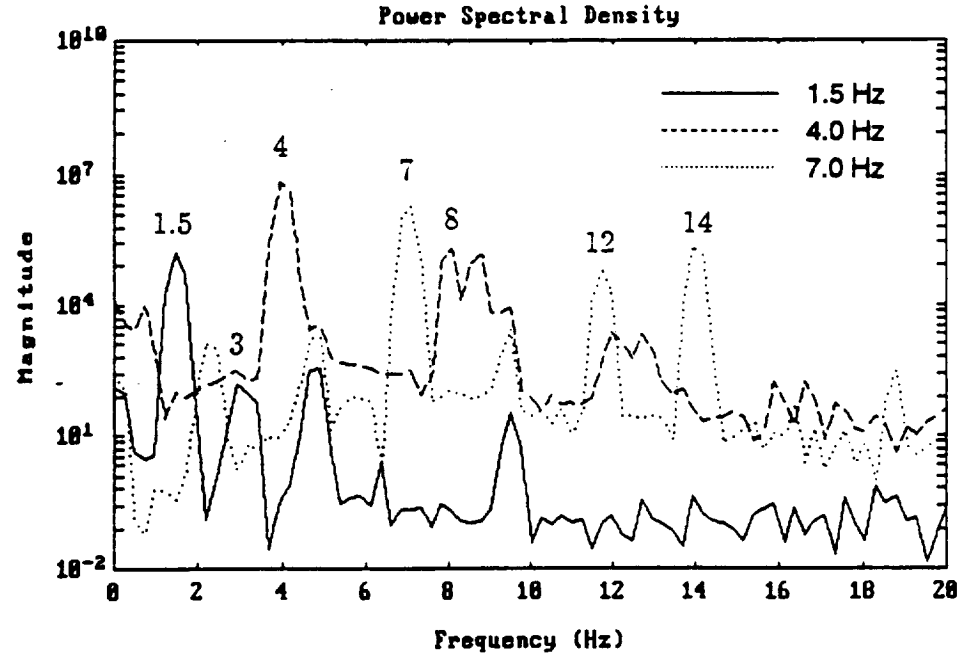

Fig. 5.15.b: The power spectral density of the tip acceleration for the different excitation frequencies

Table 5.2.a: Peaks of power density spectrum of flexible RALF model for different excitation amplitudes

	1st harmonic	2nd harmonic	3rd harmonic	1st/2nd harmonic
0.05 rad	1.73E5	1.53E2	3.36E2	1.13E3
0.1 rad	7.00E5	2.55E3	1.22E3	2.74E2
0.5 rad	2.47E7	1.50E6	2.96E5	1.65E1

Table 5.2.b: Peaks of power density spectrum flexible RALF model for different excitation frequencies

	1st harmonic	2nd harmonic	3rd harmonic	1st/2nd harmonic
1.5 Hz	1.73E5	1.53E2	3.36E2	1.13E3
4.0 Hz	7.25E6	2.18E5	2.40E3	3.33E1
7.0 Hz	1.88E6	2.38E5	1.76E4	0.79E1

The significance of the harmonics grows dramatically in both cases (factor of about 70 and 140) Therefore, the flexibility has a significant effect on the system dynamics as shown by comparison of Fig. 5.9 and Fig. 5.15.

5.3.2 Experiment of Nonlinear Dynamics

To test the nonlinear dynamics, fast motion of each link is required. The flow rate of the current hydraulic servovalve is 5 gpm. The effective piston area is different for each cylinder (See Appendix C.2). Therefore, the maximum linear speeds of the lower link actuator are 6.127 in/sec and 8.170 in/sec for extension and retraction, respectively [28]. The maximum linear speeds of the upper link actuator are 2.320 in/sec and 3.268 in/sec for extension and retraction, respectively. The transformation of the hydraulic cylinder's displacement to the joint angle rotation results in 18.8 deg/sec, 24.4 deg/sec for the lower link and 7.34 deg/sec, 10.29 deg/sec for the upper link at the nominal joint angles of the experiment. The maximum displacement of the cylinder is calculated as follows.

$$\dot{\theta} = A Sin\omega t \tag{5.1}$$

$$\theta = \frac{A}{\omega} Sin\omega t \tag{5.2}$$

Therefore, the maximum displacement of the lower link with 1.5 Hz frequency is 0.65 in (1.99 deg or 0.035 rad) and 0.87 in (2.59 deg or 0.045 rad) for extension and retraction. The maximum displacement of the upper link with 1.5 Hz frequency is 0.25 in (0.78 deg or 0.014 rad) and 0.35 in (1.09 deg or 0.019 rad) for extension and retraction. As we can see from comparison with simulation, the speed is too small for testing the nonlinear dynamics. Within the current maximum speed, the power spectral density is measured for different amplitudes and frequencies. Fig. 5.16.a is the power spectral density by increasing the amplitude from 2 in, to 4

in, to 6.5 in of the lower link and 2.5 in of the upper link with 0.15 Hz frequency. The relative peaks decrease. Fig. 5.16.b is the power spectral density obtained by increasing the frequency from 0.36 Hz, to 0.59 Hz, to 0.82 Hz with 1 in amplitude of both actuators. Fig. 5.16.c is the power spectral density obtained by increasing the frequency from 3.6 Hz, to 5.5 Hz, to 7.9 Hz with 0.1 in amplitude of both actuators. As shown in these figures, the harmonic peaks grow slightly in the wide range with increasing excitation amplitude and frequency. A slight nonlinearity is observed under the current hydraulic cylinder's speed.

5.4 Hydraulic Actuator Dynamics

In this section, the hydraulic actuator dynamics are modelled and compared with dynamics of the more commonly used electric D.C. motor. The difference in velocity feedback for the two actuators is shown to result in significantly different joint behavior for the two cases for a flexible structure. A simple single link system is used to illustrate this point.

Dynamics of an asymmetric or a single - rod hydraulic cylinder is more complicated than that of a symmetric or a double - rod hydraulic cylinder. Because the area of each chamber of the cylinder is different, the retraction and extension speed is different. Therefore, the dynamics of the asymmetric hydraulic cylinder is nonlinear. As shown in many studies on an asymmetric hydraulic cylinder [24,75,36], the exact dynamics of a real actuator is high order and therefore hard to apply in real time control. Therefore, in this thesis, a linear time invariant model is used by assuming the actuator is a symmetric hydraulic motor. Furthermore, in a crank mechanism, the relationship between the link rotation angle and the hydraulic piston displacement is nonlinear so that the dynamics change depend on the operating

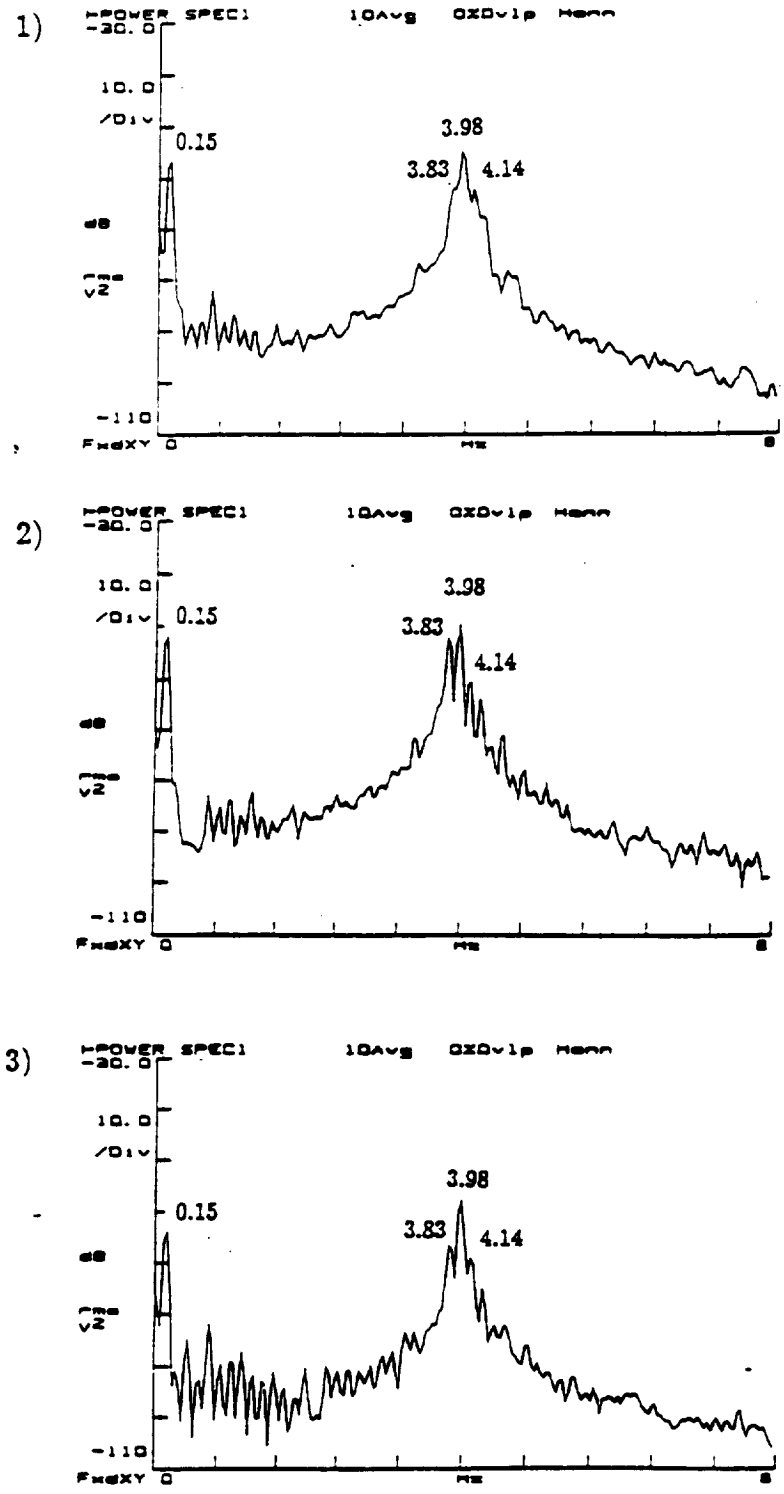

Fig. 5.16.a: Measured power spectral density of the tip acceleration for the different excitation amplitudes (0.15 Hz frequency) (1) 1.0 in, (2) 3.0 in, (3) 6.5in

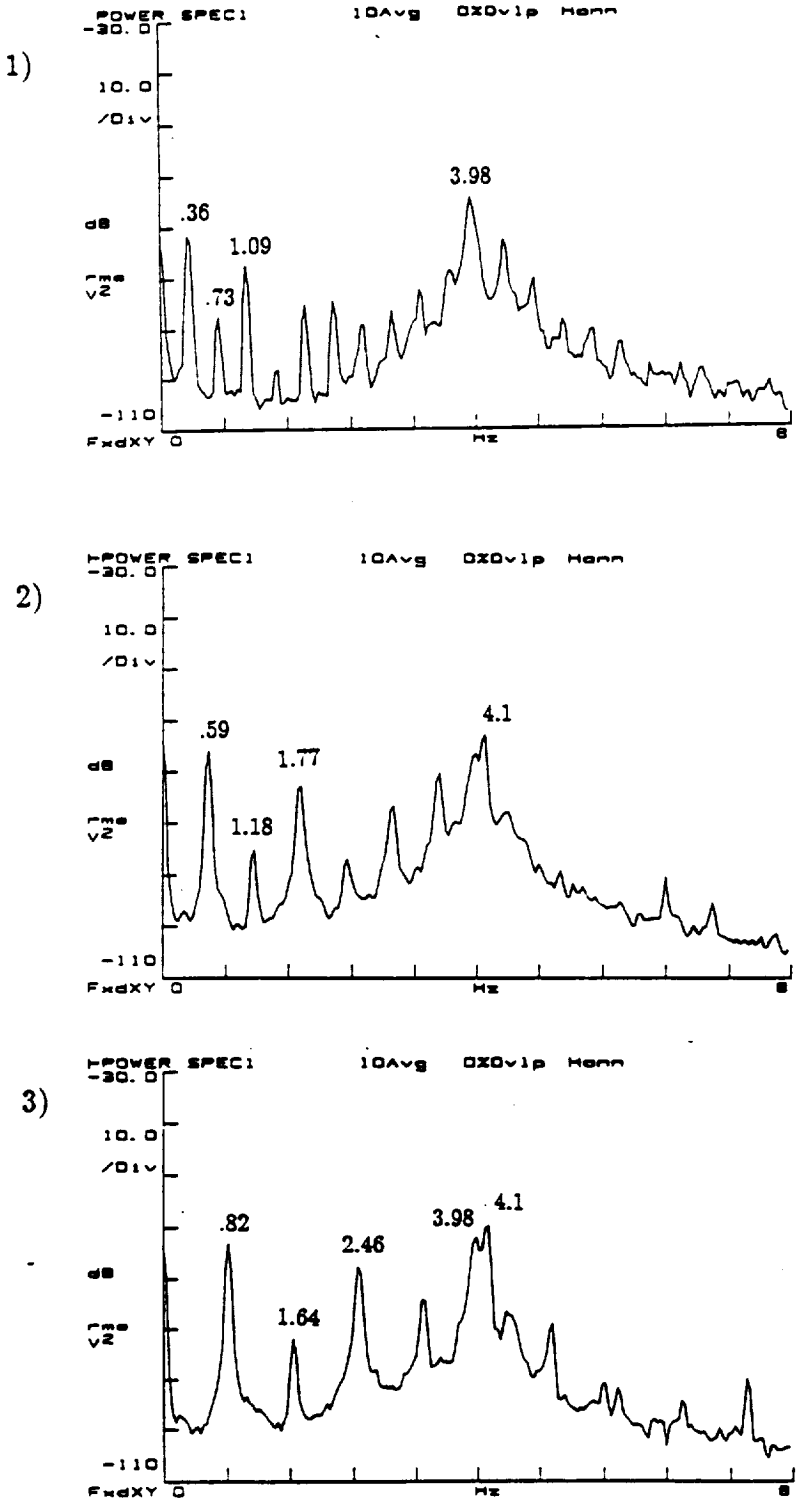

Fig. 5.16.b: Measured power spectral density of the tip acceleration for the different excitation frequencies (1.0 in amplitude) (1) 0.35 Hz, (2) 0.59 Hz, (3) 0.82 Hz

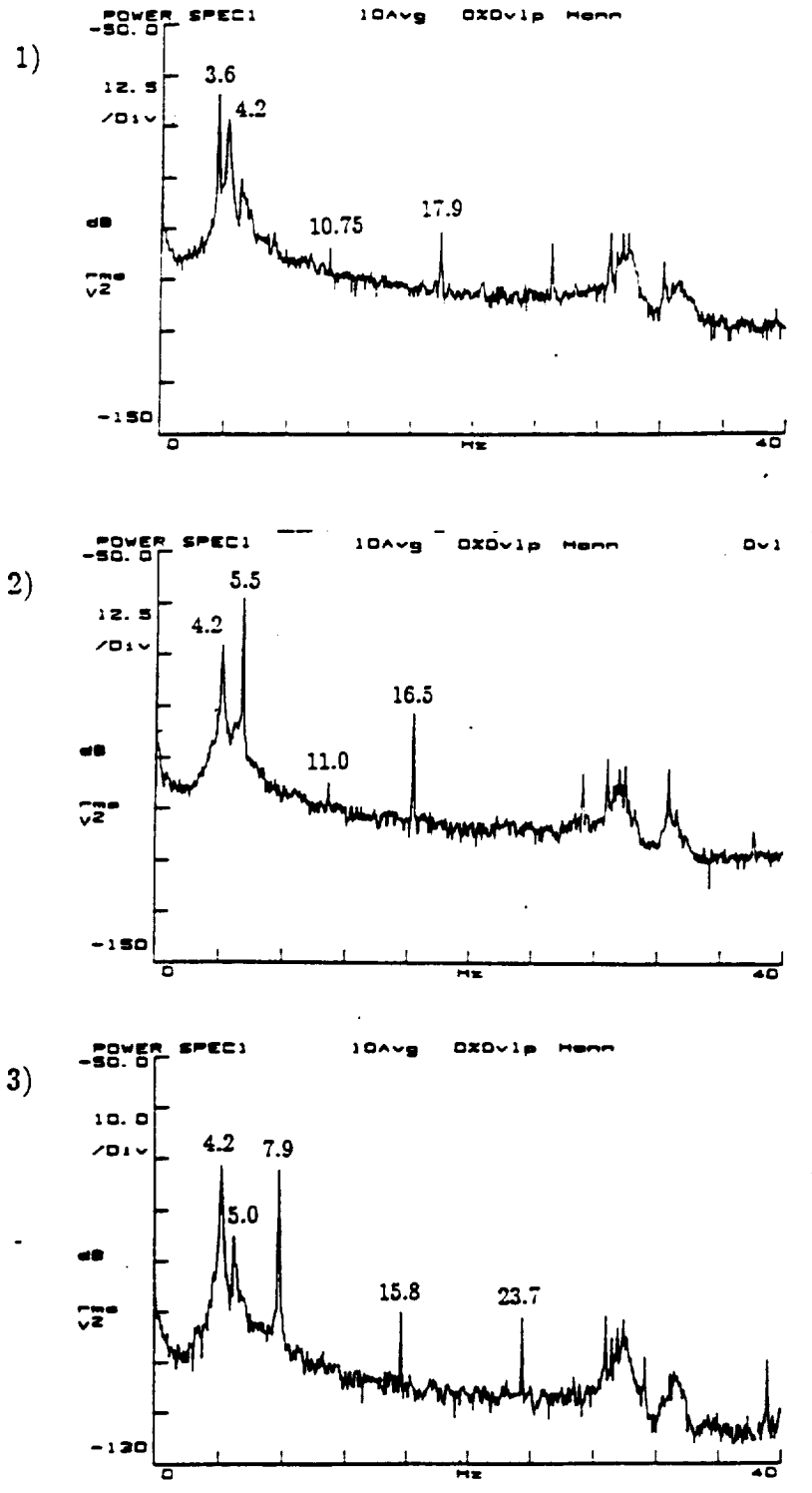

Fig. 5.16.c: Measured power spectral density of the tip acceleration for the different excitation frequencies (0.1 in amplitude) (1) 3.6 Hz, (2) 5.5 Hz, (3) 7.9 Hz

point.

As shown in Appendix B, the governing equations of an electric armature controlled servomotor and a hydraulic motor are similar each other. In the electric armature controlled servomotor, the dynamic equations are

$$T = K_t i_a = J\ddot{\theta} \tag{5.3}$$

$$L_a \frac{di_a}{dt} + R_a i_a = e_a - K_b \dot{\theta} \tag{5.4}$$

In the hydraulic motor, the dynamic equations are

$$T = D_m P_l = J\ddot{\theta} \tag{5.5}$$

$$\frac{V}{4\beta}\frac{dP_l}{dt} + K_{ce} P_l = K_q X_v - D_m \dot{\theta} \tag{5.6}$$

Equations (5.3) and (5.4) are similar to equations (5.5) and (5.6), respectively. The block diagram of the two models also show the similarity as shown in Fig. 5.17.a and 5.17.b. The actuator dynamics can be embedded into the plant dynamics. The linearized state equations of the plant are

$$\dot{x}_p = A_p x_p + B_p u_p \tag{5.7}$$

$$y = C_p x_p \tag{5.8}$$

The state equation of the actuator is

$$\dot{x}_a = A_a x_a + B_a u_a \tag{5.9}$$

$$u_p = C_a x_a \tag{5.10}$$

If the loop is closed, the input vector is

$$u_a = G_a x_r - C_p x_p \tag{5.11}$$

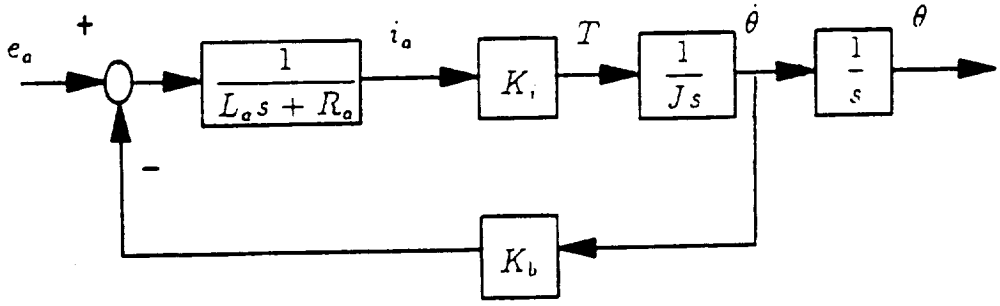

Fig. 5.17.a: The block diagram of the electric armature controlled servomotor

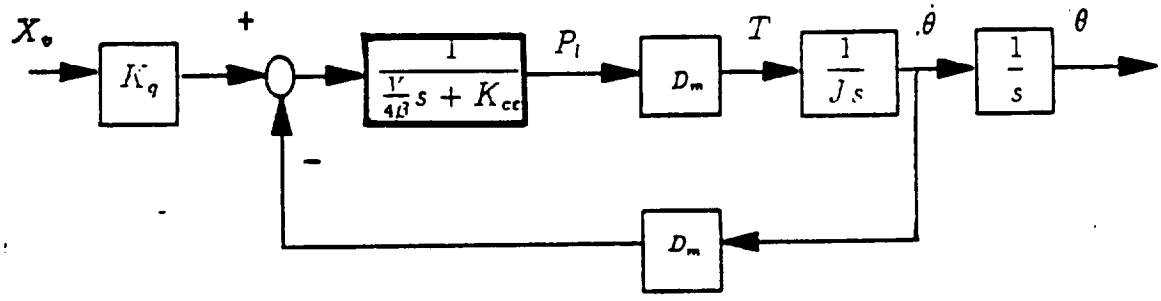

Fig. 5.17.b: The block diagram of the hydraulic motor

Fig. 5.18 clarifies the interconnection of the plant and the controller. The corresponding augmented state equations are

$$\begin{Bmatrix} \dot{x}_p \\ \dot{x}_a \end{Bmatrix} = \begin{bmatrix} A_p & B_p C_a \\ -B_a C_p & A_a \end{bmatrix} \begin{Bmatrix} x_p \\ x_a \end{Bmatrix} + \begin{bmatrix} 0 \\ B_a G_a \end{bmatrix} x_r \tag{5.12}$$

$$y = C_p x_p \tag{5.13}$$

This general form of augmented equation can apply to a flexible robot. The state equations of a flexible robot are

$$\begin{Bmatrix} \dot{\theta} \\ \dot{\xi} \\ \ddot{\theta} \\ \ddot{\xi} \end{Bmatrix} = \begin{bmatrix} 0 & 0 & 1 & 0 \\ 0 & 0 & 0 & 1 \\ a_{11} & a_{12} & 0 & 0 \\ a_{21} & a_{22} & 0 & 0 \end{bmatrix} \begin{Bmatrix} \theta \\ \xi \\ \dot{\theta} \\ \dot{\xi} \end{Bmatrix} + \begin{Bmatrix} 0 \\ 0 \\ b1 \\ b2 \end{Bmatrix} u_p \tag{5.14}$$

where

$$M = \begin{bmatrix} M_{rr} & M_{rf} \\ M_{fr} & M_{ff} \end{bmatrix}$$

$$K = \begin{bmatrix} 0 & 0 \\ 0 & K_{ff} \end{bmatrix}$$

$$-M^{-1}K = \begin{bmatrix} a_{11} & a_{12} \\ a_{21} & a_{22} \end{bmatrix} \tag{5.15}$$

$$M^{-1} \begin{Bmatrix} D_m \\ 0 \end{Bmatrix} = \begin{Bmatrix} b_1 \\ b_2 \end{Bmatrix}$$

M_{rr}, M_{ff}, and M_{rf} are the generalized inertia matrices which are related to the rigid body, the flexible body, and the coupling between the rigid body and the flexible body respectively. K_{ff} is the generalized stiffness matrix. θ and ξ are

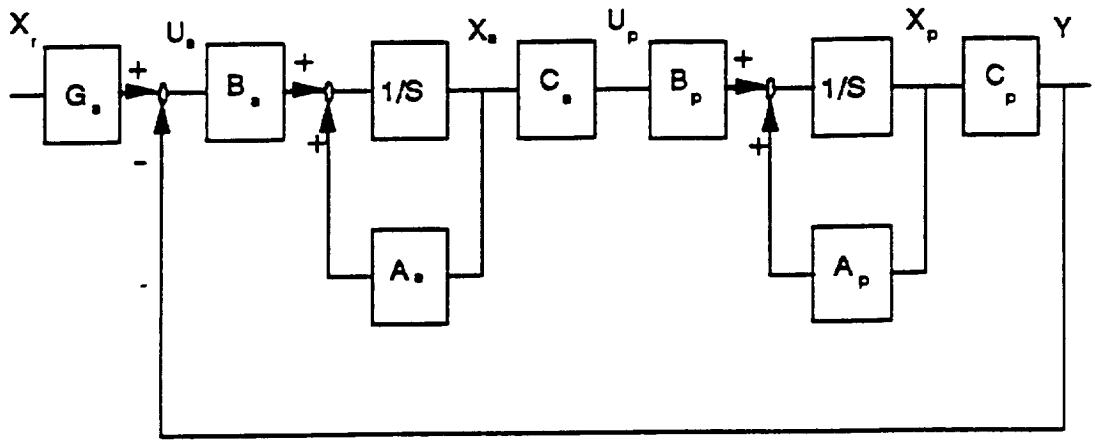

Fig. 5.18: The block diagram interconnection between the plant and the actuator

the generalized coordinates of the rigid body motion and the flexible body motion respectively.

Using the actuator equations, the state equations of the flexible robot augmented with the electric armature controlled servomotor and the hydraulic motor are as follows.

$$\begin{Bmatrix} \dot{\theta} \\ \dot{\xi} \\ \ddot{\theta} \\ \ddot{\xi} \\ \dot{i}_a \end{Bmatrix} = \begin{bmatrix} 0 & 0 & 1 & 0 & 0 \\ 0 & 0 & 0 & 1 & 0 \\ a_{11} & a_{12} & 0 & 0 & K_i b_1 \\ a_{21} & a_{22} & 0 & 0 & K_i b_2 \\ 0 & 0 & -\frac{K_b}{L_a} & 0 & -\frac{R_a}{L_a} \end{bmatrix} \begin{Bmatrix} \theta \\ \xi \\ \dot{\theta} \\ \dot{\xi} \\ i_a \end{Bmatrix} + \begin{bmatrix} 0 \\ 0 \\ 0 \\ 0 \\ \frac{1}{L_a} \end{bmatrix} e \qquad (5.16)$$

$$\begin{Bmatrix} \dot{\theta} \\ \dot{\xi} \\ \ddot{\theta} \\ \ddot{\xi} \\ \dot{P}_l \end{Bmatrix} = \begin{bmatrix} 0 & 0 & 1 & 0 & 0 \\ 0 & 0 & 0 & 1 & 0 \\ a_{11} & a_{12} & 0 & 0 & D_m b_1 \\ a_{21} & a_{22} & 0 & 0 & D_m b_2 \\ 0 & 0 & -\frac{D_m}{V/4\beta} & 0 & -\frac{K_{ce}}{V/4\beta} \end{bmatrix} \begin{Bmatrix} \theta \\ \xi \\ \dot{\theta} \\ \dot{\xi} \\ P_l \end{Bmatrix} + \begin{bmatrix} 0 \\ 0 \\ 0 \\ 0 \\ \frac{K_q}{V/4\beta} \end{bmatrix} X_v \qquad (5.17)$$

The only difference in the models is the values of each parameter as shown in Table 5.3 [3,59]. As shown in the block diagrams of Fig. 5.17, the velocity is fed back when the actuator dynamics is included. If the velocity feedback terms, $\frac{K_b}{L_a}$ and $\frac{D_m}{V/4\beta}$, are not included, the system poles are determined by the eigenvalues of $(sI - A_p)(sI - A_c)$ as shown in Eq. 5.12. The poles of the combined system are the combination of those of A_p and A_a. However, if the velocity feedback terms are included, the system poles are changed. Fig. 5.19 shows the root locus of a single flexible link when the velocity feedback terms of the electric motor and the hydraulic motor are changed from zero to the values shown in Table 5.3. When

Table 5.3: Comparison of system parameters between a electrical motor and a hydraulic motor

	Electric Motor			Hydraulic Motor	
L_a	3.0E-3	H	$\frac{V}{4\beta}$	2.6E-12	$\frac{m^5}{N}$
K_i	0.5296	$\frac{Nm}{A}$	D_m	15.2E-4	m^2
$\frac{K_b}{L_a}$	1.750E2	$\frac{V}{H}$	$\frac{D_m}{V/4\beta}$	5.846E8	$\frac{N}{m^3}$
$\frac{R_a}{L_a}$	1.167E3	$\frac{\Omega}{H}$	$\frac{K_{ce}}{V/4\beta}$	2.053E0	$\frac{N}{m.sec^2}$
$\frac{1}{L_a}$	0.333E3	$\frac{1}{H}$	$\frac{K_q}{V/4\beta}$	0.573E12	$\frac{N}{m^3.sec}$

the electric motor is added, the closed loop system poles move a little bit from the open loop system poles. On the other hand, when the hydraulic motor is added, the closed loop system poles move almost to the open loop system zeros. This is due to the large value of $\frac{D_m}{V/4\beta}$ compared to $\frac{K_b}{L_a}$.

This phenomenon also can be observed in the Bode plot. Fig. 5.20 and 5.21 show the Bode plot for the angular position of the single flexible link with the electric motor and the hydraulic motor respectively. The several peaks observed in Fig. 5.20 can not be found in Fig. 5.21 because the system pole is located near the system zero. The closer a pole is to a zero, the less that mode appears in the output. In the experiments, Fig. 5.22.a is the Bode plot for the angular velocity of the single flexible link when it is excited by the electric motor. Because of the encoder resolution, the angular velocity is measured. Fig. 5.22.b shows the Bode plots for the positions of two hydraulic cylinders of RALF. The peaks of corresponding to the system frequencies are not found as predicted in Fig. 5.21. Note that the different size actuators are compared because of the hardware limitations. Therefore, only

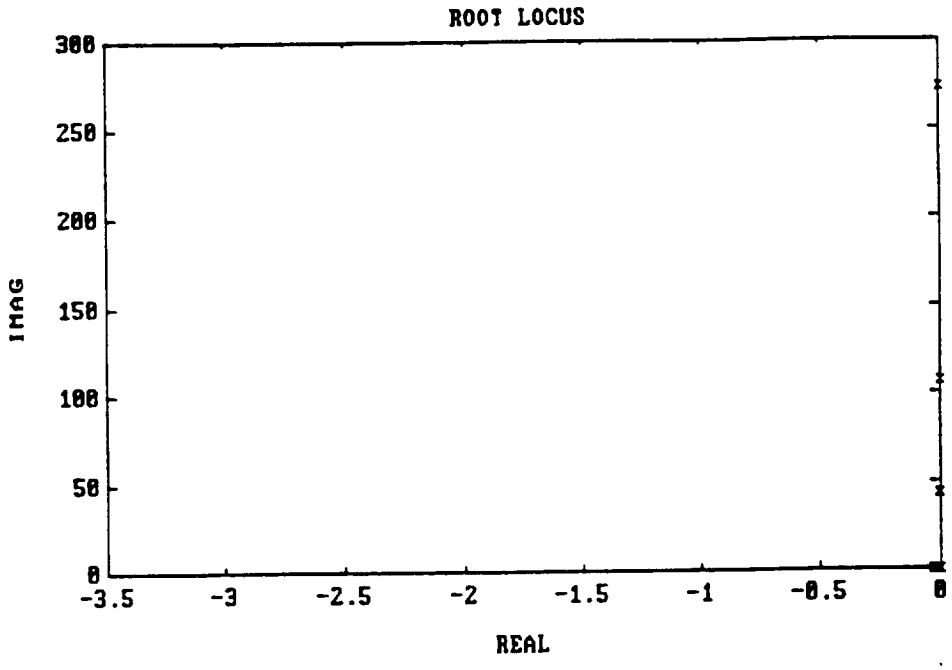

Fig. 5.19.a: The root locus of a single flexible link with the electric motor

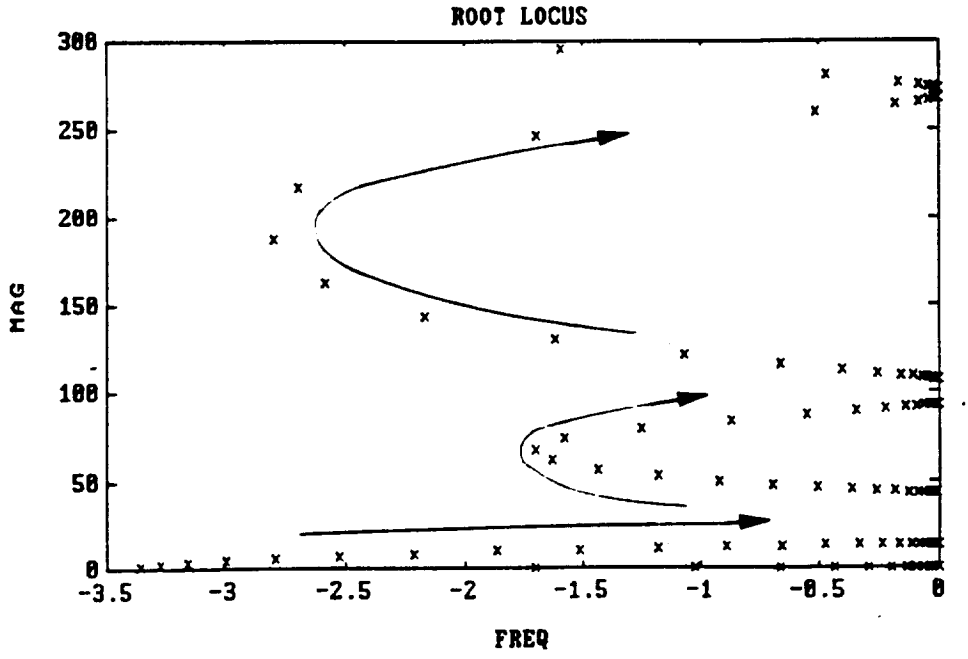

Fig. 5.19.b: The root locus of a single flexible link with the hydraulic motor

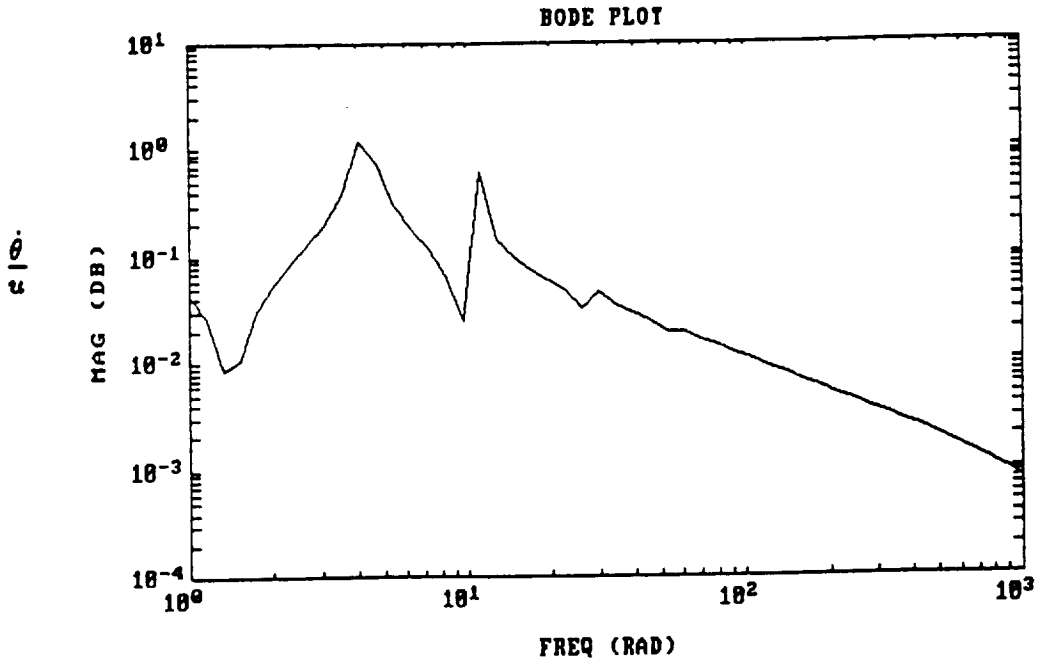

Fig. 5.20: The Bode plot of a single flexible link with the electric motor

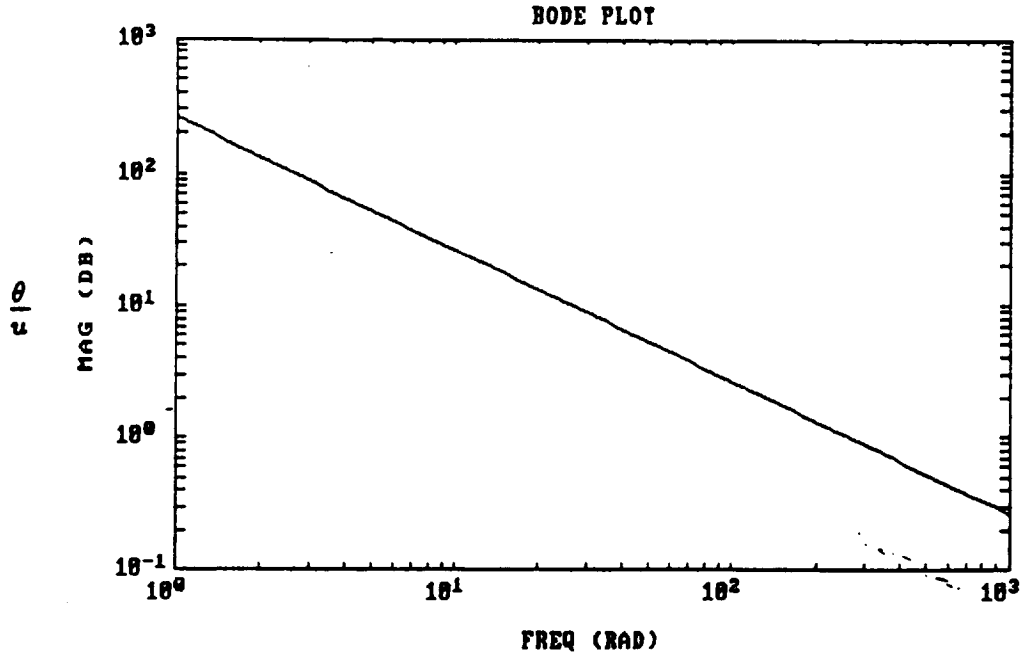

Fig. 5.21: The Bode plot of a single flexible link with the hydraulic motor

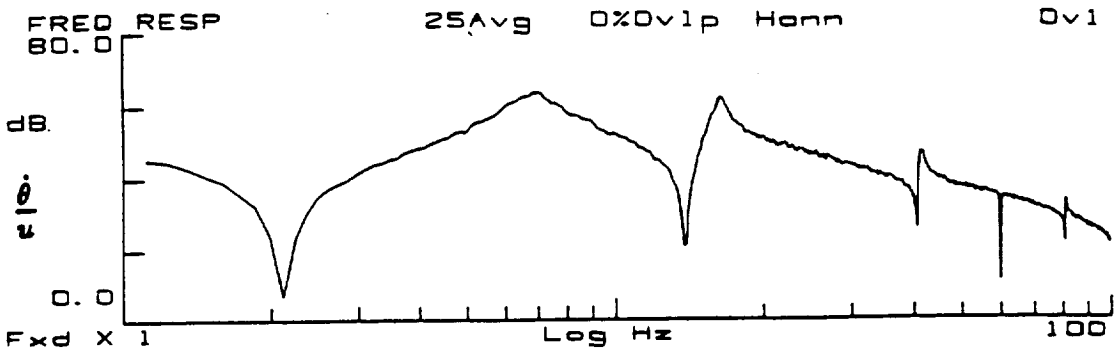

Fig. 5.22.a: Measured Bode plot of a single flexible link with the electric motor for the angular velocity to input

a)

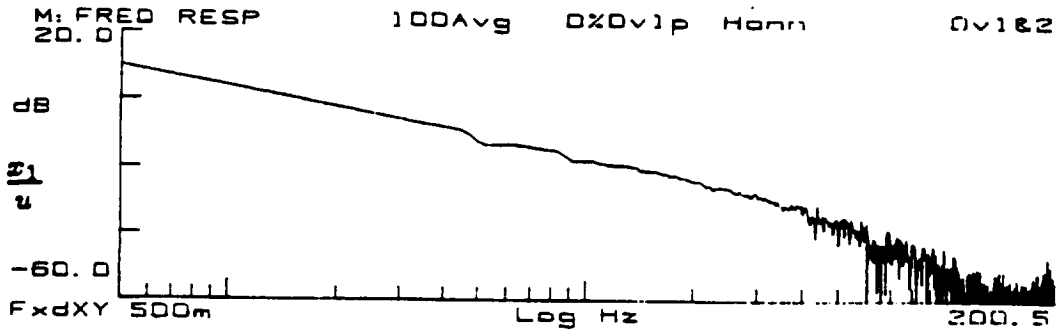

b)

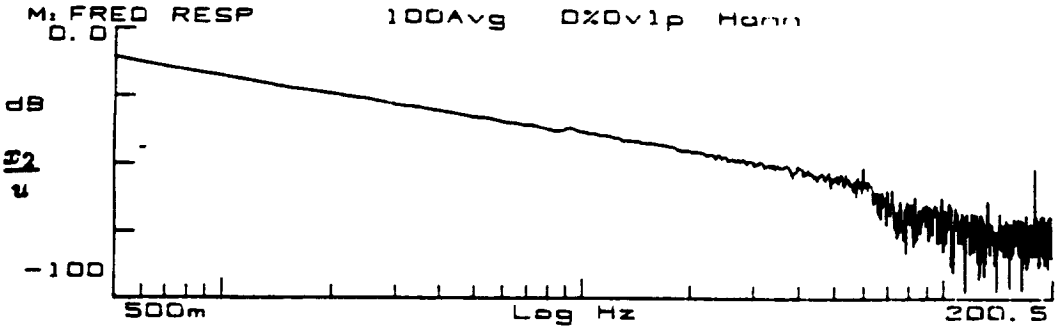

Fig. 5.22.b: Measured Bode plot of each link of RALF with the hydraulic cylinder for the cylinder position to input (a) the lower link, (b) the upper link

the qualitative characteristic can be compared. From the above discussion, the actuator dynamics has a significant effect on the flexible dynamics. The pole-zero cancellation observed for joint variables as the output is not observed for other outputs, of course. Tip position or strain will continue to show the resonances of the arm. In addition. it should be noted that high velocity feedback gains in the control will also increase the coupling term and thus make the actuator stiff with respect to the disturbances caused by arm dynamics.

5.5 Conclusion

The TREETOPS model of RALF is used for the verification of the analytical model. The step responses of both models match each other very well. It is verified that SVD is a stable algorithm for a constrained dynamic system simulation. For verification of the nonlinear dynamics of RALF, a sinusoidal excitation method is used with various amplitudes and frequencies. The response is measured at the tip acceleration. As shown in the phase plots and the power spectra, the nonlinear dynamics of a flexible robot is significant compared to that of a rigid robot. The differences the amplitude of between harmonic peaks as shown in the power spectra can be used to check the degree of nonlinearity. However, because of the speed limitation of the current hydraulic cylinder, the nonlinear dynamics of RALF is not fully checked experimentally.

The actuator dynamics effect on the flexible robot is also investigated. Even though the electric motor and the hydraulic motor have the same form of dynamic equations, the effect on the flexible robot can be different due to the difference of their system parameters. The differences are analyzed by the root locus and the Bode plot, both theoretically and experimentally.

CHAPTER VI

Control of RALF

6.1 Introduction

The current RALF structure has some complicated components and geometries which are hard to describe analytically. As mentioned in the previous chapter, the actuator dynamics is an important component in the flexible arm dynamics. The dynamics of an asymmetric hydraulic cylinder is nonlinear. In a large and fast motion, the nonlinear effect of the asymmetric hydraulic cylinder might be significant. The crank mechanism of the hydraulic cylinder and the offsets (See Appendix Fig. C.1) make the symbolic modelling difficult. Therefore, before implementing a modern control algorithm which requires an accurate dynamic model, a single input multi output controller is implemented using cylinder position and beam strain at each link independently. The performance of the classical controller can be used as the base performance for implementation of a more advanced control algorithm in the future.

6.2 Controller Design and Experiment

The position of each hydraulic cylinder is fed back using an LVDT sensor for the rigid body motion control. Because the hydraulic actuator has a velocity feedback loop internally, the position feedback with lag compensator has been generally used

for the position control of the hydraulic system [49].

$$\frac{u_i}{e_i} = K_i \frac{s + \omega_i}{s + \omega_i/\beta_i} \qquad for \quad i = 1, 2 \tag{6.1}$$

The lag compensator Eq. (6.1) is used to compensate the steady state error due to the friction. However, because the gravitational torque is much larger than the dynamic error correction torque, the compensation speed is slow. Therefore, the addtional constant torque is included to compensate the external torque due to gravity force. Gains and coefficients of the lag compensator are adjusted to obtain the underdamped step response. The parameters of the lag compensator are shown in Table 6.1. A cycloid curve is used for the trajectory profile. The reference trajectories used consist of the combination of the extension and retraction motion of two joints as shown in Table 6.2. The controller is digitized using a bilinear transformation method, $s = \frac{2}{T_s}\frac{z-1}{z+1}$, and implemented in a Micro-Vax II computer. The sampling frequency used, T_s, is 8 ms. The controller implementation is described in Appendix C. The control loop of the upper link is closed first and followed by the lower link. Fig. 6.1 and 6.2 are experimentally measured time histories of each cylinder position in cases of small motion and large motion respectively. In the two cases, the system follows the reference trajectories well. Fig. 6.3 shows measured time history of each cylinder position when a 30 lb payload is added at the tip. The system still follows the reference trajectories well.

The strain is fed back to suppress the beam vibration. The strain feedback controller can be designed by root locus. The direct strain feedback pushes system poles into the right half plane as shown in Fig. 6.4. Therefore, the strain rate feedback is required to give flexible mode damping. The strain rate can be obtained by numerical differentiation of the measured strain. However, a low pass filter is additionally needed to reduce the noise effect. The strain rate also can be obtained

Table 6.1: Parameters of a lag compensator

	ω	β	K
Lower Link	0.5 Hz	2.0	5000.
Upper Link	2.0 Hz	4.0	5000.

Table 6.2.a: Reference trajectory I (small motion)

	1st	2nd	3rd	4th
Lower Link [*in*]*	2.0	2.0	4.0	2.0
Upper Link [*in*]*	2.0	4.0	4.0	2.0
Moving Time [sec]	2.0	2.0	2.0	2.0
Pause Time [sec]	10.	10.	10.	10.

Table 6.2.b: Reference trajectory II (large motion)

	1st	2nd	3rd	4th
Lower Link [*in*]*	2.0	2.0	8.0	2.0
Upper Link [*in*]*	2.0	4.0	4.0	2.0
Moving Time [sec]	2.0	1.0	1.0	1.0
Pause Time [sec]	10.	15.	15.	15.

* absolute displacement of the cylinder

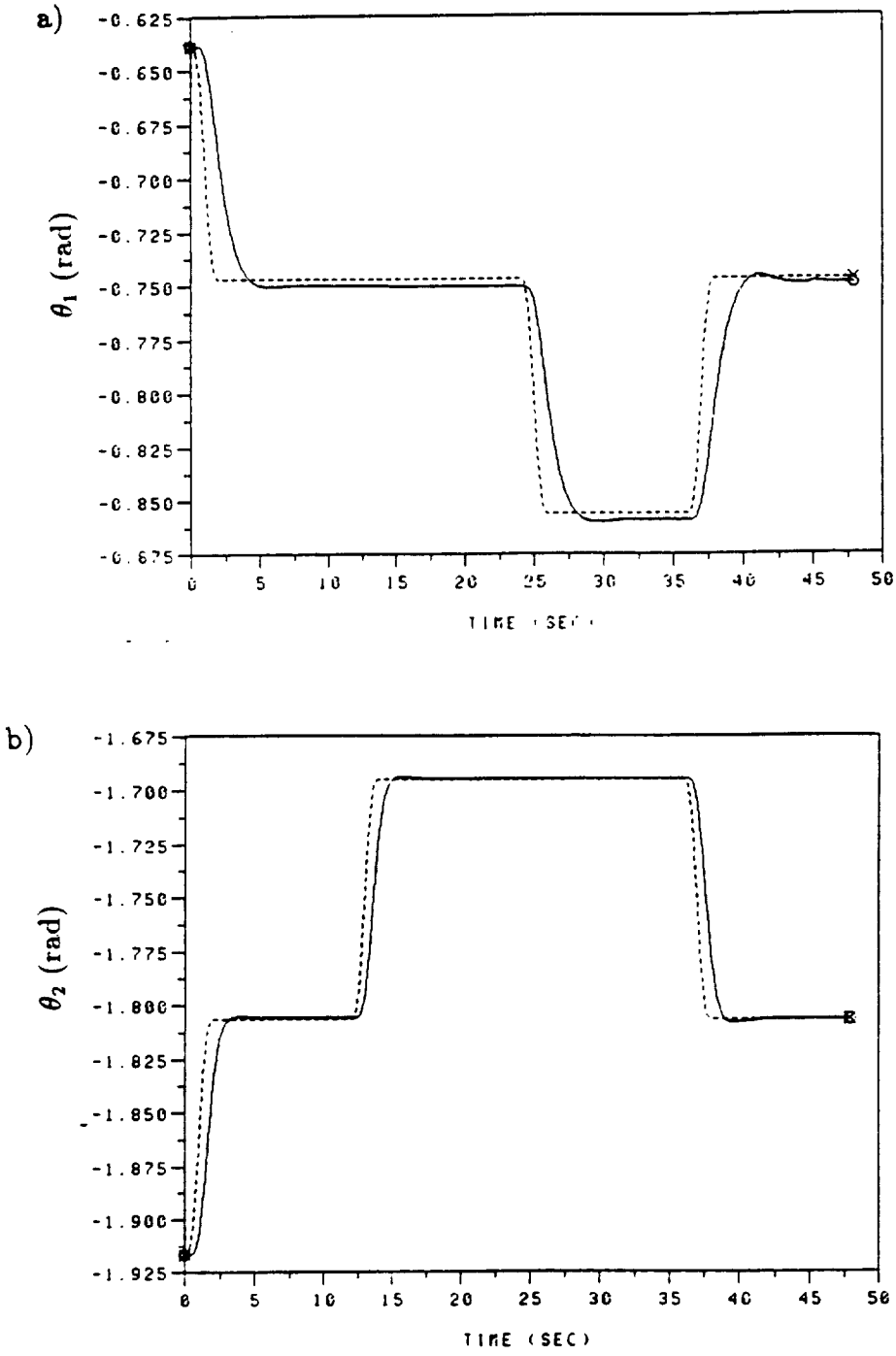

Fig. 6.1.a: Measured time response of RALF to a small step input a) θ_1, b) θ_2

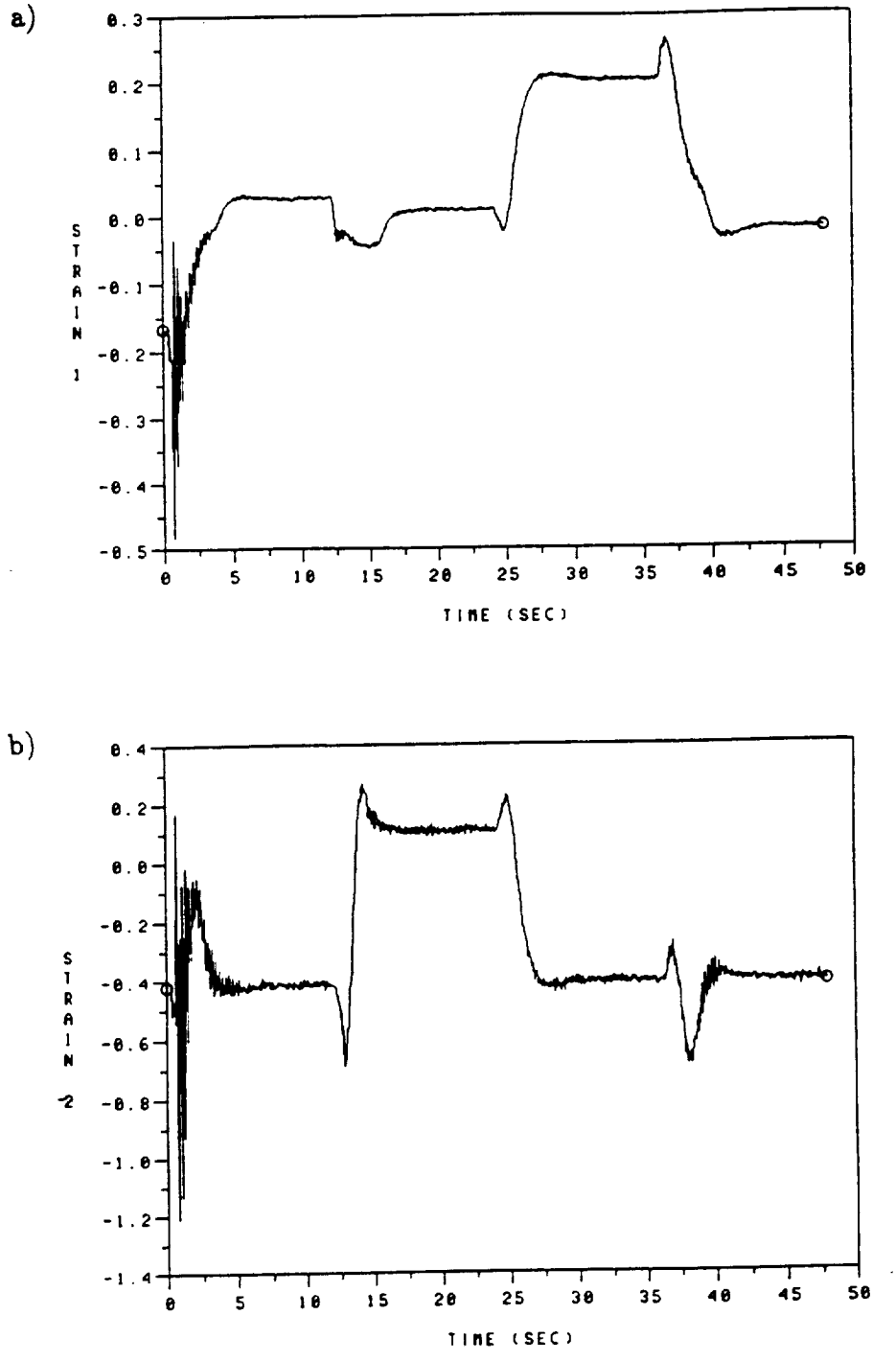

Fig. 6.1.b: Measured time response of RALF to a small step input
a) Upper link strain, b) Lower link strain

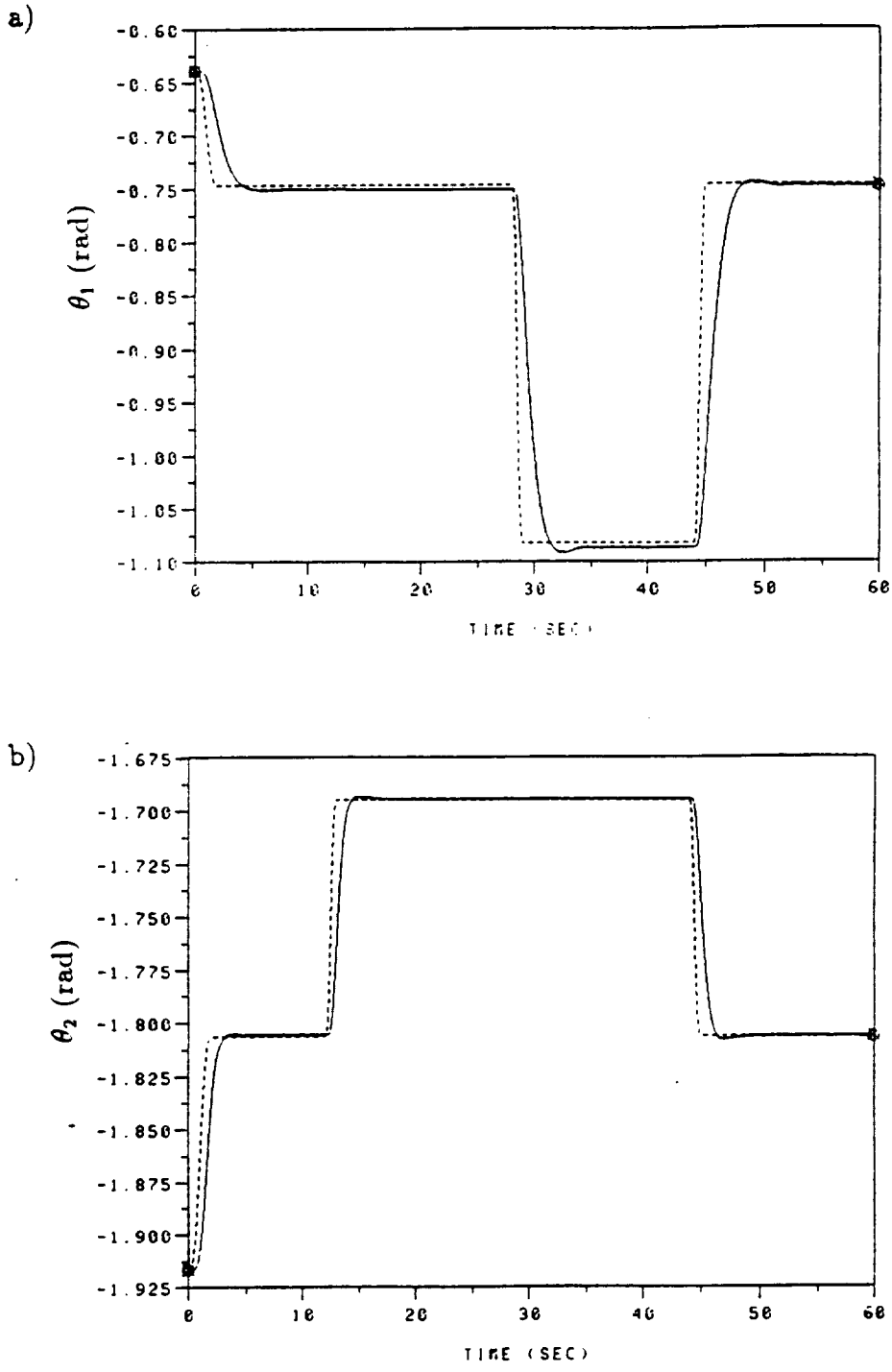

Fig. 6.2.a: Measured time response of RALF to a large step input a) θ_1, b) θ_2

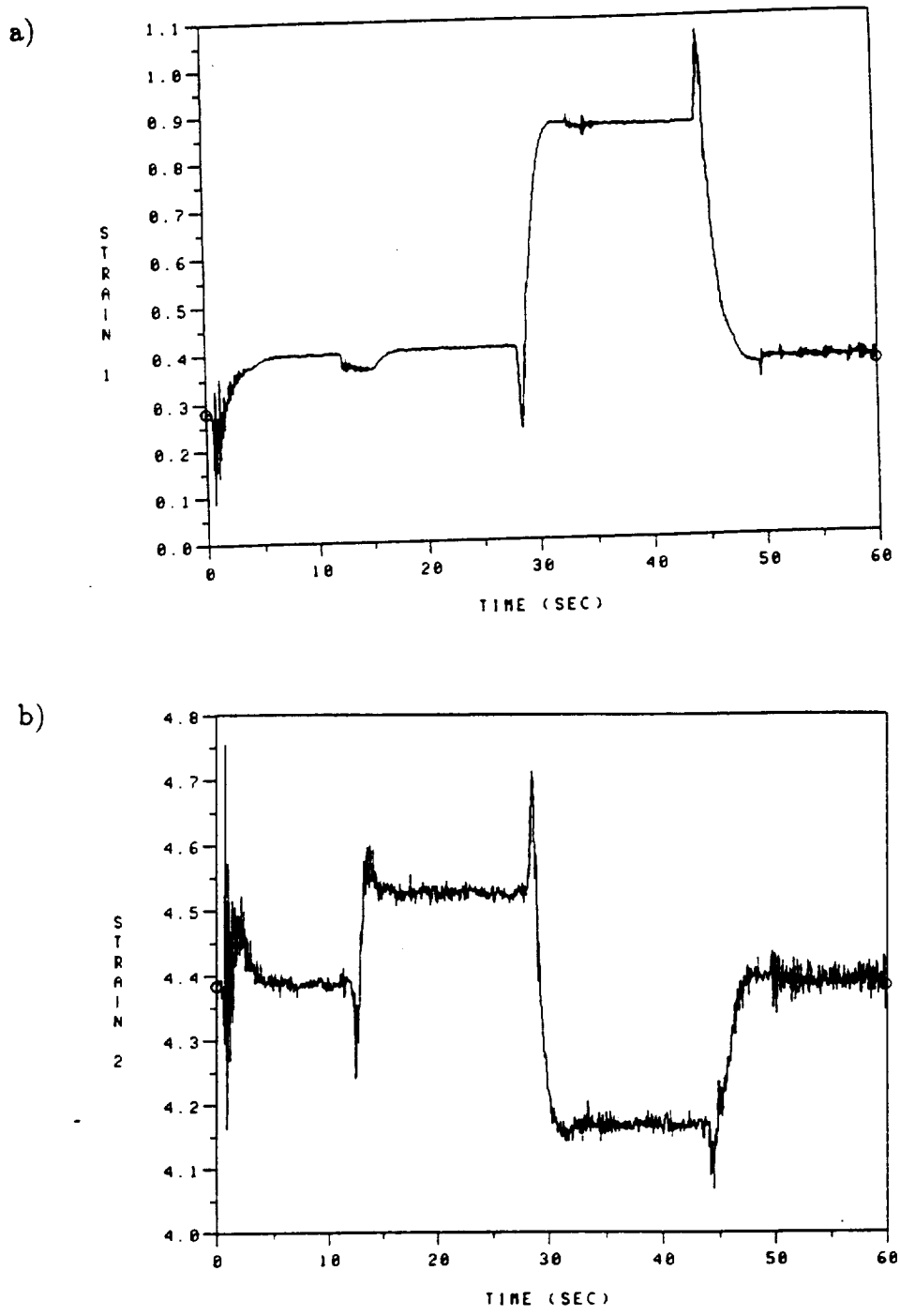

Fig. 6.2.b: Measured time response of RALF to a large step input
a) Upper link strain, b) Lower link strain

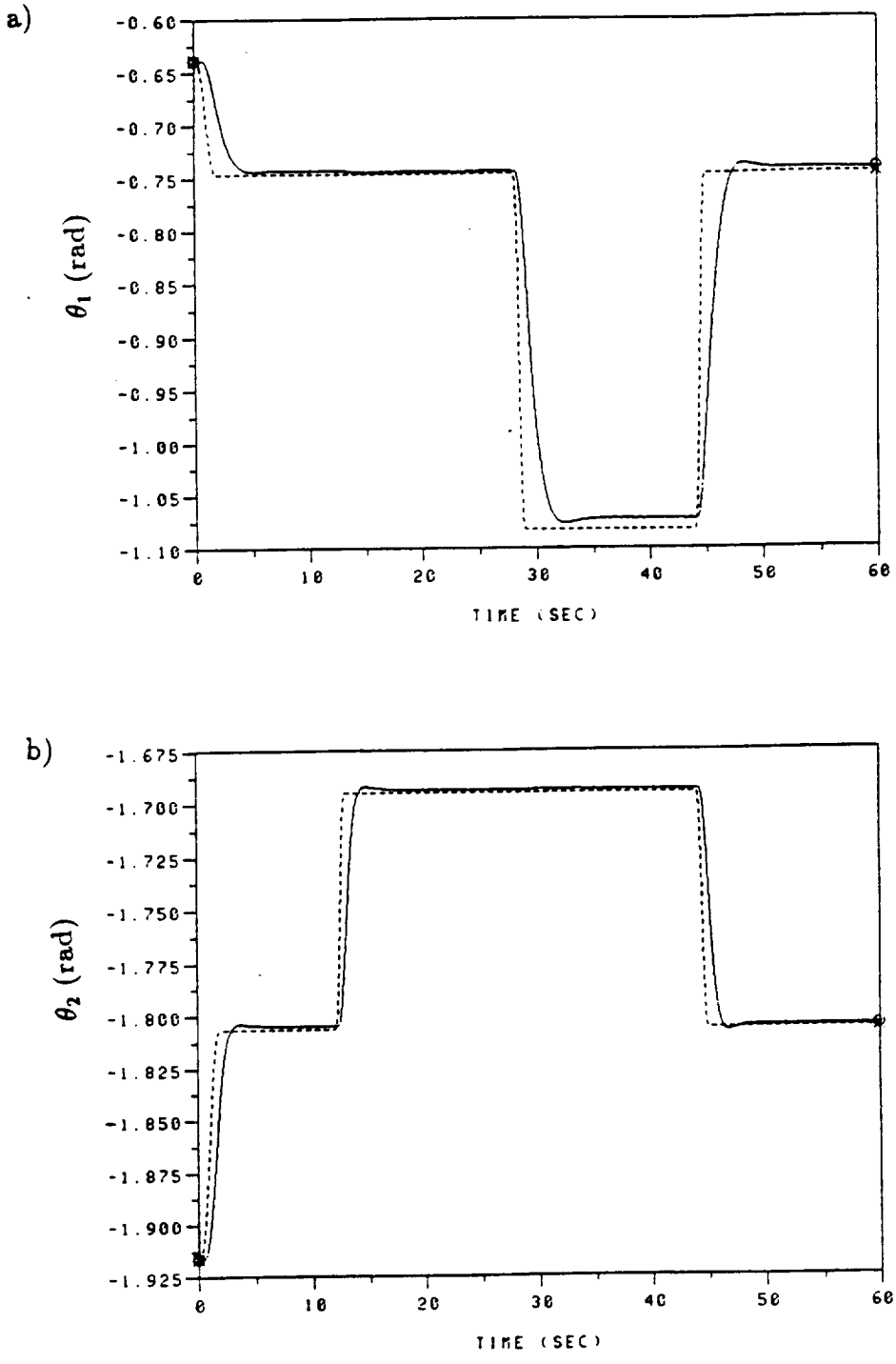

Fig. 6.3.a: Measured time response of RALF to a large step input when a payload is attached
a) θ_1, b) θ_2

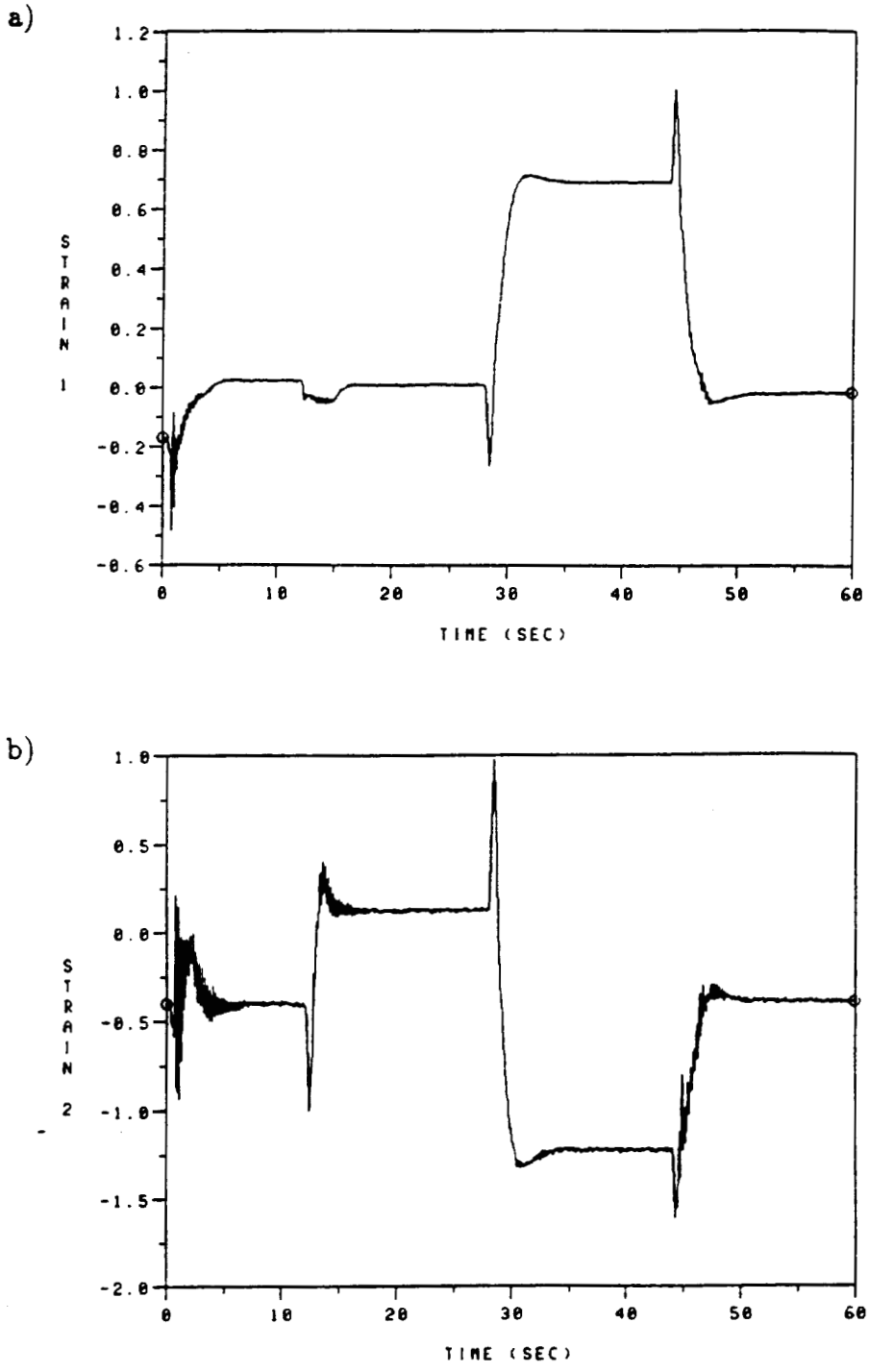

Fig. 6.3.b: Measured time response of RALF to a large step input when a payload is attached
a) Upper link strain, b) Lower link strain

from a filter. The generalized structural filter presented by Wie [78] is an extension of the phase -lead, -lag, bandpass, and notch filter. This approach for controlling flexible systems has been proposed for control of large space structures. We will explore its use for flexible arm control. The concept is based on various pole-zero patterns that can be realized from a second order filter presented as follows.

$$\frac{(s^2/\omega_z^2 + 2\zeta_z s/\omega_z + 1)}{(s^2/\omega_p^2 + 2\zeta_p s/\omega_p + 1)} \tag{6.2}$$

By different choices of the coefficients of the above second order filter, several frequency shaping filters such as phase lead and lag, notch, bandpass can be easily realized. In addition to these minimum-phase filters, various nonminimum-phase filters can also be realized from this second order filter. For stabilization of flexible modes, a phase stabilization technique and a gain stabilization technique using the phase lead or the notch filter have been used in practice [77,17,81]. Phase stabilization provides the proper gain and phase characteristics at the desired frequency to obtain a closed loop damping. Gain stabilization provides attenuation of the control loop gain at the desired frequency to ensure stability. In the system whose parameters are not known precisely, phase stabilization is more desirable. High loop gain can be realized if the desired mode does not cross the -180 deg. $\pm$ n*360 deg.

The first approach for vibration suppression is to change the phase by the phase lead filter. The phase lead filter can be obtained by setting $\omega_p > \omega_z$ and $\zeta_p = \zeta_z = \zeta_c$ as shown in Fig. 6.5.a. As shown in Fig. 6.5.b, the gain increase at higher frequency can be approximated as $40 * log(\frac{\omega_p}{\omega_z})$. Ratio $\frac{\omega_p}{\omega_z}$ greater than 2 should be avoided because a large ratio amplifies measurement noise. The filter coefficients are chosen by setting ω_p and ω_z on either side of the mode to be stabilized. The damping ratio of the filter can be changed arbitrarily. For $\zeta_c = 1$, the conventional phase lead filter with poles and zeros on the real axis can be realized. Fig. 6.6 and 6.7 show the

root locus when the phase lead filter is used. The filter gain is varied. The phase lead filter can stabilize the modes of the upper link and the lower link conditionally. The effect of filter damping ζ_c is not significant.

The second approach is to employ the nonminimum phase allpass filter which maintains the control loop gain and provides the proper phase lag to the flexible mode as shown in Fig. 6.8.b. As shown in Fig. 6.8.a, the nonminimum phase allpass filter can be obtained by setting $\omega_p = \omega_z = \omega_c$ and $\zeta_p = -\zeta_z$. In Fig. 6.9, several filter frequencies, ω_p and ω_z, are tried for the stabilization of the upper link mode. 30 filter gains which are logarithmically equally spaced between 1 and 1000 are chosen. If the filter frequency is higher than that of the upper link mode to be stabilized as shown in Fig. 6.9.c, it is hard to stabilize the upper link mode by the filter. However, if filter frequency is lower than that of the upper link mode, the filter can stabilize the upper link mode. As shown in Fig. 6.9.a and 6.9.b, the system poles move more slowly by the lower filter frequency for the same gain. Therefore, the lower filter frequency of Fig. 6.9.a is more desirable. In Fig. 6.10, the same technique is applied to the lower link mode. In this case, if the filter frequency is lower than that of the lower link mode to be stabilized, it is hard to stabilize the lower link mode by the filter as shown in Fig. 6.10.a. However, if the filter frequency is higher than that of the lower link mode, the filter can stabilize the lower link mode conditionally. As shown in Fig. 6.10.b and 6.10.c, the system poles also move more slowly by the lower filter frequency for the same gain. Therefore, the filter whose frequency is close to the lower link mode is more desirable. Fig. 6.11 and 6.12 are simulated time responses of an analytical model to verify the results observed in Fig. 6.9 and 6.10 respectively. As shown in Fig. 6.9 and Fig. 6.10, the system response is dominated by the lower link mode because the lower link mode is close to the imaginary axis. As expected in the previous discussion. Fig. 6.11.a

a)

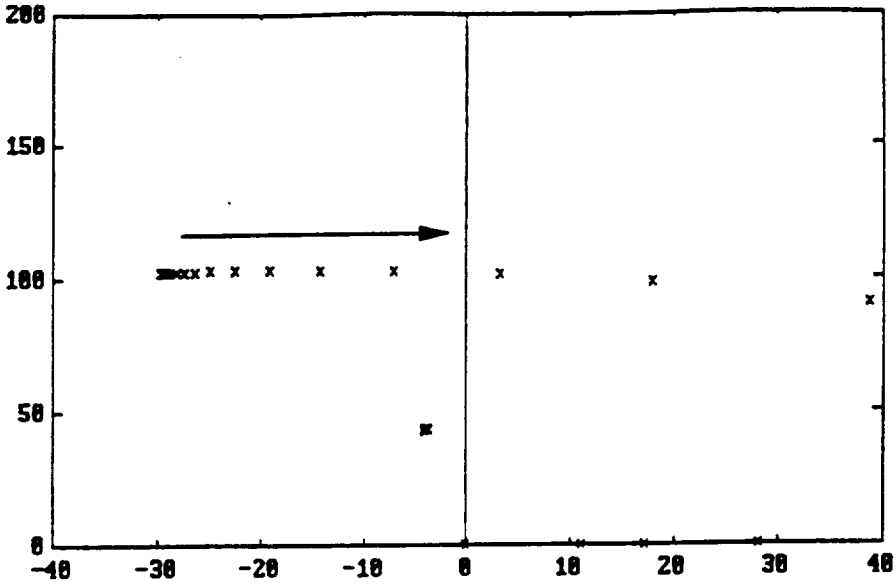

b)

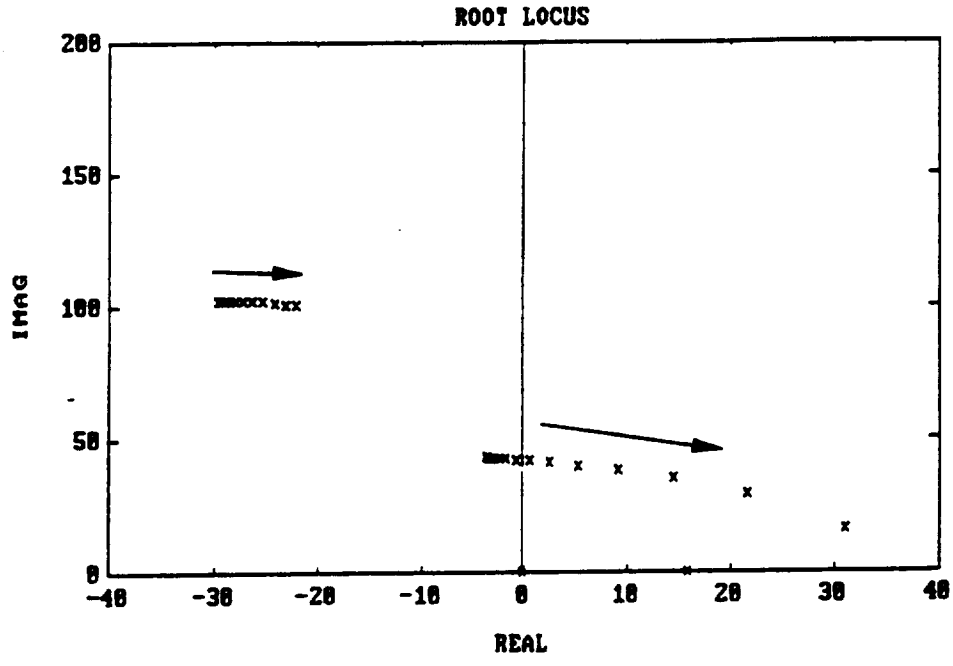

Fig. 6.4: Root locus of direct strain feedback
a) Upper link, b) Lower link

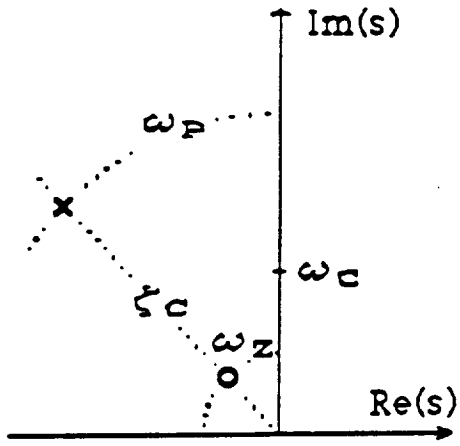

Fig. 6.5.a: Pole - Zero plot of the phase lead filter

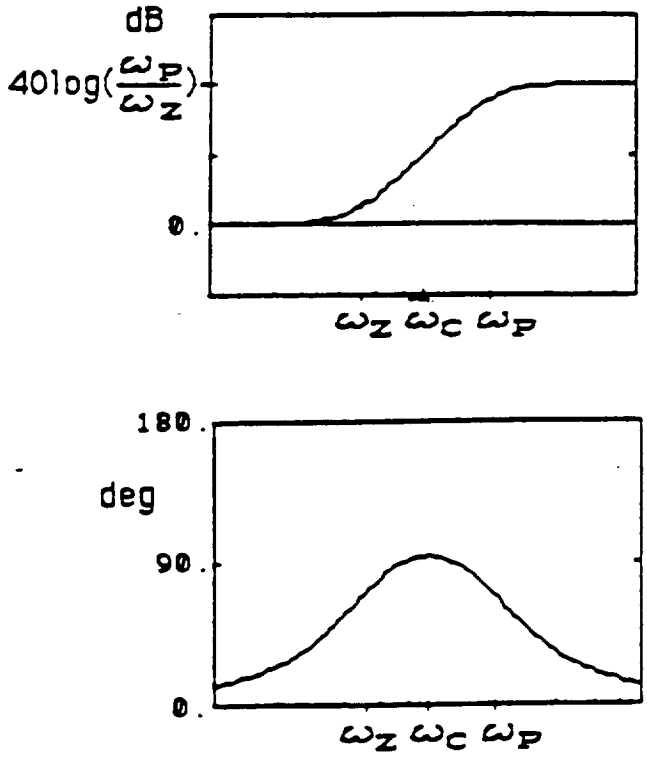

Fig. 6.5.b: Gain - Phase plot of the phase lead filter

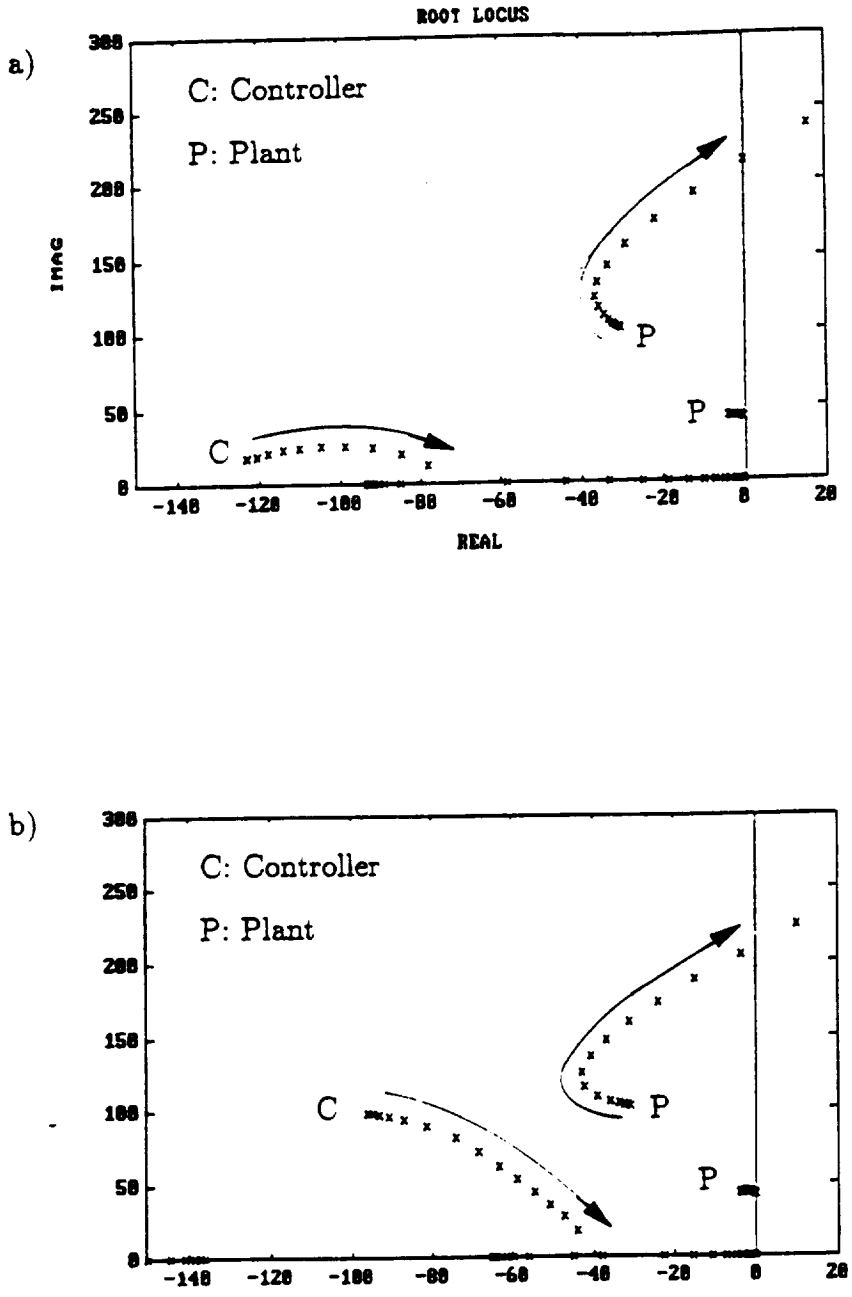

Fig. 6.6: Root locus of the upper link when strain is fed back through a phase lead filter
a) $\zeta_c = 1.$, b)$\zeta_c = .7$

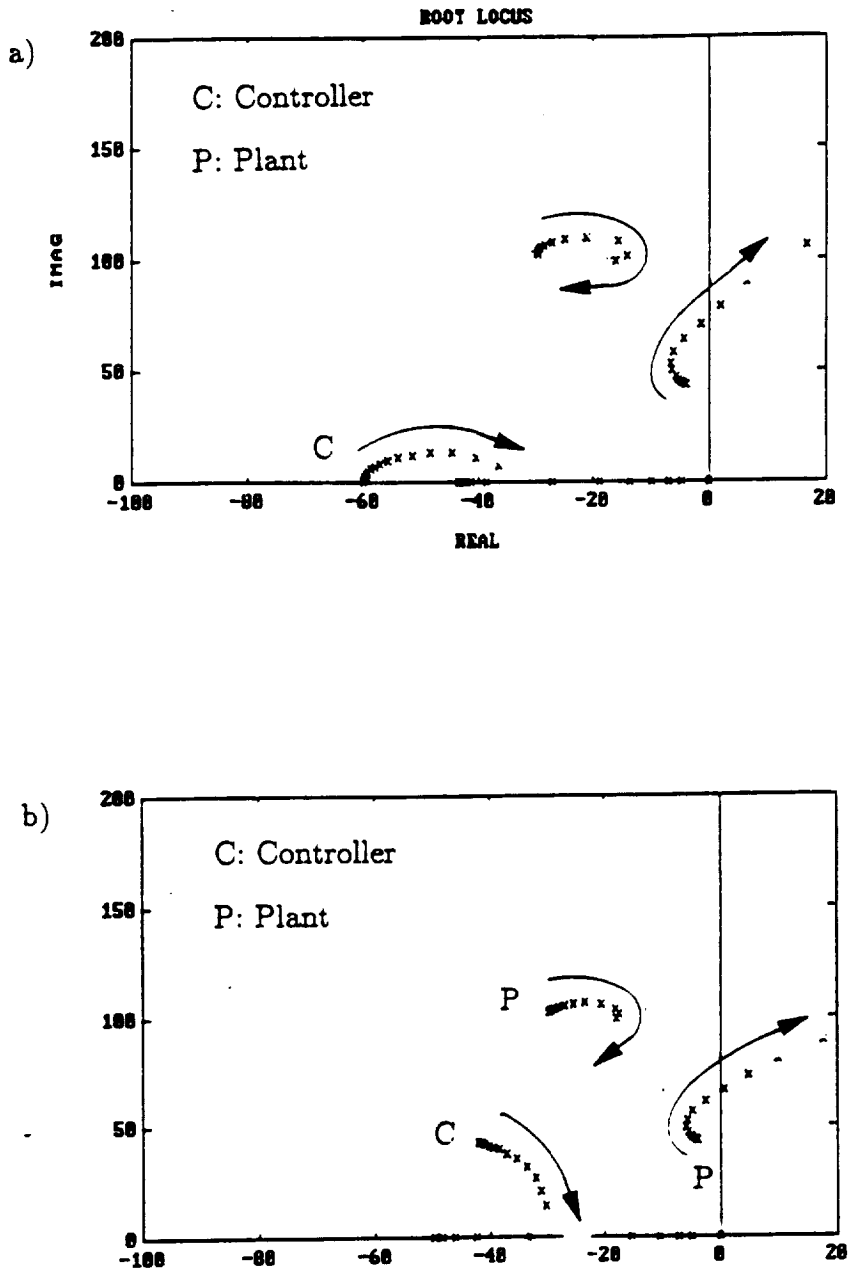

Fig. 6.7: Root locus of the lower link when strain is fed back through a phase lead filter
a) $\zeta_c = 1.$, b)$\zeta_c = .7$

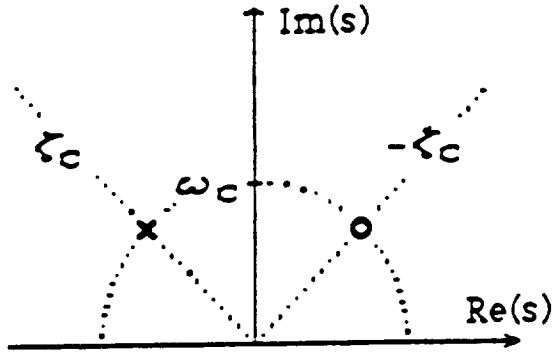

Fig. 6.8.a: Pole - Zero plot of nonminimum-phase allpass filter

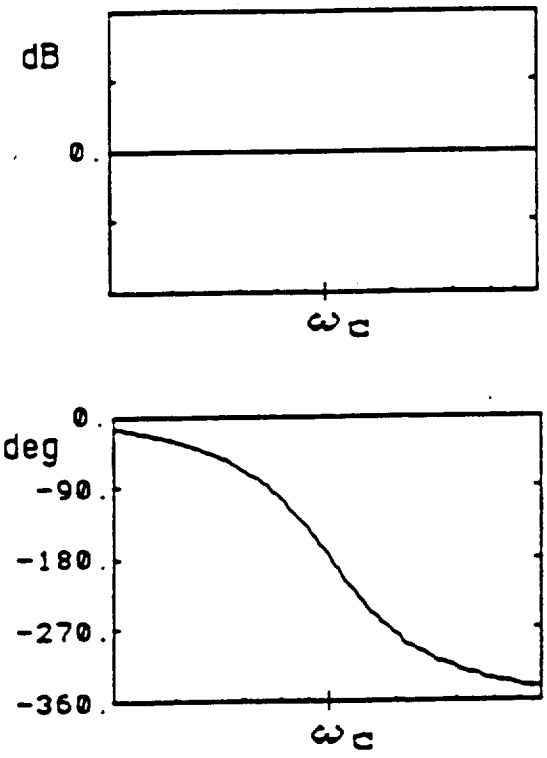

Fig. 6.8.b: Gain - Phase plot of nonminimum-phase allpass filter

a)

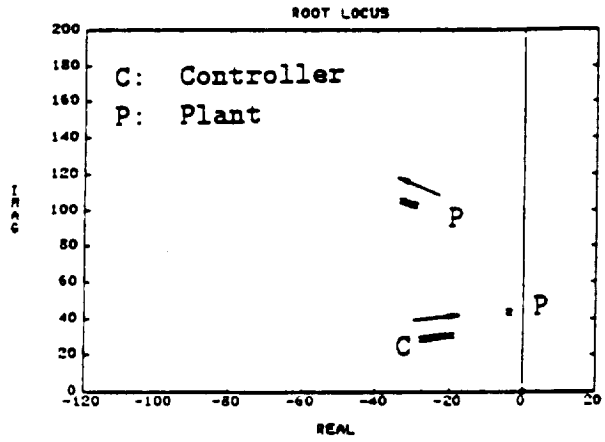

b)

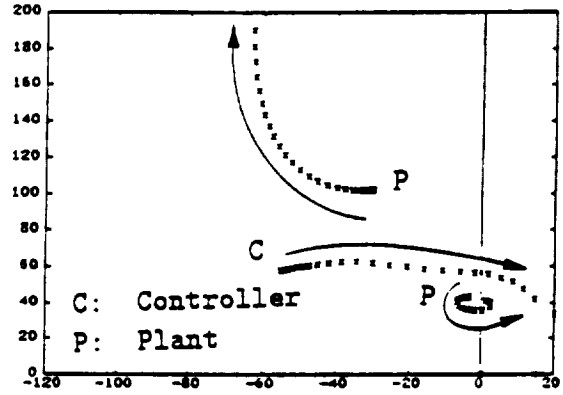

c)

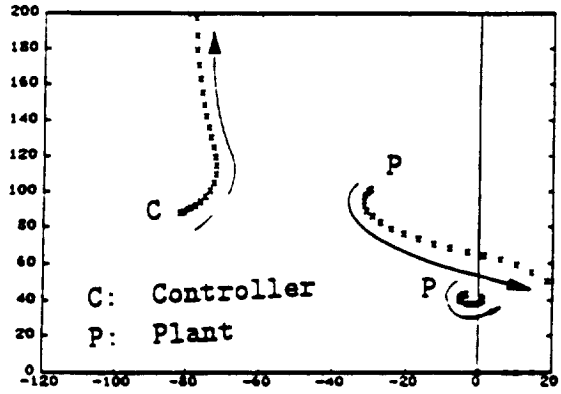

Fig. 6.9: The root locus of the upper link when the strain is fed back through a nonminimum phase allpass filter
a) $\omega_c = 40$, b) $\omega_c = 80$, c) $\omega_c = 120$

a)

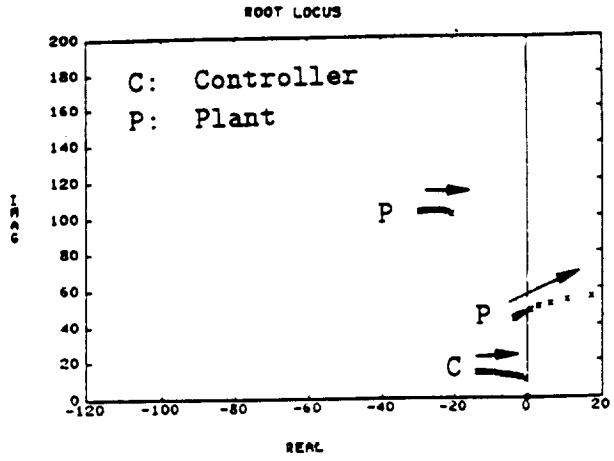

b)

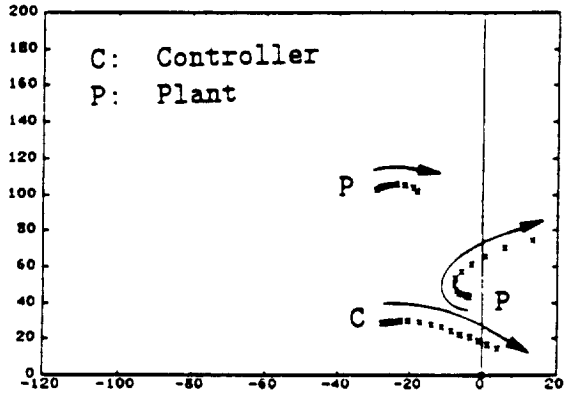

c)

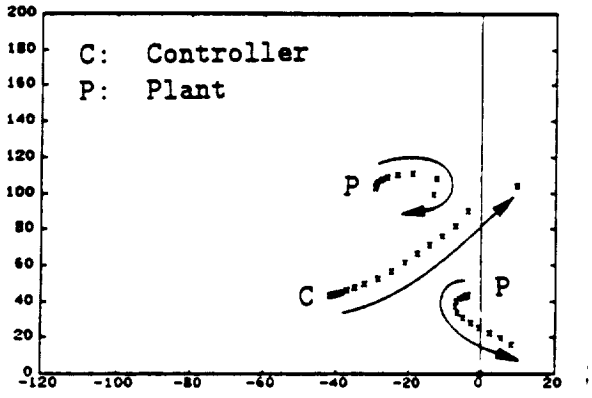

Fig. 6.10: The root locus of the lower link when the strain is fed back through a nonminimum phase allpass filter
a) $\omega_c = 20.$, b) $\omega_c = 40.$, c) $\omega_c = 60.$

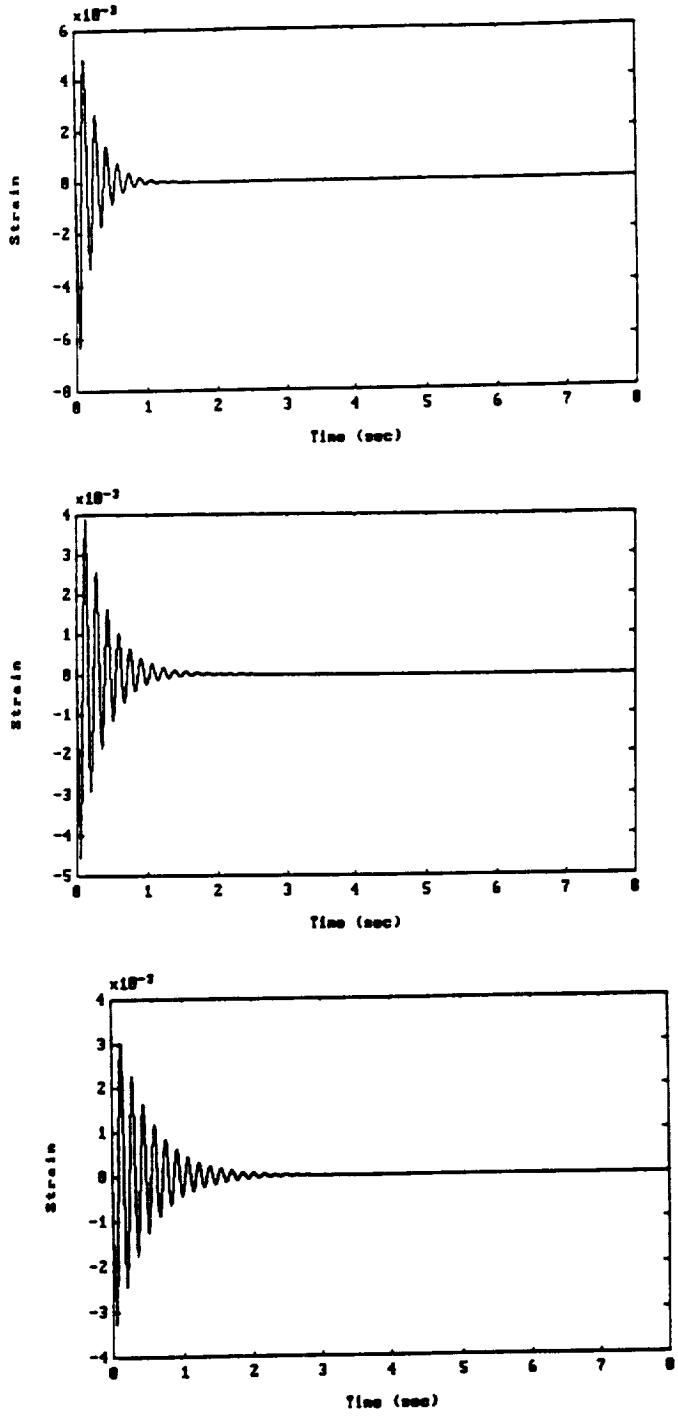

Fig. 6.11: Simulated time response of the upper link when the strain is fed back through a nonminimum phase allpass filter a) $\omega_c = 40$, b) $\omega_c = 80$, c) $\omega_c = 120$

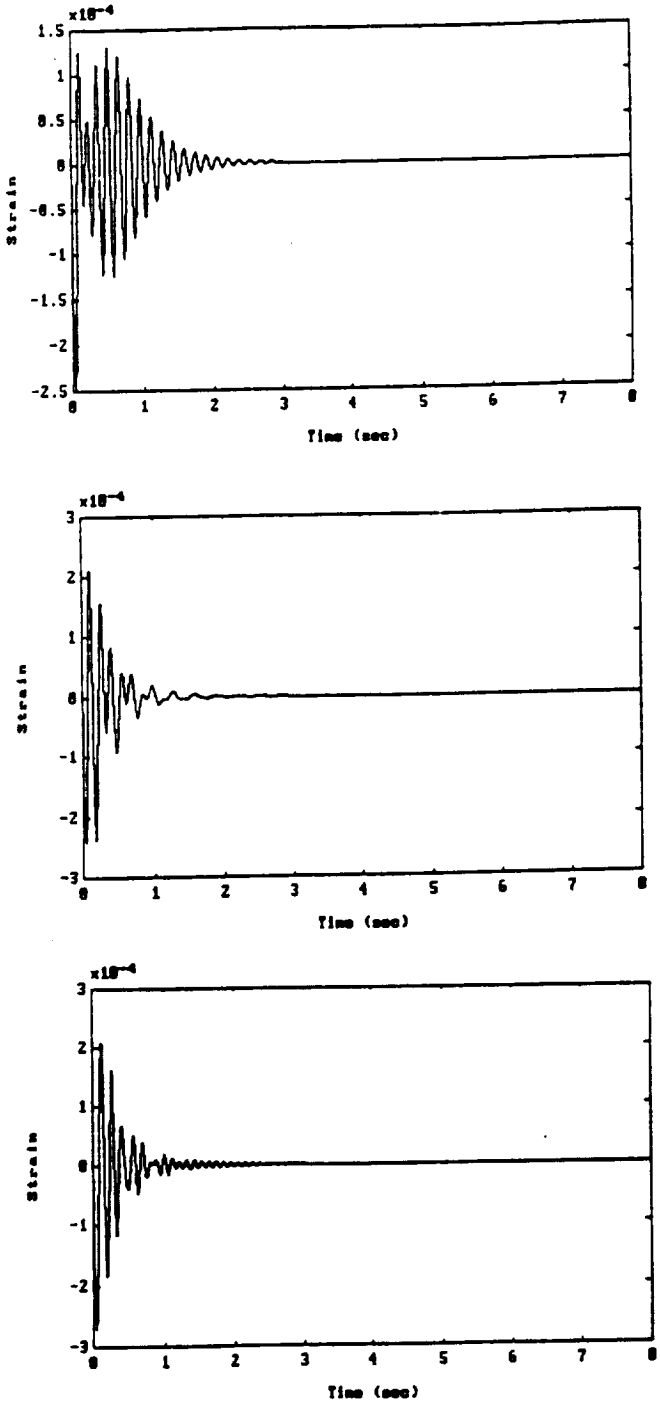

Fig. 6.12: Simulated time responses of the lower link when the strain is fed back through a nonminimum phase allpass filter a) $\omega_c = 20.$, b) $\omega_c = 40.$, c) $\omega_c = 60.$

and Fig. 6.12.b show the best response for the same filter gain ($K_f = 10$).

In experiment, the strain is detected near the connecting points of the hydraulic cylinder and the link (Appendix Fig. 6.11). Fig. 6.1.b, 6.2.b, and 6.3.b show the strain histories of the previous three cases. The beam does not vibrate much except when starting the motion because of current speed limit and smooth cycloid trajectory. In order to magnify the vibration, a faster reference trajectory is chosen. New reference trajectory is 2 *in* move of the lower beam and 1 *in* move of the upper link during 0.1 sec. The controller is also digitized using a bilinear transformation method.

First, the strain is fed back through the phase lead filter. Fig. 6.13.a shows the strain history of the upper link strain when no strain is fed back. As shown in Fig. 6.13.b, the frequency spectrum has two peaks corresponding to the lower and the upper link frequency respectively. Fig. 6.14.a shows the strain history of the upper link when the strain is fed back by the phase lead filter. As shown in Fig. 6.14.b, the peak corresponding to the upper link is significantly reduced. Fig. 6.15.a shows the strain history of the lower link strain when no strain is fed back. As shown in Fig. 6.15.b, frequency spectrum has two peaks corresponding to the lower and the upper link frequency respectively. Fig. 6.16.a shows the strain history of the lower link when the strain is fed back by the phase lead filter. As shown in Fig. 6.16.b, the peak corresponding to the lower link is also reduced. However, a higher gain makes the system unstable. Because the phase lead filter excites higher modes while changing the phase, high gain may excite the unmodelled dynamics. Furthermore, the restriction on $\frac{\omega_p}{\omega_z}$ limits the selection of filter parameters.

Secondly, the strain is fed back through the nonminimum-phase allpass filter to give a proper phase margin without changing the gain. Because this filter does not change the loop gain, it is easy to adjust the filter coefficients and high feedback

gain is possible. Based on the root locus analysis, the filter frequency for the upper link is chosen as 3.0 Hz which is below the upper link frequency (9.8 Hz). The filter frequency for the lower link is chosen as 5.4 Hz which is the same as the lower link frequency (5.4 Hz). The filter damping ratio is chosen as 0.7. Therefore, coefficients of the nonminimum phase allpass filter used are shown in Table 6.3.

Fig. 6.17 and 6.18 show the strain histories and frequency spectrum of the upper link and the lower link when the strain is fed back through the nonminimum phase allpass filter. The filter is designed for each link using the information of the corresponding strain. The vibration is significantly reduced. However, the frequency corresponding to the other link still remains in the time response as shown in Fig. 6.17.a and 6.18.a. Suppression of both frequencies at the same time is difficult because it requires a higher order filter. Furthermore, because the two frequencies have different phase, the phase adjustment for one frequency makes the other frequency unstable.

Until now, each controller is designed independently when only the corresponding link is moved. Next, the responses are measured when the both joints are moved at the same time. Fig. 6.19.a shows the time response of the upper link when no strain is fed back. Fig. 6.19.b shows the corresponding frequency spectrum. However, when the strain is fed back through the nonminimum phase allpass filter, the vibration is significantly reduced as shown in Fig. 6.20. Similarly, the vibration of the lower link also reduced as shown in Fig. 6.21 and Fig. 6.22. Compared to Fig. 6.11.a and Fig. 6.12.b, time responses of each link have more damping because of the structural damping. Furthermore, measured strain has offset due to the gravity effect.

In order to check the robustness to frequency change, the 30 lb payload is attached at the tip. The same type test as above has been performed. Fig. 6.23 and

6.24 show the strain histories of the upper and the lower link respectively when no strain is fed back. By attaching the payload, the frequency of the upper link becomes the fundamental frequency. That frequency is dominant as shown in the both frequency spectra. Fig. 6.25 and 6.26 show the strain histories of the two links when the strain is fed back through the nonminimum phase allpass filter. The original filter makes the system unstable. Even though the gain is reduced to one fourth of filter gain, the strain feedback cannot reduce the vibration. However, by changing the filter frequencies of the upper link slightly, the vibrations are reduced as shown in Fig. 6.27 and 6.28. The filter coefficients of the upper link are changed as shown in Table 6.4. However, the better response is hard to obtain just by the filtering technique because the two system frequencies are close together when the payload is attached. Fig. 6.29, 6.30, and 6.31 show the strain histories when strain is fed back through the nonminimum phase allpass filter. These use the same trajectory as Fig. 6.1, 6.2, and 6.3.

6.3 Conclusion

The independent control scheme using position and strain is applied for the control of RALF. Position feedback with a lag compensator is successfully implemented for the rigid body motion control. However, the direct strain feedback does not reduce the vibration. For the vibration suppression, a phase lead and a nonminimum phase allpass filter are used. In experiment, a nonminimum phase allpass filter is easier to implement than a phase lead filter. As shown in strain histories of an analytical model and experiment, the proper filter frequencies can be selected using root locus. Therefore, even though there is a limitation in using these filters for a system with changing frequencies, the beam vibration is reduced significantly

Table 6.3: Nonminimum phase allpass filter coefficients

	Lower	Upper
Gain	50.	80.
ω_p	5.4	3.
ω_z	5.4	3.
ζ_p	0.7	0.7
ζ_z	-0.7	-0.7

Table 6.4: Nonminimum phase allpass filter coefficients when the payload is attached

	Lower	Upper
Gain	12.	20.
ω_p	5.4	1.
ω_z	5.4	1.
ζ_p	0.7	0.7
ζ_z	-0.7	-0.7

by the nonminimum phase allpass filter. The sensitivity to payload variation is pronounced, however and is a deterrent to using the allpass filter in manipulator control.

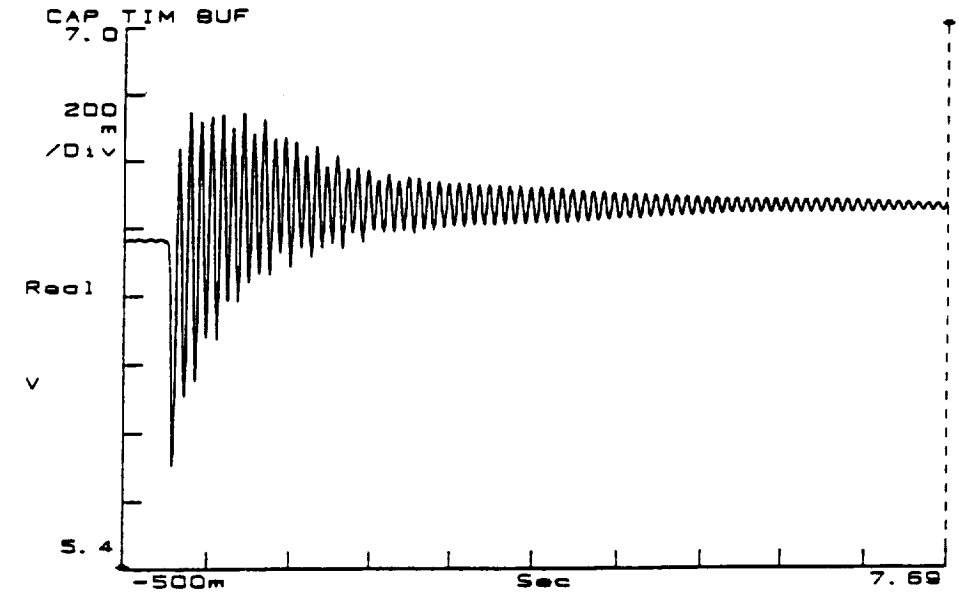

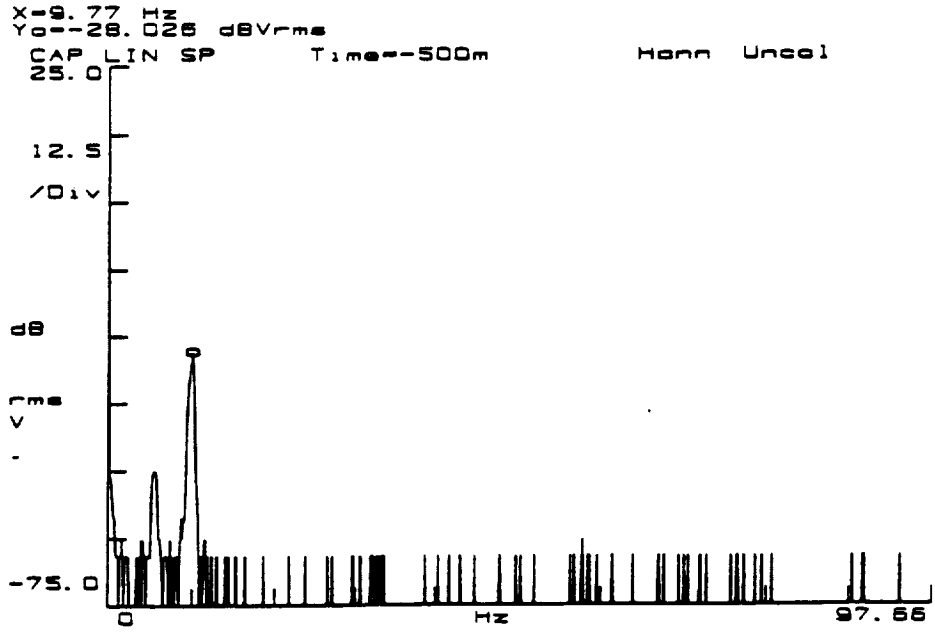

Fig. 6.13: Measured time history and frequency spectrum of the upper link strain when no strain is fed back

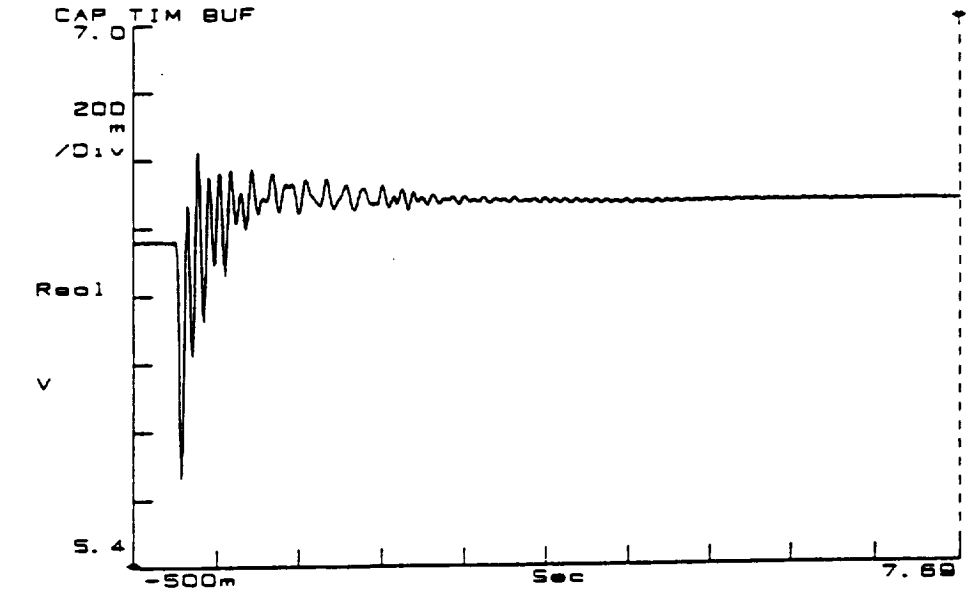

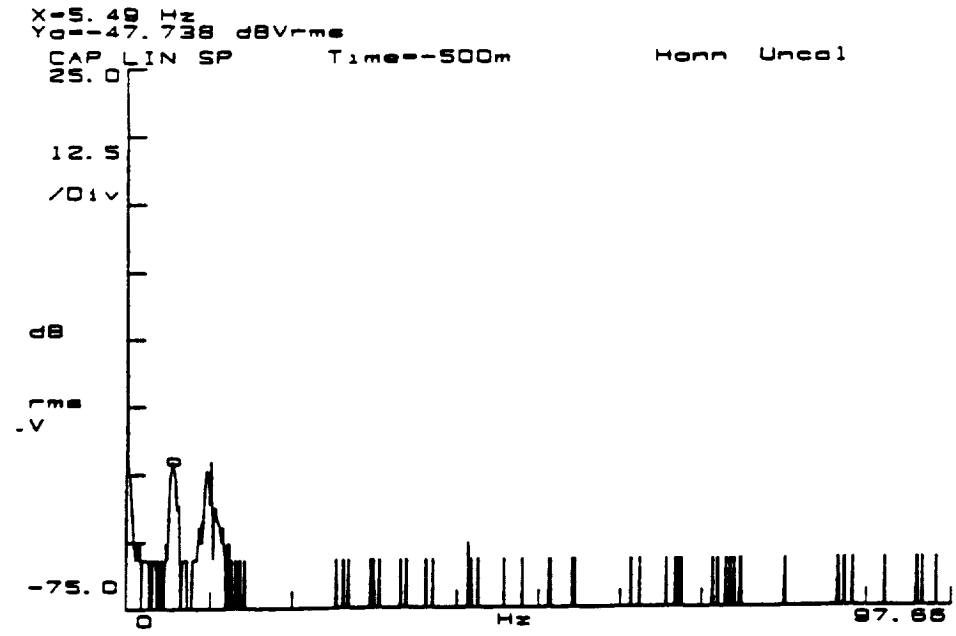

Fig. 6.14: Measured time history and frequency spectrum of the upper link strain when strain is fed back through a phase-lead filter

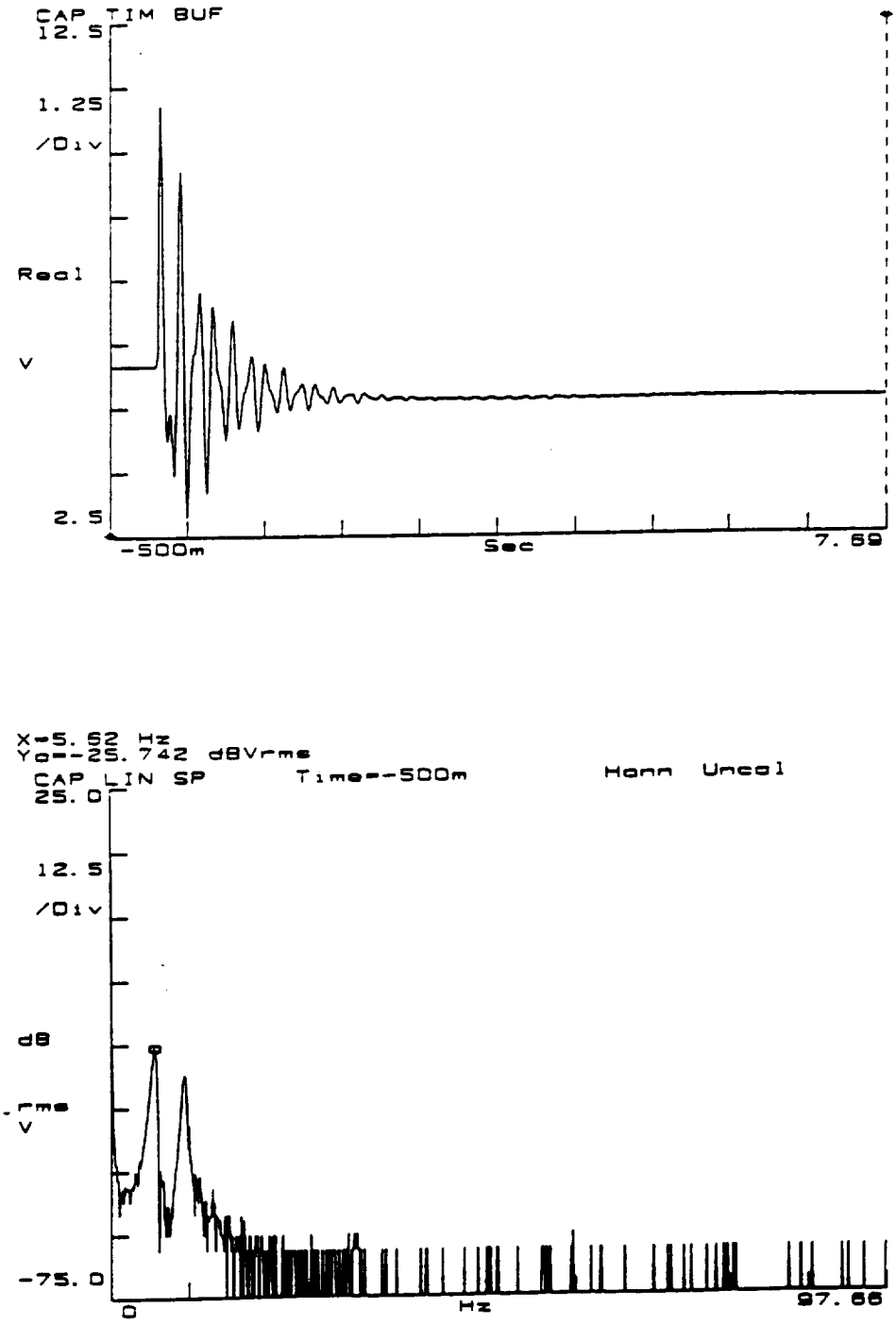

Fig. 6.15: Measured time history and frequency spectrum of the lower link strain when no strain is fed back

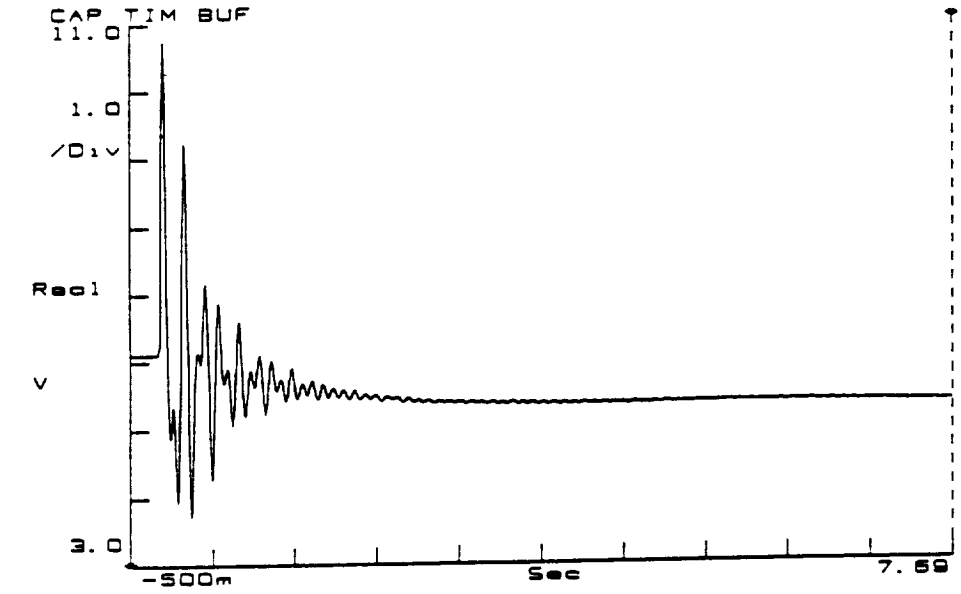

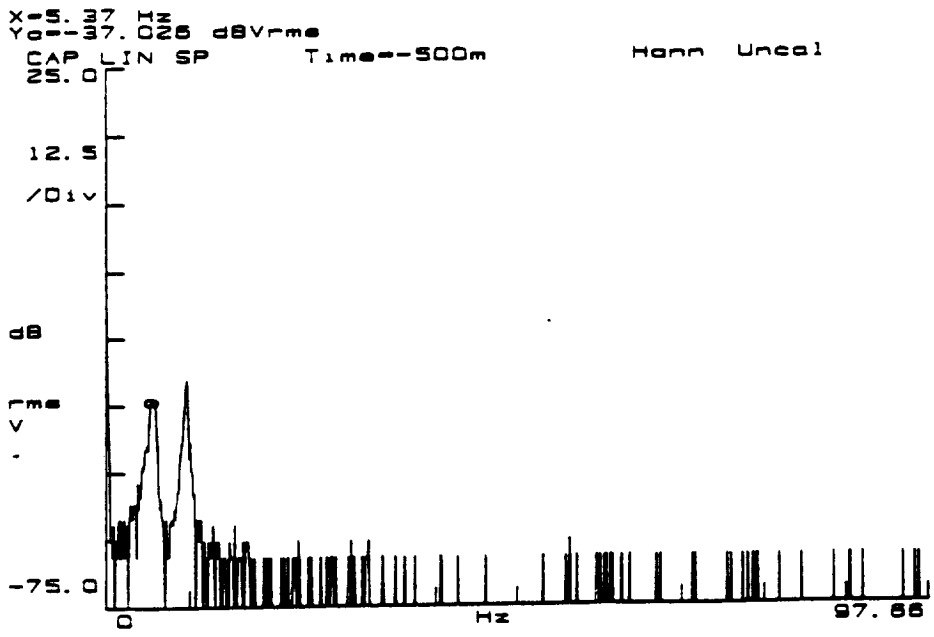

Fig. 6.16: Measured time history and frequency spectrum
of the lower link strain
when strain is fed back through a phase-lead filter

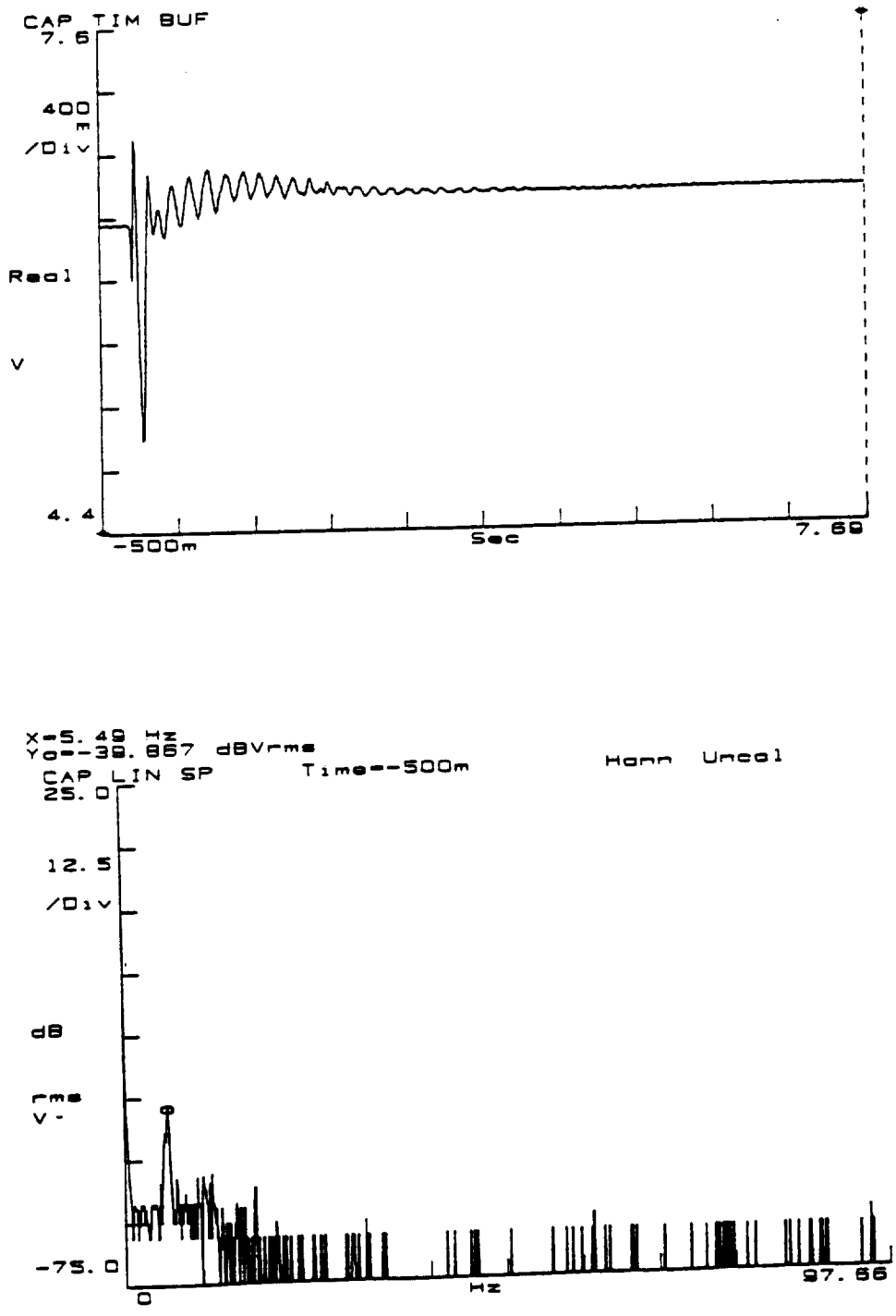

Fig. 6.17: Measured time history and frequency spectrum
of the upper link strain
when strain is fed back through a nonminimum-phase allpass filter

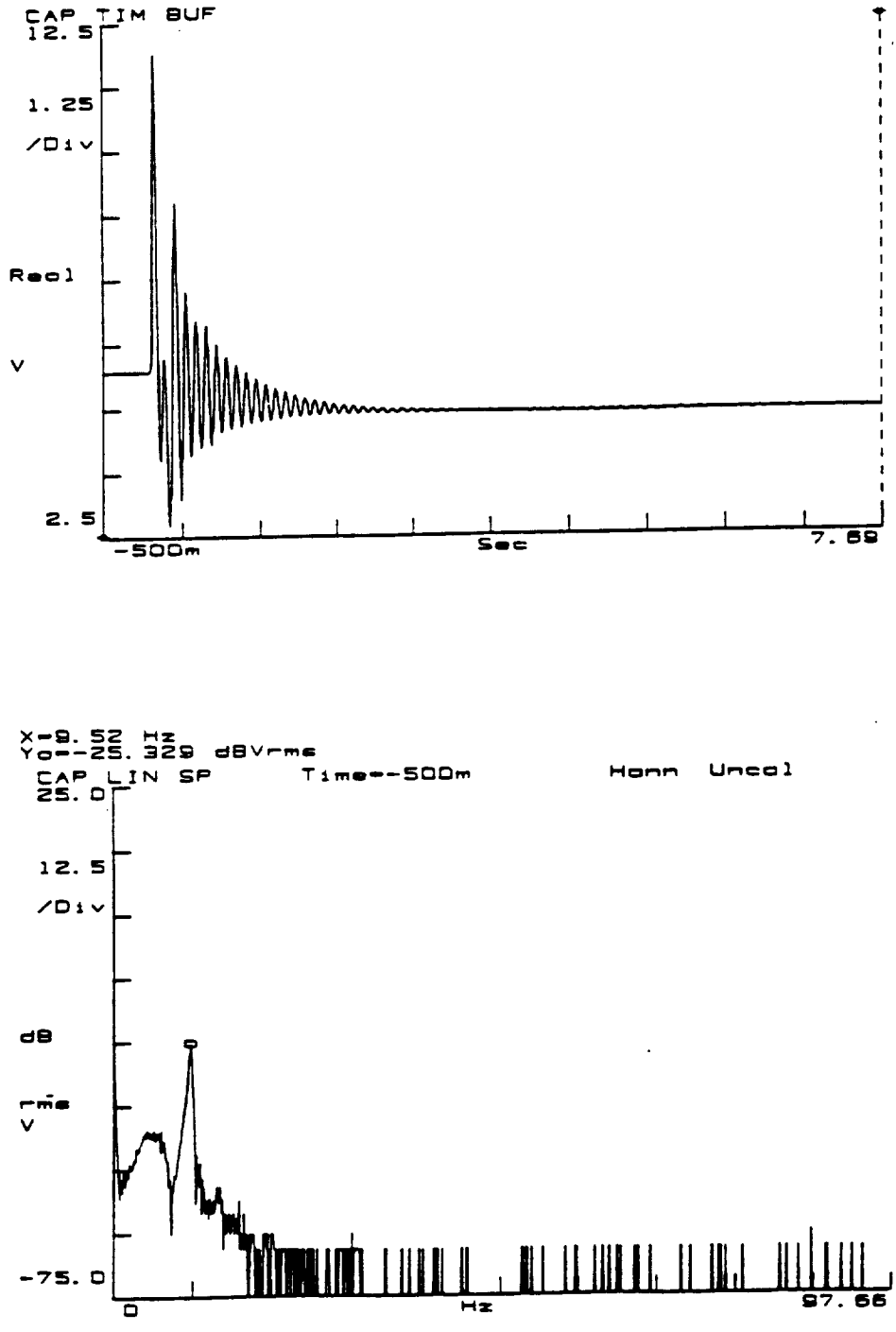

Fig. 6.18: Measured time history and frequency spectrum
of the lower link strain
when strain is fed back through a nonminimum-phase allpass filter

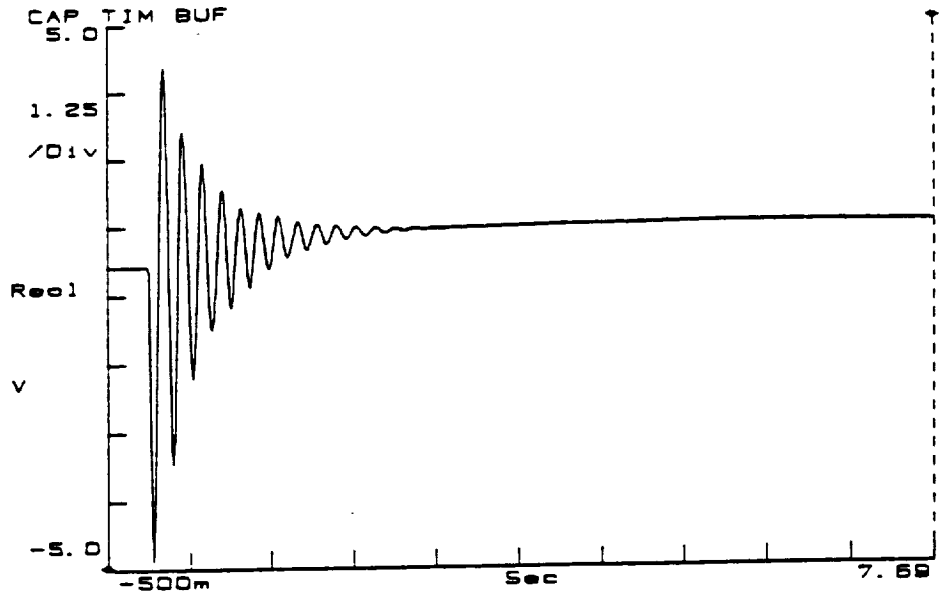

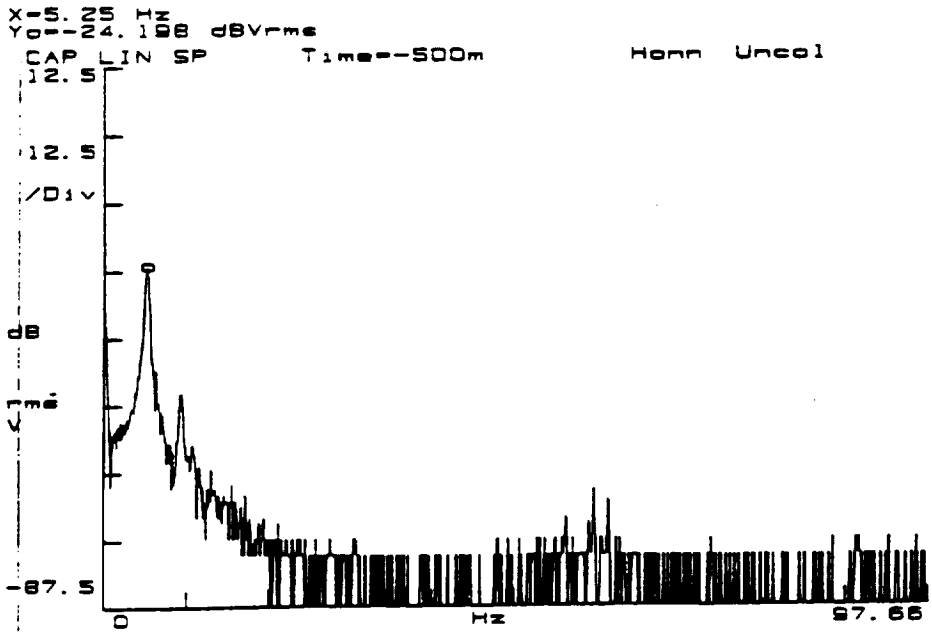

Fig. 6.19: Measured time history and frequency spectrum of the upper link strain when no strain is fed back (both joints move)

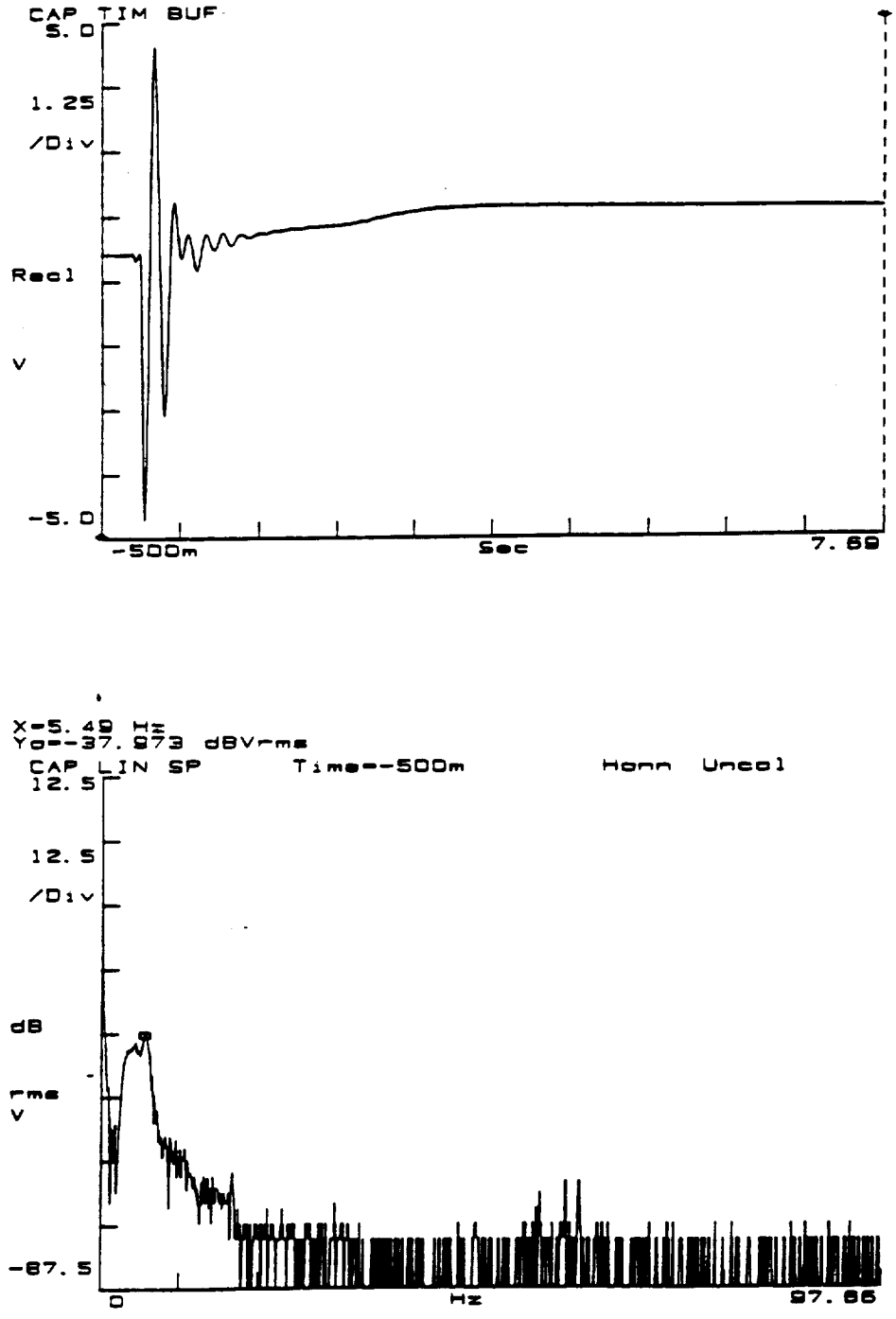

Fig. 6.20: Measured time history and frequency spectrum
of the upper link strain
when strain is fed back through a nonminimum-phase allpass filter
(both joints move)

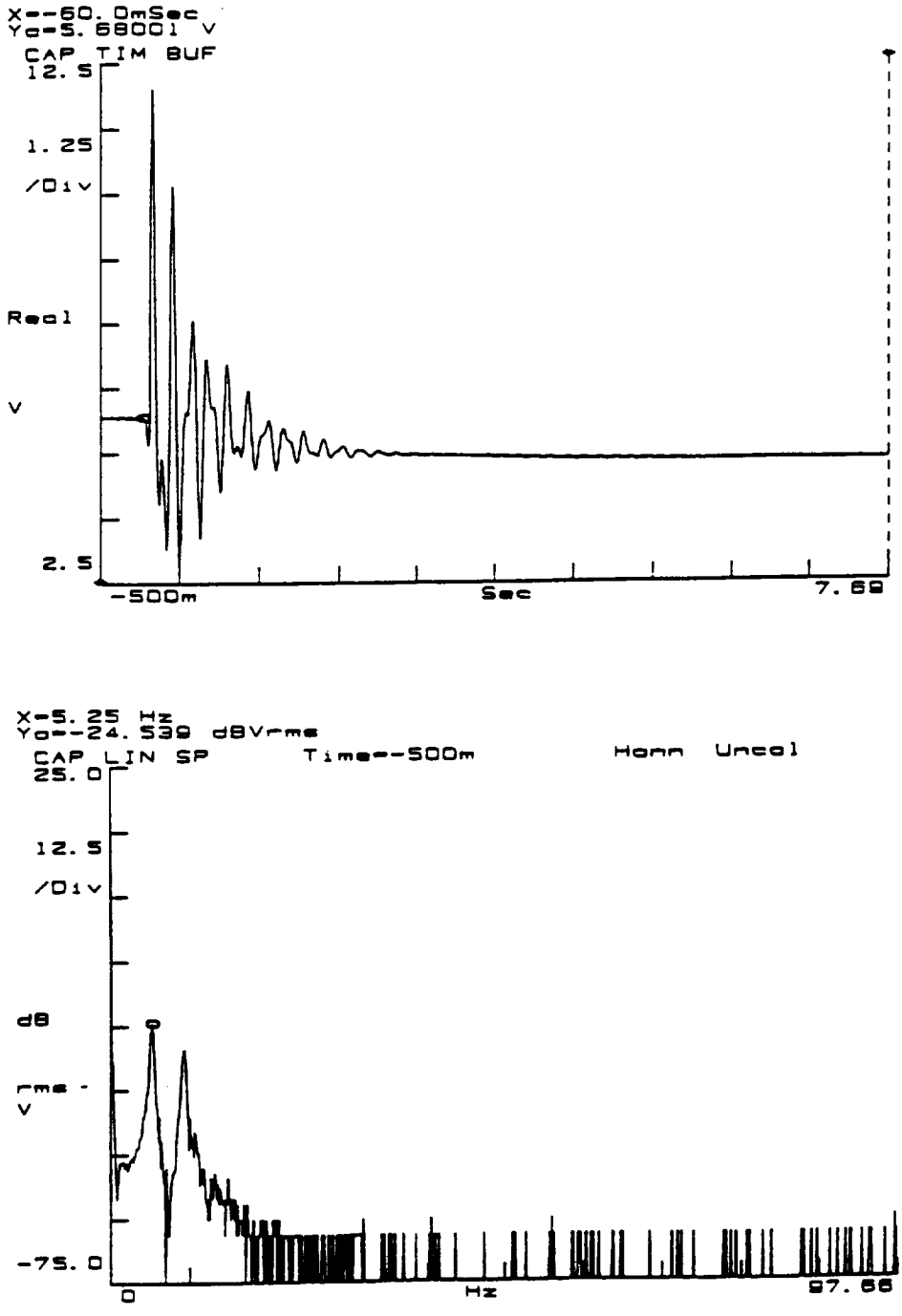

Fig. 6.21: Measured time history and frequency spectrum of the lower link strain when no strain is fed back (both joints move)

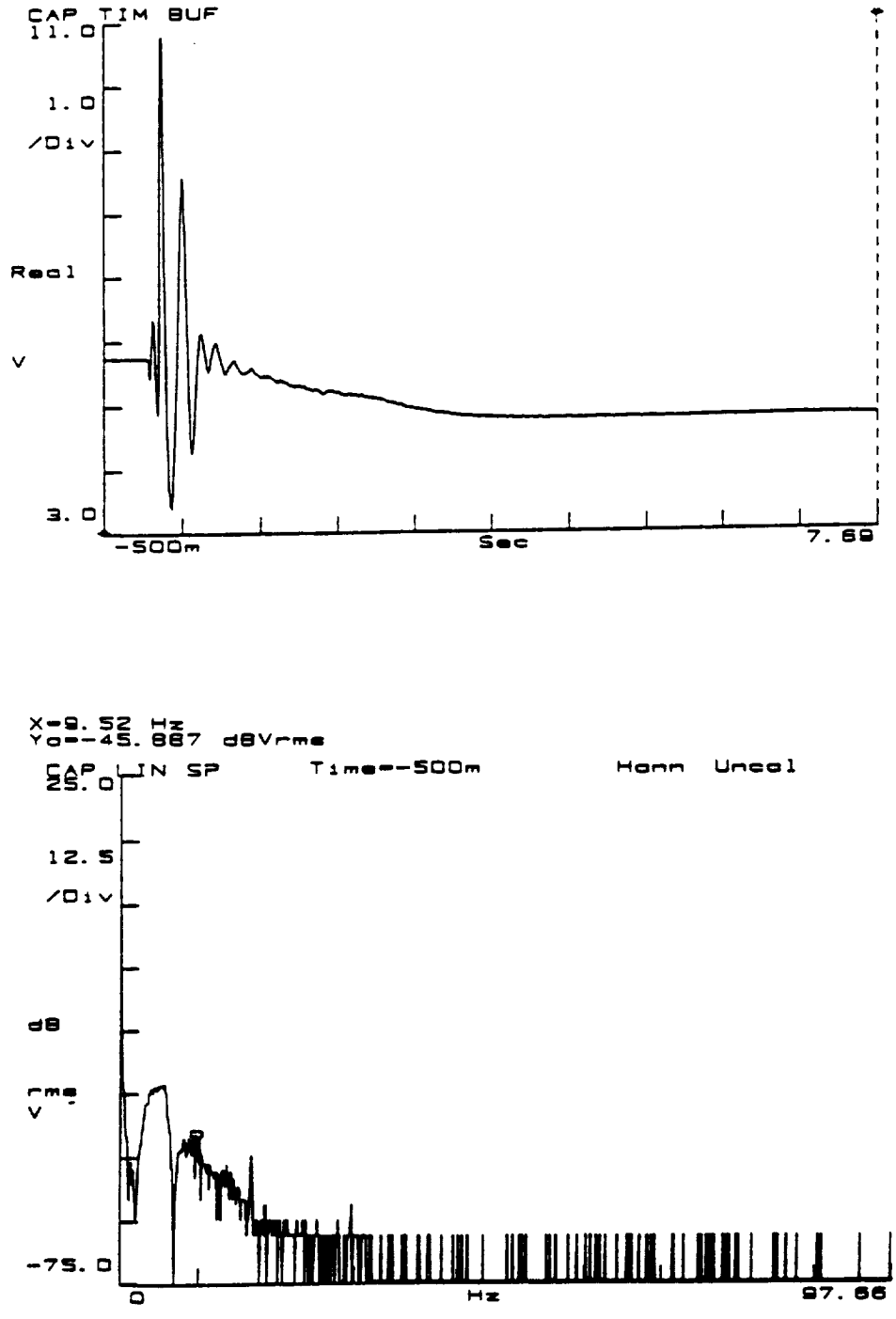

Fig. 6.22: Measured time history and frequency spectrum
of the lower link strain
when strain is fed back through a nonminimum-phase allpass filter
(both joints move)

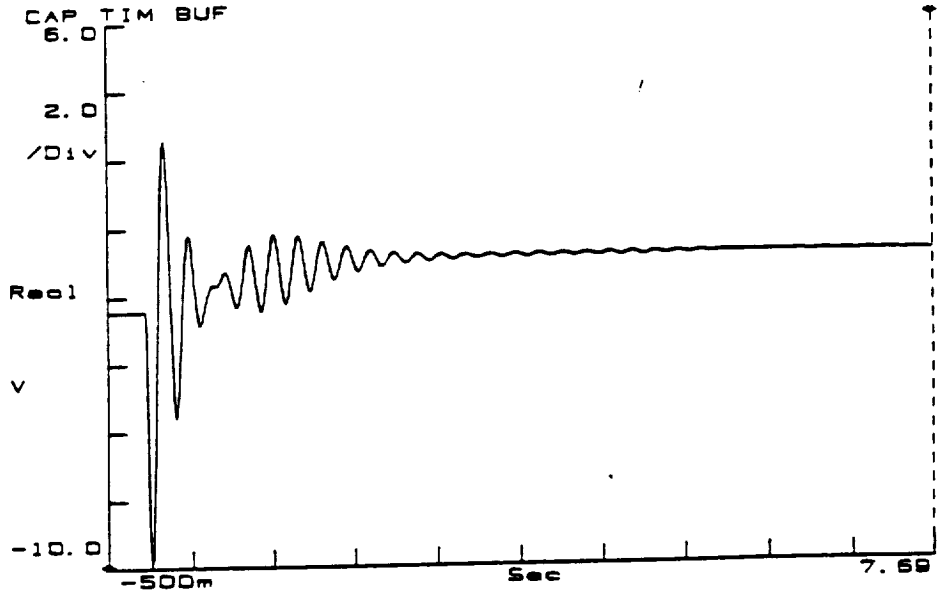

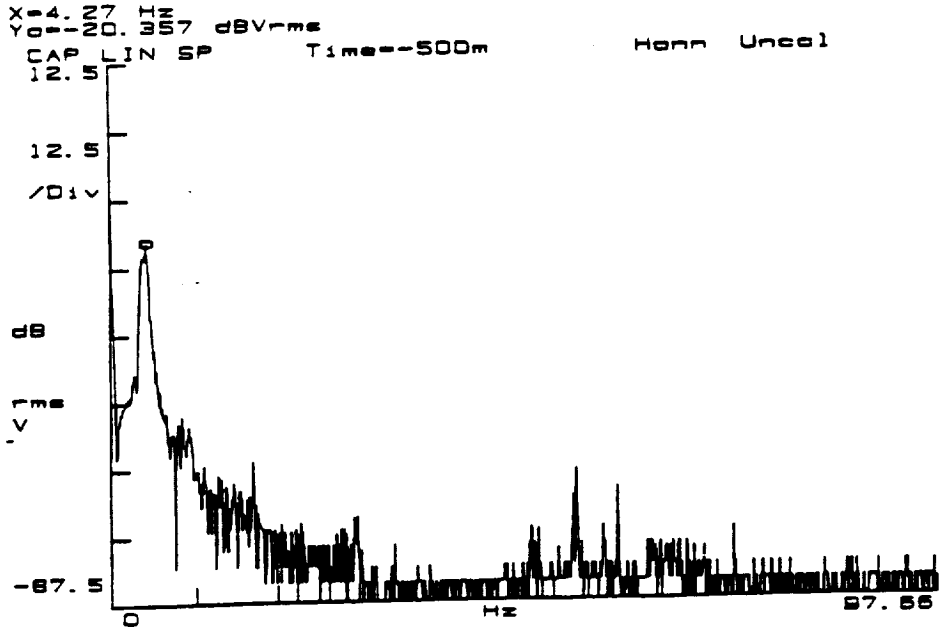

Fig. 6.23: Measured time history and frequency spectrum
of the upper link strain
when no strain is fed back
(both joints move & payload)

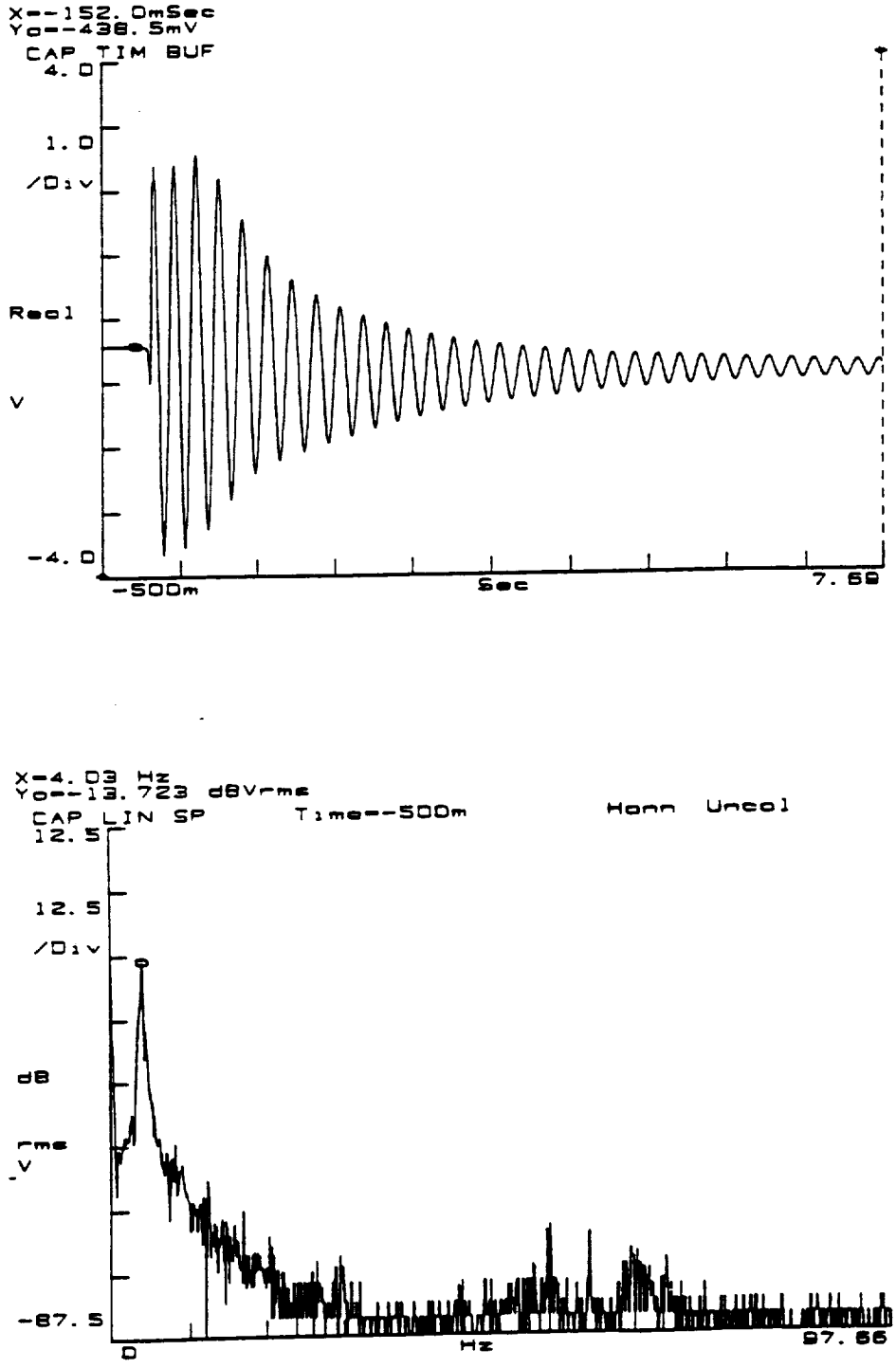

Fig. 6.24: Measured time history and frequency spectrum
of the upper link strain
when strain is fed back through a nonminimum-phase allpass filter
(both joints move & payload)

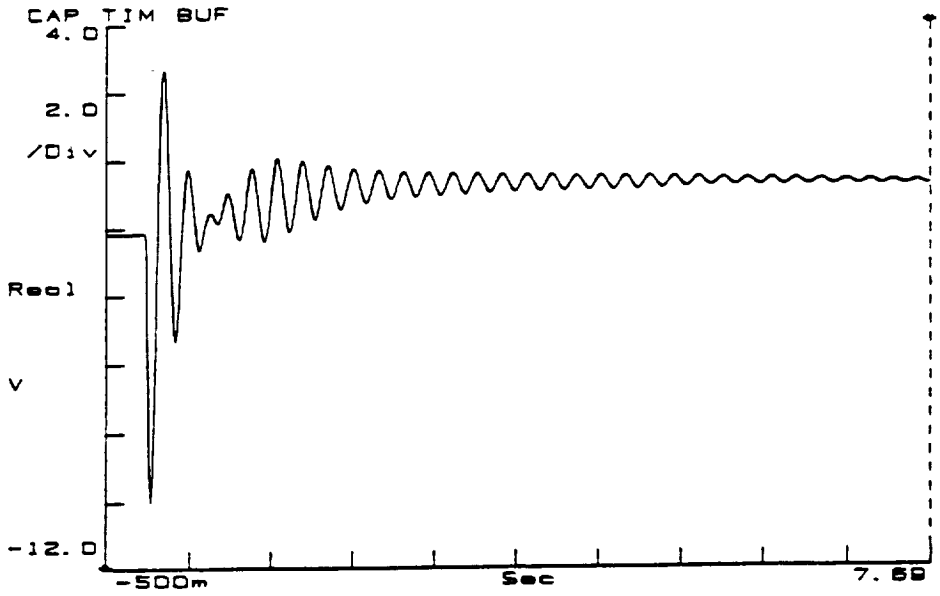

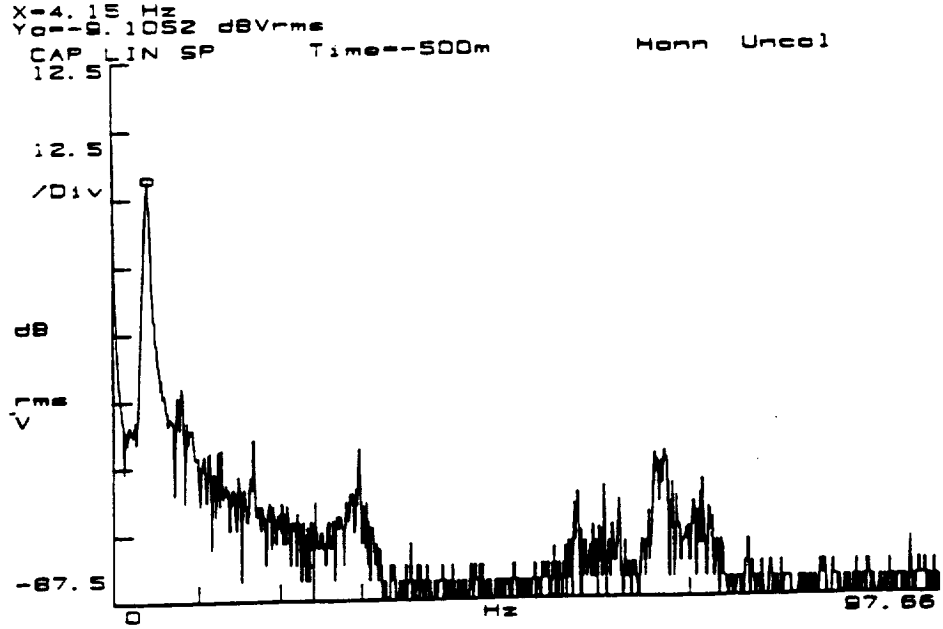

Fig. 6.25: Measured time history and frequency spectrum
of the lower link strain
when no strain is fed back
(both joints move & payload)

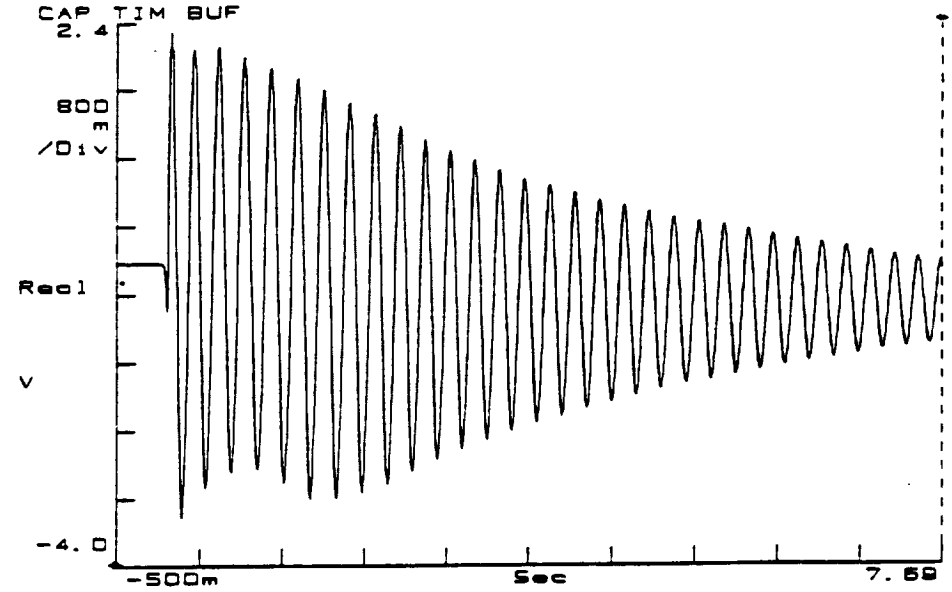

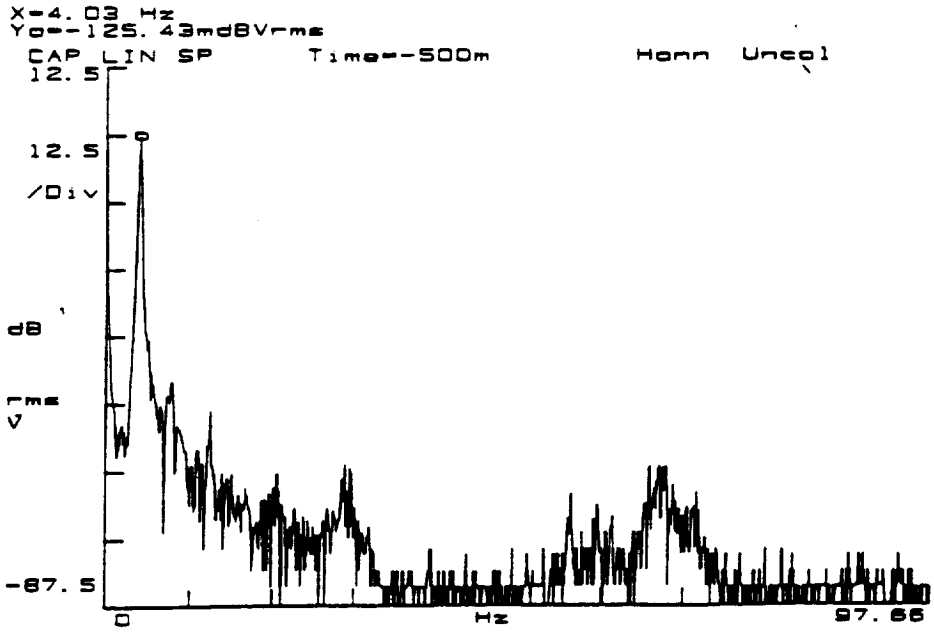

Fig. 6.26: Measured time history and frequency spectrum
of the lower link strain
when strain is fed back through a nonminimum-phase allpass filter
(both joints move & payload)

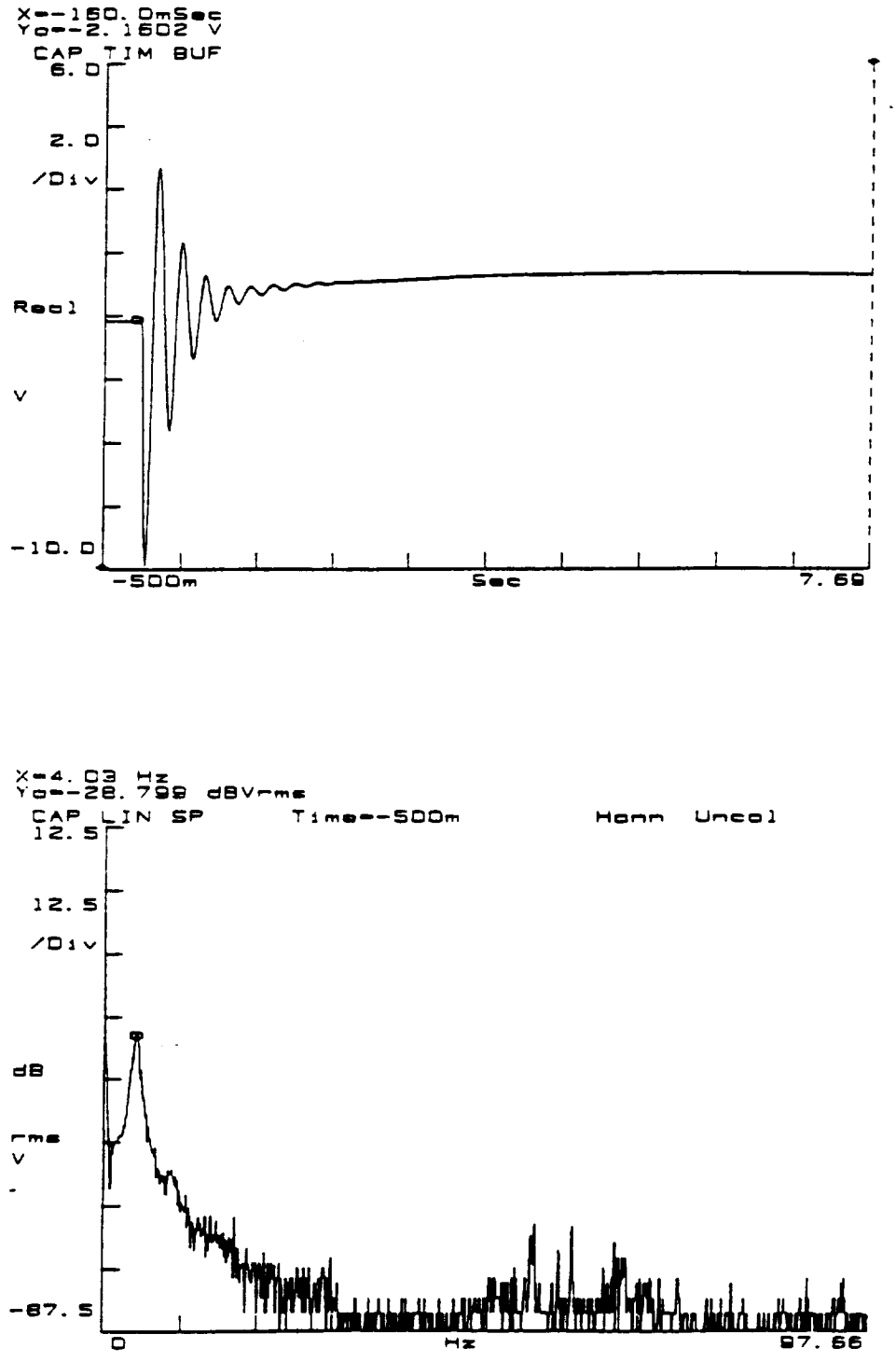

Fig. 6.27: Measured time history and frequency spectrum
of the upper link strain
when strain is fed back through an adjusted nonminimum-phase
allpass filter (both joints move & payload)

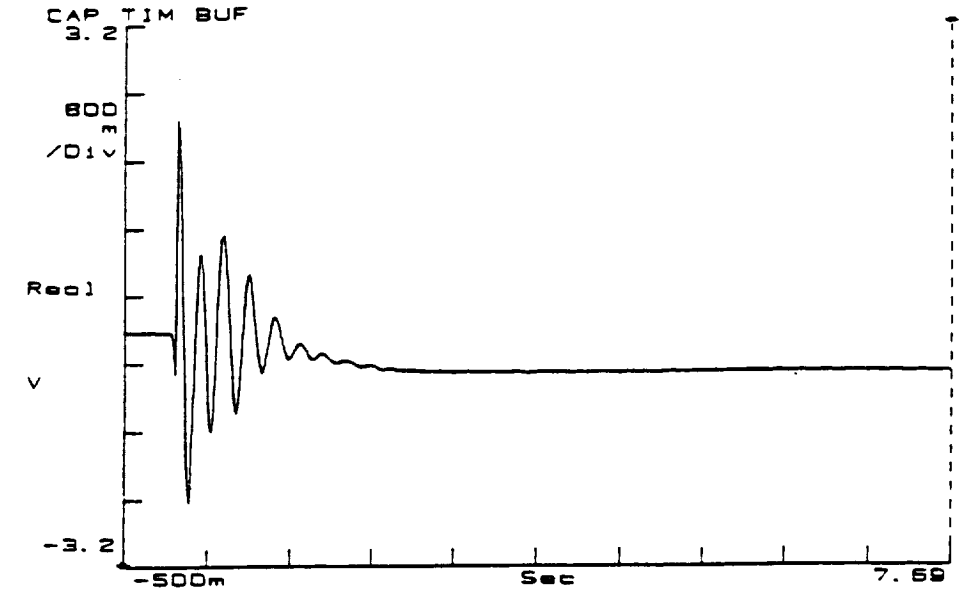

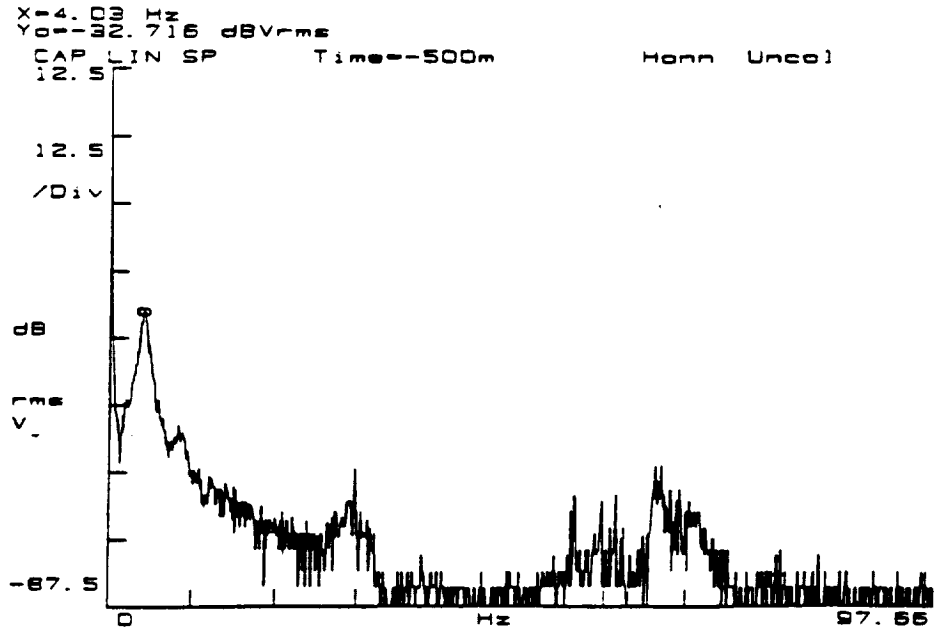

Fig. 6.28: Measured time history and frequency spectrum
of the lower link strain
when strain is fed back through an adjusted nonminimum-phase
allpass filter (both joints move & payload)

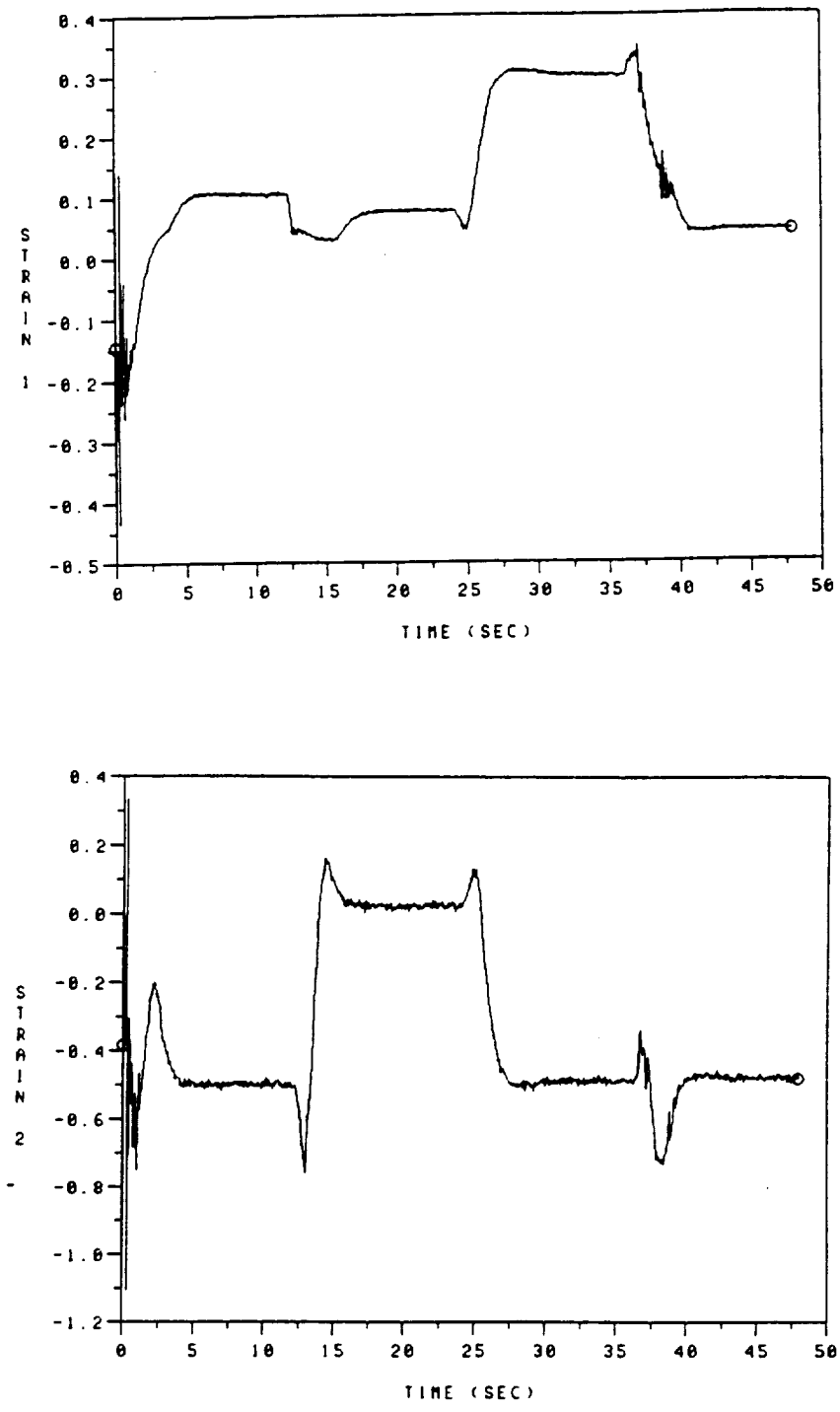

Fig. 6.29: Measured time histories
of the upper and the lower link strain
when strain is fed back through a nonminimum-phase allpass filter
(both joints move & small motion)

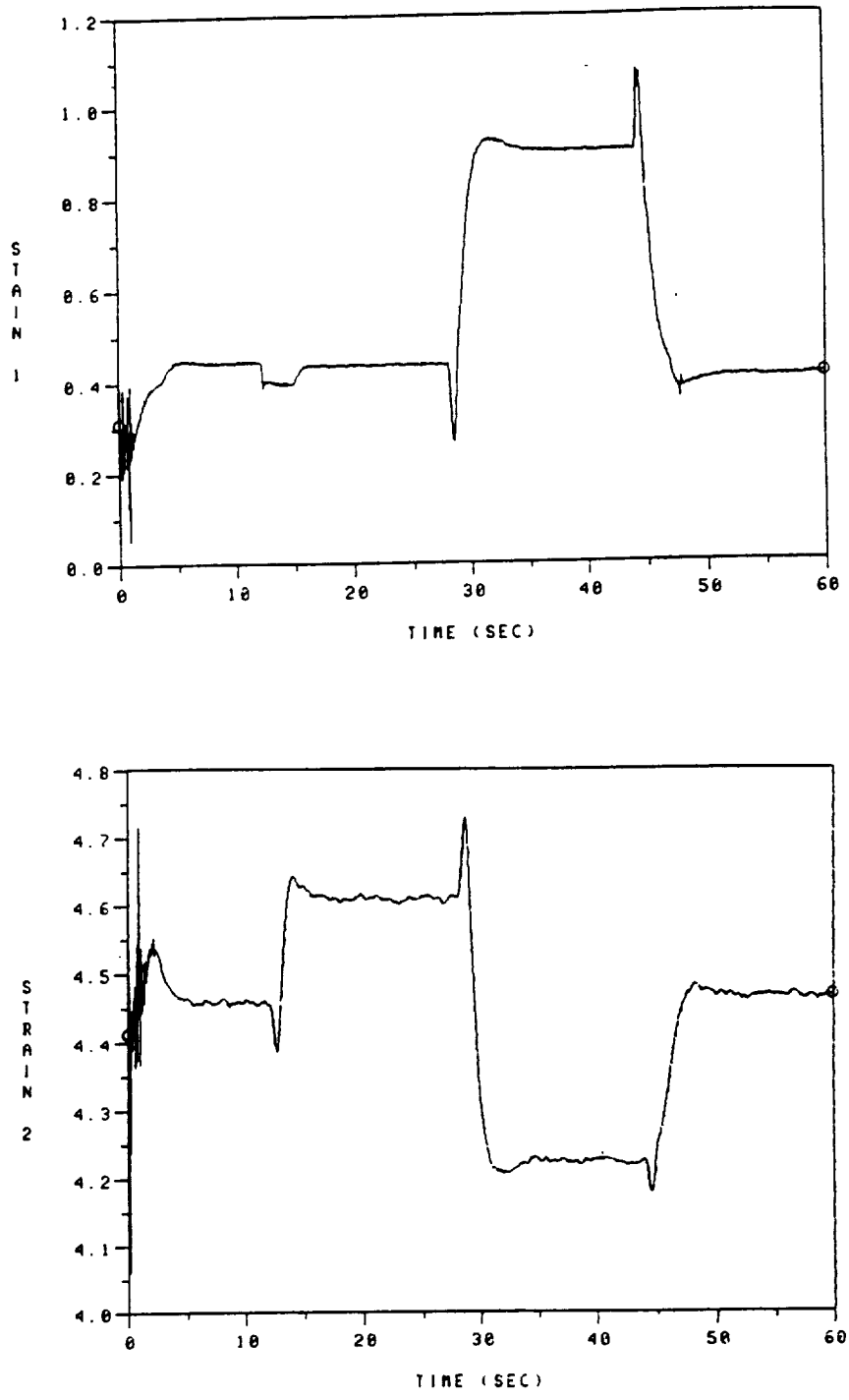

Fig. 6.30: Measured time histories
of the upper and the lower link strain
when strain is fed back through a nonminimum-phase allpass filter
(both joints move & large motion)

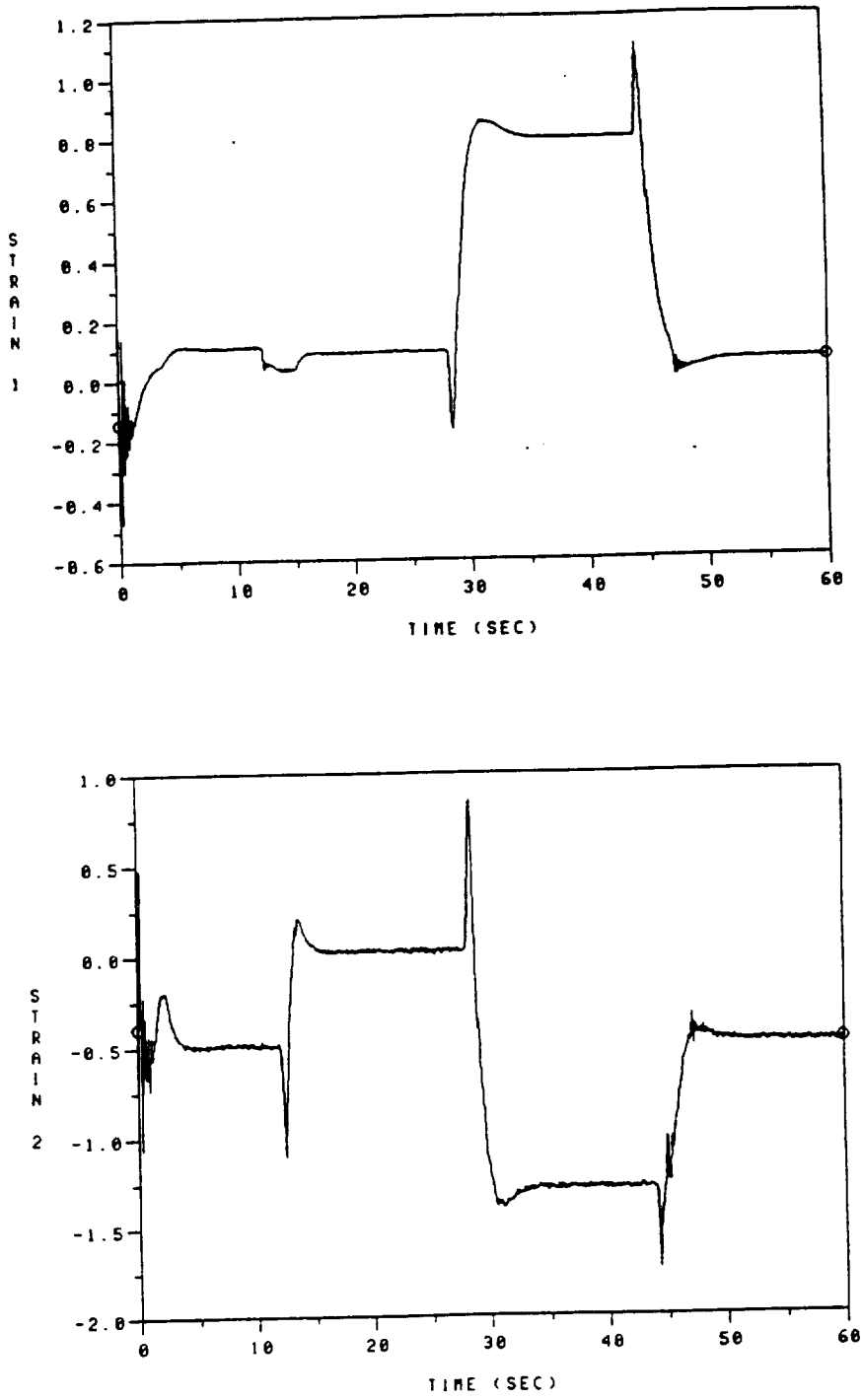

Fig. 6.31: Measured time histories
of the upper and the lower link strain
when strain is fed back through a nonminimum-phase allpass filter
(both joints move & large motion & payload)

CHAPTER VII

Summary and Future Work

7.1 Summary

For the purpose of exploring possible industrial applications, a large lightweight manipulator was previously constructed at the Flexible Automation Laboratory of the Georgia Institute of Technology. For added payload capacity, the flexible parallel mechanism is added to sustain the load without increasing weight very much. If RALF is assumed as rigid, the dynamics of RALF can be easily analyzed using the theories which have been developed for rigid robots. However, in a flexible robot, there are several problems which are not observed in a rigid robot. In this thesis, solutions of these problems are evaluated. This section briefly summarizes the important observations and results of the previous sections.

First, the dynamic equations of motion of flexible robots are complicated because of the link deformation which is expressed by the summation of admissible functions. The existing symbolic method generates complicated equations of motion. This thesis develops a structurally well organized and computationally efficient form of the equations of motion using the Jacobian matrix. The Jacobian matrices are derived from the position vectors directly using the MJac function of SMP. Using this Jacobian matrix, the mass matrices and the gravity force vectors are derived. The velocity coupling terms are derived from the mass matrices using the Christoffel symbol. One problem of this method is that the velocity coupling terms comprise

many elements. However, using some structural properties, such as symmetry and reflective coupling, these elements can be expressed by a few parameters. The resulting equations of motion have a structure which is useful to reduce the number of terms to be calculated, to check correctness, or to extend the model to higher order.

Secondly, the parallel link mechanism with flexible links requires nonlinear algebraic constraint equations to describe the relationship between angles within the closed loop chain. Therefore, a mixed set of differential equations and algebraic equations must be solved simultaneously for the constrained system dynamics. Because the integration of these equations is sensitive to numerical error, the conventional numerical methods are not adequate to solve these equations. Among several methods available to solve these numerical difficulties, a coordinate partitioning method is used in this thesis. The generalized coordinates are transformed to a set of independent coordinates on the tangent hyperplane of the constraint surface. The transformation matrix used is the null space matrix of the constraint Jacobian matrix which can be derived by the singular value decomposition. Because the Lagrange multiplier is eliminated from the equations of motion by the transformation, the constraint forces do not affect the motion on the constraint surface and only maintain the system on the constraint surface. Therefore, numerical integration on the tangent hyperplane does not result in significant constraint violation. This thesis applies this constrained system analysis technique to a flexible parallel link mechanism. It is numerically verified that the SVD method is a stable algorithm to solve a constrained system.

Third, mode shape functions are employed to describe the elastic deformation of the flexible manipulator. In the assumed mode method, mode shape functions need only to be admissible functions which satisfy the geometric boundary conditions.

However, a large number of modes are required to obtain accurate frequencies. The number of modes to be included can be reduced by choosing appropriate functions which satisfy static equilibrium at the interface between the links. These functions can be derived systematically using component mode synthesis. Various component mode synthesis approaches have been developed depending on the assumed boundary condition. Different boundary condition assumptions require different coordinate systems to describe the elastic deformation. Therefore, the method which fits with the current coordinate system was chosen. In this thesis, proper mode shape functions for a reduced order model of RALF are obtained using the loaded interface component mode synthesis method. Comparison between the finite element model, the component mode synthesis model, and the analytical model of RALF show that the mode shape functions which are determined by component mode synthesis improve the convergence. However, there are some discrepancies between the analytic model and the experiment because the real system has a complex structure which is difficult to analyze with the analytical method. For example, the upper link requires a detailed model to predict the better approximate boundary condition. These discrepancies are explained using a simplified and a detailed finite element model in this thesis.

Fourth, a direct comparison between the analytical model and the real system was difficult because of the unmodelled dynamics and the parameter uncertainty of the real system. Therefore, as an intermediate step, a general multibody flexible dynamics code - TREETOPS - was used for the verification. The step response of the models match each other very well.

Fifth, it is an important job for control to detect the degree of the nonlinearity in the dynamics. In this thesis, the nonlinearity of RALF is studied using a sinusoidal excitation. As shown in the phase plot and power spectra, the flexibility effect in

nonlinear dynamics is significant. However, the nonlinearity of RALF is not fully excited due to the speed limitation of the hydraulic cylinder.

Sixth, the actuator dynamic effect on the flexible robot was investigated. Even though the electric motor and the hydraulic motor have the same form of dynamic equations, their effect on the flexible robot is different due to the difference of their system parameters. In this thesis. the effects of an actuator dynamics on a flexible robot are analyzed by root loci and Bode plots, both theoretically and experimentally.

Seventh, in order to show the base performance for an advanced control, this thesis uses a decentralized control scheme using cylinder position and beam strain for trajectory following and vibration suppression. The rigid body motion is controlled by the position feedback using a lag compensator. The beam vibration is reduced significantly by strain feedback using the nonminimum phase allpass filter. Using these simple controllers, a good result is obtained.

7.2 Future Work

First, the proposed derivation method of equations of motion using Jacobian matrix has been applied only to a two joint planar system, RALF. Furthermore, some procedures for deriving the velocity coupling terms are not computerized. In the future, an even more computerized derivation method is required for multi-link flexible body dynamics.

Secondly, one problem of a coordinate partitioning method is the preservation of continuity in the basis of the nullspace. Since the constraint Jacobian matrix is time-varying, the basis of the nullspace which forms a basis orthogonal to the tangent plane of the constraint surface is also time-varying. However, performing

singular value decomposition at each integration step would result in a tremendous increase in computing time and requires numerical integration algorithms which use information only from the current step. To overcome this problem, Liang and Lance [39] proposed a differentiable null space method. This method generates a set of independent coordinates that are on the constraint surface rather than only on the tangent hyperplane. Another solution is the modification of the constraint violation method. Chang and Nikravesh [16] applied an adaptive algorithm to stabilize the violation. Park and Haug [57] developed a hybrid numerical method which combines a constraint stabilization method and a generalized coordinate partitioning method. As we can see here, the subject of numerical methods for solving a mixed set of algebraic and differential equations is still an open research area.

Third, mode shape functions of RALF were derived by hand calculation using component mode synthesis method from the output of MSC/PAL. An computerized program is required for different configurations of the structure. Furthermore, natural frequencies and modes of the system can be varied due to several effects - payloads, contact with the environment, joint position and velocity feedback gains [11]. The study of these uncertainties will require much work in the future.

Fourth, nonlinear dynamics verification is a difficult job and has not been fully studied. Chaotic vibration theory might be useful to study the nonlinear vibration [50].

Fifth, as mentioned before, there are some uncertainties in the dynamic model of the flexible robot under the current theories. Furthermore, the system dynamics has a strong interaction with the controller output because it changes the boundary condition of the beam. Therefore, control schemes which are sensitive to the model uncertainty are difficult to apply. Furthermore, even the characteristics of the linear control of the multi-link flexible robot have not fully been studied. Root loci help us

to understand the control characteristics of the flexible robot [7]. The combination of state space and frequency domain techniques through a model update procedure has been shown effective in determining the feedback gains of the flexible robot [9]. Recently, a frequency domain analysis of a multi input and multi output system has been studied [44,20] in many areas. Especially, the *Multivariable Frequency Domain Toolbox* of *Matlab* [12] implements several frequency domain design techniques such as the Nyquist Array method, the Characteristic Locus method, the Quasi- Classical Design method, and the Multivariable Root Locus method. Using these computer aided design techniques, better studies on the linear control of the multi -link flexible robot can be expected.

APPENDIX A

Derivation of Equations of Motion using Jacobian Matrix

In this appendix, a Lagrangian method is used to derive the equations of motion for a flexible robot. The Jacobian matrices are used to derive the mass matrices and gravity force vectors. The coefficients of centrifugal and Coriolis force are derived from the mass matrices.

The total kinetic energy of an elastic link can be written as

$$T = \frac{1}{2}\sum_{p=1}^{b}\int_0^{l_p} \dot{r}_p^T \dot{r}_p \rho_p A_p dx_p \tag{A.1}$$

where b is the number of links, $\dot{r}_p$ is the velocity vector of any point on the elastic link p, and ρ_p, A_p, l_p are the density, the area, and the length of link p respectively. The velocity vector can be expressed by the Jacobian matrix and generalized velocity vectors $\dot{q}_p$.

$$\dot{r}_p = J_p \dot{q}_p \tag{A.2}$$

Substitute (A.2) into (A.1),

$$\begin{aligned} T &= \frac{1}{2}\sum_{p=1}^{b}\int_0^{l_p} (J_p\dot{q}_p)^T (J_p\dot{q}_p)\rho_p A_p dx_p \\ &= \frac{1}{2}\sum_{p=1}^{b} \dot{q}_p^T \left(\int_0^{l_p} J_p^T J_p \rho_p A_p dx_p\right)\dot{q}_p \end{aligned} \tag{A.3}$$

Equation (A.3) can be written in a scalar form as

$$T = \frac{1}{2}\sum_{i=1}^{n}\sum_{j=1}^{n}\left(\sum_{p=1}^{b} D_{ijp}\right)\dot{q}_i\dot{q}_j \tag{A.4}$$

where n is the number of the generalized coordinates, D_{ijp} is ij element of the mass matrices $\int_0^{l_p} J_p^T J_p \rho_p A_p dx_p$ for the pth link. If M_{ij} is defined as

$$M_{ij} = \sum_{p=1}^{b} D_{ijp} \tag{A.5}$$

Equation (A.4) can be written as follows

$$T = \frac{1}{2} \sum_{i=1}^{n} \sum_{j=1}^{n} M_{ij} \dot{q}_i \dot{q}_j \tag{A.6}$$

The potential energy due to gravity is

$$U_g = \sum_{p=1}^{b} \int_0^{l_p} g^T r_p \rho_p A_p dx_p \tag{A.7}$$

where g is the 3 x 1 gravity acceleration vector. The potential energy due to elastic deformation is

$$U_e = \frac{1}{2} \sum_{p=1}^{b} \int_0^{l_p} E_p I_p (\frac{\partial^2 u_p}{\partial x_p^2})^2 dx_p \tag{A.8}$$

where E is Young's modulus of elasticity, and I is the area moment of inertia. u is the elastic deflection which can be expressed by m modes and modal coordinates.

$$u_p(x,t) = \sum_{k=1}^{m} \psi_{pk}(x) \xi_{pk}(t) \tag{A.9}$$

Therefore, the elastic energy can be rewritten as (A.11)

$$U_e = \frac{1}{2} \sum_{p=1}^{b} \sum_{k=1}^{m} \int_0^{l_p} E_p I_p (\frac{\partial^2 \psi_{pk}}{\partial x_p^2})^2 (\xi_{pk})^2 dx_p$$

$$= \frac{1}{2} \sum_{p=1}^{b} \sum_{k=1}^{m} K_{pk} \xi_{pk}^2 \tag{A.10}$$

where

$$K_{pk} = \int_0^{l_p} E_p I_p (\frac{\partial^2 \psi_{pk}}{\partial x_p^2})^2 dx_p \tag{A.11}$$

If the generalized coordinate is expressed as

$$\{q_j\} = \{\theta_p, \xi_{pk}\}^T, \qquad j = 1, ..., n \tag{A.12}$$

where n (= b + m) is the number of the generalized coordinates, θ_p is the rigid body motion coordinates of link p, ξ_{pk} is the k th modal coordinates of link p, the elastic energy can be rewritten by the generalized coordinates as follows.

$$U_e = \frac{1}{2}\sum_{i=1}^{n}\sum_{j=1}^{n} K_{ij} q_j^2 \tag{A.13}$$

Using the kinetic energy and the potential energy, each term of Lagrange's equation

$$\frac{d}{dt}(\frac{\partial T}{\partial \dot{q}_i}) - \frac{\partial T}{\partial q_i} + \frac{\partial (U_g + U_e)}{\partial q_i} = Q_i \tag{A.14}$$

can be written as follows. If the kinetic energy (A.6) is substituted into (A.13),

$$\frac{d}{dt}(\frac{\partial T}{\partial \dot{q}_i}) = \frac{d}{dt}(\sum_{j=1}^{n} M_{ij}\dot{q}_j) = \sum_{j=1}^{n} M_{ij}\ddot{q}_j + \sum_{j=1}^{n}\frac{dM_{ij}}{dt}\dot{q}_j \tag{A.15}$$

where

$$\frac{dM_{ij}}{dt} = \sum_{k=1}^{n}\frac{\partial M_{ij}}{\partial q_k}\frac{dq_k}{dt} = \sum_{k=1}^{n}\frac{\partial M_{ij}}{\partial q_k}\dot{q}_k \tag{A.16}$$

the first term becomes

$$\begin{aligned}\frac{d}{dt}(\frac{\partial T}{\partial \dot{q}_i}) &= \sum_{j=1}^{n} M_{ij}\ddot{q}_j + \sum_{j=1}^{n}\sum_{k=1}^{n}\frac{\partial M_{ij}}{\partial q_k}\dot{q}_j\dot{q}_k \\ &= \sum_{j=1}^{n} M_{ij}\ddot{q}_j + \sum_{j=1}^{n}\sum_{k=1}^{n}\frac{1}{2}(\frac{\partial M_{ij}}{\partial q_k} + \frac{\partial M_{ik}}{\partial q_j})\dot{q}_j\dot{q}_k\end{aligned}$$

and the second term becomes

$$\begin{aligned}\frac{\partial T}{\partial q_i} &= \frac{\partial}{\partial q_i}(\frac{1}{2}\sum_{j=1}^{n}\sum_{k=1}^{n} M_{jk}\dot{q}_j\dot{q}_k) \\ &= \sum_{j=1}^{n}\sum_{k=1}^{n}\frac{1}{2}\frac{\partial M_{jk}}{\partial q_i}\dot{q}_j\dot{q}_k\end{aligned} \tag{A.17}$$

Next, if the potential energy (A.7) and (A.11) are substituted into (A.13), the third term becomes

$$\begin{aligned}\frac{\partial U_g}{\partial q_i} &= \sum_{p=1}^{b}\int_0^{l_p} g^T\frac{\partial r_p}{\partial q_i}\rho_p A_p dx_p \\ &= \sum_{p=1}^{b}\int_0^{l_p} g^T J_p^{(i)}\rho_p A_p dx_p\end{aligned} \tag{A.18}$$

where $J_p^{(i)}$ is the i th column of Jacobian matrix J_p. The third term can be written by a scalar because the gravity is acting in one direction. Therefore, if the gravity vector has nonzero term in r th row,

$$U_g = G_i g \tag{A.19}$$

where

$$G_i = \sum_{p=1}^{b} \int_0^{l_p} J_p[r,i]\rho_p A_p dx_p \tag{A.20}$$

where $J_p[r,i]$ is r th row and i th column of J_p. The fourth term becomes

$$\frac{\partial U_e}{\partial q_j} = \frac{\partial}{\partial q_j}(\frac{1}{2}\sum_{i=1}^{n}\sum_{j=1}^{m} K_{ij}q_j^2)$$

$$= \sum_{j=1}^{m} K_{ij}q_j \tag{A.21}$$

Therefore, the Lagrangian equations of motion can be written symbolically as follows.

$$\sum_{j=1}^{n} M_{ij}\ddot{q}_j + \sum_{j=1}^{m} K_{ij}q_j + \tag{A.22}$$

$$\sum_{j=1}^{n}\sum_{k=1}^{n} \frac{1}{2}(\frac{\partial M_{ij}}{\partial q_k} + \frac{\partial M_{ik}}{\partial q_j} - \frac{\partial M_{jk}}{\partial q_i})\dot{q}_j\dot{q}_k + G_i g = \tau_i$$

or

$$\sum_{j=1}^{n} M_{ij}\ddot{q}_j + \sum_{j=1}^{n} K_{ij}q_j + \sum_{j=1}^{n}\sum_{k=1}^{n} C_{jk}(i)\dot{q}_j\dot{q}_k + G_i g = \tau_i \tag{A.23}$$

where q is the vector of generalized coordinates, M is the generalized mass matrix, K is the elastic stiffness matrix, C is the coefficient matrix of Coriolis and centrifugal forces, G is the gravity force vector, τ is the generalized force vector.

APPENDIX B

ACTUATOR DYNAMICS

The dynamics of a hydraulic motor is similar to that of an armature-controlled servomotor. In this appendix, the dynamics of the electric motor and the hydraulic motor are summarized and compared.

B.1 Armature Controlled Servomotor

Consider the armature-controlled dc motor shown in Fig. B.1 [55]. In this system, For a constant field current, the flux becomes constant, and the torque becomes directly proportional to the armature current.

$$T = K_i i_a \tag{B.1}$$

where K_i is a motor-torque constant. For a constant flux, the induced voltage e_b is directly proportional to the angular velocity $\dot{\theta}$.

$$e_b = K_b \dot{\theta} \tag{B.2}$$

where K_b is a back emf constant. The differential equation for the armature circuit is

$$L_a \frac{di_a}{dt} + R_a i_a + e_b = e_a \tag{B.3}$$

or

$$L_a \frac{di_a}{dt} + R_a i_a = e_a - K_b \dot{\theta} \tag{B.4}$$

R_a = armature-winding resistance, ohms

L_a = armature-winding inductance, henrys

i_a = armature-winding current, amperes

i_f = field current, amperes

e_a = applied armature voltage, volts

e_b = back emf, volts

θ = angle of the motor, radians

T = torque delivered by the motor, N - m

J = equivalent moment of inertia of the motor and load referred to the motor shaft, $Kg - m^2$

The armature current produces the torque which is applied to the inertia.

$$T = K_i i_a = J\ddot{\theta} \tag{B.5}$$

B.2 Hydraulic Actuator

Consider the servovalve controlled hydraulic motor shown in Fig. B.2 [49]. In this system, The linearized servovalve flow equations are

$$Q_L = K_q x_v - K_c P_L \tag{B.6}$$

where

$Q_L = \frac{Q_1+Q_2}{2}$ = load flow, m^3/sec

$P_L = P_1 - P_2$ = load pressure difference, N/m^2

From the continuity equation of each motor chamber, the continuity equation for all hydraulic actuators is

$$Q_L = D_m\dot{\theta} + C_{tm}P_L + \frac{V_t}{4\beta}\dot{P}_L \tag{B.7}$$

Q_1, Q_2 = forward and return flows, m^3/sec

P_1, P_2 = forward and return pressures, N/m^2

x_v = valve displacement from neutral, m

K_q = valve flow gain, $m^3/sec/m$

K_c = valve flow-pressure coefficient, $m^4.sec/Kg$

D_m = volumetric displacement of motor, m^3/rad

C_{tm} = total leakage coefficient of motor, $m^4.sec/Kg$

V_t = total contained volume of both chamber, m^3

β = effective bulk modulus, N/m^2

T = torque generated by motor, $N-m$

J = total moment of inertia of motor and load referred to motor shaft, $Kg-m^2$

$K_{ce} = K_c + C_{tm}$

= total flow-pressure coefficient, $m^4.sec/Kg$

Thus the load flow Q_L is consumed by flow to displace the actuator, leakage, and flow stored due to compressibility. The leakage is usually neglected. From (B.6) and (B.7),

$$D_m\dot{\theta} + \frac{V_t}{4\beta}\dot{P}_L = K_q x_v - K_{ce}P_L \tag{B.8}$$

or

$$\frac{V_t}{4\beta}\dot{P}_L + K_{ce}P_L = K_q x_v - D_m\dot{\theta} \tag{B.9}$$

where

The torque balance equation is

$$T = P_L D_m = J\ddot{\theta} \tag{B.10}$$

Equations (B.4) and (B.5) resemble equations (B.9) and (B.10), respectively.

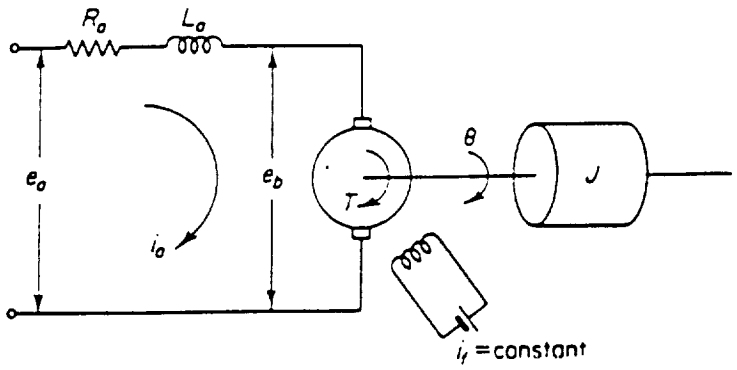

Figure B.1: Schematic diagram of an armature-controlled DC motor

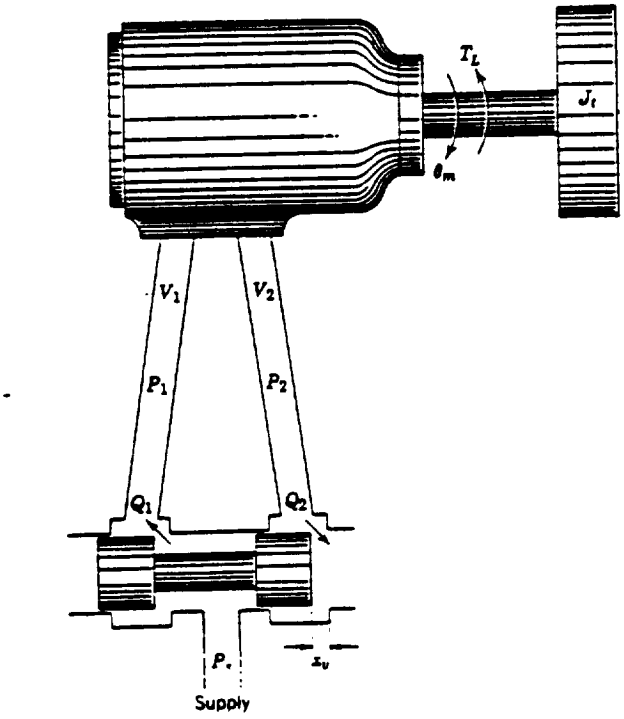

Figure B.2: Schematic diagram of a hydraulic motor

APPENDIX C

Controller Implementation

C.1 Software Implementation

This section gives some comment on data acquisition, transducer voltage conversion, and the computer implementation of path planning of the current controller. The detailed descriptions of controller implementation were explained in J.D. Huggins's thesis [28].

1) A set of assembly language subroutines that could be called from Fortran or C programs are used to derive a programmable clock and the A/D and D/A board. The data is read into the buffer using the subroutine DTSBR and DTSBWB. DTSBR reads the A/D channels. DTSBWB causes the computer to wait until the buffer is full before processing. After initialization, the DTSBR and DTSBWB subroutines can be called repeatedly to transfer the data.

2) Calculate the length of the actuators from read data. The minimum and maximum values of each cylinder length and its digital numbers are measured as in Table C.1. Therefore, the relation between the cylinder length y_i and its digital numbers x_i can be described as equation (C.1).

$$y_i = m_i x_i + b_i \quad (i = 1, 2) \tag{C.1}$$

The coefficient m_i and b_i can be calculated as follows

$$m_1 = \frac{28.750 - 34.406}{1080 + 1941} = -1.4144 \times 10^{-3} \tag{C.2}$$

$$b_1 = 28.750 + 1.41444 \times 10^{-3} \times 1080 = 31.566 \tag{C.3}$$

$$m_2 = \frac{29.625 - 35.375}{1080 + 1941} = -1.903343 \times 10^{-3} \tag{C.4}$$

$$b_2 = 29.625 + 1.903343 \times 10^{-3} \times 1080 = 31.6806 \tag{C.5}$$

3) As shown in Fig. C.1, the attachment points of actuators are offset from the centerline of the beams. The initial angles of each link are calculated from geometry as shown in Fig. C.2.

$$\theta_{10} = \theta_{11} - \theta_{12} + \theta_{13} = 36.575° \tag{C.6}$$

$$\theta_{20} = \theta_{21} - \theta_{22} + \theta_{23} = 70.334° \tag{C.7}$$

where the connecting link and the upper link are not parallel each other due to the bracket offset of the upper link. Therefore, θ_{23} is the angle difference between the connecting link and the upper link.

Table C.1: Cylinder length and its digital number

Cylinder		Length	Number
1	Min	28.750 in	+ 1991
	Max	34.406 in	- 2008
2	Min	29.625 in	+ 1080
	Max	35.375 in	- 1941

4) The path planning algorithm needs the initial position, final position, and the time for the move. The flow chart of path planning and controller is depicted in Fig. C.3.

5) The cylinder position is inversely proportional to the cylinder bore size. Because the two cylinder bore diameters are different, the gains of two amplifiers are different from each other.

C.2 Equipment List

COMPUTER

Model	: Microvax II (vector of VS21W - A2)
Company	: Digital Equipment Co.

ADDITIONAL BOARDS for Micro Vax

Model	: DT2769 - Real Time Clock Board
Model	: DT2785 - Analog I/O system
	8 channels A/D multiplexed
	2 channels D/A
	12 bit resolution
Company	: Data Translation

SIGNAL ANALYZER and DISK STORAGE UNIT

Model	: 3562A - Digital Signal Analyzer
Model	: 9122 - Disk Storage Unit
Company	: Hewlett - Packard Co.

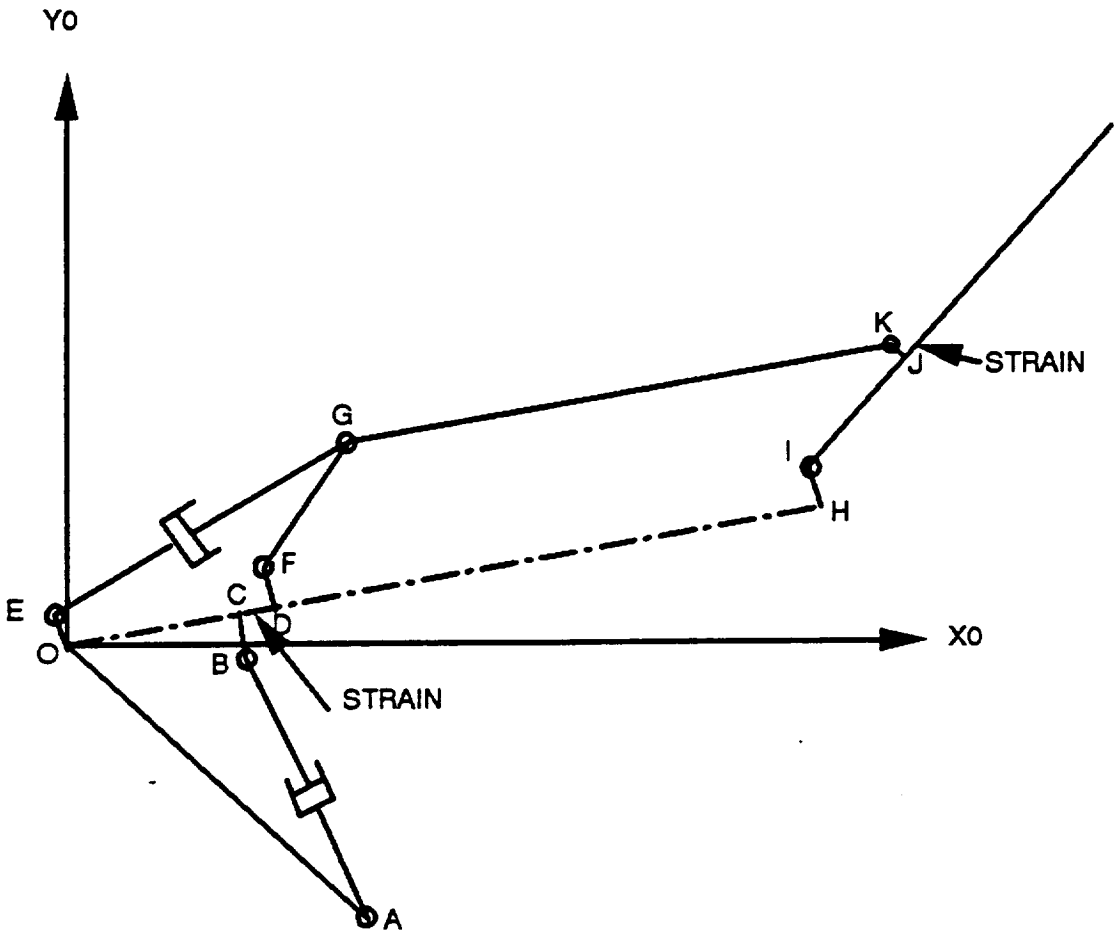

Figure C.1: Attachment points of actuators and bracket offsets of links

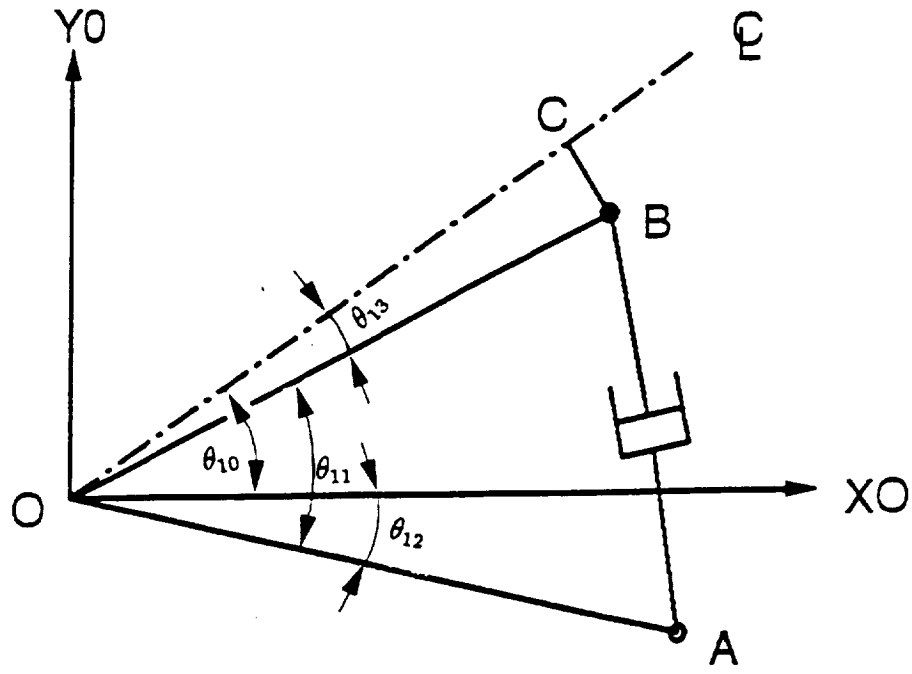

Figure C.2.a: Initial angle of the lower link

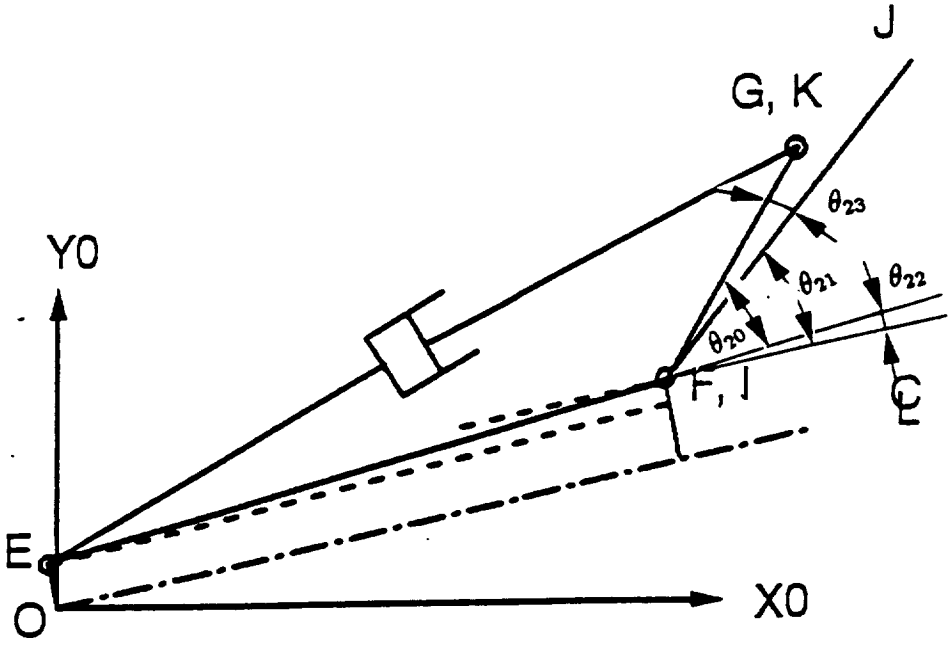

Figure C.2.b: Initial angle of the upper link

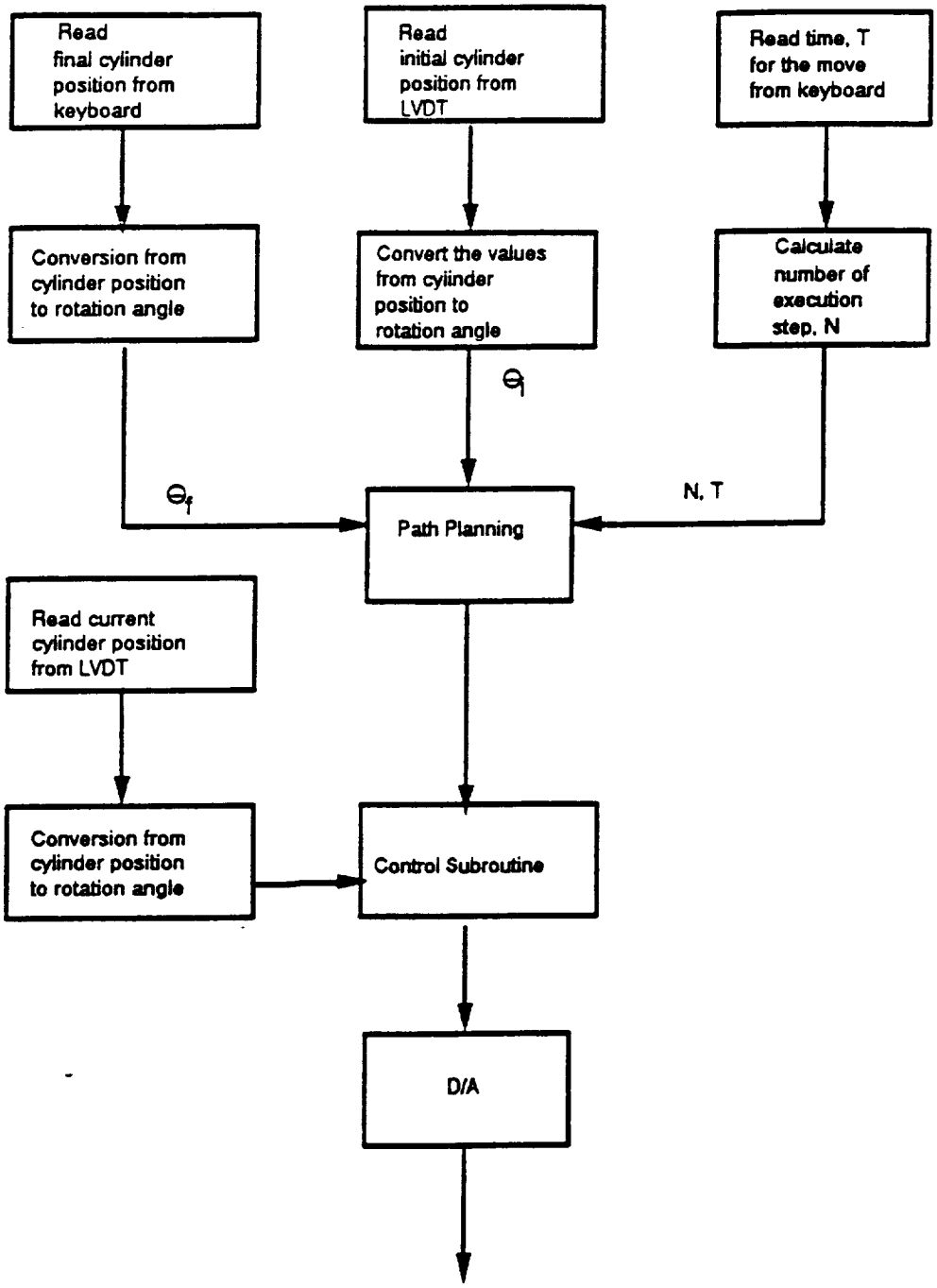

Figure C.3: Flow chart of path planning

STRAIN GAUGE

Model : A - 13 -250MQ - 350

Company : Measurements Group Inc, Micro Measurement Div.

STRAIN GAUGE AMPLIFIER

Model : 3B18 - Wide band

Company : Analog Devices

HYDRAULIC COMPONENTS

Servo Valves

Model : 73 - 102A Two Stage Servovalves - 5 gpm

Company : Moog, Inc

Cylinder of Lower Link

Model : H - PB - 2 Cylinder

Bore : 2.0 in.

Stroke : 20 in.

Rod Diameter : 1.00 in.

Seals : Teflon

Weight : 35 lbs.

Company : Atlas Cylinder Corp.

Cylinders of Upper Link

Model : N2C - 3.25 x 40 Cylinder

Bore	: 3.25 in.
Stroke	: 40 in. (modified to 17 in.)
Rod Diameter	: 1.75 in.
Seals	: Buna - N
Weight	: 52 lbs.
Company	: Hydroline Mfg. Co.

POWER AMPLIFIER

Model	: BOP15 - 20M
Spec.	: 20amp, 15 volt, 300kHz crossover
Company	: KEPCO

APPENDIX D

SMP Code

In this appendix, SMP codes for the derivation of symbolic equations of motion of the lower and the upper links are described. Figure D.1 is the flow chart of SMP code. In these codes, program is separated into several files because one program depletes computer memory. First, Jacobian matrices are derived from the position vectors using MJac function of SMP as shown in Fig. D.2. Several simplication procedures are required to generate a compact form of output. Secondly, elements of the mass matrices and the gravity force vectors are obtained using Jacobian matrices as shown in Fig. D.3. Third, the symmetric elements and the reflective coupling elements of Christoffel symbol are generated as shown in Fig. D.4 and D.5, respectively. Properties which are unique in flexible body dynamics are also included in Fig. D.4. For obtaining more reduced elements of velocity coupling matrices, additional simplications of the output are required by the supervision of the analyst. Finally, velocity coupling matrices are derived as shown in Fig. D.6. using the Christoffel symbol and the matrices are simplified from Fig. D.4 an D.5.

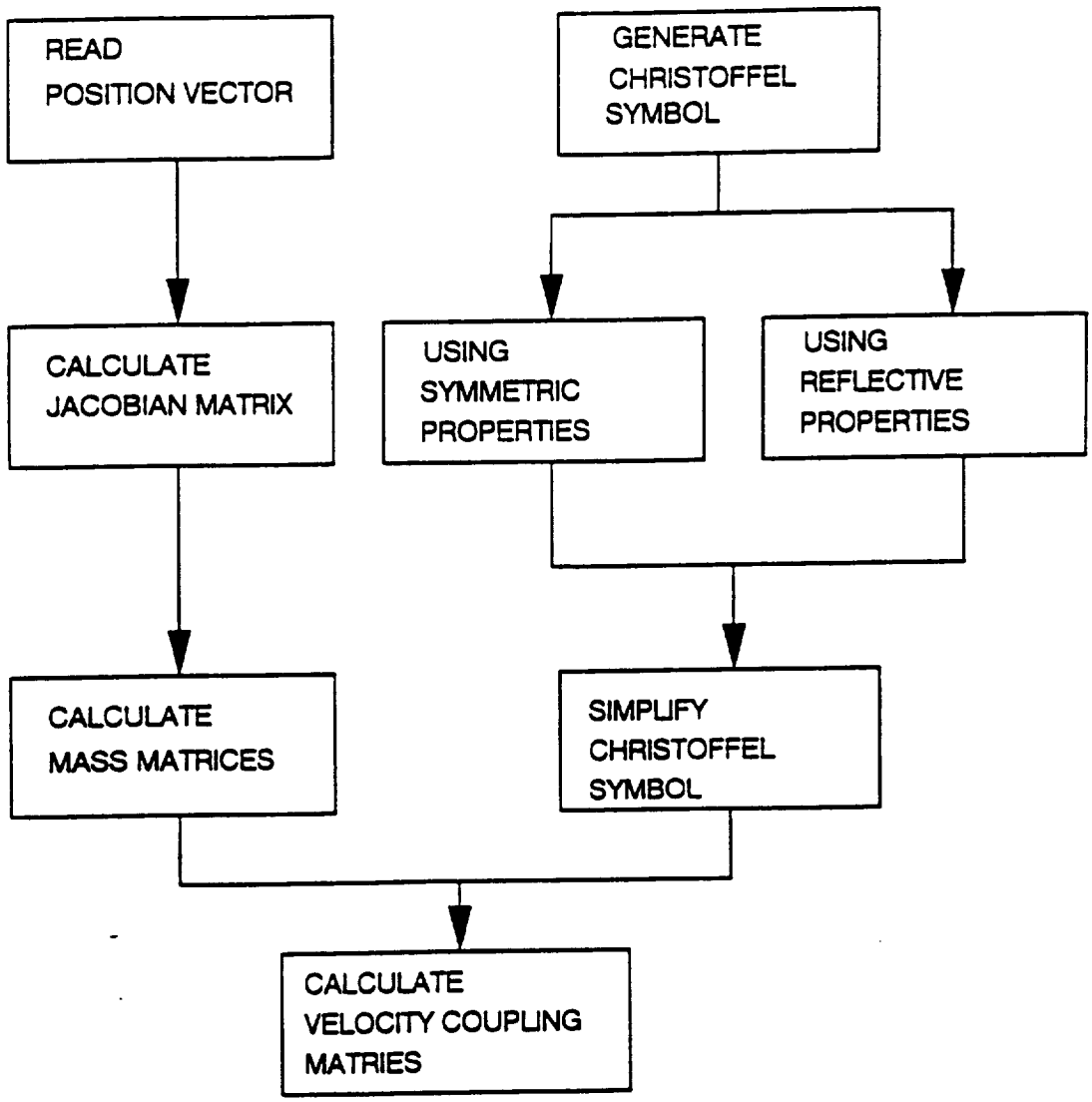

Figure D.1: Flow chart of symbolic program

```
/*  Symbolic Program of Lower and Upper Link */

c1:Cos[th1]
s1:Sin[th1]
c12:Cos[th1+th2]
s12:Sin[th1+th2]

/*   Position vectors */
/*   2 modes per each link */

r1:{x1 c1 - p11 q11 s1 - p12 q12 s1\
      ,x1 s1 + p11 q11 c1 + p12 q12 c1}
r2:{l1 c1-p11e q11 s1-p12e q12 s1 \
     + x2 c12-p21 q21 s12-p22 q22 s12 \
      ,l1 s1+p11e q11 c1+p12e q12 c1 \
     + x2 s12+p21 q21 c12+p22 q22 c12}

/* generalized coordinates */

q:{th1,th2,q11,q12,q21,q22}

/*   Substitutions */

sb0:Sin[$x]^2->1-Cos[$x]^2
sb1:c1 c12->c2-s1 s12
sb2:c1 s12->s2+c12 s1

sb5:p11 q11  + p12 q12 ->u1
sb6:p11e q11 + p12e q12 ->u1e
sb7:p21 q21 + p22 q22 ->u2

/*   Find Jacobian matrices */

<XMJac

jc1:Cb[MJac[r1,q],{-c1,-s1}]          /* Cb: Combine */
jc2:Cb[MJac[r2,q],{-c1,-c12,-s1,-s12}]

jv1:S[jc1,{sb5,sb6,sb7}]              /* S: Substitute */
jv2:S[jc2,{sb5,sb6,sb7}]

jv1t:Trans[jv1]                       /* Trans: Transpose */
jv2t:Trans[jv2]
```

Figure D.2: Symbolic program of Jacobian matrices

```
/*  Find Mass Matrices */

m:(a1 jv1t.jv1 + a2 jv2t.jv2 )

m11:Ex[S[Ex[m[1,1]],{sb0,sb1,sb2}]] /* Ex : Expension */
m12:Ex[S[Ex[m[1,2]],{sb0,sb1,sb2}]]
m13:Ex[S[Ex[m[1,3]],{sb0,sb1,sb2}]]
m14:Ex[S[Ex[m[1,4]],{sb0,sb1,sb2}]]
m15:Ex[S[Ex[m[1,5]],{sb0,sb1,sb2}]]
m16:Ex[S[Ex[m[1,6]],{sb0,sb1,sb2}]]

m22:Ex[S[Ex[m[2,2]],{sb0}]]
m23:Ex[S[Ex[m[2,3]],{sb0,sb1,sb2}]]
m24:Ex[S[Ex[m[2,4]],{sb0,sb1,sb2}]]
m25:Ex[S[Ex[m[2,5]],{sb0}]]
m26:Ex[S[Ex[m[2,6]],{sb0}]]

m33:Ex[S[Ex[m[3,3]],{sb0}]]
m34:Ex[S[Ex[m[3,4]],{sb0}]]
m35:Ex[S[Ex[m[3,5]],{sb0,sb1,sb2}]]
m36:Ex[S[Ex[m[3,6]],{sb0,sb1,sb2}]]

m44:Ex[S[Ex[m[4,4]],{sb0}]]
m45:Ex[S[Ex[m[4,5]],{sb0,sb1,sb2}]]
m46:Ex[S[Ex[m[4,6]],{sb0,sb1,sb2}]]

m55:Ex[S[Ex[m[5,5]],{sb0}]]
m56:Ex[S[Ex[m[5,6]],{sb0}]]

m66:Ex[S[Ex[m[6,6]],{sb0}]]

/*  Find Gravity Vectors  */

g1:a1 jv1[2,1] + a2 jv2[2,1]
g2:a2 jv2[2,2]
```

Figure D.3: Symbolic program of mass matrices and gravity vectors

```
/* Symmetric Property of Christoffel Symbol */

sym::Put[c[j,k,i]=(m[i,j,k] + m[i,k,j] - m[j,k,i])/2, "c1.out"]

/* Simplication */

m[$x,$y,1]:0                          /* independent of theta 1 */
m[$x,$y,$z] - m[$y,$x,$z]:0  /* symmetry */

/* flexible mass matrix is not      */
/* function of flexible coordinates */

Do[i,3,n,Do[j,3,n,m[i,j,$z]:0]]

Do[i,2,Do[j,2,Do[k,j,2,sym]]]
Do[i,2,Do[j,2,Do[k,3,n,sym]]]
Do[i,2,Do[j,3,n,Do[k,j,n,sym]]]
Do[i,3,n,Do[j,2,Do[k,j,2,sym]]]
Do[i,3,n,Do[j,2,Do[k,3,n,sym]]]
```

Figure D.4: Symbolic program of symmetric Christoffel symbol

```
/*  Reflective Coupling Property of Christoffel Symbol*/

ref::If[i>=j & k>=j, Put[c[j,i,k]=-c[j,k,i],"c2.out"]]

Do[i,2,Do[j,2,Do[k,j,2,ref]]]
Do[i,2,Do[j,2,Do[k,3,n,ref]]]
Do[i,2,Do[j,3,n,Do[k,j,n,ref]]]
Do[i,3,n,Do[j,2,Do[k,j,2,ref]]]
Do[i,3,n,Do[j,2,Do[k,3,n,ref]]]
```

Figure D.5: Symbolic program of reflective Christoffel symbol

```
/* Output of Mass matrices Symbolic Program */

c2  : Cos[th2]
s2  : Sin[th2]
u1  : p11 q11 + p12 q12
u1e : p11e q11 + p12e q12
u2  : p21 q21 + p22 q22

/* Mass matrices */

m11 : a1*u1^2 + a1*x1^2 + a2*l1^2 + a2*u1e^2 + a2*u2^2 \
      + a2*x2^2 + 2(a2*c2*l1*x2) + 2(a2*c2*u1e*u2) \
      + -2(a2*l1*s2*u2) + 2(a2*s2*u1e*x2)
m12 : a2*u2^2 + a2*x2^2 + a2*c2*l1*x2 + a2*c2*u1e*u2 \
      + -(a2*l1*s2*u2) + a2*s2*u1e*x2
m13 : a1*p11*x1 + a2*l1*p11e + a2*c2*p11e*x2 + -(a2*p11e*s2*u2)
m14 : a1*p12*x1 + a2*l1*p12e + a2*c2*p12e*x2 + -(a2*p12e*s2*u2)
m15 : a2*p21*x2 + a2*c2*l1*p21 + a2*p21*s2*u1e
m16 : a2*p22*x2 + a2*c2*l1*p22 + a2*p22*s2*u1e
m22 : a2*u2^2 + a2*x2^2
m23 : a2*c2*p11e*x2 + -(a2*p11e*s2*u2)
m24 : a2*c2*p12e*x2 + -(a2*p12e*s2*u2)
m25 : a2*p21*x2
m26 : a2*p22*x2
m33 : a1*p11^2 + a2*p11e^2
m34 : a1*p11*p12 + a2*p11e*p12e
m35 : a2*c2*p11e*p21
m36 : a2*c2*p11e*p22
m44 : a1*p12^2 + a2*p12e^2
m45 : a2*c2*p12e*p21
m46 : a2*c2*p12e*p22
m55 : a2*p21^2
m56 : a2*p21*p22
m66 : a2*p22^2

m21:m12
m31:m13; m32:m23
m41:m14; m42:m24; m43:m34
m51:m15; m52:m25; m53:m35; m54:m45
m61:m16; m62:m26; m63:m36; m64:m46; m65:m56
```

Figure D.6: Symbolic program of velocity coupling matrices

```
/* Elements of Velocity Coupling Matrices */
/* Using Simplified Christoffel Symbol */

 c121 : Ex[1/2*D[m11,th2] ]
 c221 : D[m12,th2]
 c131 : Ex[1/2*D[m11,q11] ]
 c141 : Ex[1/2*D[m11,q12] ]
 c151 : Ex[1/2*D[m11,q21] ]
 c161 : Ex[1/2*D[m11,q22] ]
 c231 : 1/2(D[m12,q11] + D[m13,th2])
 c241 : 1/2(D[m12,q12] + D[m14,th2])
 c251 : Ex[1/2(D[m12,q21] + D[m15,th2]) ]
 c261 : Ex[1/2(D[m12,q22] + D[m16,th2]) ]
 c341 : 1/2(D[m13,q12] + D[m14,q11])
 c351 : 1/2(D[m13,q21] + D[m15,q11])
 c361 : 1/2(D[m13,q22] + D[m16,q11])
 c451 : 1/2(D[m14,q21] + D[m15,q12])
 c461 : 1/2(D[m14,q22] + D[m16,q12])
 c561 : 1/2(D[m15,q22] + D[m16,q21])

 c222 : 1/2*D[m22,th2]
 c132 : Ex[1/2(-D[m13,th2] + D[m21,q11])]
 c142 : Ex[1/2(-D[m14,th2] + D[m21,q12])]
 c152 : 1/2(-D[m15,th2] + D[m21,q21])
 c162 : 1/2(-D[m16,th2] + D[m21,q22])
 c232 : 1/2*D[m22,q11]
 c242 : 1/2*D[m22,q12]
 c252 : 1/2*D[m22,q21]
 c262 : 1/2*D[m22,q22]
 c342 : 1/2(D[m23,q12] + D[m24,q11])
 c352 : 1/2(D[m23,q21] + D[m25,q11])
 c362 : 1/2(D[m23,q22] + D[m26,q11])
 c452 : 1/2(D[m24,q21] + D[m25,q12])
 c462 : 1/2(D[m24,q22] + D[m26,q12])
 c562 : 1/2(D[m25,q22] + D[m26,q21])

 c223 : Ex[1/2(-D[m22,q11] + 2D[m32,th2])]
 c143 : 1/2(-D[m14,q11] + D[m31,q12])
 c153 : 1/2(-D[m15,q11] + D[m31,q21])
 c163 : 1/2(-D[m16,q11] + D[m31,q22])
 c243 : 1/2(-D[m24,q11] + D[m32,q12])
 c253 : 1/2(-D[m25,q11] + D[m32,q21])
 c263 : 1/2(-D[m26,q11] + D[m32,q22])

 c224 : Ex[1/2(-D[m22,q12] + 2D[m42,th2])]
 c154 : 1/2(-D[m15,q12] + D[m41,q21])
 c164 : 1/2(-D[m16,q12] + D[m41,q22])
 c254 : 1/2(-D[m25,q12] + D[m42,q21])
 c264 : 1/2(-D[m26,q12] + D[m42,q22])

 c165 : 1/2(-D[m16,q21] + D[m51,q22])
 c265 : 1/2(-D[m26,q21] + D[m52,q22])
 c225 : 1/2(-D[m22,q21] + 2D[m52,th2])

 c226 : 1/2(-D[m22,q22] + 2D[m62,th2])
```

Figure D.6: (Continued)

APPENDIX E

Modeling of RALF using TREETOPS

In this appendix, the modeling procedures of RALF using TREETOPS are described.

TREETOPS requires several model definition data as follows:

- Bodies
- Modal Data
- Hinges
- Sensors
- Actuators
- Controllers
- Function Generators
- Interconnects
- Devices (Spring/Damper)
- Gravity
- Constraints

The USER'S MANUAL for TREETOPS [73] is recommended reading for more detailed information.

RALF can be expressed by six bodies which are connected by six hinges as shown in Fig. 5.1. Bodies 1, 3, and 5 are assumed as rigid while bodies 2, 4, and 6 are assumed as flexible. The modal data which must be supplied for each of the individual flexible bodies are defined in Table 5.1. These modal data can

Table E.1: Modal data

Modal Mass	$\Psi^T N \Psi$
Modal Stiffness	$\Psi^T K \Psi$
Modal Damping (Optional)	$\Psi^T D \Psi$
Mode Shape of End Point	$\psi(l)$
Mode Slope of End Point	$\psi'(l)$
Modal Linear Momentum	$\int \psi dm$
Modal Angular Momentum	$\int x\psi dm$

be obtained from a NASTRAN output file. However, a NASTRAN/TREETOPS interface program is not available now. The MSC/PAL program can also provide the modal data. The mass properties and center of mass (C.o.M) of rigid bodies and the modal data of the first and the second mode of flexible bodies are shown in Table 5.2. TREETOPS uses MKS units.

Note that the nodal mass matrix, N, is the unaugmented nodal masses and the mode shape matrix, Ψ, is based on the augmented mode shapes. From the loaded interface component mode synthesis, only the augmented masses are obtained. Therefore, the modal mass cannot be obtained from MSC/PAL directly. The modal linear momentum and the modal angular momentum also cannot be

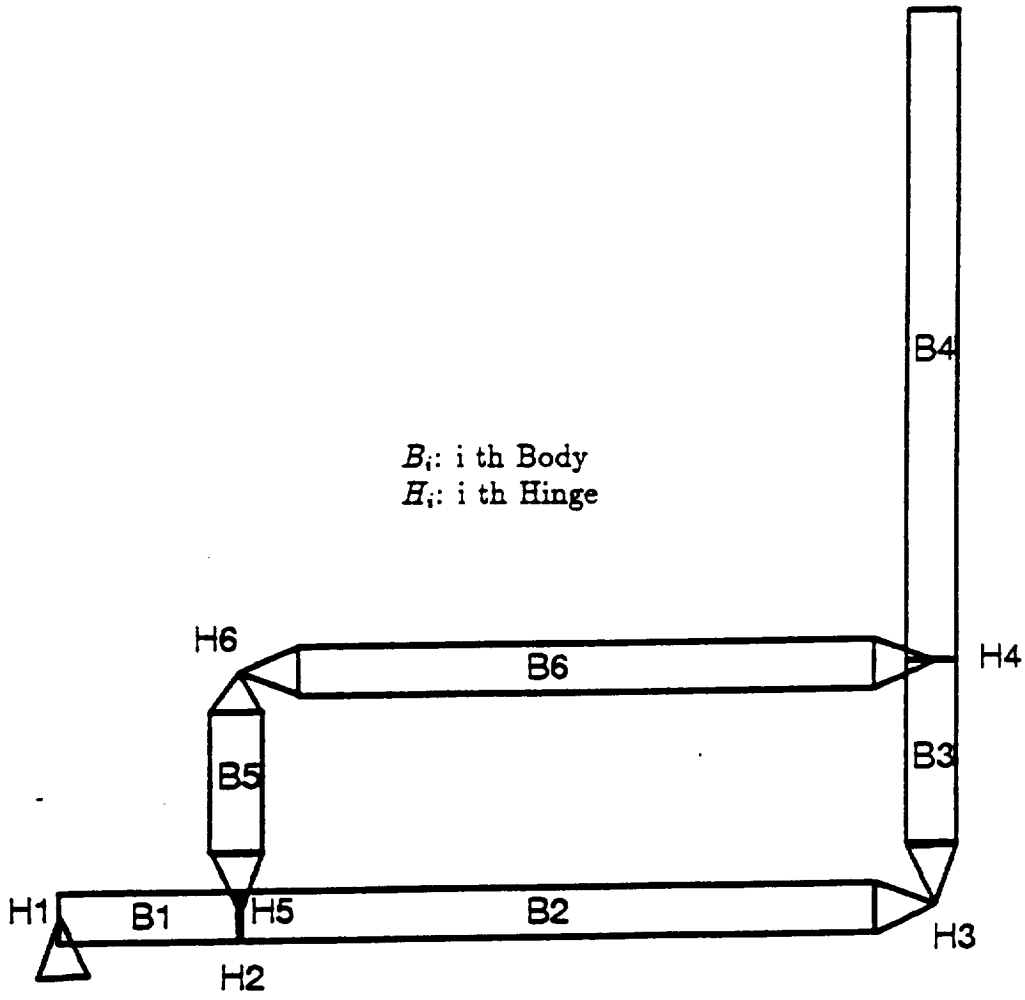

Fig. E.1: Schematic diagram of RALF

Table E.2: Body input data and modal data of RALF

Body Number	1	2	3	4	5	6
Type	Rigid	Flexible	Rigid	Flexible	Rigid	Flexible
Mass[Kq]	9.9577	8.3534	5.9544	8.3470	0.963	5.4465
Inertia [N-m-s^2]	2.3323	13.5980	0.7377	18.944	0.1193	8.8665
C.o.M [m]	0.4191	1.1049	0.3048	1.3208	0.3048	1.1049
$\Psi_1^T N \Psi_1 [Kg]$		7.224		0.8052		0.4804
$\Psi_2^T N \Psi_2 [Kg]$		0.762		0.7879		0.6187
$\Psi_1^T K \Psi_1$ [N/m]		2.2136E4		0.7793E4		1.6711E4
$\Psi_2^T K \Psi_2$ [N/m]		43.0465E4		28.9837E4		34.4127E4
$\sum_{i=1}^{N} \psi_{i1} m_i / m_T$		0.2365		0.2640		0.300
$\sum_{i=1}^{N} \psi_{i2} m_i / m_T$		-0.2886		-0.1408		0
$\sum_{i=1}^{N} x \psi_{i1} m_i$ [Kg-m]		2.9148		3.8867		1.7151
$\sum_{i=1}^{N} x \psi_{i2} m_i$ [Kg-m]		2.6581		-0.5129		0.7611
$\psi_{11}(l)$		0.6054		0.6282		0
$\psi_{12}(l)$		-0.0459		0.6154		0
$\psi'_{11}(l)$		-0.4043		-0.3262		-0.5579
$\psi'_{12}(l)$		0.7854		-1.1028		-1.0134

Notes:

1) Ψ_1, Ψ_2 : the node displacement vectors of 1st and 2nd mode.

2) ψ_{i1}, ψ_{i2} : the node displacement of node i of 1st and 2nd mode.

calculated by MSC/PAL directly. Therefore, a post processing program is required. The modal linear momentum and the modal angular momentum are computed from the lumped mass method. In TREETOPS data, the modal linear momentum is divided by the total mass m_T. The modal angular momentum terms are obtained from the cross product of the beam length axis and the link deflection. Therefore, the direction of the modal angular momentum is perpendicular to the plane defined by the x axis and the link deflection. Tachometer, position sensors, and torque motors are located at the hinge 1 and 5. The decentralized PD controllers which are composed of the feedback of angular positions and angular velocities are added at the hinge 1 and 5. Interconnection between sensors, function generator, controller, and actuator are shown in Fig. E.2. The constraint is imposed between the body 3 and 6.

There are two basic steps to running the program. TREESET is an interactive preprocessor to define model data. It generates the PROBLEM.INT file. TREETOPS is a batch processor to run the PROBLEM.INT file. Time response is saved in the PROBLEM.PLT file. Mass, stiffness, and damping matrices are saved in the PROBLEM.AUX file. The linear coefficients in matrix form (A,B,C,D) are saved in PROBLEM.MAT.

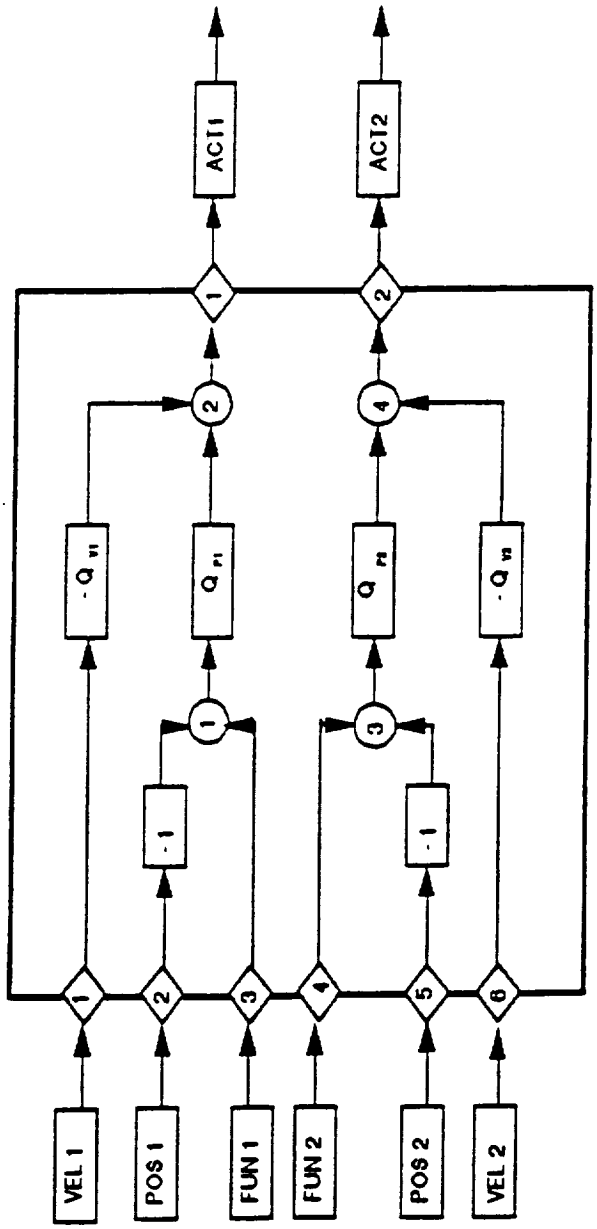

Fig. E.2: Interconnection between sensors, controllers, and actuators

Bibliography

[1] Asada, H., and Youcef-Toumi, K., "Analysis and Design of a Direct-Drive Arm with a Five-Bar-Link Parallel Drive Mechanism," *ASME Journal of Dynamic Systems, Measurement, and Control*, 106, Sep. 1984, pp 225-230.

[2] Asada, H., and Slotine, J.-J.E., "Robot Analysis and Control," *John Wiley & Sons, Inc*, 1986.

[3] Barbieri, E., and *Özgüner, Ü.*, "Unconstrained and Constrained Mode Expansions for a Felxible Slewing Link," *ASME Journal of Dynamic Systems, Measurement, and Control*, Vol. 110, Dec. 1988, pp 416-421.

[4] Baumgarte, J., "Stabilization of Constraints and Integrals of Motion," *Computational Methods in Applied Mechanics in Engineering*, Vol.1, 1982, pp 1-16.

[5] Bayo, E., "Computed Torque For The Position Control Of Open-Chain Flexible Robots," *Proc. IEEE International Conf. on Robotics and Automation*, 1988, pp 316-321.

[6] Benfield, W.A., and Hruda, R.F., "Vibration Analysis of Structures by Component Mode Substitution," *AIAA Jounal*, 9(7), Jul. 1971, pp 1255-1261.

[7] Book, W.J., Maizza-Neto, O., and Whitney, D.E., "Feedback Control of Two Beam, Two Joint Systems With Distributed Flexibility," *ASME Journal of Dynamic Systems, Measurement, and Control*, 97(4), Dec. 1975, pp 424-431.

[8] Book, -W.J., " Analysis of Massless Elastic Chains With Servo Controlled Joints," *ASME Journal of Dynamic Systems, Measurement, and Control*, 101(3), Sep. 1979, pp 187-192.

[9] Book, W.J., Majette, M., "Controller Design for Flexible, Distributed Parameter Mechanical Arms Via Combined State Space and Frequency Domain Technique," *Journal of Dynamic Systems, Measurement, and Control*, 105, Dec. 1983, pp 245-254.

[10] Book, W.J., "Recursive Lagrangian Dynamics of Flexible Manipulator Arms," *The International Journal of Robotics Research*, 3(3), Fall 1984, pp 87-101.

[11] Book, W.J., "Modeling, Design, and Control of Flexible Manipulator Arms: Status and Trends," *Proc. the NASA conference on Space Telerobotics*, Jan. 31 - Feb. 2, 1989, Pasadena, CA.

[12] Boyle, J-M. Ford, M.P., and Maciejowski, J.M., "A Multivariable Toolbox for use with Matlab," *American Control Conference*, June 1988, Atlanta, GA, pp 707-712.

[13] Burdick, J., "An Algorithm for Generation of Efficient Manipulator Dynamic Equations," *Proc. IEEE International Conf. on Robotics and Automation*, San Francisco, CA, 1986, pp 212-218.

[14] Cetinkunt, S., "Symbolic Modelling and Dynamic Analysis of Flexible Manipulators," *Proc. IEEE International Conf. on Robotics and Automation*, Rayleigh, NC, 1987, pp 2074 - 2080.

[15] Cetinkunt, S., "On Motion Planning and Control of Multi-Link Lightweight Robotic Manipulators," *Ph.D. Thesis, School of Mechanical Engineering, Georgia Institute of Technology*, Dec. 1987.

[16] Chang, C.O., and Nikravesh, P.E., "An Adaptive Constraint Violation Stabilization Method for Dynamic Analysis of Mechanical Systems", *ASME Journal of Mechanisms, Transmissions, and Automation in Design*, 107, Dec 1985, pp 488-493.

[17] Chodas, J.L, and Man, G.K., "Design of the Galieo Scan Platform Control," *Journal of Guidance, Control, and Dynamics*, Vol. 7, July - Aug. 1984, p422.

[18] Chung, Y.C., Book,W.J., and Lu,S.S., "Modeling and Optimal Control of Lightweight Bracing Manipulator," *Internal Report, School of Mechanical Engineering, Georgia Tech*, May, 1986.

[19] Craig, R.R. Jr., and Bampton, M.C.C., "Coupling of Substructures for Dynamic Analysis," *AIAA Journal*, 6(7), Jul. 1968, pp 1313-1319.

[20] Doyle, J.C., and Stein, G., "Multivariable Feedback Design: Concepts for a Classical/Modern Synthesis," *IEEE Transaction on Automatic Control*, 26, Feb. 1981, pp 4-16.

[21] Golla, D.F., Garg, S.C., and Hughes, P.C., "Linear State-Feedback Control of Manipulators," *Mechanism & Machine Theory*, Vol.16, 1981, pp 93 - 103.

[22] Greewood, D.T., "Classical Mechanics", *Prentice - Hall*, 1977.

[23] Hablani, H.B., "Constrained and Unconstrained Models: Some Modeling Aspect of Flexible Spacecraft," *Journal of Guidance and Control*, 5(2), 1982, pp 164-173.

[24] Hanafusa, H., Asada, H., and Mikoshi, T., "Design of Electrohydraulic Servo Systems for Articulated Robot Arm Control," *IFAC Pneumatic & Hyraulic Components*, Warsaw, Poland, 1980, pp 223-228.

[25] Hastings, G.G., "Controlling Flexible Manipulators, An Experimental Investigation," *Ph.D. Thesis, School of Mechanical Engineering, Georgia Institute of Technology*, Aug. 1986.

[26] Hollerbach, J.M., "A Recursive Lagrangian Formulation of Manipulator Dynamics and a Comparative Study of Dynamic Formulation Complexity," *IEEE Trans. Systems, Man. and Cybernetics*, 10(11), Nov. 1980, pp 730-736.

[27] Hou, S.N., "Review of Modal Synthesis Techniques and a New Approach," *Shock and Vibration Bulletin*, 40(4), 1969, pp 25-30.

[28] Huggins, J.D., " Experimental Verification of a Model of a Two-Link Flexible, Lightweight Manipulator," *M.S. Thesis, School of Mechanical Engineering, Georgia Institute of Technology*, June 1988.

[29] Hughes, P.C., "Modal Identities for Elastic Bodies with Application to Vehicle Dynamics and Control," *Journal of Applied Mechanics*, 47(1), Mar. 1980, pp 177-184.

[30] Hughes, P.C., "Space Structure Vibration Modes: How Many Exist? Which Ones Are Important?," *IEEE Control Systems Magazine*, FEb. 1987, pp 22-28.

[31] Hurty, W.C., "Vibrations of Structural Systems by Component Mode Synthesis," *Proc. of the American Society of Civil Engineering*, Aug. 1960 Vol86, pp 51-69.

[32] Ider, S.K., Amirouche, F.M.L., "Coordinate Reduction in the Dynamics of Constrained Multibody Systems - A New Approach," *Journal of Applied Mechanics*, Dec. 1988, Vol. 55, pp 899-904.

[33] IMSL Reference Manual, IMSL Inc, 1985.

[34] Kane, T.R., and Levinson, D.A., "The Use of Kane's Dynamical Equations in Robotics," *The International Journal of Robotics Research*, 2(3), Fall 1983, pp 3-20.

[35] Kanoh, H., and Lee, H.G., "Vibration Control of One-Link Flexible Arm," *Proc. of 24th IEEE Conf. on Decision and Control*, 3, Dec. 1985, pp 1172-1177.

[36] Katic, D. and Vukobratovic, M., "The Influence of Actuator Model Complexity on Control Synthesis for High Performance Robot Trajectory Tracking," *IFAC Theory of Robotics*, Vienna, Austria, 1986, pp 217-222.

[37] Kim, S.S., Vanderploeg, M.J., "QR Decomposition for State Space Representation of Constrained Mechanical Dynamic Systems," *ASME Journal of Mechanisms, Transmissions, and Automation in Design*, 108, Jun 1986, pp 183-188

[38] Klema, V.C., and Laub, A.J., "The Singular Value Decomposition; Its Computation and Some Applications," *IEEE Transaction on Automatic Control*, 25, 1980, pp 164-176.

[39] Liang, C.G., and Lance, G.M., "A Differential Null Space Method for Constrained Dynamic Analysis", *ASME Journal of Mechanisms, Transmissions, and Automation in Design*, 109, Dec 1987, pp 405-411.

[40] Krishnan, H., and Vidyasagar, M., "Bounded Input Discrete-Time Control of A Flexible Beam: Theory, Simulation and Experimental Results", *ASME Winter Meeting*, Chicago, 1988, pp 1 - 16.

[41] Low, K.H., "A Systematic Formulation of Dynamic Equations for Robot Manipulators with Elastic link," *Journal of Robotic Systems*, 4(3) 1987, pp 435-456.

[42] Luh, J.Y.S., Walker, M.W., and Paul, R.P.C., " On-Line Computational Scheme for Mechanical Manipulators," *ASME Journal of Dynamic Systems, Measurement, and Control*, 102, June 1980, pp 69-76.

[43] Luh, J.Y.S., and Zheng, Y.F., "Computation of Input Generalized Forces for Robots with Closed Kinematic Chain Mechanism," *IEEE Journal of Robotics and Automation*, 1(2), Jun. 1985, pp 95-103.

[44] MacFarlane, A.G.J. ed., "Frequency-Response Methods in Control Systems," *IEEE Press*, 1979.

[45] Maizza - Neto, O., "Modal Analysis and Control of Flexible Manipulator Arms," *PhD Thesis, Dept. of Mechanical Engineering, MIT*, 1974.

[46] Mani, N.K., Haug, E.J, and Atkinson, K.E., "Application of Singular Value Deconposition for Analysis of Mechanical System Dynamics," *ASME Journal of Mechanisms, Transmissions, and Automation in Design*, 107, Mar. 1985, pp. 82-87.

[47] Meldrum, D.R., and Balas, M.J., "Application of Model Reference Adaptive Control to a Flexible Remote Manipulator Arm," *Proc. American Control Conference*, 1986, pp 825-832.

[48] Megahed, S., and Renaud, M., "Dynamic Modelling of Robot Manipulators Containing Closed Kinematic Chains," *Advanced Software in Robotics*, Liege, Belgium, May 1984, pp 147-159.

[49] Merritt, H.E., "Hydraulic Control Sytem," *John Wiley & Sons, Inc*, 1967.

[50] Moon, F.C., " Chaotic Vibration: An Introduction for Applied Scientists and Engineers," *John Wiely & Sons*, 1987.

[51] MSC/PAL2 Users Manual, MSC Inc, 1987.

[52] Murray, J.J., and Neuman, .C.P., "ARM: An Algebraic Robot Dynamic Modeling Program," *Proc. of the First International IEEE Conference in Robotics*, Mar. 1984, pp 103-114.

[53] Nelson, W.L., and Mitra, D., "Load Estimation and Load Adaptive Optimal Control for a Flexible Robot Arm," *Proc. IEEE International Conf. on Robotics and Automation*, San Francisco, CA, Mar. 1986, pp 206-211.

[54] Nikravesh, P.E, "Some Methods for Dynamic Analysis of Constrained Mechanical System: A Survey," *Computer Aided Analysis and Optimization of Mechanical System Dynamics, E.J.Haug, ed., Springer-Verlag*, Heidelberg, West Germany, 1984.

[55] Ogata, K, "Modern Control Engineering," *Prentice-Hall*, 1970.

[56] Ower, J.C., and Van De Vegte, J., "Classical Control Design and a Flexible Manipulator: Modeling and Control System Design", *IEEE Journal of Robotics and Automation*, RA-3, 5, Oct., 1987, pp 485-489.

[57] Park, T.W., and Haug. E.J., "A Hybrid Numerical Integration Method for Machine Dynamic Simulation", *ASME Journal of Mechanisms, Transmissions, and Automation in Design*, 108, Dec 1986, pp 211-216.

[58] Pfeiffer, F., Gebler, B., and Kleemann, U., "On Dynamics and Control of Elastic Robots," *IFAC-Symposium on Robot Control*, 1988, pp 4.1-4.5.

[59] Punyapas, N., "The design of Hydraulic Valve Circuit under Microprocessor Control for Increasing efficiency of Hydraulic Servo System," *Ph.D. Thesis, School of Mechanical Engineering, Georgia Institute of Technology*, Mar. 1982.

[60] Rovnēr, D.M., and Cannon, R.H.,Jr., "Experiments Toward On-line Identification and Control of a Very Flexible One-Link Manipulator," *The International Journal of Robotic Research*, 6(4), 1987, pp 3-19.

[61] Sakawa, Y., Mauno, F., and Fukushima, S., "Modeling and Feedback Control of a Flexible Arm," *Journal of Robotic Systems*, 2(4), 1985, pp 453-472.

[62] Schmitz, E., "Experiments on The End-Point Position Control of a Very Flexible One-Link Manipulator," *Ph.D. Thesis, Department of Aeronautics and Astronautics, Stanford University*, Jun. 1985.

[63] Schutter, J.D., et al., "Control of Flexible Robots Using Generalized Nonlinear Decoupling," *IFAC-Symposium on Robot Control*, 1988, pp 98.1-98.6.

[64] Siciliano, B. and Book, W.J., "A Singular Perturbation Approach to Control of Lightweight Flexible Manipulator," *The international Journal of Robotics Research*, 7(4), 1988, pp 79-89.

[65] Siciliano, B., Yuan, B., Book, W.J., "Model Reference Adaptive Control of a One Link Flexible Arm," *IEEE Conf. Decision and Control*, 1986, pp 91-95.

[66] Shabana, A.A., "Substructure Synthesis Method for Dynamic Analysis of Multi-Body Systems," *Journal of computers and Structures*, 20(4), 1985, pp 737-744.

[67] Singh, R.P., and Linkins, P.W., "Singular Value Decomposition for Constrained Dynamic Systems," *ASME Journal of Applied Mechanics*, 52(4), Dec. 1985, pp 943- 948.

[68] Skelton, R.E., Hughes, P.C., and Hablani, H.B., "Order Reduction for Models of Space Structures Using Modal Cost Analysis," *Journal of Guidance and Control*, 5(4), 1982, pp 351-357.

[69] SMP Reference Manual. *Inference Corporation*, 1983.

[70] Sunada, W., and Dubowsky, S., "On the Dynamic Analysis and Behavior of Industrial Robotic Manipulator with Elastic Members," *Journal of Mechanisms, Transmissions, and Automation in Design*, 105, Mar. 1983, pp 42-51.

[71] Tourassis, V.D., and Neuman, C.P., "Properties and Structure of Dynamic Robot Models for Control Engineering Applications," *Mechanism and Machine Theory*, 20(1), 1985, pp 27-40.

[72] Tourassis, V.D., and Neuman, C.P., "The Inertial Characteristics of Dynamic Robot Models," *Mechanism and Machine Theory*, 20(1), 1985, pp 41-52.

[73] TREETOPS Users Manual, *DYNACS*, Clearwater, Florida, 1989.

[74] Tsujisawa, T., "A Reduced Order Model Derivation for Lightweight Arms with A Parallel Mechanism," *Proc. IEEE International Conf. on Robotics and Automation*, Scottsdale, AZ, May 1989.

[75] Venkatraman, V. and Mayne, R.W., "Dynamic Behavior of a Hydraulically Actuated Mechanism part 1: Small Perturbations," *Journal of Mechanisms, Transmissions, and Automation in Design*, 108, June 1986, pp 245-249.

[76] Wehage, R.A., and Haug, E.J., "Generalized Coordinate Partitioning for Dimension Reduction in Analysis of Constrained Dynamic Systems," *ASME Journal of Mechanical Design*, 104(1), 1982, pp 247-255.

[77] Wie, B., Lehner, J.A., and Plescia, C.T., "Roll/Yaw Control of a Flexible Spacecraft Using Skewed Bias Momentum Wheels," *Journal of Guidance, Control, and Dynamics*, Vol. 8, July-Aug. 1985, pp 447-453.

[78] Wie, B., and Byun, K., "New Generalized Structural Filtering Concept for Active Vibration Control Synthesis," *Journal of Guidance and Control*, 12 (2), Mar.-Apr. 1989, pp 147-154.

[79] Wilson, T.R., "The Design and Construction of a Flexible Manipulator," *M.S. Thesis, School of Mechanical Engineering, Georgia Institute of Technology*, Dec. 1985.

[80] Yang, Y.P., and Gibson, J.S., "Adaptive Control of a Manipulator with a Flexible Link," *Journal of Robotic Systems*, 6(3), 1989, pp 217-232.

[81] Yocum, J.F., and Slater, L.I., "Control System Design in the Presence of Severe Structural Dynamics Interactions," *Journal of Guidance, Control, and Dynamics*, Vol. 1, Mar.- Apr., 1978, pp 109-116.

[82] Yuan, B. -S., "Adaptive Strategies for Position and Force Controls of Flexible Arms," *Ph.D. Thesis, School of Mechanical Engineering, Georgia Institute of Technology*, Mar. 1989.

[83] Yuh, J., "Application of Discrete-Time Model Reference Adaptive Control to a Single-Link Flexible Robot," *Journal of Robotic Systems*, 4(5), 1987, pp 621-630.

[84] Yurkovich, S., and Pacheco, F.E., "On Controller Tuning for a Flexible-Link Manipulator with Varying Payload," *Journal of Robotic Systems*, 6(3), 1989, pp 233-254.

VITA

Jeh Won Lee was born in [redacted] on [redacted]. He received the B.S. degree in Mechanical Engineering from Seoul National University in 1979 and the M.S. degree in Mechanical Engineering from Korea Advanced Institute of Science and Technology (KAIST) in 1981. After graduation, he worked in Daewoo Motor Company for one year and in Daewoo Heavy Industries for three and half years.

During that time. he was married to a lovely lady, Kyung[redacted] and had one daughter, Yoo Jin.

He started his doctor degree program at the school of mechanical engineering of Georgia Institute of Technology in January, 1985. He was a teaching assistant and a research assistant.

His master thesis topic was *An application of PID control law to machine tool chatter control using electro - hydraulic actuator.* In Daewoo Heavy Industries, he was a key member of development of an arc welding robot. He currently works at Pointing Control Branch of Structures & Dynamics Division of Marshall Space Flight Center in Huntsville. His current interesting research area is Robotics, Dynamics and Control of multi-body flexible structures.